SQUID Detected Low-Field NMR for the Evaluation of Internal Fruit Quality

By

Derrick Steven van Zyl

Thesis presented in partial fulfilment of the requirements for the degree of *Master of Science in Engineering*
at
Stellenbosch University

Supervisor: Prof. W. J. Perold
Department of Electric and Electronic Engineering

December 2010

Declaration

By submitting this thesis electronically, I declare that the entirety of the work contained therein is my own, original work, that I am the owner of the copyright thereof (unless to the extent explicitly otherwise stated) and that I have not previously in its entirety or in part submitted it for obtaining any qualification.

December 2010

Abstract

SQUID Detected Low-Field NMR for the Evaluation of Internal Fruit Quality

D.S. van Zyl

Department of Electrical and Electronic Engineering,
University of Stellenbosch,
Private Bag X1, Matieland 7602, South Africa.

Thesis: M.Sc.Eng. (Elec)

December 2010

Assessing the quality of fruit has become vitally important for farmers and growers. With retailers placing ever stricter requirements on fresh produce, growers have to spend a greater amount of time and effort sorting and grading their harvest. Increasingly, vendors are placing requirements not only on external factors like colour, and firmness, but on internal quality factors such as sugar content and acidity, because, although consumers buy fruit based on their external appearances, the taste of the fruit is what determines whether the consumer will buy again. Different techniques exist that probe the internal quality of fruit non-destructively. The technique most widely used today is Near Infrared Spectroscopy. This technique is powerful, but has certain limitations such as poor reliability and the need for constant recalibration. This thesis suggests an alternative method for evaluating internal fruit quality based on low-field nuclear magnetic resonance detected by superconducting quantum interference devices. It introduces the theory of SQUIDs and NMR, and evaluates the use of SQUID detected NMR spectroscopy as a method for determining the internal quality of fruit. The fabrication techniques and processes are explained in detail and a design for a SQUID detected NMR spectrometer is given. Relevant simulations and simulation results are also

given. No working SQUID could be fabricated and, as such, no working NMR spectrometer was demonstrated. This thesis serves as a reference work for future research.

Opsomming

SKWIT-bespeurde Lae-Veld KMR vir die Beöordeling van Interne Vrugtekwaliteit

("SQUID detected Low-Field NMR for the Evaluation of Internal Fruit Quality")

D.S. van Zyl

Departement Elektries en Elektroniese Ingenieurswese,
Universiteit van Stellenbosch,
Privaatsak X1, Matieland 7602, Suid Afrika.

Tesis: M.Sc.Ing. (Elek)

Desember 2010

Bepaling van die gehalte van vrugte het vir boere uiters belangrik geword. Met kleinhandelaars wat al strenger vereistes plaas op vars produkte moet boere meer tyd en inspanning bestee met die sortering en gradering van hul oes. Handelaars plaas nie net vereistes op eksterne kwaliteitsfaktore soos kleur en fermheid nie, maar begin al hoe strenger vereistes plaas op interne kwaliteitsfaktore soos suikerinhoud en suurgehalte, want, hoewel verbruikers vrugte koop op grond van hul eksterne kwaliteitsfaktore, is dit die smaak van die vrug wat bepaal of die verbruiker weer die vrug sal koop. Verskillende tegnieke bestaan wat die interne kwaliteit van vrugte op 'n nie-destruktiewe manier kan bepaal. Die mees algemene tegniek is Naby Infrarooi Spektroskopie. Hierdie tegniek is kragtig maar het sekere beperkings soos swak betroubaarheid en die noodsaaklikheid van konstante herkalibrasie. Hierdie tesis stel 'n alternatiewe metode vir die evaluering van interne vrugkwaliteit gebaseer op lae-veld kernmagnetiese resonans waargeneem deur supergeleidende kwantum inmenging toestelle voor. Dit stel die teorie van SKWITs en KMR bekend, en evalueer die gebruik van SKWIT-bespeurde KMR spektroskopie as 'n metode vir die bepaling van die

interne kwaliteit van vrugte. Die fabrikasie tegnieke en prosesse word in detail verduidelik en 'n ontwerp vir 'n SWKIT opgevangde KMR spektrometer word gegee. Toepaslike simulasies en simulasie resultate word ook gegee. Geen werkende SKWIT kon vervaardig word nie en as gevolg daarvan kon geen werkende KMR spektrometer gedemonstreer word nie. Hierdie tesis dien as 'n naslaan werk vir toekomstige navorsing.

Acknowledgements

I would like to express my sincere gratitude to the following people and organisations:

Ulrich Büttner for always being prepared to help, always coming up with new ideas and always going above and beyond the call of duty to ensure that everything was ready and available for me to conduct my research.

Alexis van Zyl for always helping me with problems and answering my questions, no matter how busy he was, and for being my "interactive whiteboard", off of whom I bounced many ideas and problems.

Elian van Zyl for never letting me take myself too seriously

Tina van Zyl for reading and rereading every inch of this thesis looking for errors.

Prof. Willem J. Perold for his unerring enthusiasm and for providing guidance when needed.

Bernard van Zyl and Vizier Systems for funding this work.

Dedications

This thesis is dedicated to my parents, Dirk and Tina.

Contents

Declaration **i**

Abstract **ii**

Opsomming **iv**

Acknowledgements **vi**

Dedications **vii**

Contents **viii**

List of Figures **xii**

List of Tables **xx**

1 Introduction **1**

1.1 An Introduction to Fruit Quality Measurements 1

1.2 An Overview of this Thesis 2

2 Fruit Quality Measurements **4**

2.1 Introduction 4

2.2 Fruit Quality 4

2.3 Measuring Fruit Quality 6

2.4 Measuring Table Grape Quality 7

3 Nuclear Magnetic Resonance **12**

3.1 Introduction 12

3.2 A Brief History of NMR 13

3.3 Basic Principles of Nuclear Magnetic Resonance 13

3.4 NMR Spectroscopy 22

4 Superconductivity 28
4.1 Introduction 28
4.2 A Brief History of Superconductivity 28
4.3 Fundamental Considerations of Superconductivity 31
4.4 Current Flow in a Superconductor 41
4.5 Flux Quantization 42
4.6 Josephson Junctions and the Josephson Effects 44

5 SQUID Theory 59
5.1 Introduction 59
5.2 The Basic DC SQUID 60
5.3 Loop Inductance and the Screening Parameter 63
5.4 Flux-to-Voltage Conversion 64
5.5 Practical SQUIDs 66
5.6 Noise Theory in SQUIDs 71

6 SQUID Electronics 75
6.1 Introduction 75
6.2 SQUID Small Signal Response 75
6.3 Basic Flux-Locked Loop 77
6.4 Flux-Locked Loop Design 77
6.5 Line Delay 80
6.6 Additional Positive Feedback 80

7 Design and Manufacture of Practical SQUIDs 83
7.1 Introduction 83
7.2 DC SQUID Magnetometer Design 83
7.3 Grain Boundry Junctions 88
7.4 Fabrication Parameters and Procedures 91

8 SQUID detected NMR 100
8.1 Introduction 100
8.2 Motivation for SQUID detected NMR 101
8.3 Detecting NMR signals using SQUIDs 102
8.4 Prepolarization 105

9 Simulations **107**
9.1 Introduction . . . 107
9.2 Josephson Junction Simulations . . . 108
9.3 SQUID simulations . . . 112
9.4 NMR Simulations . . . 124

10 Design and Fabrication **139**
10.1 Introduction . . . 139
10.2 SQUID Design and Manufacture . . . 139
10.3 NMR Spectrometer Design and Manufacture . . . 145
10.4 Design of a Flux Locked Loop . . . 152

11 Measurements and Results **162**
11.1 Introduction . . . 162
11.2 Cryogenic Cooling and the Measurement of Superconductive Properties . . . 162
11.3 Four-Point Measurement Setup . . . 166
11.4 Results of Study . . . 167

12 Conclusion **169**
12.1 Review of Chapters . . . 169
12.2 Review of Results . . . 170
12.3 Future Work . . . 171

Appendices **173**

A Quantum Mechanical Formalism **174**
A.1 Introduction . . . 174
A.2 Review of Quantum Theory . . . 174
A.3 Extending the Schrödinger Equation to Three Dimensions . . . 176
A.4 Function Spaces . . . 177
A.5 Formalism . . . 179
A.6 The Uncertainty Principle . . . 180
A.7 Angular Momentum . . . 182

B Quantum Spin **187**
B.1 Introduction . . . 187

B.2 Quantum Spin 187
B.3 Measurement of Angular Momentum: Quantum Indeterminacy . 189
B.4 Ensemble of Spin Particles 189

C Derivation of the London Equations **191**

D Program Listing **194**
D.1 MATLAB Programs for Creating Segmented FastHenry Structures 194
D.2 MATLAB Programs for Simulating NMR 198
D.3 C Program for Magnet Control Board 202

E Datasheets **206**
E.1 Introduction 206
E.2 PIC18F2520 206
E.3 OPA657U 255
E.4 M1000 260

Bibliography **265**

List of Figures

2.1 A customer evaluates the intrinsic properties of a product to assign quality. This assigned quality is combined with the customer's preferences and the current market situation to determine acceptability [1]. 5

3.1 The Energy levels of the ^2H nucleus, and the nuclear spin quantum numbers associated with each. 15
3.2 Randomly directed spin polarizations in a sample. 18
3.3 The splitting of degenerate energy levels of ^1H in a magnetic field. . 18
3.4 Spin precession. 19
3.5 A sample of particles develops a nett magnetic moment after being placed in a magnetic field. 21
3.6 Rotating the Nett Magnetic Moment (NMM) by $\pi/2$ radians. (The externally applied magnetic field is in the z-direction.) (a) Before the RF magnetic pulse is applied the NMM is in the same direction as the externally applied magnetic field. (b) After the RF magnetic pulse the NMM lies in the x-y plane and rotates at the Larmor frequency. If a coil is placed perpendicular to the x-y plane the passing NMM induces a current in it (Faraday detection). 21
3.7 A simple pulse sequence. 25
3.8 Spin-echo pulse sequence [2]. 25

4.1 Transition of a material from the normal state to the superconducting state. 32
4.2 Levitation of a small magnet above a superconductor, demonstrating the Meissner effect [3]. 34

4.3 Change in electron and superelectron densities in a superconductor near T_c. (n_n represents the normal electron density.) 35
4.4 The different states of a Type II superconductor. H_{c1} represents the first critical field and H_{c2} the second. With an applied field below H_{c1} the superconductor is in its normal superconducting, or Meissner, state. Above H_{c2} the superconductive properties of the material are lost and the material is normal. Between H_{c1} and H_{c2} the superconductor is in the vortex state. [4]) 40
4.5 Contour of integration around a non-superconducting hole in a superconductor.) 43
4.6 Josephson junction structures. (a) Different weak link structures: (i) Superconductor-Normal metal-Superconductor (SNS) junction, (ii) Micro-bridge structure, (iii) Point-contact structure. (b) Tunnel junction structure: Superconductor-Insulator-Superconductor (SIS) structure. [5]) 45
4.7 A schematic representation of the wave functions of two superconductors separated by an insulator. (a) The width of the insulating barrier is small enough that the wave functions can overlap ($width < \zeta$) and tunnelling can occur. (b) The width of the insulating barrier is so large that the wave functions do not overlap ($width > \zeta$) and tunnelling does not occur. [5] 46
4.8 The $I - V$ curve for a Josephson junction. [4] 47
4.9 A Josephson junction. 47
4.10 Josephson junction circuit symbol. 48
4.11 (a)Josephson junction circuit symbol. (b) Equivalent circuit of a Josephson junction according to the RCSJ model. 51
4.12 (a)Josephson junction circuit symbol. (b) Equivalent circuit of a Josephson junction according to the RSJ model. 52
4.13 Normalized Voltage-Current characteristic curve of an overdamped Josephson junction. 53
4.14 Normalized instantaneous voltage across an overdamped Josephson junction for different values of applied current. 54
4.15 Average current through an overdamped Josephson junction driven by an AC voltage source. 56

4.16 Current versus average voltage of an overdamped Josephson junction driven by an AC current source (Shapiro Steps). 57
4.17 Magnetic field dependence of the critical current of a Josephson junction. 58

5.1 Superconducting loop interrupted by two Josephson junctions, forming a DC SQUID. 60
5.2 Maximum critical current of a DC SQUID with negligible loop inductance as a function of applied flux. 62
5.3 Voltage-current characteristic curve of a DC SQUID with $\beta_L = 1$. . 65
5.4 Voltage-flux response of a DC SQUID with $\beta_L = 1$ for various biasing currents. 66
5.5 Schematic representation of a flux transformer. 67
5.6 Schematic representation of the layout of a large-area washer DC SQUID 68
5.7 Schematic representation of a directly coupled DC SQUID (not to scale) [6]. 70

6.1 Actual output voltage and straight line approximation for the output of a DC SQUID with $\beta_L = 1$ and $I_b = 3.4$ for small signals. . . 76
6.2 Schematic layout of a basic flux-locked loop. 77
6.3 Block diagram of FLL system. (a) Complete system block diagram. (b) Simplified block diagram. 78
6.4 Schematic of APF circuit. 81
6.5 Average voltage across a DC SQUID (a) without APF (b) with APF. 82

7.1 Two nodes, N1 and N2, connected by an element E1 in *FastHenry*. . 85
7.2 A schematic to show a problem in *FastHenry* simulations. (a) Two elements connected by *FastHenry*. (b) Because the elements are connected by the nodes, the current flowing through the elements is forced to concentrate at each node (note that in this figure red means a high, yellow a medium and green a low current density. . . 86
7.3 A *FastHenry* line that has been segmented. The width of the line has been divided into 5 segments, while the length has been divided into 18. (a) Actual segmented line. (b) Segmented line with widths of segments reduced to a fifth of the size for clarity 87

7.4 YBCO deposited onto a step-edge forming a Josephson junction. The differently shaded areas of the YBCO layer represent different crystal orientations. 89
7.5 YBCO deposited onto a bi-epitaxial substrate forming a Josephson junction. The differently shaded areas of the YBCO layer represent different crystal orientations. 90
7.6 YBCO deposited onto a bicrystal substrate forming a Josephson junction. The differently shaded areas of the YBCO layer represent different crystal orientations. 91
7.7 Schematic diagram of a PLD system [5]. 95
7.8 Cutaway schematic of an ICM system. 96
7.9 Photolithography process. (a) Sample after photoresist is applied. (b) Sample after developing. P - Photoresist layer; Sup - Superconductor layer; Sub - Substrate 97
7.10 Milling process. (a) Sample after photoresist is applied and developed. (b) Sample after milling. P - Photoresist layer; Sup - Superconductor layer; Sub - Substrate 98

8.1 Schematic diagram of a SQUID detected cw NMR spectrometer [7]. 103
8.2 Schematic diagram of a SQUID detected pulsed NMR spectrometer [8]. 104
8.3 Timing diagram for magnets in SQUID detected pulsed NMR experiment [8]. 105
8.4 Evolution of the magnetization of a sample in a SQUID detected NMR experiment. (a) The magnetization is almost entirely along the x-axis, with the prepolarization field in the x-direction and the measurement field in the y-direction. (b) The magnetization is in the y-direction after the prepolarization field is switched off. (c) A $(\pi/2)$ pulse flips the magnetization into the z-direction. (d) The magnetization precesses in the x-z-plane, creating the NMR signal. (e) The pulse sequence of the magnetic fields applied to the sample. The direction of each magnetic field is indicated in brackets after its name. [9] 106

9.1 *SPICE* model of a Josephson junction. Note the value of C is equal to $\frac{\Phi_0}{2\pi}$. 109

9.2 Simulation results of a Josephson with $I_c = 10\mu A$ and $R_n = 10\Omega$ with an applied current of $20\mu A$. Note that *V(out)* is the voltage across the junction. 110
9.3 Simulation results of a Josephson with $I_c = 10\mu A$ and $R_n = 10\Omega$ with an applied current of $5\mu A$. Note that *V(out)* is the voltage across the junction. 110
9.4 Simulation results of a Josephson with $I_c = 10\mu A$ and $R_n = 10\Omega$ with an applied current of $11\mu A$. Note that *V(out)* is the voltage across the junction. 111
9.5 Simulation results of a Josephson with noise. Here $I_c = 30\mu A$ and $R_n = 10\Omega$ with an applied current of $31\mu A$. 112
9.6 Broadening of Josephson junction power spectral density due to noise. 113
9.7 *SPICE* model of DC SQUID. 114
9.8 *SPICE* model of inductances used to apply flux to simulated SQUID loop. 114
9.9 *SPICE* model for $500MHz$, 2-pole Butterworth filter. 114
9.10 *SPICE* simulation results of DC SQUID with $\beta_L = 3$: current-voltage relationship. (a) No thermal noise present. (b) Thermal noise with $500MHz$ bandwidth present. Note that the outside I-V curve shows the response to an applied flux of Φ_0, while the inside I-V curve shows the response to an applied flux of $\Phi_0/2$. 116
9.11 *SPICE* simulation results of DC SQUID with $\beta_L = 1$: current-voltage relationship. (a) No thermal noise present. (b) Thermal noise with $500MHz$ bandwidth present. Note that the outside I-V curve shows the response to an applied flux of Φ_0, while the inside I-V curve shows the response to an applied flux of $\Phi_0/2$. 116
9.12 *SPICE* simulation results of DC SQUID with $\beta_L = 1/2$: current-voltage relationship. (a) No thermal noise present. (b) Thermal noise with $500MHz$ bandwidth present. Note that the outside I-V curve shows the response to an applied flux of Φ_0, while the inside I-V curve shows the response to an applied flux of $\Phi_0/2$. 117

9.13 *SPICE* simulation results of DC SQUID with $\beta_L = 3$: flux-voltage relationship. (a) No thermal noise present. (b) Thermal noise with $1MHz$ bandwidth present (c) Thermal noise with $500MHz$ bandwidth present. The applied flux is swept from $-3\Phi_0$ to $3\Phi_0$. 118
9.14 *SPICE* simulation results of DC SQUID with $\beta_L = 1$: flux-voltage relationship. (a) No thermal noise present. (b) Thermal noise with $1MHz$ bandwidth present (c) Thermal noise with $500MHz$ bandwidth present. The applied flux is swept from $-3\Phi_0$ to $3\Phi_0$. 119
9.15 *SPICE* simulation results of DC SQUID with $\beta_L = 1/2$: flux-voltage relationship. (a) No thermal noise present. (b) Thermal noise with $1MHz$ bandwidth present (c) Thermal noise with $500MHz$ bandwidth present. The applied flux is swept from $-3\Phi_0$ to $3\Phi_0$. 120
9.16 *SPICE* simulation results of DC SQUID with $\beta_L = 3$: small signal response. (a) No thermal noise present. (b) Thermal noise with $1MHz$ bandwidth present (c) Thermal noise with $500MHz$ bandwidth present. 121
9.17 *SPICE* simulation results of DC SQUID with $\beta_L = 1$: small signal response. (a) No thermal noise present. (b) Thermal noise with $1MHz$ bandwidth present (c) Thermal noise with $500MHz$ bandwidth present. 122
9.18 *SPICE* simulation results of DC SQUID with $\beta_L = 1/2$: small signal response. (a) No thermal noise present. (b) Thermal noise with $1MHz$ bandwidth present (c) Thermal noise with $500MHz$ bandwidth present. 123
9.19 Results of a *MATLAB* simulation of a ^1H nucleus in a z-directed magnetic field: Evolution of the expectation value of spin $\langle S \rangle$ . . . 126
9.20 Results of a *MATLAB* simulation of a ^1H nucleus in a z-directed magnetic field: $\langle S_x \rangle$ vs. Time 127
9.21 *MATLAB* code used to model fluctuation in spin during precession. a and b represent the spin state's values (9.4.3). 128
9.22 Simulation of 1^H nucleus in a z-directed magnetic field with spin fluctuations. 129
9.23 Simulation of rotation of 1^H nucleus in a z-directed magnetic field. 129

9.24 Simulation results of the traverse magnitization of an ensemble of 6 non-interacting spin-1/2 particles in a $50\mu T$ z-directed magnetic field. 134
9.25 Simulation results showing the FFT of the traverse magnitization of an ensemble of 6 non-interacting spin-1/2 particles in a $50\mu T$ z-directed magnetic field. 135
9.26 A dichloroacetaldehyde molecule. 136
9.27 Simulation results showing the FFT of the traverse magnitization of an ensemble of 2 interacting spin-1/2 particles in a $50\mu T$ z-directed magnetic field. This is the simulated spectrum of dichloroacetaldehyde in a $50\mu T$ magnetic field. 137
9.28 A $2, 2, 2$-trifluoroethanol molecule. 137
9.29 Simulation results showing the FFT of the traverse magnitization of an ensemble of 6 interacting spin-1/2 particles in a $53.9\mu T$ z-directed magnetic field. This is the simulated spectrum of $2, 2, 2$-trifluoroethanol in a $53.9\mu T$ magnetic field. 138
9.30 Experimentally obtained spectrum of $2, 2, 2$-trifluoroethanol in a $53.9\mu T$ magnetic field, as reported by [10]. 138

10.1 New heating element for the ICM at the Department of Electrical and Electronic Engineering at the University of Stellenbosch. (a) New heating element. (b) Close-up of sample holder on heating element. (c) Close-up of sample clamp. 142
10.2 Light incident on a bicrystal line. (a) Light incident perpendicular to the bicrystal line is not reflected by the bicrystal line, and the bicrystal line is therefore invisible. (b) Light incident at a angle is scattered by the bicrystal line, making it visible. 143
10.3 Fabricated Josephson junctions on a $SrTiO_3$ bicrystal mounted on a PCB. 144
10.4 A Helmholtz pair. (a) Physical construction. [11] (b) Generated magnetic field. [12] 146
10.5 Electromagnet in Helmholtz pair configuration for x-directed magnetic field. 147
10.6 Electromagnet in Helmholtz pair configuration for y-directed magnetic field. 147
10.7 Schematic for the control board for the NMR spectrometer. 149

10.8 Schematic of relay connections on control board. 150
10.9 Control board for NMR spectrometer. 150
10.10Pseudo code for experiment algorithm. 152
10.11Basic layout of flux locked loop. 153
10.12Flux locked loop feedback electronics. 154
10.13Schematic of the flux locked loop pre-amplifier design. 156
10.14Schematic of the flux locked loop integrator design. 156
10.15Schematic of the full flux locked loop design. 157
10.16*SPICE* model used for the simulation of the FLL. 158
10.17Simulation results of FLL with the input flux of the SQUID linearly varied between 0 and Φ_0, and then to $-\Psi_0$. 159
10.18Simulation results of FLL with the input flux of the SQUID a sinusoidal signal with an amplitude of Φ_0 and a $10MHz$ frequency. . 159
10.19Simulation results of FLL with the input flux of the SQUID a sinusoidal signal with an amplitude of Φ_0 and a $50MHz$ frequency. . 160
10.20Simulation results of FLL with the input flux of the SQUID a sinusoidal signal with an amplitude of $10\Phi_0$ and a $10MHz$ frequency. 160
10.21Fabricated FLL. 161

11.1 Cryogenic cooler setup. (a) The cooling chamber and the vacuum pump. (b) The cryogenic cooling unit. 164
11.2 Control unit for cryogenic cooler. 165
11.3 Susceptibility test setup. 165
11.4 Susceptibility test results of a YBCO layer grown using the new heating element. 166
11.5 Four-Point measurement setup. 167
11.6 *Mr. SQUID* control and measurement box. 168

List of Tables

2.1 General Composition of Grapes [13]. 9

3.1 A List of Nuclear Isotopes and their Properties. 16
3.2 RF pulse phase jargon [2]. 26

4.1 Critical temperatures of several superconducting materials. The top four are low-T_c materials while the bottom three are high-T_c materials. [5] 33

7.1 Different substrates for YBCO thin film devices [5]. 93

9.1 Properties of Simulated SQUIDs. 115

Chapter 1

Introduction

The beginning of the twentieth century was marked by an incredible technological breakthrough - the liquefaction of helium - and with it the discovery of one of the most exciting phenomena ever observed, superconductivity.

Superconductors are materials which display remarkable electric and magnetic properties at very low temperatures. Because of their properties they find applications in a wide variety of places, from space exploration to the medical sciences. One of the most common applications of superconductors today is the Superconducting QUantum Interference Device or SQUID, a device that can be used to measure magnetic fields with incredible sensitivity.

1.1 An Introduction to Fruit Quality Measurements

Intensive research in many countries has resulted in the development of a large variety of different cultivars of every species of fruit and vegetable. These cultivars are grown in different regions, under different conditions, using different practices and techniques, and thus vary greatly in every quality index, both internal and external. Assessing the quality of fruit has therefore become vitally important for growers in order for them to grade and sort their harvest.

With vendors placing ever stricter requirements on fresh produce, growers have to spend a greater amount of time and effort sorting and grading their harvest.

Increasingly, vendors are placing requirements not only on external factors

like colour, and firmness, but on internal quality factors such as sugar content and acidity, because, although consumers buy fruit based on their external appearances, the taste of the fruit is what determines whether the consumer will buy again.

Methods for determining the internal quality factors, however, rely on destructive techniques. These techniques can cause the grower to incur huge losses. The need for machines that test internal quality factors non-destructively is therefore great.

Today different non-destructive techniques exist. The most widely used technique today is called Near Infrared Spectroscopy and works by irradiating the fruit with infrared light and extracting information from either the transmitted or reflected light, or both [14]. This technique suffers from certain limitations, though, such as poor reliability, the frequent need for recalibration and high cost [15].

The motivation therefore exists to search for novel methods of measuring fruit quality non-destructively. Nuclear Magnetic Resonance (NMR), being a non-invasive and sensitive technique, is a prime candidate for such non-destructive techniques.

NMR is the same technology used in medical MRI scanners. These machines are very large and very expensive. This is because the magnets required are very large and need to be very homogeneous. Large magnets are needed because the NMR signal is extremely weak, but scales with magnetic field strength. Conventional sensors consist of coils that detect NMR signals by the change in magnetic flux threading the coil.

By replacing the conventional sensor in an NMR device with the extremely sensitive SQUID device the requirement of very large magnetic field strengths greatly relaxes and it becomes possible to build small, inexpensive NMR devices to measure the internal quality of fruit.

1.2 An Overview of this Thesis

This thesis describes the basic theory, design and manufacture of a SQUID-detected NMR machine to detect the internal quality of table grapes. In order to understand the design and operation of the SQUID-detected NMR machine, a basic understanding of superconductivity, SQUIDs and the theory of NMR,

as well as the fabrication procedures and techniques for SQUIDs is required.

Chapter 2 introduces the somewhat elusive concept of fruit quality, and how it is measured. Special attention is given to the physiology and quality indices of table grapes.

Chapter 3 describes the theory of nuclear magnetic resonance. This chapter introduces the basic principles of NMR and NMR spectroscopy. A brief history of the development of NMR is also included.

In Chapter 4 superconductivity is introduced. A thorough understanding of the theory and principles of superconductivity is required in order to understand SQUIDs, and it is described in detail in this chapter. The Josephson junction is also introduced and mathematically described.

The Josephson junction is the most fundamental building block of the Superconducting QUantum Interference Device, introduced in Chapter 5. In this thesis only the direct current (DC) SQUID is considered. Chapter 5 describes the theory and operation of the DC SQUID in great detail.

The DC SQUID requires electronics to linearize its output. The principles and design of these electronics are discussed in Chapter 6.

Chapter 7 describes how practical DC SQUIDs are designed and manufactured, detailing the fundamental constraints to consider when designing DC SQUIDs and the entire fabrication process.

In Chapter 8 the two main subjects of the thesis up to this point, NMR and SQUIDs, are combined. This chapter explains how SQUID-detected NMR operates and how to implement it.

Simulations are invaluable in understanding the operation of Josephson junctions, SQUIDs and NMR. Chapter 9 describes how such simulations can be done, and reports the results of different simulations that were done to confirm the theory of Josephson junctions, SQUIDs and NMR.

The design and manufacture of the entire SQUID-detected NMR machine is detailed in Chapter 10, while Chapter 11 details the measurements and results of the experiments.

The thesis concludes with discussions of the conclusions made and recommendations for future research in Chapter 12.

Chapter 2

Fruit Quality Measurements

2.1 Introduction

Fruit quality is an elusive concept, depending on many factors. Fruit quality not only depends on the fruit itself, but on the preferences of the consumer and the market environment. To clearly discuss the concept of quality, one first needs to define what is meant by quality.

In this chapter the concept of fruit quality is discussed. After an introduction to fruit quality in broad terms and a definition of what is meant by fruit quality, the chapter moves on to discuss how fruit quality is measured. Finally, special attention is given to table grapes and how to measure their quality.

2.2 Fruit Quality

Quality of fruit and vegetable products is very elusive and difficult to define [16], and many studies have been undertaken to pin down the concept of quality and determine how to control it [16, 17, 18, 19, 20]. Tijskens et al. [16] combined different aspects of these studies into one theory on product quality and acceptability. This theory was further extended by Sloof et al. in 1996 [1]. The main difference between Sloof's theory and its predecessors was the fact that it differentiated between assigned quality and acceptability of products.

Fruit quality is generally accepted to depend on three factors: the intrinsic properties of the fruit, the preferences of the consumer and the market situation [1]. The consumer assigns a quality value to the product based on its intrinsic properties (e.g. colour, shape, firmness, sweetness). This assigned quality is

combined with the consumer's own preferences (e.g. intended use of product, attitude toward the product) and the current market situation (e.g. cost of product, availability of competing products) to determine the acceptability of the product [1, 16]. The acceptability of a product determines whether the customer will purchase the product.

Figure 2.1 shows a schematic representation of the process of determining acceptability of a product.

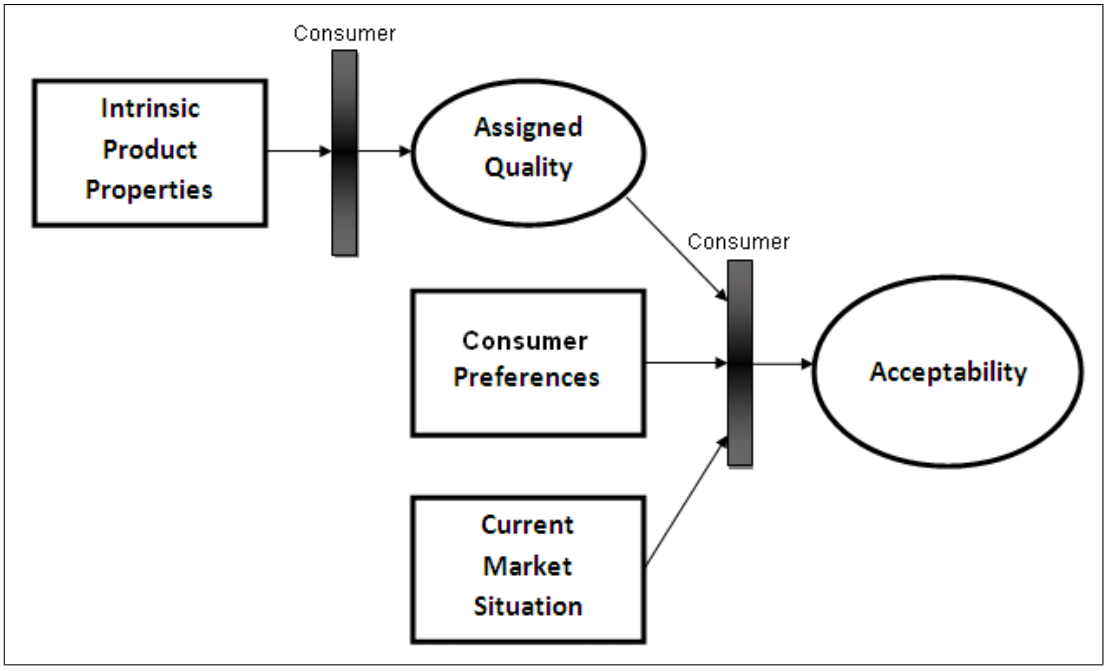

Figure 2.1: A customer evaluates the intrinsic properties of a product to assign quality. This assigned quality is combined with the customer's preferences and the current market situation to determine acceptability [1].

Consumer preference and market situation are studied by consumer and market researchers who try to increase the acceptability of a product by economic means only, without changing the product. This falls outside the scope of this thesis.

The assigned quality of a product depends solely on the intrinsic properties of the product, and is studied by producers and distributors to improve the product itself. These intrinsic properties can be quantitatively measured in different ways, as discussed in Section 2.3. The intrinsic properties of fruit are what this thesis will be concerned with.

For the remainder of this thesis we will use the term "fruit quality" to mean the intrinsic properties of fruit.

2.3 Measuring Fruit Quality

There are many attributes, both internal and external, that determine the quality of fruit. Normally fruit marketed to consumers is graded according to familiar external characteristics such as size and colour. It is, however, the internal qualities such as titratable acidity, pH and soluble solids content that determine their taste, and although consumers buy fruit based on their appearance, their satisfaction and possible repeat purchase of the fruit is based on the taste and flavour quality [21]. As such it is important to be able to measure the internal quality attributes of fruit.

2.3.1 Appearance Quality Factors

Appearance quality factors include size, shape and colour. Another important quality attribute is freedom from defects, damage and decay. [21] These attributes are external attributes and can easily be measured non-destructively.

It is important to note that external quality factors can vary over the fruit (for example, an apple can be more red on one side than the other), making it more difficult to characterize them.

2.3.2 Textural Quality factors

Quality factors that influence the texture of the fruit include firmness, crispness, juiciness and mealiness [21]. These factors are usually tested for in a destructive manner. Furthermore, although some of the textural quality attributes (e.g. firmness) can be measured in a quantitative way, others can only be tested for in a qualitative way (such as mealiness), making the use of tasters very necessary in deciding the quality of the fruit.

2.3.3 Flavour Quality Factors

Eating quality factors depend on the taste of the fruit. Factors that influence these quality factors are sweetness (types and concentrations of sugars),

sourness (types and concentrations of acids), astringency (phenol compounds) and aroma (types and concentrations of odour-active compounds). Unwanted tastes can be created by fermentative metabolites (such as ethanol and acetaldehyde). [21]

Flavour quality factors depend on the chemical composition of the fruit. The most important factors to measure are the sugar content and the acidity.

Sugar content is measured in degrees Brix (^oBx), where 1 ^oBx equals 1 gram of sucrose in 100 grams of water, and is usually measured by a refractometer[1].

Acidity is measured in two different ways. The total acidity or titratable acidity of a solution is a measure of all the hydrogen ions available, that is, both free, unbound hydrogen ions and hydrogen ions associated with weak acids that do not release all their hydrogens into a solution [22]. pH is a measure of only the unassociated hydrogen ions in solution [22]. In fruit these two values usually approximate one another.

2.4 Measuring Table Grape Quality

This section investigates the physiology of the table grape (*Vitis vinifera*), and the factors that determine its quality.

2.4.1 Botany of Grapes

The grape vine belongs to the genus *Vitis*. Although *Vitis* includes many species, over 90% of grapes produced in the world today are from the *Vitis vinifera* species, either as pure *vinifera* or as hybridized *vinifera* species. [13]

Table grapes are grapes grown for the purpose of being consumed as fresh fruit. The berries are large, attractive, have fine flesh and grow in large clusters. Table grape berries usually have low acidity and small or no seeds. [13]

[1]When a solution is measured by a refractometer, the value obtained represents the amount of all dry solids dissolved in the solution, not just sugars. For fruit, however, this value represents a good approximation of the total amount of sugar present.

2.4.2 Berry Development, Maturation and Ripening

The growth of grape berries follows a double sigmoid pattern, with the fast growth phases (phase I and III) separated by a slow (lag) growth phase (phase II). The berries expand in size during phase I and phase III. During phase I the berry is green and hard. In this phase both cell division and cell expansion causes the berry to increase in size, while during phase III only cell expansion is responsible for growth. Growth during phase III is also associated with tissue softening, loss of green colour and the development of the pigment anthocyanin in coloured varieties. [13]

The start of the ripening period in grapes is called veraison, and marks the beginning of sugar accumulation and acid loss. Grapes are a non-climacteric fruit, meaning they do not continue ripening after harvest.

As the berry matures, the amount of sugar in the berry increases and the amount of acid decreases. At ripening there is a sharp increase in total sugars, the fructose-to-glucose ratio increases and the acid concentration decreases. Tannins, the complex esters of phenolic acids and sugars that give grapes an astringent taste, increase in concentration as the berry matures. The aroma compounds only start accumulating during the last stages of ripening. [13]

Grapes harvested at a firm, ripe stage store better than grapes harvested at an under ripe or overripe stage [13].

2.4.3 Chemical Composition of Grapes

Like all fruit, the chemical composition of grapes varies according to the environment the grapes are grown in. Soil conditions, available light, temperature and moisture, along with other environmental factors, all influence the composition of the grape. Table 2.1 lists the most important components found in grapes and their respective ranges of concentration.

2.4.3.1 Sugars

In *Vinifera* grapes, glucose and fructose account for around 99% of carbohydrates in the must[2], and between 12% and 27% of the total weight of the mature berries [13]. At veraison the ratio of fructose to glucose is around 1, but there is slightly less glucose present in ripe berries.

[2]Freshly squeezed grape juice, containing the skin, seeds and stems of the fruit.

Table 2.1: General Composition of Grapes [13].

Constituents	**(%) of Volume of Fresh Juice**
Water	$70 - 80$
Carbohydrates	$15 - 25$
Dextrose(Glucose)	$8 - 13$
Levulose(Fructose)	$7 - 12$
Pentoses	$0.01 - 0.05$
Pectin	$0.01 - 0.10$
Inositol	$0.02 - 0.08$
Organic Acids	$0.3 - 1.5$
Tartaric	$0.2 - 1.0$
Malic	$0.1 - 0.8$
Citric	$0.01 - 0.05$
Tannins	$0.01 - 0.10$
Nitrogenous Compounds	$0.03 - 0.17$
Protein	$0.001 - 0.1$
AminoAcids	$0.017 - 0.11$
Humin	$0.001 - 0.002$
Minerals	$0.3 - 0.6$

The sugar content of table grapes is usually measured in degree Brix (^oBx). Although the Brix scale is defined with respect to the weight of sucrose in solution, measurements of fructose or glucose solutions give closely matching results to measurements of sucrose solutions on the Brix scale, motivating the use of the unit. (For example, an 11% weight solution of dextrose in water yields a measurement of 10.9^oBx.)

Sugar content in grapes is usually measured using a refractometer, and requires that the berries be destroyed.

2.4.3.2 Acids

In *Vinifera* grapes, tartaric and malic acids are dominant, constituting around 90% or more of the total acidity. The third most abundant acid in grapes, citric acid, only constitutes around $0.02 - 0.03\%$ of the total acidity. There are more than 20 other non-nitrogenous organic acids present in grapes in very small amounts. During ripening, the amounts of free malic and tartaric acids

decrease dramatically. The pH of ripe grapes range from 3.0 to 3.8. [13]

The acidity of grapes is usually measured by titration (measuring titratable acidity) and by a pH meter (measuring unassociated hydrogen ions in solution). These are destructive tests, requiring the berries to be destroyed to test their juice.

2.4.3.3 Tannins

Tannins are complex esters of phenolic acids and sugars that occur mainly in the seeds, skin and stems of grapes. In very small amounts, tannins add flavour to grapes, and give grapes an astringent taste. Tannins develop during ripening. [13]

2.4.3.4 Pigments

The pigment compounds in ripe grapes are antocyanina and are generally found only in the skin. Grapes are usually classified as white, red or black, with very little or no antocyanina present in the white varieties. Antocyanina compounds develop during the final stages of the ripening process. Other pigments that may be present in immature grapes are carotenoids, xanthophylls and chlorophyll and give the grape a green colour, but these compounds disappear on ripening. [13]

2.4.3.5 Minerals and Vitamins

Minerals in grapes, constituting around $0.2-0.6\%$ of the weight of the fruit, are taken from the soil by the plant. Bromine, fluorine and iodine, among others, are found in grapes, but most minerals are only present in trace amounts. [13]

Grapes contain a fair amount of vitamins, vitamin A being the most abundant. Other vitamins present include thiamine, riboflavin and folic acid. [13]

2.4.4 Grading Table Grapes

Grapes can be graded in terms of size, sugar content and appearance. Mechanical graders for size and colour are used in different growing areas around the world. Grading grapes on the basis of bunch size, texture, flavour or aroma is also done. After grading, the unacceptable grapes can be used for other purposes such as feed for cattle. [13]

The Grape Sizer produced by Vizier Systems performs grading of table grapes on a sorting line. The sizer measures berry size (accurate to $1mm$), bunch weight (accurate to $1g$) and bunch colour (as a percentage of bunch area within specified colour boundaries) and allows packers to sort grape bunches correctly. This system offers growers many advantages including reducing packing time and costs, improved classification uniformity and creating a more favourable presentation of packaged grapes to the market.

Chapter 3

Nuclear Magnetic Resonance

3.1 Introduction

In the late 1930's and 1940's, scientists discovered the phenomenon of Nuclear Magnetic Resonance or NMR [23]. This inherently Quantum Mechanical phenomenon allows one to gain information about objects and materials by applying magnetic fields to them in certain ways.

The success of NMR lies in the fact that it allows one to examine samples non-destructively. By varying the magnetic fields around a sample in a certain way, a picture of that sample can be built up, allowing one to gain information about its chemical composition, and even its structural characteristics.

The non-destructive nature of NMR makes it especially attractive for many different applications, especially in the food industry, where pre- and post-harvest analysis of fresh produce and the monitoring of processed foodstuffs non-destructively are of vital importance.

Starting with a brief history of the development of NMR, this chapter describes the basic principles of NMR and the concept of nuclear relaxation, followed by a brief discussion on the detected NMR signal. Finally, it moves on to describe the basic techniques behind NMR spectroscopy. The principles and techniques described in this chapter were used to develop an NMR sensor for measuring the internal quality of fruit, as described in later chapters.

3.2 A Brief History of NMR

In 1924 the extraordinarily talented Viennese physicist, Wolfgang Pauli, put forward the idea that atomic nuclei have magnetically related spins [23], thus creating the theoretical basis on which NMR is established [24].

Many physicists set out to test Pauli's ideas on nuclear magnetism, but in 1938 Isidor Rabi beat all competitors when he successfully designed an experiment to detect and measure the magnetic spin of atomic nuclei in gasses [25], thus proving Pauli's ideas right and earning Rabi the 1944 Nobel Prize in Physics.

Eight years after Rabi's discovery, when scientists returned to peaceful pursuits after the end of World War 2, two physicists independently discovered that the magnetic resonance effects that Rabi had observed in gasses could also be detected in liquids and solids [23]. Edward Purcell and Felix Bloch both published papers in 1946 describing their observations [26, 27], earning them each the Nobel Prize for Physics in 1952. Bloch also filed a patent for the very first NMR spectrometer at the end of 1946 [28]. Their discovery ushered in the modern era of NMR.

Purcell made another contribution to the field. Work by Purcell and Hermann Carr [29], together with refinements made by Saul Meiboom and David Gill [30], led to the CPMG pulse sequence that forms the backbone of many NMR experiments today.

Finally, special mention must also be made of Erwin Hahn for his development of the "spin echo" technique [31] that is an invaluable tool in modern NMR and MRI.

Today NMR techniques are used for many different industrial and scientific applications, from medicine to geology.

3.3 Basic Principles of Nuclear Magnetic Resonance

The phenomenon of Nuclear Magnetic Resonance is, at its heart, a macroscopic manifestation of a quantum mechanical property of particles called spin. As such, it is important to have a basic understanding of quantum spin in order to understand NMR.

In this section the concept of spin is introduced, and a description of a particle with spin in a magnetic field is given. The concept of nuclear relaxation is also introduced.

3.3.1 Spin

In classical mechanics, objects have two kinds of angular momentum – orbital angular momentum associated with orbital motion around a centre of mass (for example the earth orbiting the sun) and spin angular momentum associated with rotation of the body (for example the Earth rotating about its own axis). This distinction is really just a matter of convenience, though, as an object possessing spin angular momentum can also be seen as a collection of particles, each possessing an orbital angular momentum (think of the Earth as a collection of rocks, each of which orbits around the centre of the Earth at the same speed as the Earth's rotation).

Quantum mechanics, however, deals with point particles. As these have no structure, they can only have orbital angular momentum. It turns out, however, that each of these point particles also has an intrinsic property that has many similarities with classical spin. This quantum mechanical phenomenon is therefore, rather unimaginatively, called spin as well.

As with all other quantum phenomena, spin has a quantum number associated with it, usually denoted by s. Unlike with, say, the angular momentum quantum number, l, which can take on any integer value, the value of s is specific and unchangeable for every species of particle, and can have half-integer values. For example, for electrons $s = 1/2$, for photons $s = 1$, for gravitons $s = 2$, etc. [32]. Particles with integer spin are called bosons, whereas particles with half-integer spin are called fermions.

The spin quantum numbers of particles in a system can be combined in certain ways, in order to give the entire system a spin quantum number of its own. Consider a system consisting of two particles with spin quantum numbers s_1 and s_2. The total spin of the entire system is described by a new quantum

number, s_3, which can take on any of the values [2]

$$s_3 = \begin{cases} |s_1 - s_2| \\ |s_1 - s_2| + 1 \\ \quad \vdots \\ |s_1 + s_2| \end{cases} . \tag{3.3.1}$$

For example, consider a ^2H nucleus consisting of a proton and a neutron. We find that $s_1 = s_2 = 1/2$ (as both the proton and the neutron are spin-1/2 particles), therefore s_3 can take on either a value of 1 or a value of zero. These values correspond to different energy states that the system can occupy. Figure 3.1 shows the two energy levels that the ^2H system can occupy [2].

This same method can be used for systems with more than two particles.

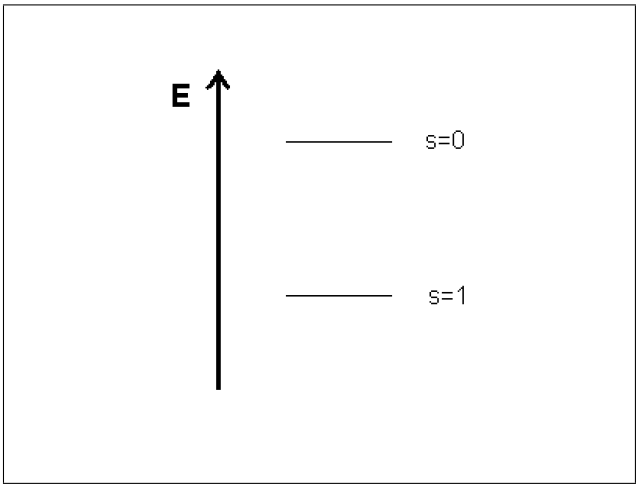

Figure 3.1: The Energy levels of the ^2H nucleus, and the nuclear spin quantum numbers associated with each.

As can be seen from Figure 3.1, the spin quantum number corresponding to the lowest energy level in the ^2H system is $s = 1$. The spin quantum number corresponding to the lowest energy nuclear state is called the ground state nuclear spin [2]. For NMR applications the energies involved are generally much lower than the energies required to lift the nucleus out of its ground state. The nuclear excited states may therefore be ignored, and only the ground state nuclear spin considered [2].

Table 3.1: A List of Nuclear Isotopes and their Properties.

Isotope	**Ground-state Spin**	**Natural Abundance (%)**	**Gyromagnetic Ratio, γ ($rad.s^{-1}.T^{-1}$)**
^{1}H	1/2	∼100	267.522×10^6
^{2}H	1	0.015	41.066×10^6
^{10}B	3	19.9	28.747×10^6
^{11}B	3/2	80.1	85.847×10^6
^{13}C	1/2	1.1	67.283×10^6
^{14}N	1	99.6	19..338×10^6
^{15}N	1/2	0.37	-27.126×10^6
^{17}O	5/2	0.04	-36.281×10^6
^{19}F	1/2	∼100	251.815×10^6
^{23}Na	3/2	∼100	70.808×10^6
^{29}Si	1/2	4.7	-53.190×10^6
^{31}P	1/2	∼100	108.394×10^6
^{35}Cl	3/2	75.77	10.610×10^6
^{113}Cd	1/2	12.22	5.961×10^6
^{195}Pt	1/2	33.8	5.8385×10^6

Unfortunately, there is no simple rule to determine which of the many possible states that a nucleus can reside in will be the ground state, but what is certain is that, from (3.3.1), nuclei with equal numbers of nucleons will have integer ground state spin while nuclei with odd numbers of nucleons will have half-integer ground state spin.

Table 3.1 lists a selection of nuclear isotopes and their properties [2].

Nuclei with a spin quantum number of zero are NMR silent. Nuclei with spin quantum numbers equal to 1 and larger are called quadrupolar nuclei. NMR spectroscopy of these elements is relatively difficult, although the information one can gather from them may be prolific. NMR of quadrupolar nuclei falls outside the scope of this thesis, but reference [33] can be consulted if the reader is interested in these nuclei.

The most studied isotopes in NMR experiments are ^{1}H and ^{13}C. In this thesis only ^{1}H nuclei will be considered. As can be seen from Table 3.1, this isotope is very abundant in nature, making it a good choice for NMR studies.

3.3.2 Particles in a Magnetic Field

It is a well known fact that a spinning charged (classical) particle has a magnetic dipole moment associated with it. In a similar way, a quantum mechanical particle with spin has a magnetic dipole moment, $\vec{\mu}$, associated with it. This magnetic moment is given by [32]

$$\vec{\mu} = \gamma \vec{S}, \tag{3.3.2}$$

where $\vec{S}$ is the system's spin[1] and γ is a constant called the gyromagnetic (or, sometimes, the magnetogyric) constant.

It is easy to see from (3.3.2) that a particle's magnetic moment is either directed in the same direction as the particle's spin vector, or in the opposite direction, depending on the sign of the gyromagnetic ratio. Table 3.1 lists the gyromagnetic ratios of different nuclear isotopes.

Consider now a sample containing a collection of particles, as shown in Figure 3.2. The spin vectors of the particles in the sample can point in any direction [32][2]. It is important to note that, since the spins are all orientated in random directions, the sample has no nett magnetic moment.

Now suppose we place the sample in a magnetic field. The energy level of a particle corresponding to the spin quantum number s is $(2s + 1)$-fold degenerate [32, 2]. This degeneracy is broken when the particle is placed in a magnetic field. In other words, when a particle is placed in a magnetic field, its energy levels are split, as shown in Figure 3.3 for the ^1H nucleus.

As stated earlier, we can ignore the higher nuclear energy levels and focus only on the ground state energy level. In the example of the ^1H nucleus, this ground state energy is split into three energy levels, as depicted in Figure 3.3.

[1]The system's spin is actually a quantum mechanical operator, but it is convenient to picture it as a vector pointing along the 'axis' of spin for our purposes. This, although not completely correct in the mathematical sense, makes visualizing the rest of this chapter much easier. For a more complete and mathematically correct description of quantum spin, see Appendix B.

[2]Some quantum mechanics texts often claim that a particle's spin may only point in certain directions. This is incorrect. See Appendix B.

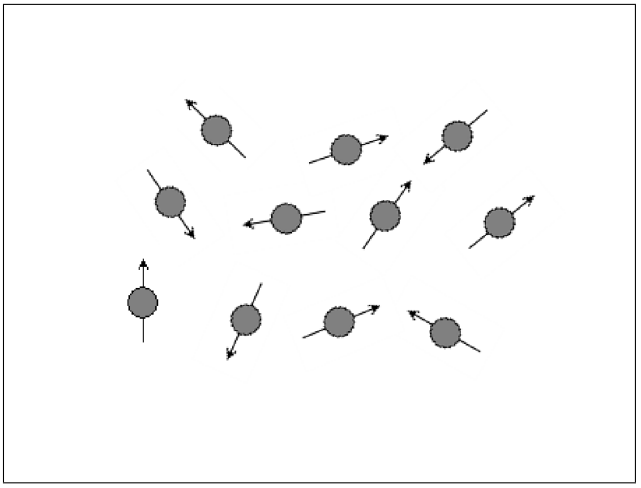

Figure 3.2: Randomly directed spin polarizations in a sample.

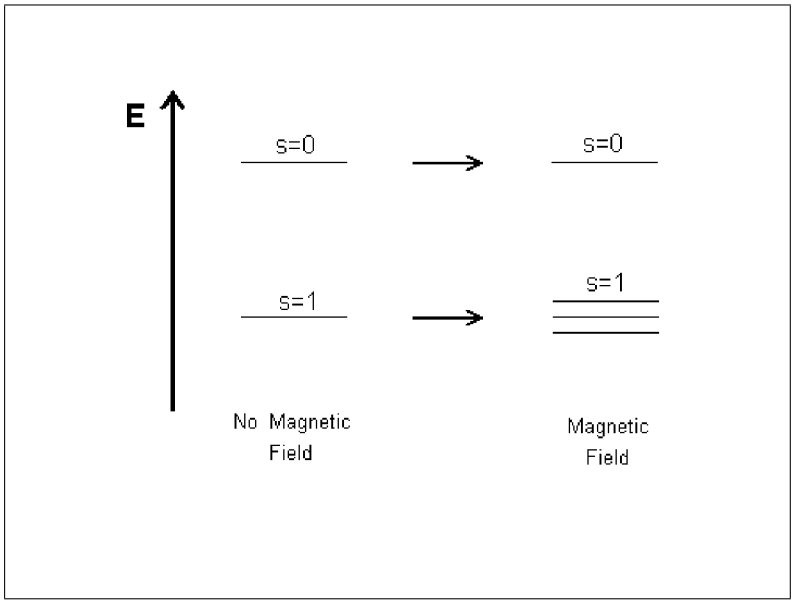

Figure 3.3: The splitting of degenerate energy levels of ^1H in a magnetic field.

Before the magnetic field was applied to the sample, therefore, the particles in it were all in the ground state and their spin could be pointing in any direction (as all directions represent states with equal energy). After the magnetic field is applied, however, the energy levels for the particles split, making some spin orientations more energy efficient than others. The particles therefore

want to align themselves in such a way that they are in the lowest energy level, just like a compass needle moving to align with an external magnetic field.

The particles, however, have spin angular momentum and, as a result, cannot flip around like the compass needle to align themselves with the magnetic field. What actually happens is that the particles start precessing around the axis of the applied magnetic field [32, 2]. This precession is depicted in Figure 3.4.

The frequency of this precession is given by [2]

$$\omega^0 = -\gamma B^0, \tag{3.3.3}$$

and is called the Larmor Frequency. Here B^0 is the magnitude of the externally applied magnetic field and γ is the gyromagnetic constant of the particle. ω^0 is measured in $rad.s^{-1}$.

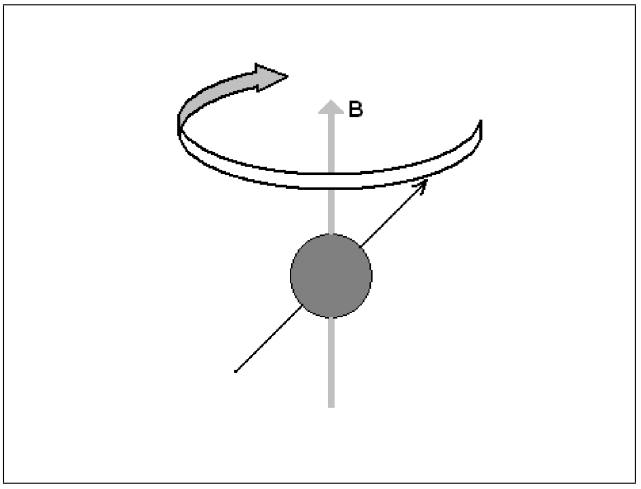

Figure 3.4: Spin precession.

This precessional motion is essentially invisible and initially it does not change the total magnetic moment of the sample [2]. The particles in the sample, however, also undergo constant vigorous motion (consider for example a sample of water in which the water molecules that carry the precessing protons are in constant motion). As each particle is a source of magnetic fields, this motion of particles ensures that particles experience slight fluctuations in

their local magnetic fields, changing both the spin magnitude and direction [2]. Each particle therefore has a slightly different nuclear spin.

These variations are extremely small. They are, however, large enough to break the isotropy of the nuclear spin polarization. Because of the degeneracy of the magnetic fields is broken by applying a magnetic field to the sample, some spin orientations are more favoured than others. Obviously, more particles line up so as to minimize their energy (that is to say, move to the lower energy level)[3]. As a result of this the sample develops a nett magnetic moment, as shown in Figure 3.5

This nett magnetic moment can be detected directly using SQUIDs (see, for example, [7]), but in traditional NMR experiments a different detection scheme is used. By applying a RF magnetic pulse of an appropriate frequency and duration, all the particles (and therefore the nett magnetic moment) can be rotated by $\pi/2$ radians[4]. The nett magnetic moment is then perpendicular to the externally applied magnetic field. For the particles in the sample, however, it is as if nothing has happened, and they continue to precess in the normal way. This causes the nett magnetic moment to rotate as well (see Figure 3.6) [2]. If a coil is placed perpendicular to the direction of the magnetic moment, a sinusoidal current is induced as the nett magnetic moment sweeps past it. This kind of detector is called a Faraday detector.

3.3.3 Spin-Lattice Relaxation (Longitudinal Relaxation)

When an external magnetic field is applied to a sample, the macroscopic nuclear magnetization does not appear instantly, but rather gradually grows from zero in an exponential form. This process is called Spin-Latice Relaxation, or Longitudal Relaxation.

The build-up of longitudal magnetization has the form [2]

$$M_z^{nuc}(t) = M_{eq}^{nuc}(1 - e^{-(t-t_{on})/T_1}), \tag{3.3.4}$$

where t_{on} is the time at which the external magnetic field is appled.

The time constant T_1 is called the Spin-Lattice Relaxation time constant, the Longitudal Relaxation time constant or, simply, the T_1 time constant, and

[3]Because the energy levels are so close together, the bias toward the lower one is very small. The bias, however, is large enough to detect.

[4]See Appendix B

is a measure of how fast the macroscopic longitudal nuclear magnetization gains strength when a sample is placed in a magnetic field.

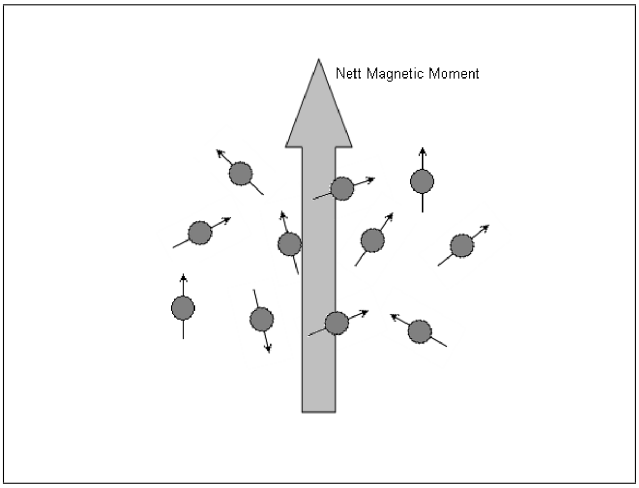

Figure 3.5: A sample of particles develops a nett magnetic moment after being placed in a magnetic field.

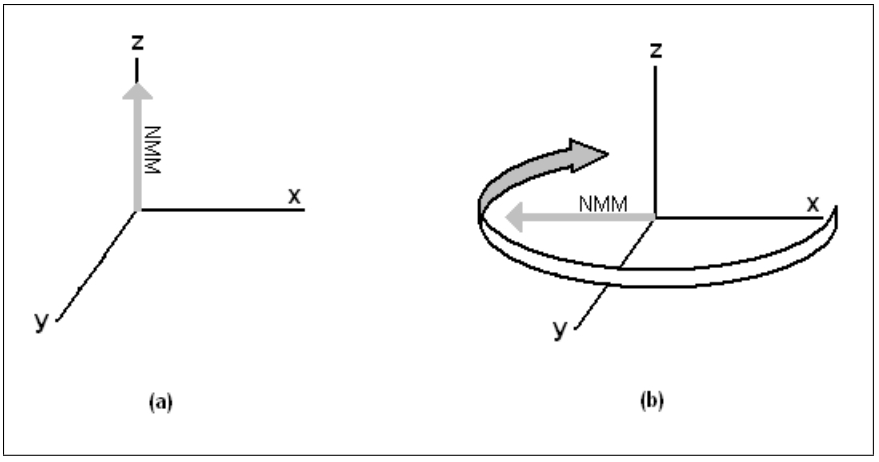

Figure 3.6: Rotating the Nett Magnetic Moment (NMM) by $\pi/2$ radians. (The externally applied magnetic field is in the z-direction.) (a) Before the RF magnetic pulse is applied the NMM is in the same direction as the externally applied magnetic field. (b) After the RF magnetic pulse the NMM lies in the x-y plane and rotates at the Larmor frequency. If a coil is placed perpendicular to the x-y plane the passing NMM induces a current in it (Faraday detection).

The T_1 time constant depends on the nuclear isotope, and on physical parameters of the sample such as viscosity and temperature. Typically T_1 is in the range of milliseconds to seconds, but can even be as high as days or years for some substances [2].

3.3.4 Spin-Spin Relaxation (Traverse Relaxation)

If the macroscopic magnetization of the sample is rotated by $\pi/2$ radians, as described above, the rotating magnetization in the x-y plane does not remain indefinitely, but decays exponentially, according to [2]

$$\begin{aligned} M_y^{nuc}(t) &= -M_{eq}^{nuc} cos(\omega^0 t)(1 - e^{-(t-t_{flip})/T_2}) \\ M_x^{nuc}(t) &= M_{eq}^{nuc} sin(\omega^0 t)(1 - e^{-(t-t_{flip})/T_2}) \end{aligned} \quad , \tag{3.3.5}$$

where t_{flip} is the time at which the magnetization of the sample is rotated.

The time constant T_2 is called the Spin-Spin Relaxation time constant, the Traverse Relaxation time constant or, simply, the T_2 time constant, and is a measure of how fast the macroscopic traverse nuclear magnetization loses strength after being rotated by $\pi/2$ radians.

The T_2 time constant of a sample is normally in about the same range as the T_1 time constant [2].

3.4 NMR Spectroscopy

The previous section (Section 3.3) described the basic principles of NMR. The concepts introduced there concern the generation of NMR signals (essentially, how NMR *works*). This section describes how these NMR signals, once detected, can be used to analyse samples. This is called NMR spectroscopy, and is essentially how one *uses* NMR.

3.4.1 The NMR Signal

The oscillating electric current induced in the Faraday detector by the rotating traverse nuclear magnetization constitutes the NMR signal and is called the Free Induction Decay or FID.

In this section the properties of the FID are explored.

3.4.1.1 Fourier Transform NMR

As discussed in Section 3.3.4, the traverse magnetization components of the sample decay exponentially. The FID signal induced in the Faraday detector therefore has the form

$$s_{FID} = A\cos(\omega^0 t)e^{-t/T_2}. \tag{3.4.1}$$

Taking the Fourier transform of this signal results in a spectrum with just one peak. A more generally applicable equation, however, is given by[5]

$$s_{FID} = \sum_l s_l(t), \tag{3.4.2}$$

where

$$s_l = A_l\cos(\omega_l^0 t)e^{-t/T_2^l}, \tag{3.4.3}$$

where A_l is the amplitude of signal component l, ω_l^0 is the frequency of signal component l and T_2^l is the spin-spin relaxation time of signal component l [2].

Taking the Fourier transform of a signal such as in (3.4.2) results in a spectrum that can be analyzed to extract information from the sample.

3.4.1.2 Signal Averaging

In general, the NMR signal is very weak and contains unwanted noise that can mask the desired signal. If the signal to noise ratio (SNR) of the detected signal is too low, a procedure called signal averaging can be used to enhance the signal.

Consider two identical NMR experiments on the same sample, yielding two signals, $s(1) = s_{NMR}(1) + s_{noise}(1)$ and $s(2) = s_{NMR}(2) + s_{noise}(2)$.

Since the NMR signal from the first experiment is identical to the NMR signal of the second experiment, the RMS value of NMR signal of the sum of

[5]See Sections 3.4.4 and 3.4.5.

$s(1)$ and $s(2)$ becomes

$$\begin{aligned}\sigma_{NMR}(1+2) &= \langle[s_{NMR}(1)+s_{NMR}(2)]^2\rangle^{1/2} \\ &= \langle[2s_{NMR}(1)]^2\rangle^{1/2} \\ &= \langle 4s_{NMR}(1)^2\rangle^{1/2} \\ &= [4\langle s_{NMR}(1)^2\rangle]^{1/2} \\ &= 2\sigma_{NMR}(1), \end{aligned} \tag{3.4.4}$$

where $\sigma_{NMR}(1)$ is the RMS value of $s_{NMR}(1)$.

Since the noise contributions of the two signals are random, $s_{noise}(1) \neq s_{noise}(2)$. We therefore have that the RMS value of the sum of the noise contributions from each signal is given by

$$\begin{aligned}\sigma_{noise}(1+2) &= \langle[s_{noise}(1)+s_{noise}(2)]^2\rangle^{1/2} \\ &= \langle s_{noise}(1)^2 + 2s_{noise}(1)s_{noise}(2) + s_{noise}(2)^2\rangle^{1/2} \\ &= [\langle s_{noise}(1)^2\rangle + \langle 2s_{noise}(1)s_{noise}(2)\rangle + \langle s_{noise}(2)^2\rangle]^{1/2}. \end{aligned}$$

But, since the RMS values of the noise contributions are equal ($\sigma_{noise}(1) = \sigma_{noise}(2)$), and the noise contributions of the two signals are uncorrelated ($\langle s_{noise}(1)s_{noise}(2)\rangle = 0$), we have that

$$\sigma_{noise}(1+2) = \sqrt{2}\sigma_{noise}(1). \tag{3.4.5}$$

From (3.4.4) and (3.4.5) the SNR is given as

$$SNR_{1+2} = \frac{\sigma_{NMR}(1+2)}{\sigma_{noise}(1+2)} = \frac{2\sigma_{NMR}(1)}{\sqrt{2}\sigma_{noise}(1)} = \frac{\sqrt{2}\sigma_{NMR}(1)}{\sigma_{noise}(1)}. \tag{3.4.6}$$

This argument can easily be extended to N signals, yielding an SNR of

$$SNR_{1+2+\ldots+N} == \frac{\sqrt{N}\sigma_{NMR}(1)}{\sigma_{noise}(1)}. \tag{3.4.7}$$

Each repetition of the NMR experiment and summation of signals increases the SNR.

3.4.2 Pulse Sequences

As discussed in the previous section, the FID is induced by allowing the nuclear spins to reach equilibrium in a large magnetic field and then rotating the nuclear spin polarizations by an RF pulse. The basic NMR technique is depicted in Figure 3.7.

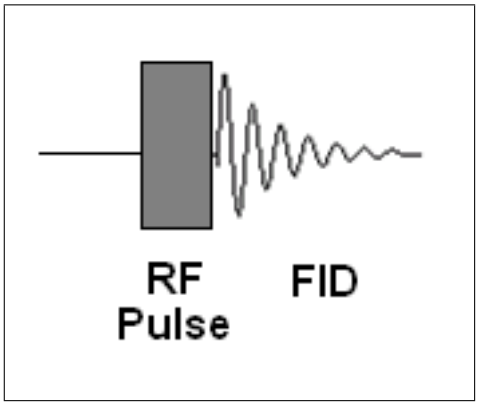

Figure 3.7: A simple pulse sequence.

For most NMR experiments, more than one RF pulse is used. For example, Figure 3.8 shows a schematic representation of a pulse sequence used to observe spin-echo. Note the annotation of the pulses in the form β_ϕ. β represents the angle by which the spins in the sample is to be rotated (and depends therefore on the length of the pulse), while the subscript ϕ represents the phase of the RF pulse. If experiments are to be repeated, for example signal averaging, the phases of the RF pulses are to remain the same for each experiment. [2]

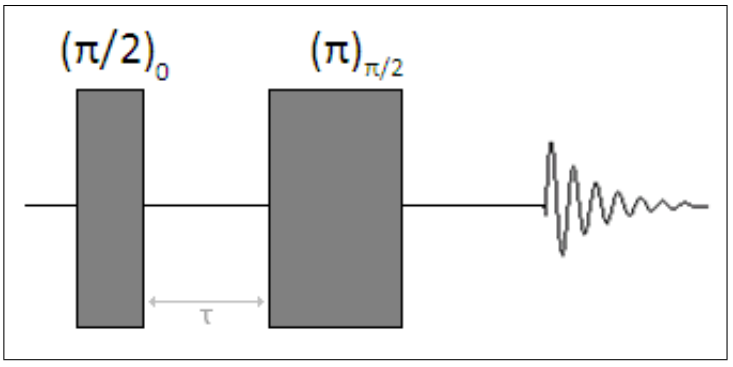

Figure 3.8: Spin-echo pulse sequence [2].

Table 3.2: RF pulse phase nomenclature [2].

RF pulse phase	**Nomenclature**
$\phi = 0$	x-pulse
$\phi = \pi/2$	y-pulse
$\phi = \pi$	$\bar{\text{x}}$-pulse *or* $-$x-pulse
$\phi = 3\pi/2$	$\bar{\text{y}}$-pulse *or* $-$y-pulse

Often, special names are used for phases that are multiples of $\pi/2$. Table 3.2 lists these names.

In practice there are many different pulse sequences, some very complicated, each measuring a different property of the sample. A detailed study of pulse sequences fall outside the scope of this thesis, but references [2] and [34] can be consulted if information on different pulse sequences is needed.

3.4.3 Inhomogeneous Broadening

Up to this point we have assumed that the magnetic field penetrating a sample during an NMR experiment was perfectly homogeneous. In general, though, this is not the case. Perfectly homogeneous magnetic fields are difficult to generate, and the sample's own magnetic susceptibility distorts the applied magnetic field even more.

Since the Larmor frequency is dependent on magnetic field strength (3.3.3), inhomogeneities in the magnetic field cause different areas of the sample to have slightly different Larmor frequencies, which effectively broadens the observed spectrum. This effect is called inhomogeneous broadening [2].

Inhomogeneous broadening causes the NMR signal to be dependent on the shape of the sample and the distribution of magnetic spins within it. This observation, independently realized by Peter Mansfield and Paul Lauterbur in 1972 earning them the Nobel Prize in Physiology or Medicine in 2003, is the basis for Magnetic Resonance Imaging (MRI) [2].

3.4.4 Chemical Shifts

Even if a sample is in a perfectly homogeneous magnetic field, there will be small variations in magnetic field on the microscopic scale. These variations arise from the fact that electrons are magnetic. The magnetic field around (and therefore the Larmor frequency of) a nucleus is thus dependant on its local electronic environment and its location in the molecule. This effect is called chemical shift [2].

Chemical shift is dependent on the magnetic field. Fortunately, to a very good approximation, the chemical shift is linearly proportional to the applied magnetic field [2]. The ratio between the chemical shift and the Larmor frequency is therefore fixed and depends only on the sample. It is therefore convenient to specify chemical shifts according to this ratio. The field-independent expression for the chemical shift is given by [2]

$$\delta = \frac{\omega^0 - \omega^0_{ref}}{\omega^0_{ref}}, \tag{3.4.8}$$

where ω^0 is the Larmor frequency of a particular nucleus and ω^0_{ref} is the Larmor frequency of a reference compound. This reference compound is usually tetramethylsilane (TMS) for the ^1H nucleus.

Chemical shifts are usually specified in parts per million (ppm), which has the same meaning as 10^{-6} .

3.4.5 J-Coupling

Each proton also magnetizes the electrons in a molecule, causing a very weak magnetic field at the site of the spins. This transmitted field, called the J-coupling or indirect dipole-dipole coupling, allows each spin-1/2 to sense the presence of neighbouring spins in the molecule. The result is that the peaks in the FID are split into multiplets whose structure depends on the molecular environment. [2]

Chapter 4

Superconductivity

4.1 Introduction

One of the most exciting discoveries of the 20^{th} century was the phenomenon of superconductivity. Certain materials, when cooled to appropriate temperatures, exhibit strange properties such as zero resistance to flowing currents and the expulsion of all magnetic fields from their interiors.

In this chapter the theory of superconductivity is discussed. The chapter starts with a brief history of the development of superconductivity and then moves on to describe the basic properties of superconductors. Current flow in a superconductor and the phenomenon of Flux Quantization are described. The chapter ends with a description of the theory of Josephson junctions.

4.2 A Brief History of Superconductivity

4.2.1 Discovery

In 1908 Heike Kamerlingh Onnes successfully liquefied helium, with a boiling point of 4.22 kelvin [5]. Following the breakthrough, the Dutch physicist proceeded to research the resistivity of metals at low temperatures. Because he was worried about impurities in other metals, he decided to use mercury, which could easily be purified by distillation owing to the fact that it is a liquid at room temperature.

In 1911 one of Onnes's research assistants, Giles Horst, found that the resistance of a tube of mercury abruptly vanished at 4.15 kelvin [5]. Although

sceptical of the result, Onnes later realized, with repeated measurements, that he had discovered something very important [35, 36]. Because the resistance of the material vanished below a certain critical temperature the phenomenon was named 'supra-conductivity' by Onnes, and was later renamed to 'superconductivity' [37].

Onnes received the Nobel Prize in Physics in 1913 for the liquefaction of helium and the discovery of the phenomenon of superconductivity.

Onnes's discovery of superconductivity in mercury sparked the search for other materials that might show the same properties, and a theory explaining the phenomenon. Many materials[1] such as zinc, tin and niobium were shown to become perfectly conductive below certain temperatures (some of them at much higher temperatures than the temperature at which mercury becomes superconducting), but a theory remained elusive.

4.2.2 The Search for a Theory

The phenomenon of superconductivity has unique properties that cannot be explained by classical electromagnetic theory.

In 1933, Walter Meissner and Robert Ochsenfeld discovered that a superconductor expels all magnetic flux from its interior [38], making it perfectly diamagnetic. This phenomenon, later named the Meissner Effect, spurred the search for a theory explaining superconductivity, and in 1934 Hendrik Casimir and Cornelis Gorter proposed the Two-Fluid Model of Superconductivity [39]. Using this theory as a base, brothers Fritz and Heinz London proposed a phenomenological theory for superconductivity in 1935 [40]. The London brothers' theory was quite successful, and was able to explain the zero resistivity and diamagnetic properties of superconductivity.

Later, Fritz London realized that superconductivity was a fundamentally quantum mechanical phenomenon that manifests itself on a macroscopic scale. Consequently he used quantum mechanical principles in developing his new Macroscopic Quantum Model (MQM) between 1935 and 1948, describing superconductive behaviour in materials much more consistently than previous theories [4]. The MQM was later expanded by Russian physicists Vitaly

[1] It is interesting to note that materials which are good conductors at room temperature such as copper and gold do not show superconducting behaviour.

Ginzburg and Lev Landau to include the thermodynamic properties of superconductors [41].

All the theories described thus far are very powerful and are still used today in many applications, but they are all phenomenological and do not address the physical mechanisms behind superconductivity. A microscopic theory explaining superconductivity remained elusive until 1957, when John Bardeen, Leon Cooper and Robert Schreiffer developed the theory known today as the B.C.S. theory [42, 43, 44]. This theory describes the behaviour of all (low-T_c) superconductors under all circumstances, and the development of it led to them winning the Nobel Prize in 1972.

4.2.3 High Temperature Superconductivity

In 1986 Alex Müller and Georg Bednorz discovered superconductivity in lanthanum-barium-copper-oxide [45]. This remarkable compound became superconducting below 30 kelvin. The discovery earned the two scientists the 1987 Nobel Prize in Physics and ushered in the era of High Temperature Superconductivity[2].

In 1987, Maw-Kuen Wu and Paul Chu, along with their graduate students, discovered that yttrium-barium-copper-oxide ($YBa_1Cu_2O_3$, commonly called simply YBCO)[3] became superconducting below a remarkable 93 kelvin [46]. This was the first superconducting material discovered which could be cooled by liquid nitrogen (which has a boiling point of 77 kelvin, and is relatively cheap and easy to produce). This material is currently the most widely used superconducting material in the world.

Many new superconducting materials that become superconducting at even higher temperatures have since been discovered. (As of 2009, the highest temperature superconductor is $HgBa_2Ca_2Cu_3O_{8+\delta}$, which becomes superconducting below 135 kelvin at ambient pressure [47].).

Although there has been much success in finding new high temperature superconducting materials, the mechanism behind it remains a mystery. The conventional B.C.S. theory does not apply to high temperature superconductors in the same way as it applies to low temperature superconductors, and

[2]High Temperature (or High-T_c) Superconductivity is defined as superconductivity above 30 kelvin.

[3]Wu and Chu were actually working with $Y_{1.2}Ba_{0.8}CuO_4$ samples.

there is, at present, no commonly accepted theory to explain high temperature superconductivity, although research is ongoing [48].

4.3 Fundamental Considerations of Superconductivity

This section describes the basic properties of superconductors and the different theories discussed in the previous section. All properties described below apply to both low temperature and high temperature superconductors.

4.3.1 Fundamental Properties of Superconductors

The most important property of superconducting materials is that they show no resistance to current moving through them, and that they therefore show perfect conductivity. This implies that a (DC) current moving through a superconductor does not cause a voltage drop across it. It is important to note that superconductors show lossless behaviour to applied DC currents only. Applied AC currents do not pass through superconductors without loss [5].

Superconductors also expel all magnetic flux from their interior, and thus show perfect diamagnetic behaviour. This expulsion is called the Meissner Effect. Indeed, the Meiddner effect is a more fundamental property of superconductivity as it defines the difference between a theoretically perfect conductor and a superconductor.

4.3.2 The Critical Parameters

Superconductive materials only become superconducting below a certain characteristic temperature called the Critical Temperature or T_c. This state change is not an immediate transition, but a broad transition over a milikelvin (although it can be as large as a few kelvin), depending on the purity and crystalline structure of the superconductor [5]. Figure 4.1 shows a typical transition of a superconductive material from the normal state to the superconducting state [50].

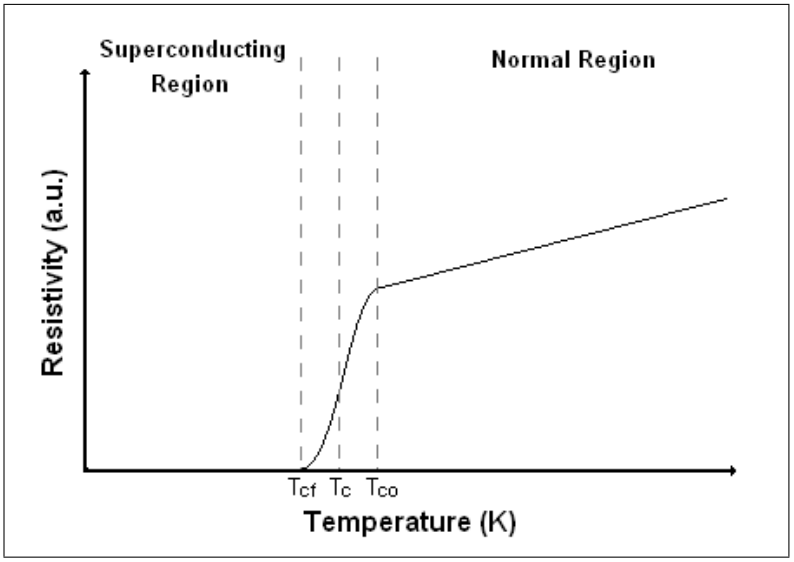

Figure 4.1: Transition of a material from the normal state to the superconducting state.

The state transition starts at a onset temperature T_{co} and ends at a final temperature T_{cf}. Below T_{cf} the material is superconducting, and above T_{co} the material is normal, and therefore not superconducting. The critical temperature of a superconducting material, T_c, is normally measured as the temperature in the middle of the transition region. For low temperature superconductors the transition region is narrow (typically in the order of 0.2 kelvin), while for high temperature superconductors it is wider (typically a few kelvin wide).

Many other parameters of superconductors are a strong function of the critical temperature. Table 4.1 shows the critical temperatures of several superconducting materials.

After the discovery of superconductivity it was soon found that large currents flowing through a superconductive material could destroy the superconductive properties of that material. The maximum amount of current that can flow through a superconductor without affecting its superconductive properties is called the Critical Current or I_c (or, for a specific area, the Critical Current Density or J_c).

It was also discovered that an applied magnetic field exceeding a certain strength could destroy superconductivity in a superconducting material. This

Table 4.1: Critical temperatures of several superconducting materials. The top four are low-T_c materials while the bottom three are high-T_c materials. [5]

Superconductor	**Critical Temperature (T_c) (K)**
Al	1.18
Hg	4.15
Nb	9.25
Nb_3Ge	23
$YBa_2Cu_3O_7$	93
$Bi_2Sr_2Ca_2Cu_3O_{10}$	105
$Tl_2Ba_2Ca_2Cu_3O_{10}$	125

value of magnetic field is called the Critical Field or H_c, and is also a strong function of temperature.

4.3.3 The Meissner Effect

The current density in a conductor is given by Ohm's law

$$\mathbf{J} = \sigma \mathbf{E}, \tag{4.3.1}$$

where $\mathbf{J}$ is the current density in the conductor and $\mathbf{E}$ is the electric field present in the conductor. σ is called the conductivity of the material and is a measure of a material's ability to conduct electricity.

For a *perfect* conductor, then, σ is infinite, and (4.3.1) would require that $\mathbf{E} = 0$.

From Faraday's law, given by

$$\nabla \times \mathbf{E} = -\frac{\partial \mathbf{B}}{\partial t}, \tag{4.3.2}$$

where $\mathbf{B}$ is the magnetic flux density, we therefore see that a perfect conductor would require that

$$\frac{\partial \mathbf{B}}{\partial t} = 0. \tag{4.3.3}$$

This means that the magnetic flux inside a perfect conductor cannot change, meaning that any magnetic flux present in the conductor at the time that the resistance goes to zero (or the conductivity goes to infinity) would be trapped

in the conductor.

Superconductors *do not* show this behaviour. They expel all magnetic flux from their interiors, regardless of their thermal or magnetic history. This means that even if they are cooled down in the presence of a magnetic field, they will expel all magnetic flux from their interiors when they transition to the superconducting state [48, 4, 51].

This phenomenon is called the Meissner effect and provides one of the most striking demonstrations of superconductivity. A small magnet can be made to levitate above a superconductor, as the penetrating magnetic flux is completely expelled from the interior of the superconductor. Figure 4.2 shows this remarkable demonstration.

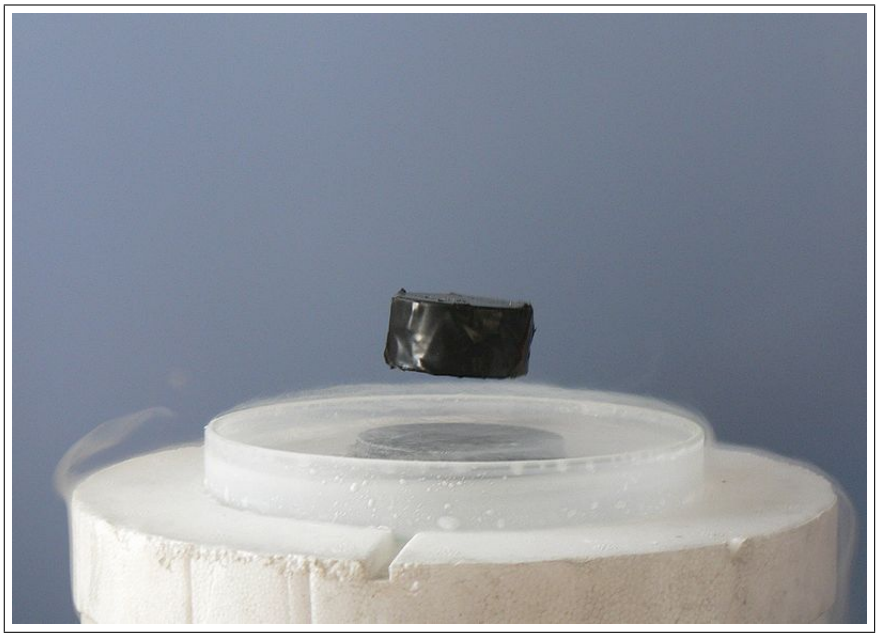

Figure 4.2: Levitation of a small magnet above a superconductor, demonstrating the Meissner effect [3].

4.3.4 The Two-Fluid Model

The Two-Fluid Model states that current flowing through a superconductive material above the critical current is due entirely to normal electrons which obey Ohm's Law, but current flowing through the material below the critical temperature is due to a combination of normal electrons and superelectrons [5].

The density of superelectrons in a superconductive material below its critical current is given by

$$n_s = n_0 \left[1 - \left(\frac{T}{T_c} \right)^4 \right], \tag{4.3.4}$$

where n_s is the density of superelectrons, n_0 is the density of superelectrons at zero temperature and T is the temperature of the material in kelvin [4].

Figure 4.3 gives a graphical representation of electron and superelectron densities in a superconductor.

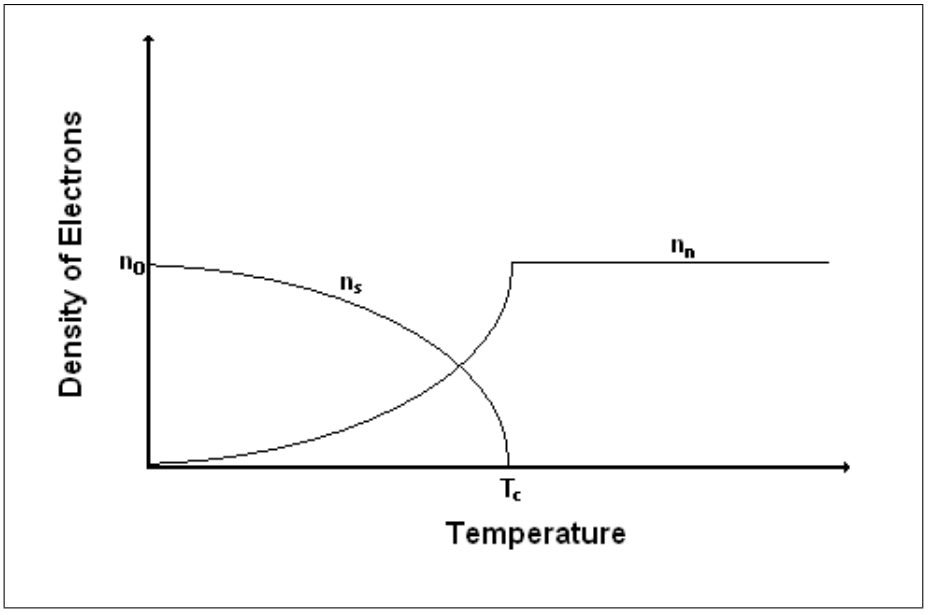

Figure 4.3: Change in electron and superelectron densities in a superconductor near T_c. (n_n represents the normal electron density.)

Superelectrons move through a superconductor without any resistive effects, while normal electrons experience normal resistance according to Ohm's Law. This explains perfect DC conductivity and why AC currents experience resistance. Under perfect conditions where electrons experience no resistance, a constant DC current would require no electric field (since the presence of an electric field would apply a force to the electrons, therefore accelerating them and increasing the current). In a superconductor the normal electrons experience resistance and the current carried by them therefore falls off, but

the current carried by the superelectrons do not experience resistance and the material therefore displays perfect conductivity. But when an AC current is applied an electric field is always present in the material (because of the force required to stop the electrons and super electrons moving in one direction and accelerating them in the other). This electric field causes some of the current to always be carried by normal electrons, causing losses. The effect of AC resistance increases with frequency and is usually only observable at very high frequencies [5].

4.3.5 The London Equations

From the two-fluid model we find that, for a superconducting material in its superconducting state, the total current flow is given as

$$\mathbf{J} = \mathbf{J_n} + \mathbf{J_s} \tag{4.3.5}$$

where $\mathbf{J_n}$ is the current density carried by the normal electrons and $\mathbf{J_s}$ is the current density carried by the superelectrons.

The normal electron current, $\mathbf{J_n}$, obeys Ohm's law, but the superelectron current, $\mathbf{J_s}$, does not.

It was the London brothers who first developed a model to describe perfect (DC) conductivity in superconductors in their theory of 1934 [40]. Known as the First London Equation, the following equation describes the supercurrent flow in a superconductive material[4]

$$\mathbf{E} = \frac{\partial}{\partial t}(\Lambda \mathbf{J_s}), \tag{4.3.6}$$

with

$$\Lambda = \frac{m^*}{n_s (q^*)^2}, \tag{4.3.7}$$

where $\mathbf{E}$ is the electric field, $\mathbf{J_s}$ is the superelectron density, m^* is the mass of a superelectron and q^* is the charge of a superelectron [4].

In order to explain the Meissner effect, the London brothers also postulated

[4]The London Equations are simply stated in this section. For a full derivation of the London Equations, see Appendix C.

that the equation governing the flux in a superconductor would be given as

$$\left(\frac{1}{\lambda_L^2} + \nabla^2\right)\mathbf{B} = 0, \tag{4.3.8}$$

where λ_L is given by

$$\lambda_L = \left(\frac{\Lambda}{\mu_0}\right)^{\frac{1}{2}}, \tag{4.3.9}$$

μ_0 being the permeability of free space.

To say that all flux is expelled from the interior of a superconductor is not strictly true. Magnetic flux does penetrate the superconductor for a short distance [52]. This distance is known as the London Penetration Depth, and is analogous to the magnetic skin depth of a normal conductor [6]. The London Penetration Depth is given by (4.3.9).[5]

Combining (4.3.8) with the Maxwell equations in magnetoquasistatic[6] form gives the Second London Equation, obtained as

$$\nabla \times (\Lambda \mathbf{J}) = -\mathbf{B}. \tag{4.3.10}$$

The Second London equation guarantees flux expulsion from the interior of a superconductor, making it consistent with the Meissner effect [6].

4.3.6 The Macroscopic Quantum Model

In 1948 Fritz London published his Macroscopic Quantum Model [5]. The central assumption of this model is that the superelectron fluid in a superconductor can be represented by a single macroscopic wave function. This macroscopic wave function is not a proper wave function, but rather an ensemble-average of the single superelectron wave functions [48]. This macroscopic wave function can be written as

$$\Psi(\mathbf{r}) = \psi(\mathbf{r})e^{\jmath\theta(\mathbf{r})}. \tag{4.3.11}$$

[5]Note that, unlike the magnetic skin depth, the London penetration depth is independent of frequency.

[6]Although the London equations are derived for MQS systems, it holds for all electrodynamic scenarios.

Normalization of (4.3.11) yields

$$\Psi(\mathbf{r}) = [n_s(\mathbf{r})]^{\frac{1}{2}} e^{\jmath\theta(\mathbf{r})}, \tag{4.3.12}$$

where we have, as before, that n_s is the density of superelectrons in a superconductor[7].

As we shall see in Section 4.4, this assumption leads to a precise description of the current flow in a superconductor and an explanation for the phenomenon of flux quantization, a phenomenon that the earlier theories could not explain. The original London equations can also be derived from it[8].

4.3.7 The B.C.S. Theory

The B.C.S. theory introduced the idea of Cooper pairs. As the temperature of a superconductor is lowered below its critical temperature, its electrons start moving into their ground states. In this ground state the electrons form into pairs. Each pair consists of two electrons with opposite spin and momentum [44]. The net spin and momentum of a Cooper pair is therefore zero. As all Cooper pairs have the same net momentum, they all tend to move in the same way, which implies that they never experience scattering and therefore move without resistance [5, 44].

As Cooper pairs are electrons in their ground state, it follows that they require a certain amount of energy to break their bonds [37]. In a superconductor there exists an energy gap between the (paired) ground state of the electrons and their (free) exited states. This energy gap is not present in a normal conductor, explaining why superconductive behaviour is not observed in them.

Cooper pairs also explain why a large magnetic field destroys the superconductive properties of a superconductor. When a magnetic field is applied to a Cooper pair, it increases the free energy density of the Cooper pair. If this increase in energy is large enough, it will cause the Cooper pair to break apart. This also explains why a superconductor has a critical current. A flowing current causes a magnetic field to be induced. If the current flowing in a superconductive material is large enough, the induced magnetic field will

[7] We assume for the rest of this chapter that n_s remains spatially constant. This is approximately true in weak fields.

[8] See Appendix C

be large enough to split Cooper pairs, destroying superconductivity in the material.

The superelectrons from the two-fluid model are therefore seen to be Cooper pairs. We therefore have that $m^* = 2m_e$ where m_e is the mass of a normal electron, and $q^* = 2e$ where e is the charge of a normal electron.

The B.C.S. theory theoretically introduced another parameter: the Coherence Length, ξ, is a measure of the mean distance between two electrons in a Cooper pair [48]. This parameter plays an important role in the design and manufacture of many superconductive devices, especially the Josephson junction[9].

The coherence length is a function of temperature, and also influences the critical current of a superconductor [48].

4.3.8 Type II Superconductivity

Type II superconductors are superconductors which possess two critical fields. Below the first critical field, the superconductor exhibits the same properties as a normal (or Type I) superconductor. Above the second critical field the superconductor is forced into its normal state and its superconductive properties are lost. Between the two critical fields the superconductor is in a mixed state called the vortex state [4, 5]. Figure 4.4 shows the different states of a Type II superconductor.

In the vortex state magnetic flux may enter the superconductor in a controlled manner. The flux penetrates the superconductor in cylindrical tubes called vortices. These vortices arrange themselves in a triangular array pattern, much like a honeycomb [4].

Flux vortices penetrating a superconductor are capable of motion if the triangular array arrangement becomes unstable [4]. This motion leads the dissipation of energy and is a source of noise in superconducting circuits. This flux motion can be stopped by 'pinning' the vortices in defects or holes in the superconductor. Flux pinning is an effective way to deal with flux noise [50].

All high-T_c superconductors are Type II superconductors.

[9] Josephson junctions are introduced in Section 4.6

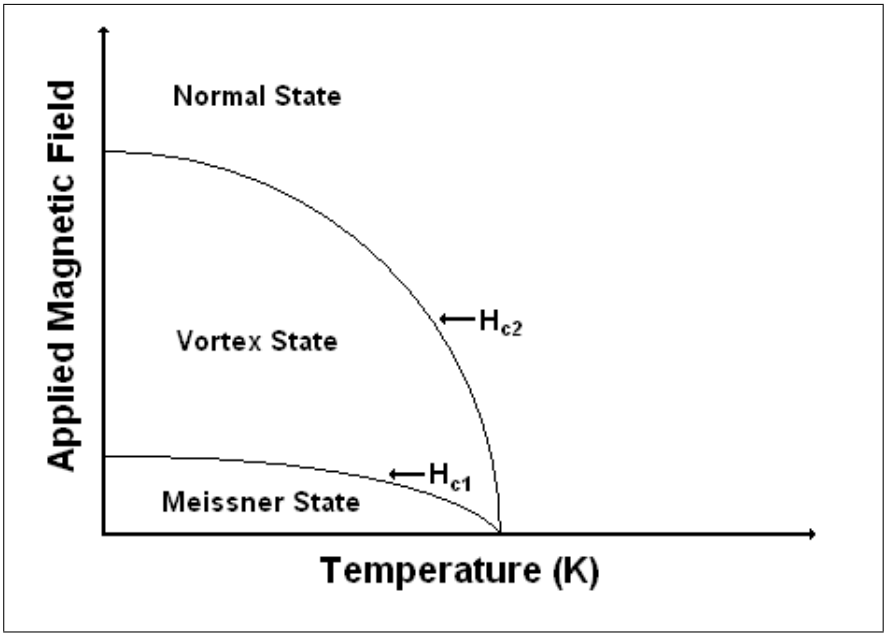

Figure 4.4: The different states of a Type II superconductor. H_{c1} represents the first critical field and H_{c2} the second. With an applied field below H_{c1} the superconductor is in its normal superconducting, or Meissner, state. Above H_{c2} the superconductive properties of the material are lost and the material is normal. Between H_{c1} and H_{c2} the superconductor is in the vortex state. [4])

4.3.9 High-T_c Superconductors

The conventional theory of superconductivity predicted that the highest critical temperature of a superconductor would be around 30 kelvin. In 1987, however, this prediction was proved false by Wu and Chu and their teams of graduate students when they discovered $YB_2Cu_3O_7$ to become superconducting at 93 kelvin [46], ushering in the age of high-T_c superconductivity.

Most high-T_c superconductors are copper oxides that have perovskite crystal structures [53]. These perovskite structures are usually layered in high-T_c superconductors, resulting in anisotropic conductivity, with higher current allowed along the CuO_2 plane than perpendicular (c-axis) to it [37].

The most commonly used and studied high-T_c material is $YBa_2Cu_3O_7$, more commonly referred to as YBCO. Not all the oxygen sites in a YBCO crystal are always filled, and it is common to state its chemical composition as $YBa_2Cu_3O_{7-\delta}$. Depending on the value of δ, YBCO can have either a orthorhombic or a tetragonal structure. For values of $\delta < 0.6$ YBCO is or-

thorhombic and superconducting, but for values of $\delta > 0.6$ YBCO has a tetragonal structure and does not show superconducting behaviour.

4.4 Current Flow in a Superconductor

In classical mechanics, the momentum of a particle with charge q and mass m in a magnetic field is given by

$$\mathbf{p} = m\mathbf{v} + q\mathbf{A}, \tag{4.4.1}$$

with $\mathbf{A}$ the magnetic vector potential associated with the magnetic field and $\mathbf{v}$ the velocity of the charged particle.

For a superelectron with mass m^* and charge q^*, (4.4.1) therefore becomes

$$\mathbf{p} = m^*\mathbf{v} + q^*\mathbf{A}, \tag{4.4.2}$$

Now we can then write the momentum density of the Cooper pairs in a superconductor, each having the same momentum, as

$$n_s\mathbf{p} = n_s\left(m^*\mathbf{v} + q^*\mathbf{A}\right), \tag{4.4.3}$$

where n_s is the density of Cooper pairs in the superconductor.

But $n_s\mathbf{p}$ is the expectation value of the canonical quantum momentum operator $-\jmath\hbar\nabla$ operating on the pair-fluid waveform [48]. Therefore

$$n_s\mathbf{p} = \langle\Psi| - \jmath\hbar\nabla|\Psi\rangle\,. \tag{4.4.4}$$

Since [48]

$$-\jmath\hbar\nabla\Psi = \hbar\left(\nabla\theta\right)\Psi, \tag{4.4.5}$$

we have that [48]

$$\mathbf{p} = \hbar\nabla\theta. \tag{4.4.6}$$

(4.4.2) then becomes

$$\hbar\nabla\theta = m^*\mathbf{v_s} + q^*\mathbf{A}. \tag{4.4.7}$$

The Cooper pair current density is given by [48]

$$\mathbf{J_s} = n_s q^* \mathbf{v_s}. \tag{4.4.8}$$

Combining (4.4.7) and (4.4.8), we find

$$\hbar\nabla\theta = q^*\Lambda\mathbf{J_s} + q^*\mathbf{A}, \tag{4.4.9}$$

with

$$\Lambda = \frac{m^*}{n_s\left(q^*\right)^2}. \tag{4.4.10}$$

(4.4.9) and (4.4.10) describe the quantum mechanical flow of current in a superconductor.

4.5 Flux Quantization

Consider a superconductor surrounding a non-superconducting hole, as shown in Figure 4.5

Taking a contour C as shown in Figure 4.5 and integrating (4.4.9) we find

$$\hbar \oint_C \nabla\theta \cdot d\mathbf{l} = q^* \oint_C (\Lambda\mathbf{J_s} + \mathbf{A}) \cdot d\mathbf{l}. \tag{4.5.1}$$

Since the phase of the wave function must be unique or differ with a multiple of 2π at each point [48] the left side of (4.5.1) becomes

$$\hbar \oint_C \nabla\theta \cdot d\mathbf{l} = \hbar 2\pi n \tag{4.5.2}$$

where n is an integer.

If the contour is taken deep enough inside the superconductor (i.e. deeper than the London penetration depth, λ_L) we have that $J_s = 0$. The right hand

side of (4.5.2) becomes (using Stokes's Theorem) [48]

$$q^* \oint_C \mathbf{A} \cdot d\mathbf{l} = q^* \iint_S (\nabla \times \mathbf{A})\, d\mathbf{s} = q^* \iint_S \mathbf{B} \cdot d\mathbf{s} = q^* \Phi_S, \tag{4.5.3}$$

since the surface integral of the magnetic field is simply the flux, Φ_S, enclosed by contour C. Combining (4.5.1), (4.5.2) and (4.5.3) we find

$$\hbar 2\pi n = q^* \Phi_S. \tag{4.5.4}$$

Because of the Meissner effect, the flux Φ_S is trapped inside the non-superconducting hole. This, together with (4.5.4), implies that magnetic flux inside the non-superconducting hole is always quantized, with multiples of

$$\Phi_0 = \frac{2\pi\hbar}{q^*} = \frac{h}{2q} \approx 2.0678 \times 10^{-15} Wb, \tag{4.5.5}$$

where h is Planck's constant and q is the charge of an electron.Φ_0 is called the flux quantum, or fluxon.

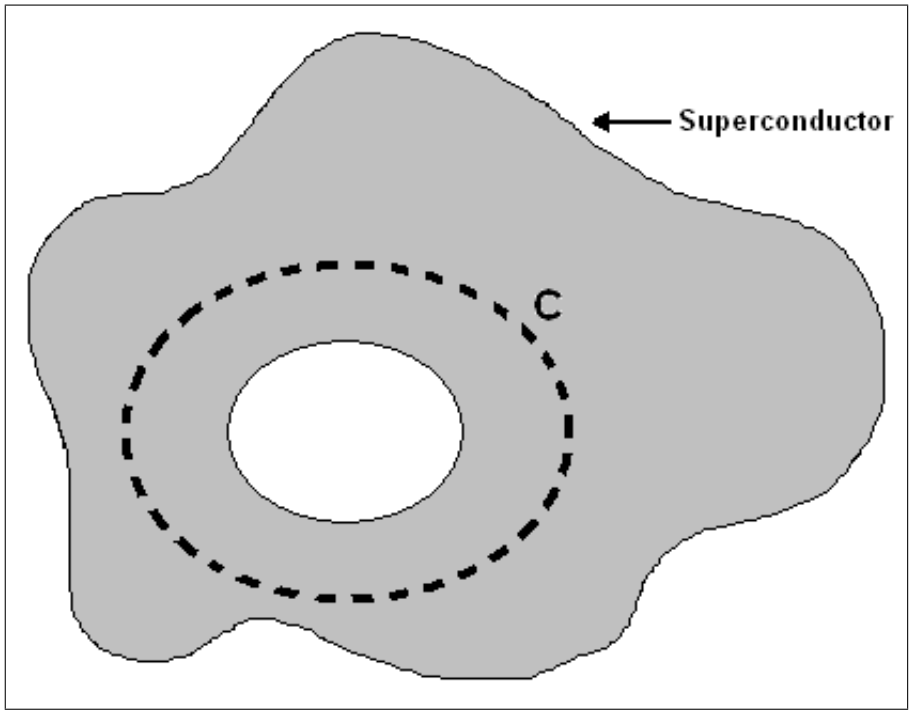

Figure 4.5: Contour of integration around a non-superconducting hole in a superconductor.)

4.6 Josephson Junctions and the Josephson Effects

The fact that there is a finite probability that a single electron can tunnel through a potential barrier was predicted in 1928, and was observed in the mid 1950s [50]. The scientific community of the time, however, speculated that, although single electron tunnelling was possible, the probability of Cooper pairs tunnelling through a potential barrier was negligibly small [4]. However, Brian Josephson, a student at Cavendish Laboratory in Cambridge, changed popular belief in 1962 when he predicted, using the B.C.S. theory, that Cooper pair tunnelling was *just* as probable as single electron tunnelling [4, 54]. The tunnelling of Cooper pairs through a potential barrier was called the Josephson effect and was experimentally confirmed in 1963 by Philip Anderson and John Rowell [4, 55]. It predicts that current can flow through an insulating barrier without a voltage drop across the barrier.

4.6.1 Josephson Junction Structures

The Josephson Effect is observed in two types of superconducting structures [56], the tunnel junction and the proximity junction or weak link. The tunnel junction consists of two superconductor layers separated by an insulating barrier layer. The weak link, on the other hand, consists of either a normal metal layer sandwiched between two superconductor layers, or a superconductor with a lower critical current between two superconductors with higher critical currents.

Cooper pairs coherently tunnel through a tunnel junction, but in a weak link structure no tunnelling is observed. The Cooper pairs pass through a weak link structure due to the proximity effect [56], which states that if a superconductor and a normal metal come into contact, the Cooper pairs will penetrate the normal metal up to a certain depth [5, 56]. Fortunately, this difference in Cooper pair tunnelling only causes slight differences[10] in the behaviour of the two junctions, and both can be analysed in the same way.

Figure 4.6 shows different Josephson junction structures. The three structures in (a) are weak links, while the structure in (b) represents a tunnel

[10]The main difference between the two types of junction in terms of application is the capacitance of the junctions [51].

junction.

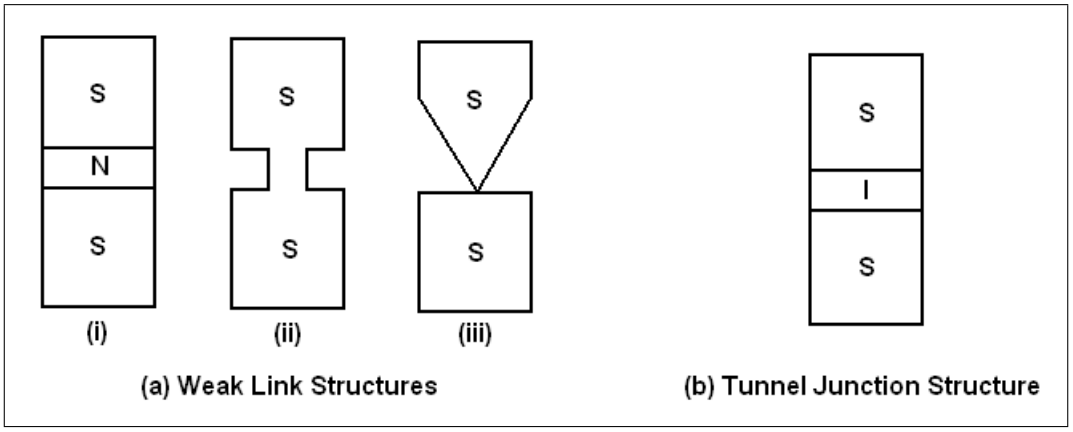

Figure 4.6: Josephson junction structures. (a) Different weak link structures: (i) Superconductor-Normal metal-Superconductor (SNS) junction, (ii) Microbridge structure, (iii) Point-contact structure. (b) Tunnel junction structure: Superconductor-Insulator-Superconductor (SIS) structure. [5])

The probability of a Cooper pair tunnelling through a barrier is strongly dependant on the thickness of the barrier. In a weak link structure, if the barrier thickness is in the order of the coherence length of a Cooper pair, ξ, tunnelling can readily take place and the Josephson Effect is observed [56]. If, however, the barrier thickness is much larger than the coherence length, tunnelling is not effective and the Josephson Effect is not observed. In a tunnel junction structure, the Josephson Effect is only observed if the barrier thickness is of the order of a few decay lengths. The decay length, ζ, is a measure of how far into an insulator the macroscopic wave function of a superconductor can exponentially penetrate [4]. The wave functions of both separated superconductors in a tunnel junction can penetrate the insulator. Since the square magnitude of a quantum wave function denotes the probability of finding a particle at a certain position [32], if these wave functions overlap, tunnelling can occur, and the Josephson Effect is observed (see Figure 4.7) [5].

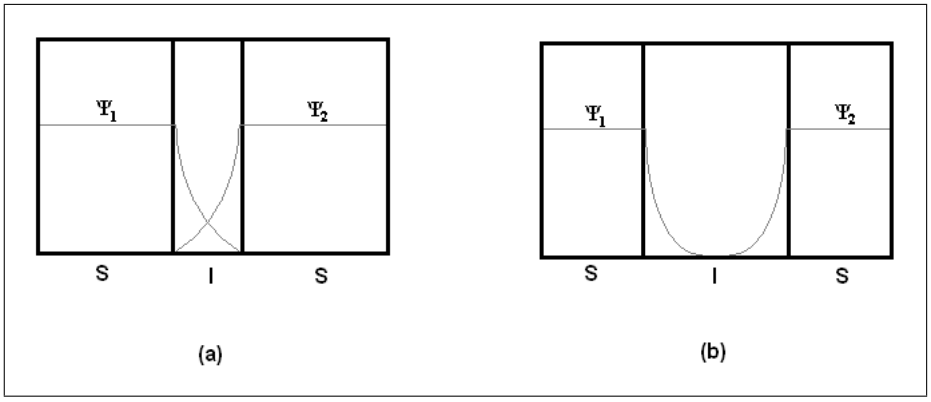

Figure 4.7: A schematic representation of the wave functions of two superconductors separated by an insulator. (a) The width of the insulating barrier is small enough that the wave functions can overlap ($width < \zeta$) and tunnelling can occur. (b) The width of the insulating barrier is so large that the wave functions do not overlap ($width > \zeta$) and tunnelling does not occur. [5]

4.6.2 The DC and AC Josephson Effects

Experiments have shown that an applied current smaller than the junction's critical current can flow through a Josephson junction without generating a voltage across it. This phenomenon is known as the DC Josephson Effect. However, if the applied current exceeds the junction's critical current, a periodic voltage develops across the junction. This is called the AC Josephson Effect.

4.6.3 The Current-Voltage Relationship of Josephson Junctions

Figure 4.8 shows a graph of the current-voltage relationship for a Josephson junction.

The behaviour of the Josephson junction in DC and AC modes can clearly be seen from Figure 4.8. If a current smaller than the junction's critical current is applied no voltage appears across the junction, but as soon as the current exceeds the critical current, a voltage appears across the junction.

The equations governing the behaviour of Josephson junctions to applied currents and voltages can be derived using (4.4.9), but are simply stated here.

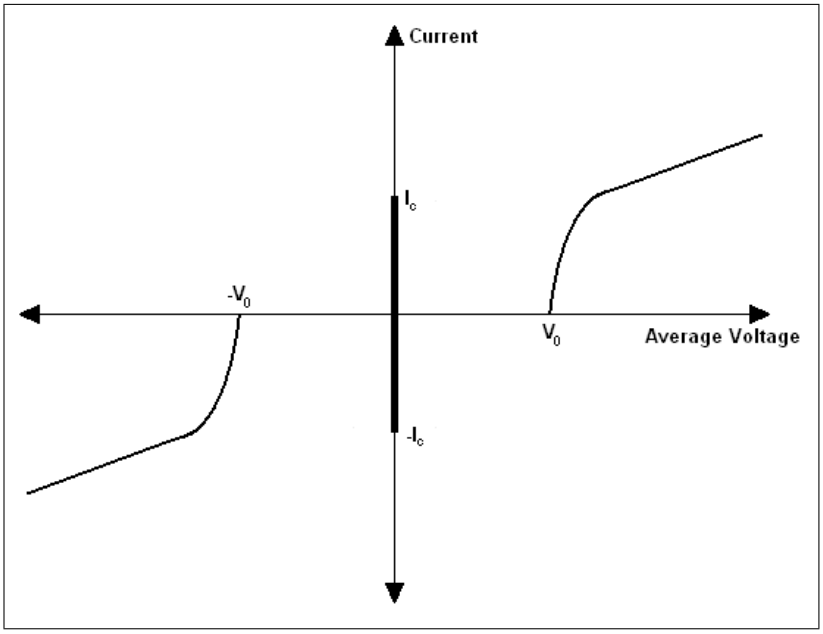

Figure 4.8: The $I - V$ curve for a Josephson junction. [4]

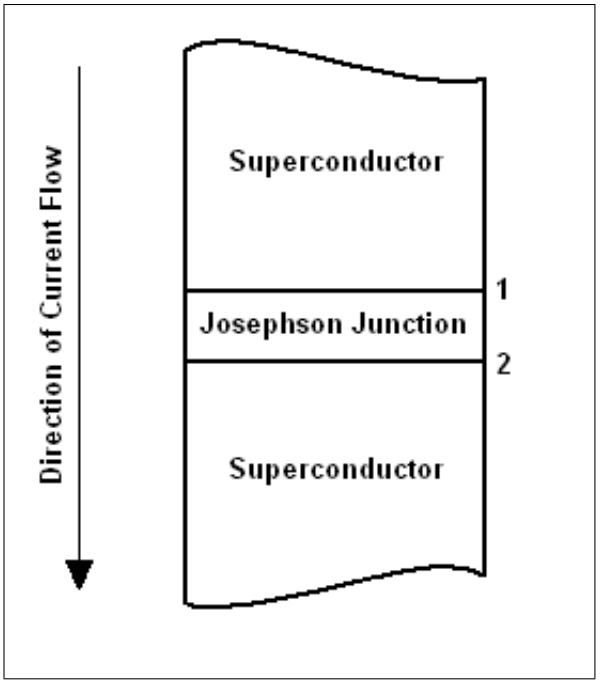

Figure 4.9: A Josephson junction.

For the junction shown in Figure 4.9, the current density, $\mathbf{J_s}$, flowing through the Josephson Junction is described as

$$\mathbf{J_s} = \mathbf{J_c} sin(\varphi) \tag{4.6.1}$$

and the voltage developed across the junction is given as

$$\frac{\partial \varphi}{\partial t} = \frac{2\pi}{\Phi_0} \int_1^2 \mathbf{E} \cdot d\mathbf{l} \tag{4.6.2}$$

where $\mathbf{J_c}$ is the critical current density of the Josephson junction and $\mathbf{E}$ is the electric field in the junction. φ is known as the Gauge Invariant Phase Difference, and is given by

$$\varphi = \theta_1 - \theta_2 - \frac{2\pi}{\Phi_0} \int_1^2 \mathbf{A} \cdot d\mathbf{l} \tag{4.6.3}$$

where θ_1 is the phase of the wave function in the first superconductor, and θ_2 is the phase of the wave function in the second.

The most important observation on these equations is the fact that the phases of the wave functions of the separated superconductors are related. This implies that the junction acts like a connected superconductor, rather than two superconductors separated by a barrier.

4.6.4 Basic Lumped Element Model for a Josephson Junction

Figure 4.10 shows the circuit diagram symbol for a Josephson junction.

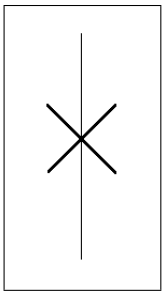

Figure 4.10: Josephson junction circuit symbol.

If we assume that the current densities and phase differences remain constant across the junction we can generate a lumped element model from (4.6.1), (4.6.2) and (4.6.3). The current-phase and voltage-phase relationships of (4.6.1) and (4.6.2) become [5]

$$i = I_c sin(\varphi), \tag{4.6.4}$$

$$\frac{d\varphi}{dt} = \frac{2\pi}{\Phi_0} v \tag{4.6.5}$$

while the phase difference is still given by (4.6.3).

This model is known as the Basic Lumped Model for Josephson Junctions, and can be used to describe sub-critical current Josephson junction behaviour to a high degree of accuracy [5].

The DC and AC Josephson effects are easily explained with this model. If a current passing through the junction is constant, it implies from (4.6.4) that the phase also is constant. This, in turn, implies from (4.6.5) that the voltage across the junction is zero, describing the DC Josephson effect [5]. If, on the other hand, a constant voltage V_0 is applied across the junction, (4.6.5) yields (after integration over time)

$$\varphi(t) = \varphi(0) + \frac{2\pi}{\Phi_0} V_0 t \tag{4.6.6}$$

where $\varphi(0)$ is the initial phase. Using this result in (4.6.4) we find

$$i = I_c sin\left(\frac{2\pi}{\Phi_0} V_0 t + \varphi(0)\right) = I_c sin(2\pi f_J t + \varphi(0)), \tag{4.6.7}$$

where f_J is known as the Josephson frequency [37], given as

$$f_J = \frac{V_0}{\Phi_0} = 483.60 \times 10^{12} V_0 \, (Hz). \tag{4.6.8}$$

It is apparent that in this case the current through the junction oscillates at $483.60 MHz$ per μV_{DC} that is applied [37]. This is the AC Josephson effect.

The basic lumped element model is only valid for currents smaller than the junction's critical current. To describe Josephson junction behaviour when applied currents exceed the critical current a new model is needed.

4.6.5 Generalized Model for a Josephson Junction (RCSJ Model)

The basic lumped element model for a Josephson junction only describes Cooper pair tunnelling through the junction and ignores secondary effects such as the shunt resistance and the capacitance of the junction [37]. The Generalized Junction Model incorporates these additional parameters into the basic lumped element model in order to describe junction behaviour when applied currents exceed the critical current [37].

According to the two-fluid model, there are always normal electrons present in a superconducting material, even when it is in the superconducting state. Some current is therefore always carried by normal electrons that experience resistance. As a result of this, not all current can be carried through the junction in a non-dispersive way. The generalized junction model models this as a resistive channel in parallel with the basic Josephson junction [5]. This resistive channel is a non-linear element dependant on temperature and voltage, but for our purposes, and to a good approximation, can be taken as constant. The resistance is given as R_n, or the normal state resistance. The product of the normal state resistance and the critical current of the junction is called the I_cR_n-product, and is always constant [4].

Since real-world junctions usually have some form of parallel plate structure, they have a small capacitive effect associated with them. This is modelled in the generalized junction model by a capacitor in parallel to the resistive channel and basic Josephson junction.

This revised model is known as the Resistively- and Capacitively-Shunted Junction (RCSJ) model. A schematic representation of the RSCJ model is shown in Figure 4.11.

In the RCSJ model, the total current flowing through the junction, i, is given as

$$i = I_c sin(\varphi) + \frac{v}{R_n} + C\frac{dv}{dt}, \tag{4.6.9}$$

which yields, when combined with the phase-voltage relation (4.6.2)

$$i = I_c sin(\varphi) + \frac{1}{R_n}\frac{\Phi_0}{2pi}\frac{d\varphi}{dt} + C\frac{\Phi_0}{2pi}\frac{d^2\varphi}{dt^2}. \tag{4.6.10}$$

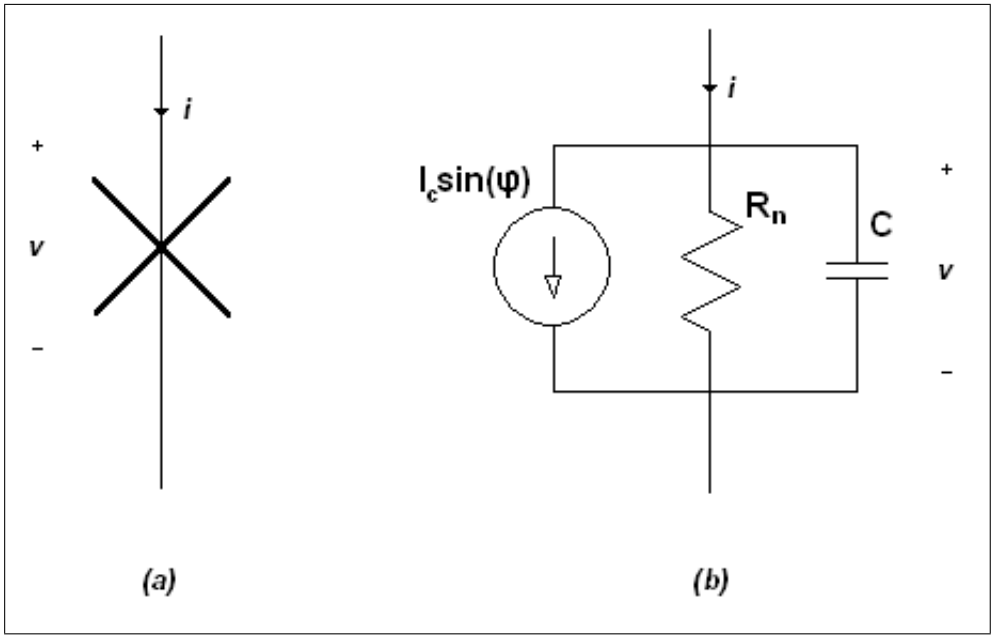

Figure 4.11: (a)Josephson junction circuit symbol. (b) Equivalent circuit of a Josephson junction according to the RCSJ model.

4.6.6 The Stewart-McCumber Parameter

The capacitance of a Josephson junction is an important parameter. It determines the possibility of hysteresis occurring in the junction [6]. The Stewart-McCumber parameter [57, 58] is a dimensionless measure of the importance of the capacitance of a junction and is given by [37]

$$\beta_c = \frac{2\pi}{\Phi_0}(I_c R_n^2 C). \tag{4.6.11}$$

A junction is usually in one of three configurations: strongly overdamped with $\beta_c \ll 1$, strongly underdamped with $\beta_c \gg 1$ or critically damped with $\beta \approx 1$. Damping affects the $I - V$ relationship of the junction [37].

4.6.7 The RSJ Model

When the Stewart McCumber parameter is very small ($\beta_c \ll 1$) a Josephson junction shows strongly overdamped behaviour. This happens when the capacitance of the junction is close to zero. In this case we can ignore the

capacitive channel of the RCSJ model and (4.6.10) reduces to

$$i = I_c sin(\varphi) + \frac{1}{R_n}\frac{\Phi_0}{2pi}\frac{d\varphi}{dt}. \tag{4.6.12}$$

The strongly overdamped Josephson junction is therefore also known as the Resistively Shunted Junction (RSJ), and is schematically shown in Figure 4.12.

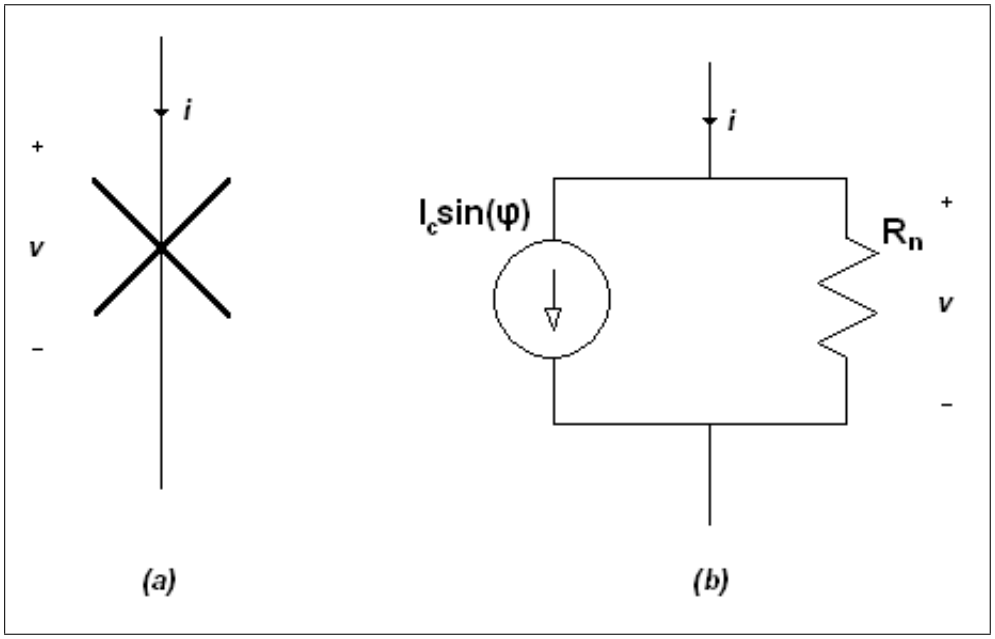

Figure 4.12: (a)Josephson junction circuit symbol. (b) Equivalent circuit of a Josephson junction according to the RSJ model.

The time average voltage response of an overdamped Josephson junction is given as [4]

$$\langle v(t)\rangle = \begin{cases} 0 & \text{for } I \leq I_c \\ I_c R_n \sqrt{\left(\frac{I}{I_c}\right)^2 - 1} & \text{for } I \leq I_c \end{cases}, \tag{4.6.13}$$

and the frequency of oscillation of the voltage across an overdamped Josephson junction is given as

$$f = \frac{\langle v(t)\rangle}{\Phi_0}. \tag{4.6.14}$$

These equations fully describe the behaviour of the overdamped Josephson junction. While $I \leq I_c$ all the current flows through the superconductive channel and no voltage appears across the junction. If the current through the junction exceeds the critical current of the junction, current is forced through the resistive channel and a voltage appears across the junction. As the current through the junction is increased, the average voltage across the junction also increases. The frequency of oscillation of the instantaneous voltage across the junction therefore increases.

The normalized current-voltage relationship of the overdamped Josephson junction is shown in Figure 4.13, while Figure 4.14 shows the instantaneous voltage across an overdamped Josephson junction for a few different values of applied current.

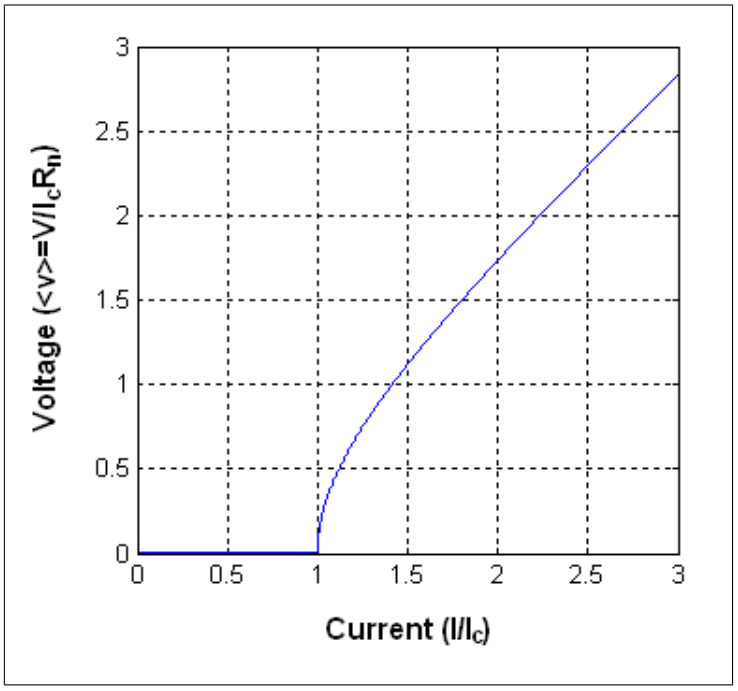

Figure 4.13: Normalized Voltage-Current characteristic curve of an overdamped Josephson junction.

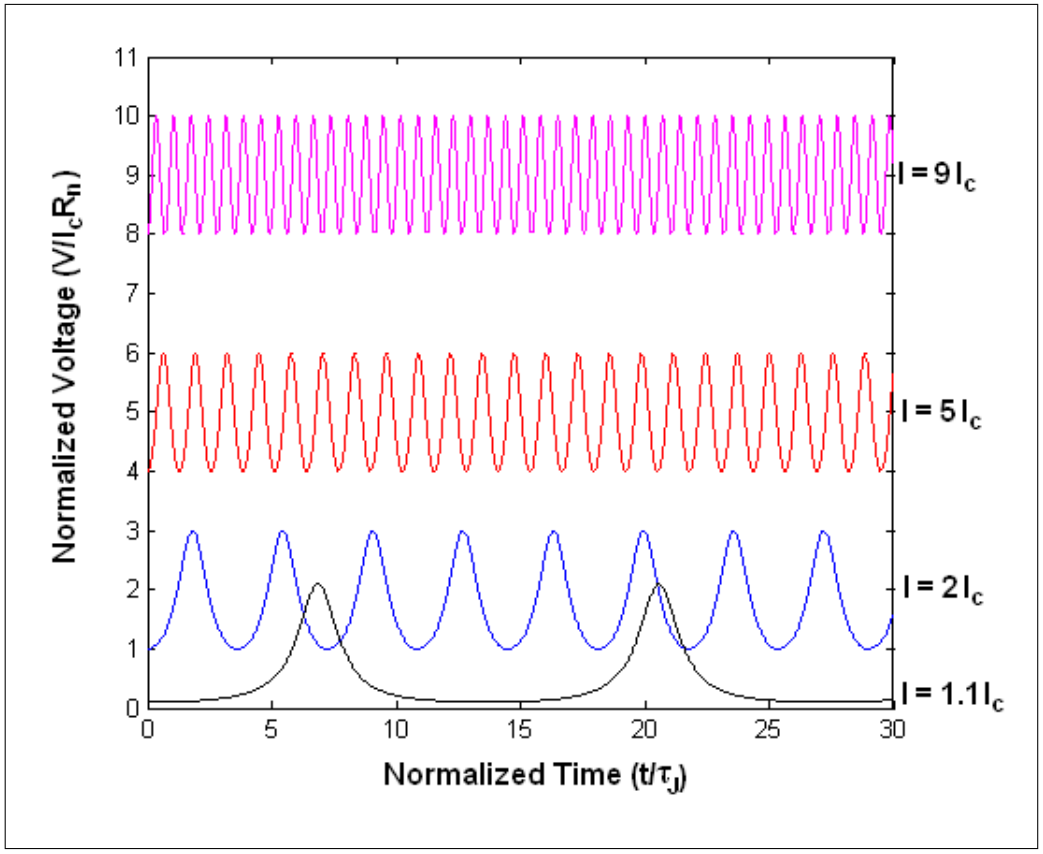

Figure 4.14: Normalized instantaneous voltage across an overdamped Josephson junction for different values of applied current.

Unlike junctions fabricated using low-T_c superconductors [59, 60], the capacitance of junctions fabricated using high-T_c superconductors such as YBCO is negligibly small [61]. One important exception, however, is when $SrTiO_3$ substrates are used in the fabrication of thin film devices [61, 62]. This substrate significantly increases the capacitance of the fabricated Josephson junction due to the high dielectric constant of this material. Fortunately, however, these capacitive effects are only observed at temperatures below 30 kelvin, and can generally be ignored. When high-T_c superconductors are used, the RSJ model therefore describes junction behaviour to a high degree of accuracy.

As only high-T_c superconductors were investigated, the underdamped ($\beta_c \gg 1$) and critically damped ($\beta \approx 1$) junctions fall outside the scope of this thesis. Reference [37] can be consulted if a description of these cases is needed.

4.6.8 RSJ Response to AC Signals

In order to fully understand the behaviour of the overdamped Josephson junction its response to AC driving signals also needs to be investigated.

For a driving AC voltage source, $v(t)$, given by

$$v(t) = V_0 + V_s \cos(\omega_s t), \tag{4.6.15}$$

the resulting current through the junction is found to be [4]

$$\begin{aligned} i_J(t) &= \frac{V_0}{R_n} + \frac{V_s}{R_n}\cos\omega_0 t \\ &\quad + I_c \sum_{n=-\infty}^{+\infty} (-1)^n J_n\left(\frac{2\pi V_s}{\Phi_0 \omega_s}\right) \sin[(2\pi f_J - n\omega_s)t + \varphi(0)]. \end{aligned} \tag{4.6.16}$$

To find the time average of the current flowing through the junction, $\langle i \rangle$, we notice that the time average of the $\cos(\omega_s t)$ term in (4.6.16) is zero, and that the time average of the final term in (4.6.16) becomes zero only when the sinusoidal term is made to vanish. This occurs when $2\pi f_J = n\omega_s$. We therefore find

$$\langle i \rangle = \frac{V_0}{R_n} + I_c \sum_{n=-\infty}^{+\infty} (-1)^n J_n\left(\frac{2\pi V_s}{\Phi_0 \omega_s}\right) \sin[\varphi(0)\delta_{2\pi f_J, n\omega_s}], \tag{4.6.17}$$

where

$$\delta_{2\pi f_J, n\omega_s} = \begin{cases} 1 & \text{if } 2\pi f_J = n\omega_s \\ 0 & \text{if } 2\pi f_J \neq n\omega_s \end{cases} . \tag{4.6.18}$$

The average current through the overdamped Josephson junction is therefore the sum of a straight line due to the resistor with current spikes at voltages $V_0 = n\omega_s(\Phi_0/2\pi)$ due to the basic Josephson junction. Figure 4.15 shows a graph of the average current through an overdamped Josephson junction driven by an AC voltage source.

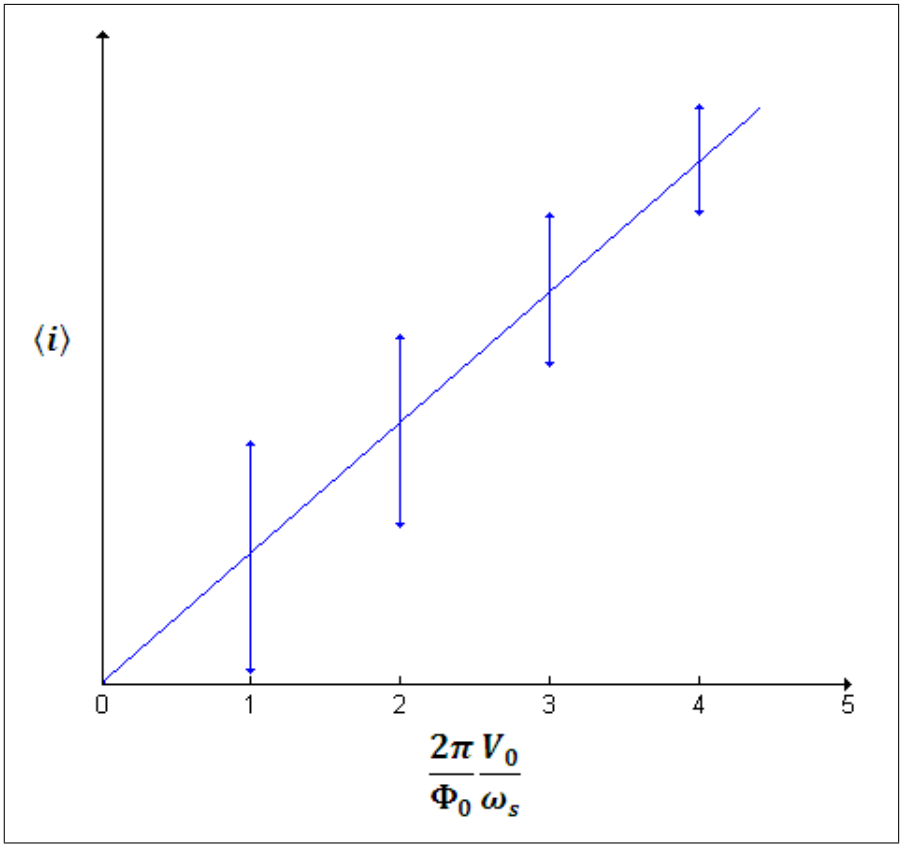

Figure 4.15: Average current through an overdamped Josephson junction driven by an AC voltage source.

For a overdamped Josephson junction driven by an AC current source given by

$$i(t) = I_0 + I_s \cos(\omega_s t), \tag{4.6.19}$$

(4.6.12) can again be used to find the dynamic response. The resulting differential equation, however, is difficult to solve and falls outside the scope of this text. The resulting graph of current versus average voltage is simply given in Figure 4.16 [4]. The characteristic pattern shown in Figure 4.16 is known as Shapiro Steps.

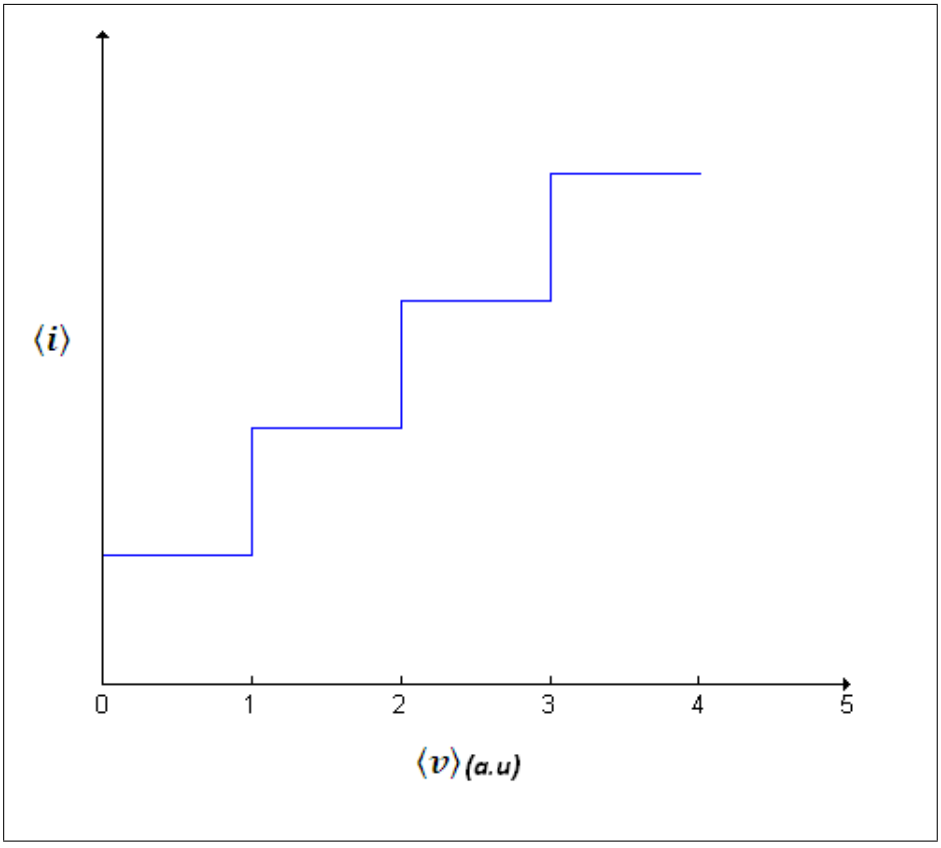

Figure 4.16: Current versus average voltage of an overdamped Josephson junction driven by an AC current source (Shapiro Steps).

4.6.9 The Effect of an Applied Magnetic Field on Josephson Junction Behaviour

The critical current of a SIS Josephson junction is dependent on the applied magnetic field [37, 4]. The critical current of a Josephson junction is modulated in the presence of an perpendicularly applied magnetic flux density, B, and is given by [37]

$$I_c(B) = I_c(0)\left|\frac{\sin\left[\pi\left(\frac{\Phi_B}{\Phi_0}\right)\right]}{\pi\left(\frac{\Phi_B}{\Phi_0}\right)}\right|, \tag{4.6.20}$$

where $I_c(0)$ is the critical current with no externally applied flux. The junction therefore exhibits a critical current that has a Frauenhofer pattern, as shown in Figure 4.17.

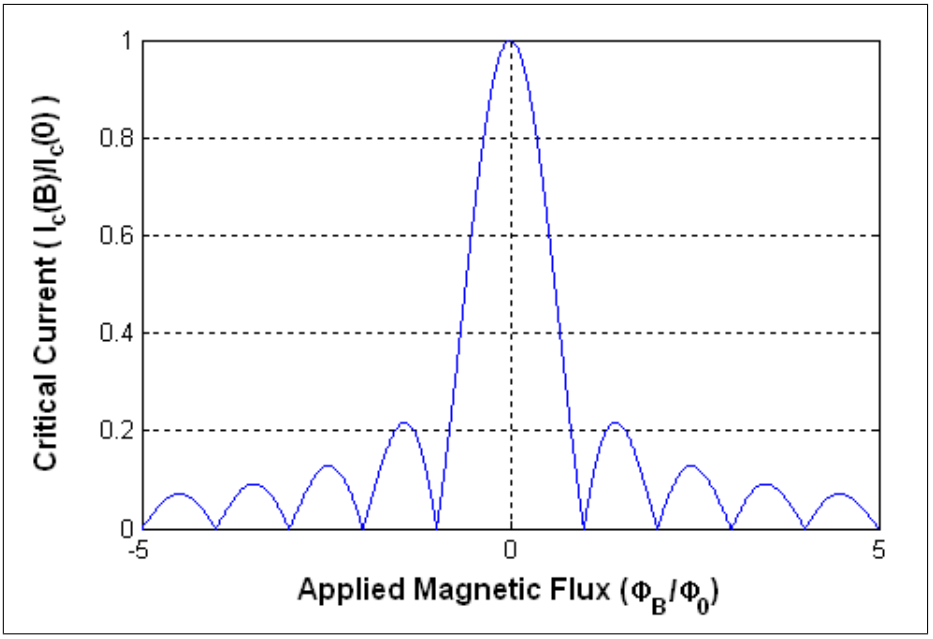

Figure 4.17: Magnetic field dependence of the critical current of a Josephson junction.

Chapter 5

SQUID Theory

5.1 Introduction

One of the most widely researched applications of superconductivity is the Superconducting QUantum Interference Device or SQUID. This device can be harnessed to create SQUID magnetometers, devices capable of measuring magnetic fields with incredibly high sensitivity (in the order of $2^{-15}Wb$).

SQUIDs consist of a superconducting ring interrupted by one or more Josephson junctions. The operation of the SQUID is based on the Josephson effect, where the tunnelling of Cooper pairs through the connected Josephson junctions causes interference of the superconducting waveform across these junctions.

The two most common configurations for SQUID sensors are the RF SQUID and the DC SQUID. The naming of these devices stem from the way in which they are biased.

The RF SQUID consists of a superconducting loop interrupted by a single Josephson junction and is biased by a radio frequency magnetic flux. The RF SQUID falls outside the scope of this text, but the literature can be consulted for a detailed description of the working of such devices [4, 61, 63].

The DC SQUID consists of two Josephson junctions connected in parallel by a superconducting loop, and is biased using a DC current. DC SQUIDs has lower intrinsic noise than RF SQUIDs.

In this chapter the theory and operation of DC SQUID is discussed.

5.2 The Basic DC SQUID

The DC SQUID consists of a superconducting loop interrupted by two Josephson junctions, as shown in Figure 5.1.

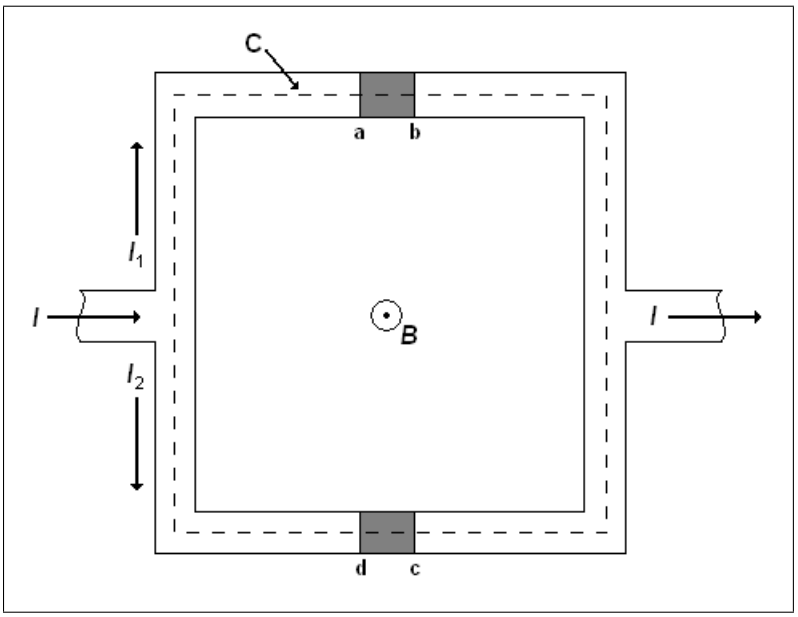

Figure 5.1: Superconducting loop interrupted by two Josephson junctions, forming a DC SQUID.

We assume for the rest of the section that both junctions are identical and that the junctions are small enough to have a homogeneous critical current density throughout their cross-sections. The shunt resistance of the junction is disregarded at first and basic Josephson junction model is used, with (4.6.3) describing the gauge invariant phase difference across the junction. The inductance of the superconducting loop is also neglected for now.

The total current flowing through the sensor, i, is given simply as the sum of the current flowing through each junction,

$$\begin{aligned} i &= i_1 + i_2 && (5.2.1)\\ &= I_c \sin\varphi_1 + I_c \sin\varphi_2 && (5.2.2)\\ &= 2I_c \cos\left(\frac{\varphi_1 - \varphi_2}{2}\right) \sin\left(\frac{\varphi_1 + \varphi_2}{2}\right), && (5.2.3) \end{aligned}$$

where I_c is the critical current of a single junction and φ_1 and φ_2 are the gauge invariant phase differences of the respective junctions [4].

The difference in the gauge invariant phase differences can be found by integration of the gradient of the wave function phase, $\nabla\theta$, around the closed contour C shown in Figure 5.1. Noting that the phase can only change by a multiple of 2π around the closed contour, this integration yields

$$\begin{aligned} \oint_C \nabla\theta \cdot d\mathbf{l} &= 2\pi n \\ &= (\theta_b - \theta_a) + (\theta_c - \theta_b) + (\theta_d - \theta_c) + (\theta_a - \theta_d), \end{aligned} \tag{5.2.4}$$

where a, b, c and d are as indicated in Figure 5.1. The first and third terms of (5.2.4) are the phase differences across the junctions and can be obtained directly from (4.6.3), yielding

$$(\theta_b - \theta_a) = -\varphi_1 - \frac{2\pi}{\Phi_0}\int_a^b \mathbf{A}\cdot d\mathbf{l}, \tag{5.2.5}$$

and

$$(\theta_d - \theta_c) = -\varphi_2 - \frac{2\pi}{\Phi_0}\int_c^d \mathbf{A}\cdot d\mathbf{l}. \tag{5.2.6}$$

The second and forth terms in (5.2.4) are the phase differences in the superconducting wire itself and can be found by rearranging the supercurrent (4.4.9) and integrating from the appropriate points in the loop. This integration yields

$$(\theta_c - \theta_b) = \int_b^c \nabla\theta \cdot d\mathbf{l} = -\frac{2\pi}{\Phi_0}\int_b^c \Lambda\mathbf{J}\cdot d\mathbf{l} - \frac{2\pi}{\Phi_0}\int_b^c \mathbf{A}\cdot d\mathbf{l}, \tag{5.2.7}$$

and

$$(\theta_a - \theta_d) = \int_d^a \nabla\theta \cdot d\mathbf{l} = -\frac{2\pi}{\Phi_0}\int_d^a \Lambda\mathbf{J}\cdot d\mathbf{l} - \frac{2\pi}{\Phi_0}\int_d^a \mathbf{A}\cdot d\mathbf{l}. \tag{5.2.8}$$

Substitution of (5.2.5), (5.2.6), (5.2.7) and (5.2.8) into (5.2.4) gives

$$\varphi_2 - \varphi_1 = 2\pi n + \frac{2\pi}{\Phi_0}\oint_C \mathbf{A}\cdot d\mathbf{l} + \frac{2\pi}{\Phi_0}\int_b^c \Lambda\mathbf{J}\cdot d\mathbf{l} + \frac{2\pi}{\Phi_0}\int_d^a \Lambda\mathbf{J}\cdot d\mathbf{l}. \tag{5.2.9}$$

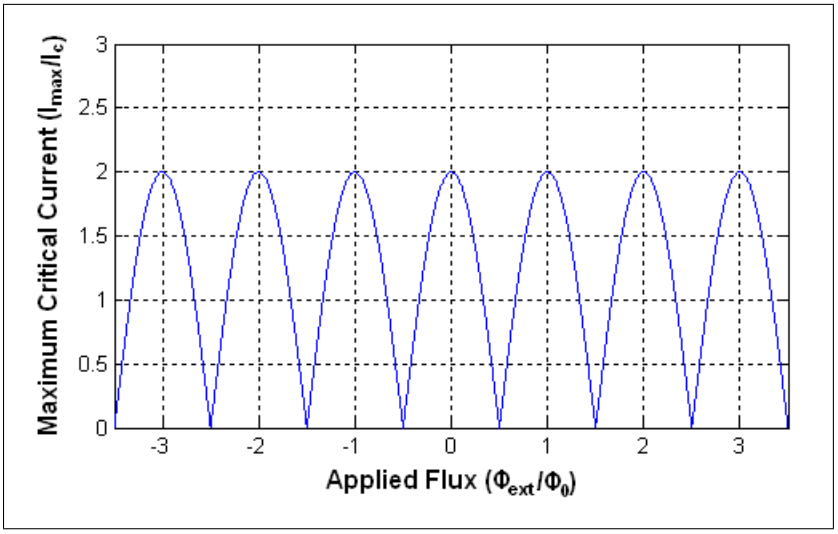

Figure 5.2: Maximum critical current of a DC SQUID with negligible loop inductance as a function of applied flux.

The integration of the magnetic vector potential around the contour C is simply the flux, Φ, threading the contour, and therefore the hole. If we assume that the integration path C is taken deeper than a few penetration depths, the integration of the current density becomes negligibly small. (5.2.9) therefore reduces to

$$\varphi_2 - \varphi_1 = 2\pi n + \frac{2\pi\Phi}{\Phi_0}. \tag{5.2.10}$$

The phase differences of the two connected Josephson junctions are therefore related. This is called quantum interference. The total current flowing through the SQUID becomes

$$i = 2I_c \cos\left(\frac{\pi\Phi}{\Phi_0}\right) \sin\left(\varphi_1 + \frac{\pi\Phi}{\Phi_0}\right). \tag{5.2.11}$$

This equation is similar to the basic Josephson junction (4.6.4) with the critical current and phase a function of the applied flux.

By maximizing (5.2.11) the maximum critical current of the SQUID can be obtained as

$$I_{max} = 2I_c \left|\cos\left(\frac{\pi\Phi_{ext}}{\Phi_0}\right)\right|, \tag{5.2.12}$$

where Φ_{ext} is the externally applied flux. Figure 5.2 shows the maximum critical current of the SQUID as a function of the applied flux.

5.3 Loop Inductance and the Screening Parameter

A practical DC SQUID always has an intrinsic loop inductance, L_{SQ}. The total flux threading the loop now becomes the sum of the externally applied flux, Φ_{ext}, and the flux generated by circulating currents flowing in the superconducting loop. Therefore

$$\Phi = \Phi_{ext} + L_{SQ} I_{cir}, \tag{5.3.1}$$

where I_{cir} is the circulating current in the superconducting loop, and is given by [4]

$$I_{cir} = \frac{i_1 - i_2}{2}, \tag{5.3.2}$$

with i_1 and i_2 the currents flowing through the Josephson junctions.

Because of the circulating current, the quantum interference in the SQUID is not complete and the maximum critical current is not reduced to zero as is the case when the loop inductance is negligible (see Figure 5.2). If the loop inductance becomes too large the interference pattern disappears and the quantum effects are not visible anymore.

A large loop inductance will cause the SQUID to show hysteresis. The largest possible loop inductance for a SQUID with no hysteresis is [37]

$$L_{SQ} = \frac{\Phi_0}{I_c}. \tag{5.3.3}$$

The Screening Parameter, β_L, is a measure of the influence of loop inductance on the SQUID, and is given by

$$\beta_L = \frac{2 L_{SQ} I_c}{\Phi_0}. \tag{5.3.4}$$

The optimum value is when $\beta_L = 1$ [37]. It is important to note, however,

that the hysteresis constraint (5.3.3) as well as noise constraints (discussed in Section 5.6) make it difficult to reach this optimum design with practical SQUIDs.

5.4 Flux-to-Voltage Conversion

To find a more realistic model for a DC SQUID, we incorporate the RSJ model into the description. This creates what is known as a magnetometer. The DC SQUID magnetometer converts an applied flux into a measurable voltage [4, 64].

The current flowing through the SQUID, i, is the sum of the currents flowing through each overdamped junction. Therefore,

$$\begin{aligned} i &= i_1 + i_2 + i_{R1} + i_{R2}. && (5.4.1)\\ &= I_c \sin\varphi_1 + I_c \sin\varphi_2 + \frac{v}{R_1} + \frac{v}{R_2} && (5.4.2)\\ &= 2I_c \cos\left(\frac{\varphi_1 - \varphi_2}{2}\right) \sin\left(\frac{\varphi_1 + \varphi_2}{2}\right) + v\left(\frac{1}{R_1} + \frac{1}{R_2}\right). && (5.4.3) \end{aligned}$$

In a similar way then for (5.2.11), combining (5.2.10) with (5.4.3) yields

$$i = 2I_c \cos\left(\frac{\pi\Phi_{ext}}{\Phi_0}\right) \sin\left(\varphi_1 + \frac{\pi\Phi_{ext}}{\Phi_0}\right) + v\left(\frac{1}{R_1} + \frac{1}{R_2}\right). \tag{5.4.4}$$

The current flowing through a DC SQUID magnetometer (5.4.4) is therefore similar to the current flowing through an overdamped Josephson junction. To see this a new phase is defined as

$$\varphi = \varphi_1 + \frac{\pi\Phi_{ext}}{\Phi_0}. \tag{5.4.5}$$

If the applied flux is constant, we therefore find that

$$\frac{d\varphi}{dt} = \frac{d\varphi_1}{dt} = \frac{2\pi}{\Phi_0} v. \tag{5.4.6}$$

Letting the critical current of the DC SQUID, I_{cSQ} be given as

$$I_{cSQ} = 2I_c \left|\cos\left(\frac{\pi\Phi_{ext}}{\Phi_0}\right)\right|, \tag{5.4.7}$$

and combining (5.4.5), (5.4.6) and (5.4.7) with (5.4.4), we find

$$i = I_{cSQ} \sin\varphi + \frac{1}{R_p}\frac{\Phi_0}{2\pi}\frac{d\varphi}{dt}, \tag{5.4.8}$$

where R_p is the parallel combination of R_1 and R_2. (5.4.8) is similar to the current through an overdamped Josephson junction (4.6.12).

If the biasing current is greater than I_{cSQ} at zero applied flux a voltage will develop across the SQUID. The average voltage across the SQUID can be found from (5.4.8) and is related to the applied flux. It is given by [4]

$$\langle v(t)\rangle = IR_p\sqrt{1-\left[\frac{2I_c}{I}\cos\left(\frac{\pi\Phi_{ext}}{\Phi_0}\right)\right]^2} \quad \text{for } I > I_{cSQ}, \tag{5.4.9}$$

where I is the DC bias current.

The voltage-current characteristic curve of a DC SQUID with $\beta_L = 1$ is shown in Figure 5.3. Figure 5.4 shows the voltage-flux response of a DC SQUID with $\beta_L = 1$ for different biasing currents.

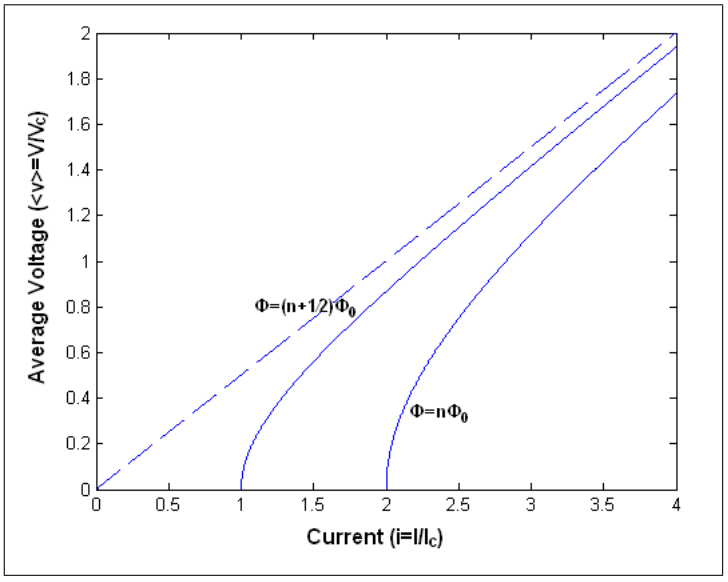

Figure 5.3: Voltage-current characteristic curve of a DC SQUID with $\beta_L = 1$.

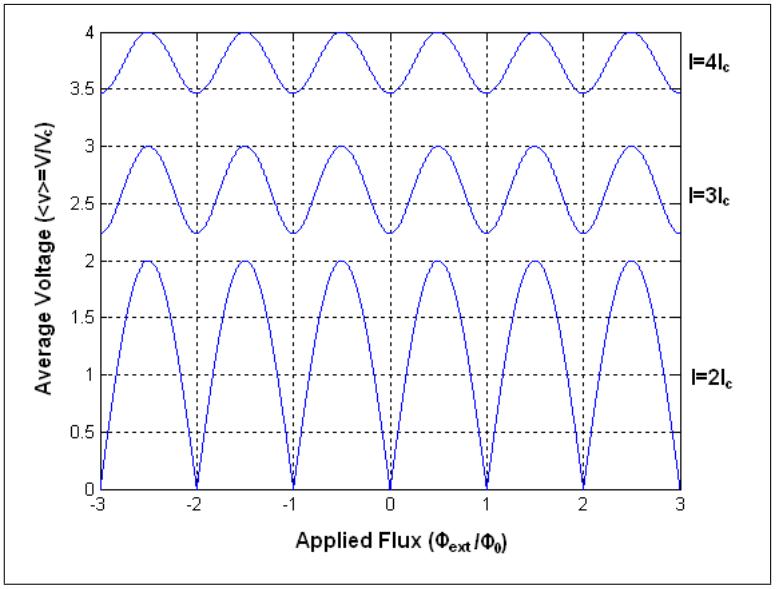

Figure 5.4: Voltage-flux response of a DC SQUID with $\beta_L = 1$ for various biasing currents.

5.5 Practical SQUIDs

5.5.1 Sensitivity

The performance of a DC SQUID is measured in terms of its sensitivity. Two factors limit the sensitivity of the DC SQUID: the magnetic flux resolution and the magnetic field resolution. The magnetic flux resolution is limited by the thermal noise present in the SQUID (discussed in Section 5.6.2) and is always less than one flux quantum [6]. The magnetic field resolution is limited by the area of the SQUID loop, A. The flux coupling into the SQUID is given by

$$\Phi_{SQ} = B_a A, \tag{5.5.1}$$

where B_a is the applied magnetic flux density perpendicular to the SQUID loop. By increasing the area of the SQUID, the magnetic field resolution can be increased.

5.5.2 SQUID layout

In order to reduce thermal noise, the SQUID loop is usually designed to have a small inductance. The resulting pickup loop therefore usually has a small area, A. For a practical SQUID, however, a large loop area is preferred for a large magnetic field resolution. As such, there are several novel methods of increasing the loop area without increasing the loop inductance.

5.5.2.1 Flux Transformers

Flux transformers consist of a pickup loop connected to an input loop that is inductively coupled to the SQUID. The pickup loop is placed in the magnetic field to be measured. The input loop is usually approximately the same size as the SQUID, with multiple turns to ensure good coupling. The pickup loop needs to have a substantial area to have an effect on the sensitivity of the SQUID, and, as such, usually has a diameter in the centimetre scale (a SQUID has a diameter in the micrometer scale). A schematic representation of a flux transformer is shown in Figure 5.5 [65].

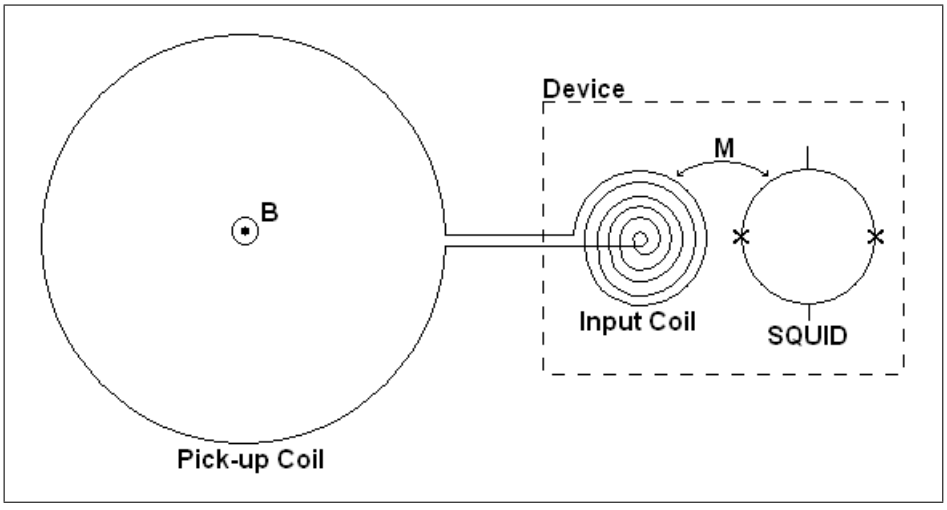

Figure 5.5: Schematic representation of a flux transformer.

Flux transformers require the input loop and the SQUID loop to be very well coupled. Multilayer devices are therefore preferred. Unfortunately high-T_c multilayer devices are difficult to manufacture [66, 67, 68]. An alternative approach is to use a flip-chip arrangement where a single layer SQUID on

one substrate is joined face-to-face with a single layer input coil on another substrate [69, 70].

5.5.2.2 Large-Area Washer DC SQUID

The large-area washer DC SQUID, shown schematically in Figure 5.6, focuses the applied magnetic field through the SQUID loop, effectively increasing the area of the SQUID [53, 71]. As flux is expelled from the interior of superconductors, the magnetic field applied to a large-area washer will be either deflected outward or inward toward the centre hole. The effective area of the SQUID, A_{eff}, becomes

$$A_{eff} = dD, \tag{5.5.2}$$

with d and D respectively the inner and outer dimensions of the washer, as shown in Figure 5.6.

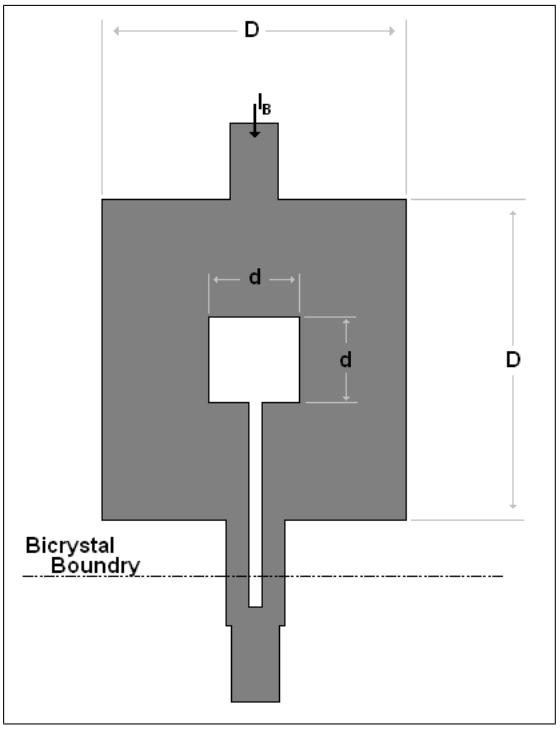

Figure 5.6: Schematic representation of the layout of a large-area washer DC SQUID

The large-area washer DC SQUID has the advantage of only needing a single layer process for manufacturing, unlike the flux transformer design. A significant disadvantage, however, is its noise performance[1]. If a large-area washer SQUID is cooled in the presence of a magnetic field a significant increase in noise is observed. This noise is caused by flux vortices hopping between pinning sites. The amount of flux vortices that form is proportional to the width and quality of the superconducting film [37]. To avoid excess flux noise, some designs include slots and holes in order to trap vortices during the cooling process [6].

5.5.2.3 Directly-Coupled DC SQUID

Because of the increase in flux noise associated with the large-area washer DC SQUID design, the directly-coupled DC SQUID design is preferred for single layer devices [6, 53].

The directly-coupled DC SQUID design is shown schematically in Figure 5.7. A pickup loop is directly coupled to the SQUID loop. The flux threading the pickup loop induces a current that is directly injected into the SQUID loop. This additional current in the SQUID loop therefore effectively increases the area of the SQUID loop without increasing the inductance [72].

[1] See Section 5.6.

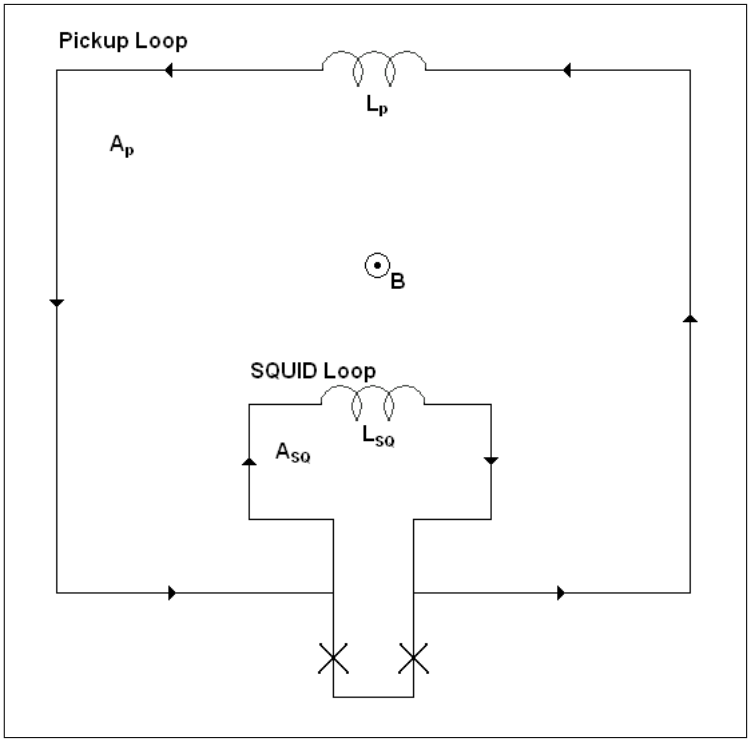

Figure 5.7: Schematic representation of a directly coupled DC SQUID (not to scale) [6].

The total flux threading the SQUID, Φ_T, is the sum of the applied flux that threads the SQUID loop and the flux induced in the SQUID loop by the injected current. Therefore,

$$\Phi_T = \mathbf{B_{ext}} A + \alpha L I_p, \tag{5.5.3}$$

where $\mathbf{B_{ext}}$ is the externally applied magnetic flux density, A is the area of the SQUID loop, L is the SQUID loop inductance, I_p is the current induced in the pickup loop due to the applied magnetic flux density and α is the coupling coefficient between the SQUID loop and the pickup loop.

By dividing (5.5.3) by the applied magnetic flux density, and noting that $\Phi_p = L_p I_p$ and $\Phi_p = \mathbf{B_{ext}} {A_p}^2$, an expression can be found for the effective area

[2]Here Φ_p is the flux threading the pickup loop, L_p is the pickup loop inductance and A_p is the area of the pickup loop.

of the directly-coupled DC SQUID:

$$A_{eff} = A + \frac{\alpha L I_p}{\mathbf{B_{ext}}} \quad (5.5.4)$$

$$= A + \alpha L \frac{A_p}{L_p}. \quad (5.5.5)$$

For practical devices, α is typically larger than 0.8, and the effective area of the SQUID can be more than three orders of magnitude larger than the SQUID loop area [72].

5.6 Noise Theory in SQUIDs

Although superconductors have excellent noise characteristics, they are not noiseless. DC SQUIDs are extremely sensitive devices and even small amounts of noise can affect them strongly. As such, it is important to understand the origin of noise in order to design a SQUID system with the highest sensitivity. In this section the various sources of noise in SQUID systems are discussed.

5.6.1 Intrinsic Noise Sources in SQUID Devices

As in other physical systems, there are a variety of noise sources in SQUID systems. These are thermal noise, shot noise and $1/f$ noise[3]. These noise sources all affect the SQUID in different ways.

Thermal noise arises from the random, thermally induced motion of electrons in resistors [73]. It has a flat power spectral density, and is considered white noise, up to a limiting frequency[4]. In DC SQUIDs, thermal noise is found in the normal state resistances of the Josephson junctions. Under most operating conditions, thermal noise is the dominant noise source.

$1/f$ noise is associated with the thermal motion of flux vortices and with critical current fluctuations. As the name implies, $1/f$ noise scales inversely to the frequency. It is dominant at low frequencies ($f < 100Hz$), but falls off rapidly as the frequency of operation is increased.

[3] $1/f$ noise is also called flicker noise, llf noise or excess noise.

[4] For the scope of this thesis we assume that all SQUIDs operate below this limiting frequency.

Shot noise is associated with current flowing through a potential barrier. Shot noise has a constant power spectral density and is therefore considered white noise. Thermal noise is usually dominant over shot noise, however, and shot noise can therefore usually be neglected.

5.6.2 Thermal Noise

Thermal noise has a significant influence on all high-T_c SQUID sensors [74]. A DC SQUID must be designed to have the lowest possible noise. For a DC SQUID, thermal voltage noise has a zero average, but a non-zero RMS value. For operating frequencies below about $1THz$, the voltage noise power spectral density is flat, and is given by [37]

$$S_v(f) = 16k_BTR_n, \tag{5.6.1}$$

where k_B is Boltzmann's constant, T is the absolute temperature and R_n is the normal state resistance of the Josephson junctions.

Thermal fluctuations in the resistive channels of the Josephson junctions generate flux noise in the SQUID loop [48]. Flux noise couples into the SQUID loop causing a decrease in sensitivity. Flux noise increases with increasing SQUID loop inductance, placing an upper limit on the loop inductance.

The thermal flux noise in a SQUID is related to the thermal voltage noise and is given by (for a SQUID with $\beta_L = 1$) [37, 5]

$$\begin{aligned} S_\Phi(f) &= \frac{S_v(f)}{V_\Phi^2} \\ &= \frac{16k_BTL_{SQ}^2}{R_n}, \end{aligned} \tag{5.6.2}$$

where V_Φ is the voltage-to-flux transfer function of the SQUID.

To ensure that the thermal noise in the SQUID remains below the sensitivity of the SQUID, the following constraint must be maintained [37]:

$$L_{SQ} \ll \frac{\Phi_0^2}{4k_BT}. \tag{5.6.3}$$

If (5.6.3) is not maintained, the quantum interference phenomenon will not be observable [37]. At 77 kelvin the maximum loop inductance should therefore

be restricted to about $1nH$.

The energy resolution, $\varepsilon(f)$, is normally used to measure SQUID noise performance [64]. The energy resolution is given by

$$\begin{aligned} \varepsilon(f) &= \frac{S_\Phi(f)}{2L_{SQ}} \\ &= \frac{8k_BTL_{SQ}}{R_n}. \end{aligned} \tag{5.6.4}$$

For a SQUID designed with $\beta_L = 1$, the energy resolution reduces to

$$\varepsilon(f) \approx \frac{4k_BT\Phi_0}{I_cR_n}. \tag{5.6.5}$$

5.6.3 1/f Noise

For SQUIDs operating at low frequencies $1/f$ noise becomes important. Although there are many sources of $1/f$ noise in SQUID systems, the two main contributors are the motion of flux vortices due to thermal agitation and the fluctuations of the critical current.

The spectral density of the flux noise, S_Φ tends to scale by $1/f$ below a certain frequency [53, 75]. Thermal flux noise is produced by flux vortices hopping between pinning sites in the material because of thermal agitation [37, 75]. Pinning sites occur naturally in high-T_c superconducting films as defects in the crystal lattice [37]. Cooling a high-T_c superconductor in the presence of a magnetic field increases the number of flux vortices penetrating the material, thereby increasing the noise. This may lead to significant performance degradation.

The $1/f$ flux noise can be greatly reduced in high-T_c SQUID systems using several different techniques. Slots and holes incorporated in the design of the SQUID can trap flux during cooling, creating strong pinning sites that prevent the vortices from hopping [76]. Flux dams (weak links inserted into the SQUID pickup loop) have been successfully used to lower the $1/f$ flux noise [77]. Using a thinner line width for the SQUID loop also increases $1/f$ flux noise performance [76].

Fluctuations in the Josephson junction critical current is another important source of $1/f$ noise [75]. These fluctuations can cause a voltage to develop across the SQUID, or a current to flow in the SQUID loop, depending

on whether they fluctuate in phase or out of phase. By using bias current reversal and flux modulation techniques, the $1/f$ noise due to critical current fluctuations can be dramatically reduced [75].

Overall, though, $1/f$ noise is due to imperfections in the superconductor crystal structure. By improving the quality of epitaxial thin films the $1/f$ noise can be significantly reduced.

5.6.4 External Noise Sources

External sources of noise also influence SQUID systems. RF signals can couple with the SQUID pickup loop reducing sensitivity [64]. Fortunately most of this noise can be reduced by operating the SQUID in a flux locked loop. Alternatively the SQUID may be shielded by using μ-metals [37].

Temperature fluctuations may cause the SQUID to output imprecise readings. This is caused by the dependence of the critical current on temperature, but also, and to a greater extent, by the dependence of the London penetration depth on temperature. A change in the London penetration depth causes the effective area of the SQUID to vary [64, 78]. This changing effective area causes erroneous readings. To solve this problem, the SQUID temperature needs to be held at a very constant value.

Chapter 6

SQUID Electronics

6.1 Introduction

The output of a DC SQUID magnetometer is a sinusoidal voltage with period Φ_0. In order to linearize and amplify the output voltage so that the SQUID can be used in practical devices, read-out electronics have to be designed.

This chapter introduces the Flux Locked Loop (FLL). The FLL is a negative feedback loop used to linearize and amplify the SQUID output.

6.2 SQUID Small Signal Response

In Section 5.4 it was shown that a DC SQUID typically has a periodic flux-to-voltage conversion. The output has a period of one flux quantum, Φ_0, and an amplitude in the μV range.

A SQUID biased at a certain operating point, W, will have a voltage sensitivity of

$$V_\Phi = \frac{\delta\langle v\rangle}{\delta\Phi_{ext}} \tag{6.2.1}$$

for small input signals, where Φ_{ext} is the externally applied flux.

At the optimum operating point, $V_\Phi \approx R_n/L_{SQ} = 2I_cR_n/\Phi_0$. Simulations indicate that the optimum bias current, resulting in the largest voltage sensitivity, is $3.3 < I_b/I_c < 3.5$ [5, 37]. The optimum operating point occurs at the steepest sections of the V-Φ output, when the applied flux is $\Phi_a \approx (\Phi_0/4 + n\Phi_0/2)$ for a SQUID with $\beta_L = 1$.

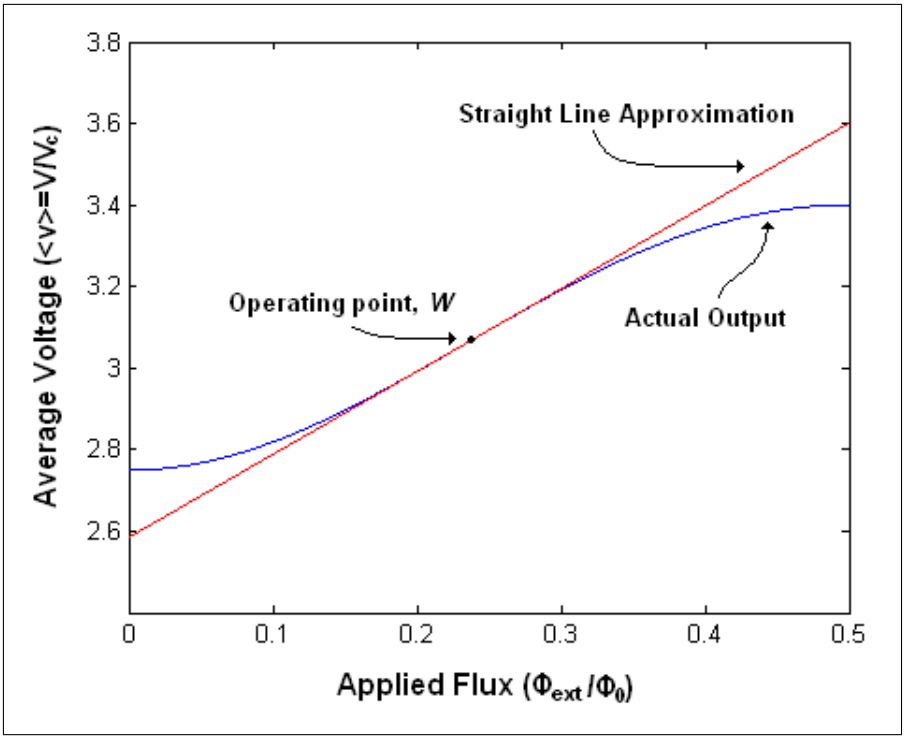

Figure 6.1: Actual output voltage and straight line approximation for the output of a DC SQUID with $\beta_L = 1$ and $I_b = 3.4$ for small signals.

For small signals the output at W will be nearly linear, as shown in Figure 6.1. As the applied flux increases, the error between the straight line approximation V_Φ and the actual output will also increase. In order to keep this non-linearity error as small as possible, the applied flux is constrained to

$$\delta\Phi_a \leq \frac{\Phi_0}{2\pi}. \tag{6.2.2}$$

By constraining the applied flux to this value, the output of the SQUID will be approximately linear. The maximum input signal, however, is not very large (smaller than a single flux quantum), not making the device very practical, especially since most environmental noise sources tend to be larger than this small signal.

6.3 Basic Flux-Locked Loop

In order to increase the maximum allowed applied flux, the SQUID can be operated in a Flux-Locked Loop (FLL) configuration. The FLL consists of a preamplifier connected (through a matching circuit) to the SQUID, an integrator and a feedback coil that couples flux back into the SQUID. The basic FLL is shown in Figure 6.2.

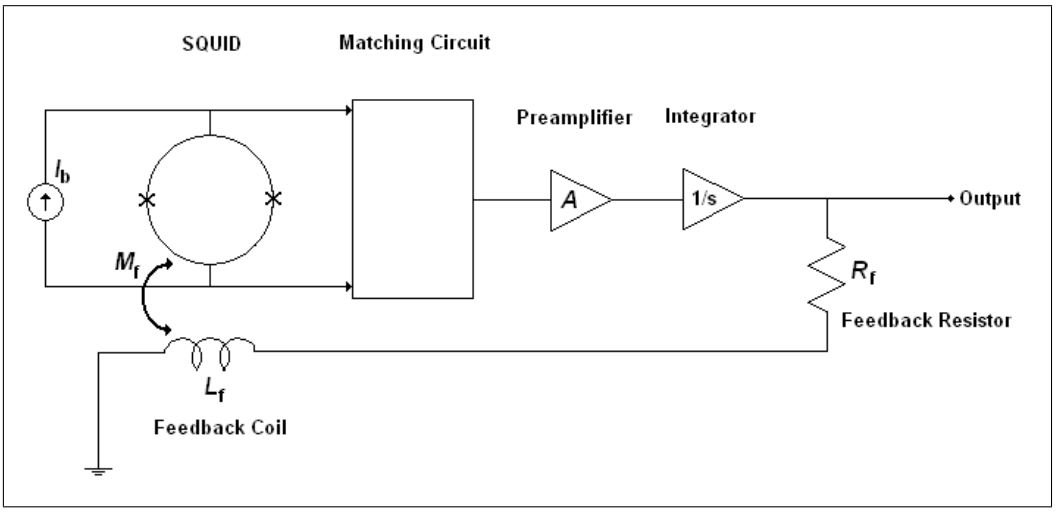

Figure 6.2: Schematic layout of a basic flux-locked loop.

For the FLL the SQUID is biased at the optimum operating point, W (see Section 6.2), and the preamplifier bias voltage is set to correspond with the offset voltage of the SQUID at W. When an external magnetic flux is applied to the SQUID the SQUID's output voltage changes. This output voltage is amplified by the preamplifier, integrated and fed back into the SQUID via the feedback coil, cancelling the applied flux and keeping the SQUID at the operating point, W. The current output of the integrator is therefore a linear representation of the applied flux.

6.4 Flux-Locked Loop Design

The FLL is a negative feedback circuit designed to keep the SQUID at its operating point, W, by keeping the magnetic flux threading the SQUID loop $\Phi_a \approx \Phi_0/4$, with a maximum deviation of $\delta\Phi \leq \Phi_0/4$ [37]. It consists of a

preamplifier with gain A, an integrator and a feedback circuit consisting of a feedback resistor, R_f and a feedback coil, L_f, with a mutual inductance M_f with the SQUID loop.

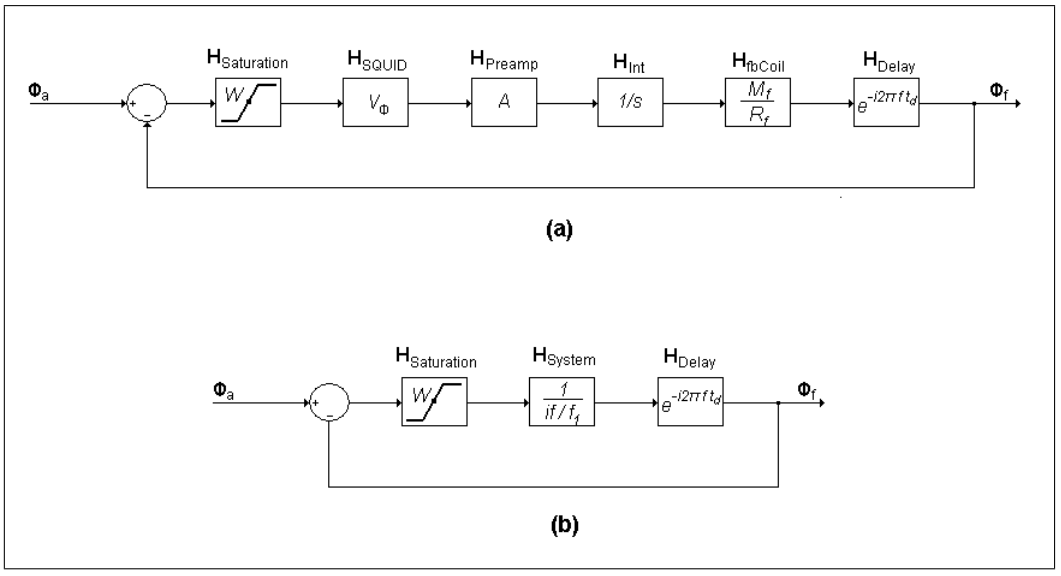

Figure 6.3: Block diagram of FLL system. (a) Complete system block diagram. (b) Simplified block diagram.

The open loop transfer function of the FLL is used to design the system [64]. The open loop transfer function of the FLL can be split into sections, and is given by [37]

$$H_{FLL,ol} = H_{Saturation} \cdot H_{SQUID} \cdot H_{Preamp} \cdot H_{Int} \cdot HfbCoil \cdot H_{Delay}, \qquad (6.4.1)$$

where $H_{Saturation}$ represents the non-linearity that occurs in the output if the applied flux is too large.

Since the arrangement of the sections in the open loop transfer function does not affect the behaviour of the closed system [79], the feedback coil transfer function can be moved in front of the SQUID transfer function. Combining the transfer functions of the SQUID and the feedback coil into a single transfer function for the entire SQUID system, and those of the preamplifier and the integrator into a transfer function for the electronics, (6.4.1) can be reduced

to

$$H_{FLL,ol} = H_{Saturation} \cdot H_{SQUIDsystem} \cdot H_{Electronics} \cdot H_{Delay}, \tag{6.4.2}$$

where

$$H_{SQUIDsystem}(i2\pi f) = H_{fbCoil} \cdot H_{SQUID} = G_{SQ} = \frac{M_f}{R_f} V_\Phi, \tag{6.4.3}$$

and

$$H_{Electronics}(i2\pi f) = H_{Preamp} \cdot H_{Int} = \frac{A}{i2\pi f}. \tag{6.4.4}$$

Combining (6.4.3) and (6.4.4) we find a transfer function for the SQUID and the feedback electronics:

$$H_{System}(i2\pi f) = H_{SQUIDsystem} \cdot H_{Electronics} = G_{SQ} A \frac{1}{i2\pi f}. \tag{6.4.5}$$

The desired unity-gain frequency for the open loop system, f_1, must be chosen[1]. Noting that $|H_{Delay}| = 1$ and, for small input signals, $|H_{Saturation}| = 1$, we find

$$|H_{FLL,ol}(i2\pi f_1)| = G_{SQ} A \left| \frac{1}{i2\pi f_1} \right| = 1, \tag{6.4.6}$$

therefore,

$$A = \frac{2\pi f_1}{G_{SQ}}. \tag{6.4.7}$$

The feedback electronics must therefore have a gain bandwidth of [37]

$$GBW_{Electronics} = |H_{Electronics}(i2\pi f_1)| \times f_1 = \frac{f_1}{G_{SQ}}. \tag{6.4.8}$$

Combining (6.4.5) and (6.4.7) a transfer function for the entire SQUID

[1]Note that, since only the transfer function of the integrator is frequency dependant, the unity-gain frequency of the system, f_1, will be the same as the unity-gain frequency of the integrator.

system is found as

$$H_{System} = H_{SQUIDsystem} \cdot H_{Electronics} = \frac{1}{if/f_1}. \tag{6.4.9}$$

The complete simplified open loop transfer function of the FLL therefore becomes

$$H_{FLL,ol} = H_{Saturation} \cdot H_{System} \cdot H_{Delay}. \tag{6.4.10}$$

The block diagrams for the complete closed loop transfer function of the FLL and the simplified closed loop transfer function of the FLL are shown in Figure 6.3 [37].

6.5 Line Delay

The line delay of the system is the sum of all the time delays in the FLL electronics and transmission lines [64]. The line delay is given by

$$H_{Delay}(i2\pi f) = e^{i2\pi f t_d}, \tag{6.5.1}$$

where t_d is the time delay in seconds and f is the frequency in Hz.

Time delays do not change the magnitude of the system, but do change the phase, and can lead to system instabilities. A system with a unity-gain frequency greater than $f_1 = 3/2\pi t_d$ will be very difficult to stabilize, and it would be impossible to stabilize a system with a unity-gain frequency greater than $f_1 = 5/2\pi t_d$ [37, 79]. Line delay can therefore reduce the bandwidth of a system. Reducing the line delay by using cables that are as short as possible and electronics with fast response times is therefore essential.

6.6 Additional Positive Feedback

The FLL successfully linearizes the SQUID output, but has a disadvantage. Since the DC SQUID has a low output impedance and the preamplifier in the FLL has a high input impedance an impedance matching circuit is required between these two elements in order to reduce noise in the system [6].

In order to abridge this problem, a direct readout scheme (one that does not require a matching circuit) was developed by Drung et al. [80] in 1990 [5]. This scheme replaces the matching circuit with an additional positive feedback (APF) circuit that increases the flux-to-voltage transfer function of the DC SQUID, making the noise contribution of the preamplifier tolerable, thus allowing the preamplifier to be directly connected to the SQUID.

The APF circuit consists of a resistor, R_{apf}, and an inductor, L_{apf} connected in series and connected to the SQUID, as shown in Figure 6.4.

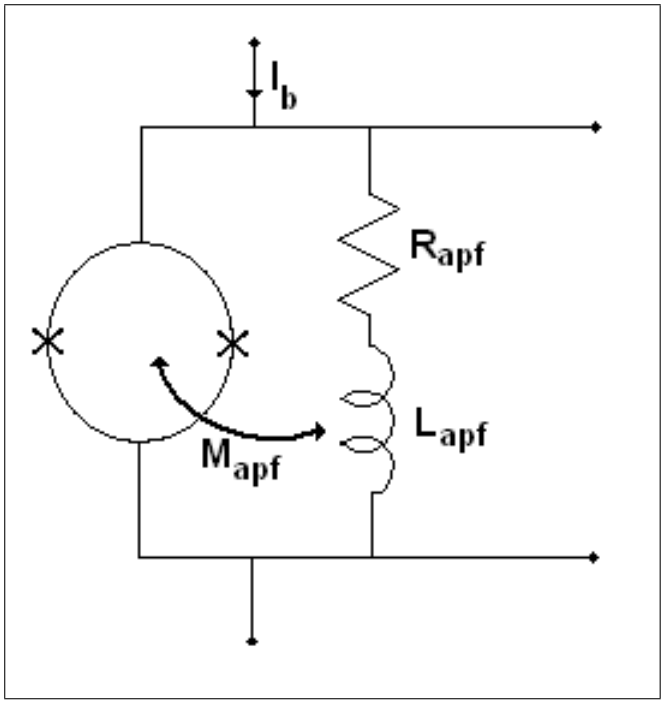

Figure 6.4: Schematic of APF circuit.

A small increase in magnetic flux threading the SQUID produces a small change in the voltage across the SQUID. The changing voltage results in a changing current through the APF circuit. This current induces a magnetic field in the APF inductor that is coupled back into the SQUID, increasing the flux-to-voltage transfer function.

The effect of the APF circuit is shown in Figure 6.5

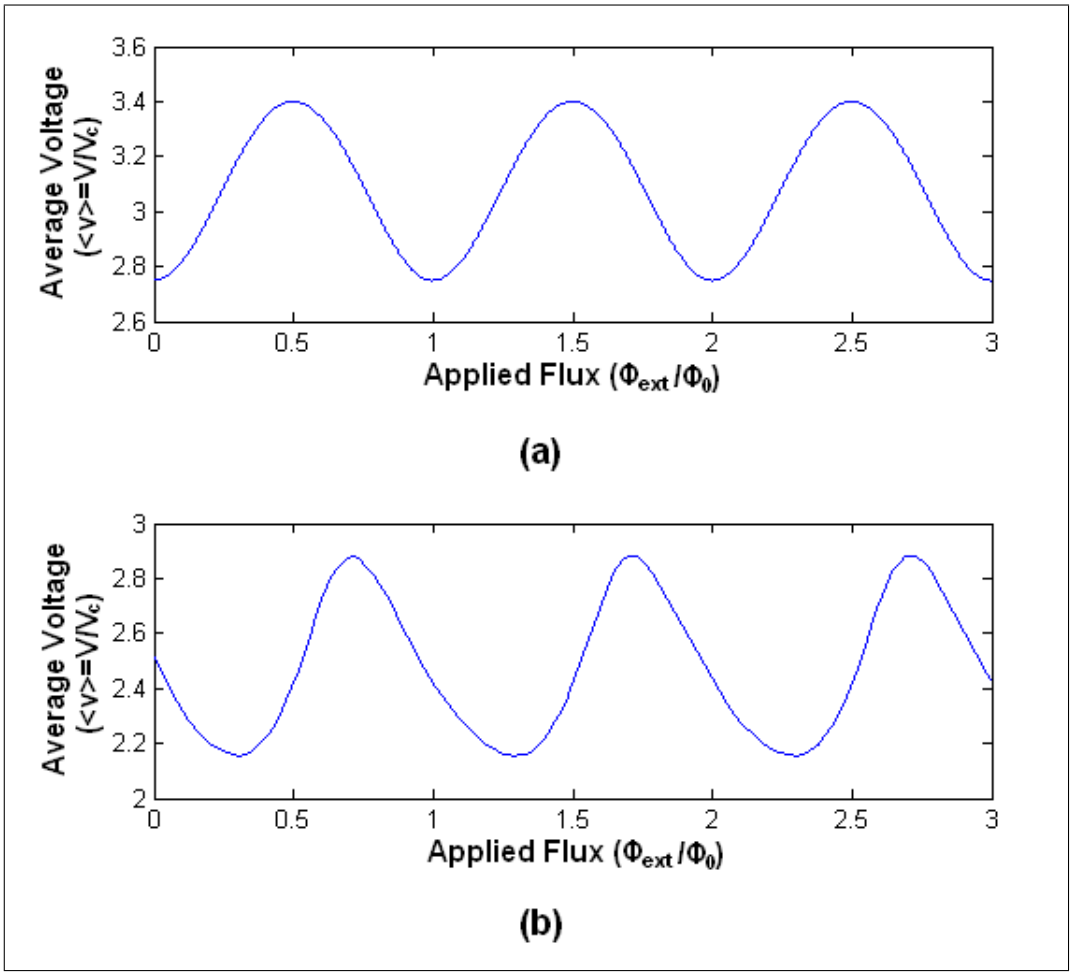

Figure 6.5: Average voltage across a DC SQUID (a) without APF (b) with APF.

Chapter 7

Design and Manufacture of Practical SQUIDs

7.1 Introduction

Practical high-T_c DC SQUIDs require a large number of special procedures and techniques to properly design and manufacture. This chapter discusses the design and manufacture of practical high-T_c DC SQUIDs using $YBa_2Cu_3O_7$ (YBCO). The first section introduces the fundamental constraints in the design of a YBCO DC SQUID, and explores the method of computer aided inductance extraction in order to design YBCO DC SQUIDs. After this the different practical Josephson junction structures are introduced and examined. The chapter ends with a discussion of the fabrication process of DC SQUIDs employed at the Department of Electric and Electronic Engineering at the University of Stellenbosch.

7.2 DC SQUID Magnetometer Design

This section details the design of a practical DC SQUID magnetometer. Emphasis is placed on the most important parameters. Using the constraints on the parameters detailed in this section, high quality SQUIDs with large modulation depths, high magnetic field sensitivities, low energy resolutions and excellent RSJ behaviour can be designed.

This section also examines ways in which to approximate SQUID inductances using numerical techniques.

7.2.1 Fundamental Constraints

The quantum interference interaction between two Josephson junctions in a SQUID is responsible for the operation of the SQUID. This interaction is severely influenced by any noise present in the system. If the amount of noise in the system is too large, the quantum interference effects completely vanish. Thermal noise in the SQUID loop therefore limits the size of the SQUID loop. The SQUID loop inductance must therefore be limited to (5.6.3)

$$L_{SQ} \ll \frac{\Phi_0^2}{4k_B T}, \tag{7.2.1}$$

where L_{SQ} is the SQUID loop inductance, Φ_0 is the flux quantum, T is the temperature and k_B is Boltzmann's constant.

Also, to ensure that the system remains free of hysteresis, the SQUID loop inductance must be constrained by (5.3.3)

$$L_{SQ} \leq \frac{\Phi_0}{I_c}, \tag{7.2.2}$$

where I_c is the critical current.

Enpuku et al. [74, 81] have shown that for high-T_c SQUIDs optimum performance is obtained when the SQUID loop inductance is less than $100pH$.

The screening parameter β_L is a measure of the influence of the loop inductance on the SQUID, and has an optimal value of $\beta_L = 1$. This constraint, however is very difficult to reach in practical DC SQUIDs, and SQUIDs generally have a value of about $\beta_L = 3$ in practice [5].

In order for Josephson junctions to show good behaviour in the presence of applied currents, the junction line widths w need to be smaller than $4\lambda_J$, where λ_J is the Josephson penetration depth [60], given by

$$\lambda_J = \sqrt{\frac{\Phi_0}{2\pi\mu_0 J_c h_{eff}}}, \tag{7.2.3}$$

where μ_0 is the permeability of free space, J_c is the critical current density of the junction and h_{eff} is equal to the sum of the penetration depths of the superconducting layers and the separating layer thickness [60, 56]. In practice this translates to a maximum width of about $8\mu m$.

7.2.2 Inductance Extraction

In order to design a DC SQUID a method of calculating the self and mutual inductances of thin film superconducting structures is required.

Using *FastHenry 3.0wr* [82], a version of the 3D inductance analysis program *FastHenry* [83] with support for superconductors, the appropriate inductance values can be extracted from a design.

FastHenry allows users to specify nodes using Cartesian coordinates. These nodes are connected by rectangular elements for which the user specifies the start node, the end node, the width and the height. Users also specify the penetration depth of the material when working with superconductors (or the conductivity when working with normal metals). From these elements *FastHenry* then extracts the inductances [84]. Figure 7.1 shows two nodes connected by an element.

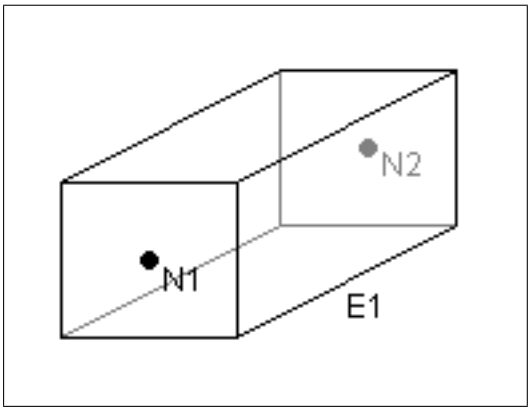

Figure 7.1: Two nodes, N1 and N2, connected by an element E1 in *FastHenry*.

The way *FastHenry* builds a model, however, may lead to inaccurate inductance approximations [85]. If two elements are connected, current is forced to concentrate at the nodes connecting them, as shown if Figure 7.2. This error is usually very small, but as SQUIDs have such small loop inductances (in the order of a few tens of picohenry), these small errors might lead to significant design errors.

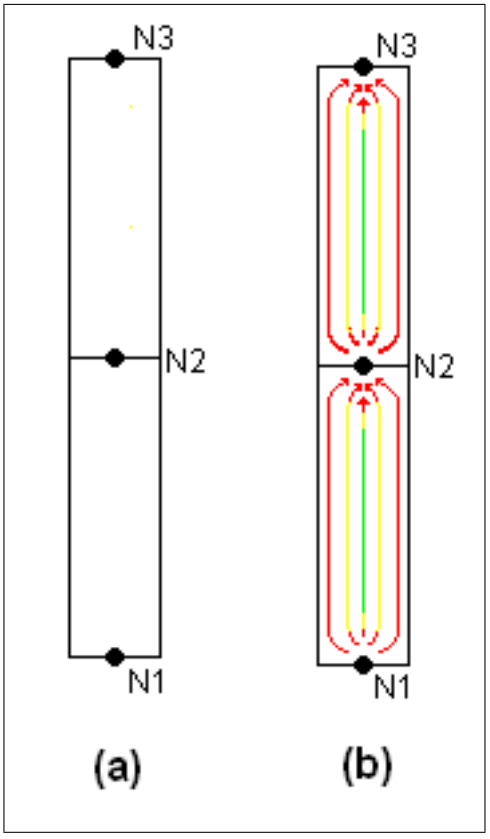

Figure 7.2: A schematic to show a problem in *FastHenry* simulations. (a) Two elements connected by *FastHenry*. (b) Because the elements are connected by the nodes, the current flowing through the elements is forced to concentrate at each node (note that in this figure red means a high, yellow a medium and green a low current density.

This problem is even more severe in structures containing corners. When current flows around a corner, the current density peaks at the inside of the corner and shows a minimum at the outer vortex of the corner [85]. *FastHenry*, however, forces all the current through the node connecting two elements, and does not allow current to flow naturally through the corner.

In order to correct these problems, the elements can be segmented by adding more nodes [85]. An example of this segmentation process is shown in Figure 7.3. Figure 7.3 also shows a schematical representation of the same segmented line where the segment widths have been reduced to a fifth of their actual size for clarity.

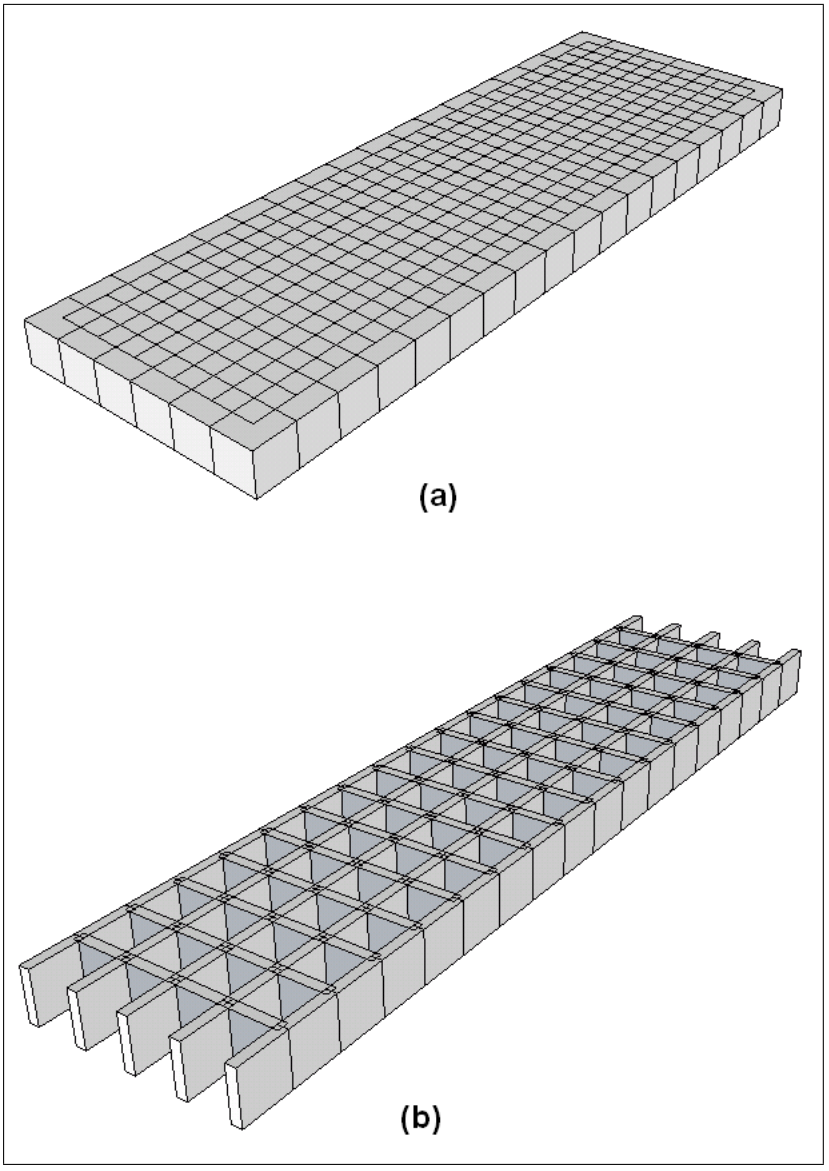

Figure 7.3: A *FastHenry* line that has been segmented. The width of the line has been divided into 5 segments, while the length has been divided into 18. (a) Actual segmented line. (b) Segmented line with widths of segments reduced to a fifth of the size for clarity

A *MATLAB* [86] program was written to create a *FastHenry* input file with the lines segmented as shown in Figure 7.3. This program is listed in Appendix D.

7.3 Grain Boundry Junctions

Various novel techniques have been introduced to fabricate Josephson junction structures from high-T_c superconductors. Most of these techniques involve very narrow grain boundary junctions (GBJs). GBJs are formed when two adjacent crystal planes have a different orientation [61]. This misorientation causes the critical current to differ at each side of the boundry that results in weak link Josephson behaviour [87].

The most common GBJs are step-edge junctions [88, 89], bi-epitaxial junctions [90, 91] and bicrystal junctions [92], although edge junctions [93] and electron-beam weakened structures [94] are also popular [5]. In this thesis only step-edge junctions, bi-epitaxial junctions and bicrystal junctions will be considered.

7.3.1 Step-Edge Junctions

When a layer of material[1] is deposited onto a substrate, and the excess is milled away on one side, a step-edge is formed. After milling there is a height difference in the layer, with the two flat surfaces separated by a ramp with a slope angle α.

When YBCO is deposited onto the step-edge, it will grow with the same orientation on the flat surfaces, but with a different orientation on the ramp. At each end of the slope a distinct GBJ therefore forms, causing the YBCO to display Josephson behaviour over the step-edge [37]. This junction structure shows RSJ behaviour at higher temperatures, but at lower temperatures, β_c becomes large and the junction starts showing RSCJ behaviour [89].

Figure 7.4 shows a schematic representation of a step-edge junction.

[1]This material consists of the same or similar material to the substrate, and has the same crystal orientation

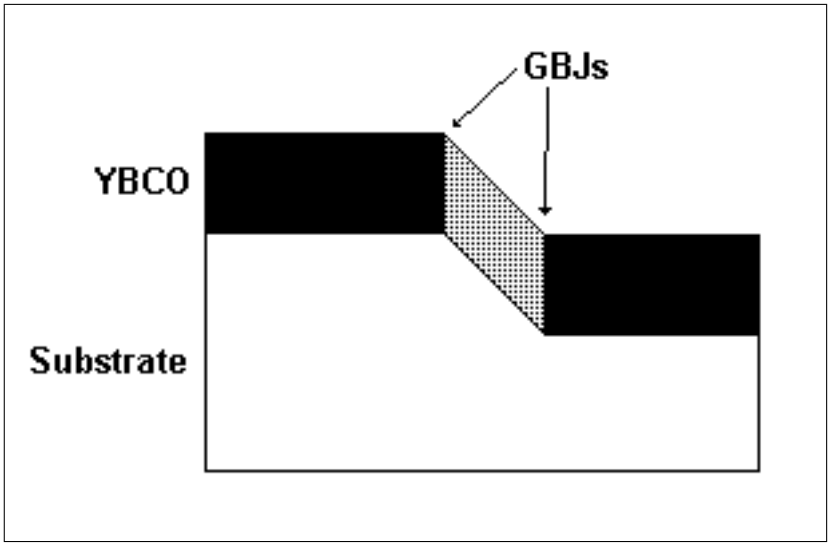

Figure 7.4: YBCO deposited onto a step-edge forming a Josephson junction. The differently shaded areas of the YBCO layer represent different crystal orientations.

7.3.2 Bi-Epitaxial Junctions

Bi-epitaxial substrates are formed when a thin layer of material is deposited onto a substrate in order to change the orientation of the substrate. This seed layer is then covered by a buffer layer, creating a suitable surface on which to deposit YBCO.

The YBCO deposited onto a bi-epitaxial substrate it will grow according to the orientation of the substrate, resulting in a crystal lattice mismatch at the interface of the seed layer. This mismatch forms a GBJ. Although this is similar to the step-edge junction, the step height in this instance is much smaller than the thickness of the YBCO layer. [37]

Figure 7.5 schematically shows YBCO deposited onto a bi-epitaxial substrate.

Bi-epitaxial substrates can be purchased pre-manufactured, or can be created using the same processes and techniques used to deposit YBCO. One drawback of these substrates, though, is that they require multiple depositions in order to achieve the desired device layout.

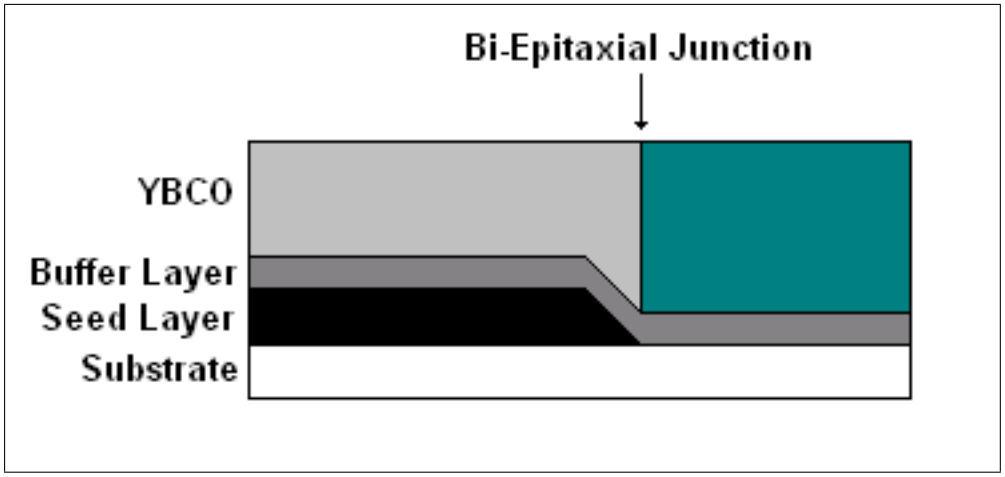

Figure 7.5: YBCO deposited onto a bi-epitaxial substrate forming a Josephson junction. The differently shaded areas of the YBCO layer represent different crystal orientations.

7.3.3 Bicrystal Junctions

Bicrystal substrates are formed by physically cutting uniform crystal substrates and rejoining them at an angle. This produces a misorientation in the crystal structures where the substrates are rejoined. This misorrientation angle can be controlled, with 24^o and 36^o misorientation angles available commercially[2]. When YBCO is deposited onto the substrate it grows according to the orientation of the crystal substrate, and therefore also has a mismatch at the bicrystal line. This mismatch causes a GBJ to be formed.

Bicrystal substrates are commercially available as pre-manufactured substrates, but are relatively expensive and can only be used for a single SQUID loop. They are also nearly impossible to re-use. The benefits of using bicrystal substrates to form Josephson junctions in high-T_c superconductors, however, far outweigh the costs. Josephson junctions created on bicrystal substrates have been well defined, are very reproducible and exhibit RSJ behaviour. Josephson junction structures created on bicrystal substrates are also relatively easy to manufacture, requiring only one deposition.

Figure 7.6 shows schematically YBCO deposited onto a bicrystal substrate.

[2]Other misorientation angles are also available commercially, although they are rarer.

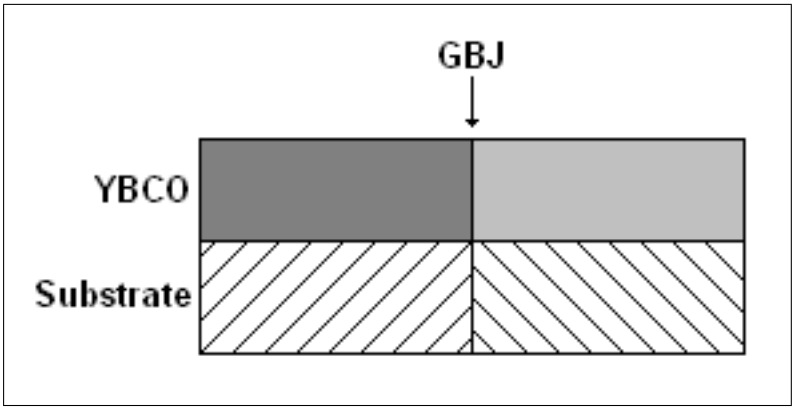

Figure 7.6: YBCO deposited onto a bicrystal substrate forming a Josephson junction. The differently shaded areas of the YBCO layer represent different crystal orientations.

7.4 Fabrication Parameters and Procedures

This section details the fabrication of a practical DC SQUID. After a brief overview of the fabrication process, the section moves on to a discussion of the important parameters when considering which substrate to use, different deposition techniques, the photolithographic process and, finally, the attachment of contact wires to the device.

7.4.1 The Fabrication Process

The fabrication of practical DC SQUIDs relies on thin film techniques. First, a chrome mask of the SQUID design has to be manufactured. Then, a thin film of YBCO is deposited onto a crystal substrate. This is done using various different deposition techniques. After YBCO has been deposited onto a substrate, the SQUID design will be etched into the YBCO layer using the mask and photolithography techniques. Finally, another mask is used to deposit noble metals onto the contact pads of the design, making it possible to bond wires to the device and attach it to a printed circuit board (PCB) for integration into different systems.

7.4.2 The Chrome Mask

The first step in the manufacture of practical DC SQUIDs is to create a mask for the photolithography process. This mask consists of a glass substrate covered with a thin layer of chrome (Cr). The pattern of the SQUID is etched out of the chrome layer, leaving opaque chrome areas on the mask where the structure of the SQUID will be[3].

The chrome can be etched away in a number of different ways. Usually, mask designs are sent to be commercially manufactured. Commercially manufactured masks, however, are extremely expensive. Recently an alternative approach was explored at the University of Stellenbosch. Laser ablation techniques were used at the University of Stellenbosch Geology Department to cut away unwanted chrome from a piece of chrome-plated glass, thus forming a chrome mask. Although only limited success was achieved using this method, research is ongoing [95].

7.4.3 Substrate Selection

A variety of different substrates have been developed and used to fabricate thin film devices using high-T_c superconductors [5, 96]. Substrates commonly used for YBCO include MgO, $SrTiO_7$, $LaAlO_3$, Al_2O_3, $NdGaO_3$ and yttria-stabilizad Zirconia (YSZ) [5]. The properties of these substrates and therefore the properties of thin film devices grown on these substrates vary significantly. This section will discuss and compare the most common of these substrates.

Substrates for thin film superconductor applications must have a crystal lattice that closely matches that of the superconductor being deposited onto it. This ensures that the superconductor deposited onto the substrate has the desired crystal structure. Also, the substrate and the superconductor must be thermally matched, meaning that the thermal expansion coefficients need to be equal. This prevents the superconductor thin film from cracking when the device is cooled or heated. It is also important to keep in mind that deposition generally requires the substrate to be heated, and provision must be made to ensure that the substrate can withstand the required temperature.

[3]This is when using positive tone photoresist (see Section 7.4.5). When using negative tone photoresist, the opaque chrome areas of the mask must be left where the structure of the SQUID will *not* be.

Table 7.1: Different substrates for YBCO thin film devices [5].

Property	***MgO***	$SrTiO_3$	Al_2O_3	$LaAlO_3$
Dielectric Constant	9.65	277	9.34	23
Tan δ	5×10^{-4}	6×10^{-2}	3×10^{-5}	3×10^{-5}
Lattice Mismatch (%)	9	2	12.2	2.2

For YBCO devices[4] Al_2O_3 substrates have a rather large lattice mismatch. Al_2O_3 also chemically reacts with YBCO and shows large thermal mismatch with YBCO. YBCO devices grown on Al_2O_3 substrates are therefore of poor quality.

Similarly, MgO substrates have a rather large lattice mismatch and therefore do not grow good quality films. However, commercial MgO substrates are generally inexpensive. This, combined with the fact that they do not react chemically with YBCO at all, ensures that they are widely used as substrates for YBCO thin film devices. Commercial MgO bicrystals can also readily be purchased.

$LaAlO_3$ substrates show good lattice agreement with YBCO, but have crystal structures that are prone to defects. These substrates are therefore not especially suitable for thin film superconducting devices.

Substrates of $SrTiO_3$ show excellent lattice agreement with YBCO and thin film devices deposited onto them are therefore of excellent quality. These substrates, however, are very expensive. Commercial $SrTiO_3$ substrates also come in bicrystal form.

Although thin film YBCO devices grown on $SrTiO_3$ are generally of better quality, MgO substrates are more commonly used due to their lower cost.

Table 7.1 summarizes the properties of four different substrates.

7.4.4 Deposition Techniques

There are various techniques for depositing YBCO thin films onto substrates. At the University of Stellenbosch two methods are employed, namely Pulsed-

[4]This thesis restricts itself to DC and low frequency applications. In microwave applications the dielectric constant of the substrate is important, and substrates with a large dielectric constant such as $SrTiO_3$ become impractical.

Laser Deposition (PLD) and Inverted Cylindrical Magnetron (ICM) sputtering. These methods are in-situ techniques, meaning that the basic crystalline structure of the deposited YBCO is formed during deposition [37]. Various ex-situ methods also exist, but generally produce films of poorer quality, and fall outside the scope of this thesis.

To produce thin films of high quality for the manufacture of DC SQUIDs the YBCO needs to be deposited uniformly, have a very uniform crystal structure and be free of any impurities. This is achieved by precisely controlling the deposition parameters.

7.4.4.1 Pulsed-Laser Deposition

Pulsed-laser deposition uses a high power laser to bombard an YBCO target. The laser ablates the YBCO, and the resulting vapour is deposited onto a heated substrate.

The YBCO target is mounted on a rotating spool and is placed in the PLD chamber. The laser is then focused onto a small point on the edge of the rotating target, and a vacuum is pulled. The laser is fired at the rotating target forming a plume of ablated YBCO material. The substrate is positioned so that the plume can condense onto the substrate.

Oxygen is usually introduced into the chamber during deposition. The YBCO plume reacts with the oxygen ensuring that material with the correct crystal structure is deposited onto the substrate[5].

The energy of the laser beam hitting the target is a critical parameter. If the energy is too large the particles in the plume will have too much energy and damage the material on the substrate. On the other hand, if the energy is too low the possibility exists that large chunks will dislodge from the target and be deposited onto the substrate, forming films with polycrystalline structures and poor surface roughness.

Figure 7.7 shows a schematic diagram of a PLD system.

[5]The oxygen present in the PLD chamber during deposition is usually not enough to ensure that YBCO with the correct crystal structure is deposited on the sample, and the sample usually has to go through an annealing phase after deposition. During this phase, the sample is placed in an oxygen environment at high temperature, allowing oxygen to diffuse through the YBCO film, resulting in the YBCO taking on the correct crystal structure.

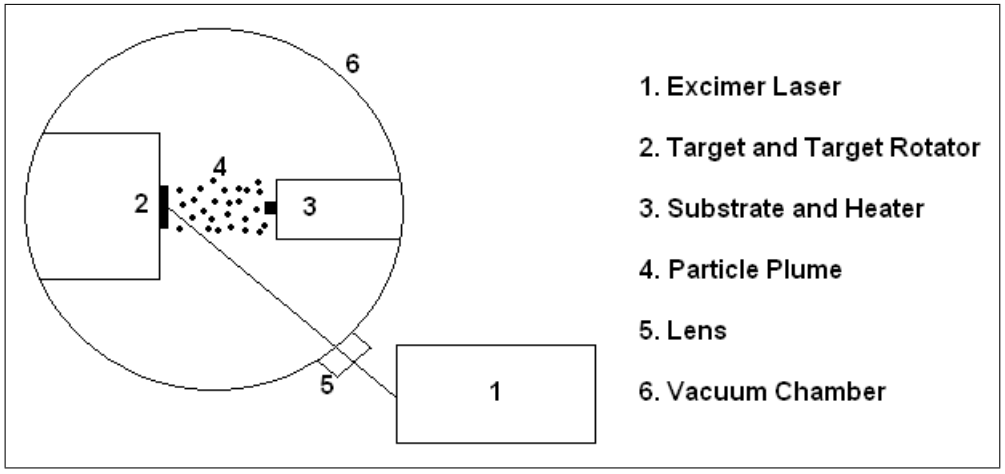

Figure 7.7: Schematic diagram of a PLD system [5].

7.4.4.2 Inverted Cylindrical Magnetron Sputtering

At the University of Stellenbosch, PLD has been surpassed by inverted cylindrical (DC) magnetron sputtering, which results in higher deposition rates, lower surface roughness and samples with higher T_c.

The ICM creates an argon (Ar) plasma that is accelerated toward the YBCO target by a DC magnetron. The plasma then tears particles off an YBCO target and deposits them onto a heated substrate. Argon is used to create the plasma since it is chemically inert.

ICM sputtering takes place under vacuum. During the deposition process oxygen is added to the chamber together with the argon. This ensures that the crystal structure of the deposited YBCO is correct[6]. The amount of oxygen and argon, and their ratio, present in the chamber during deposition are critical parameters in ICM sputtering. If too little argon is present the plasma will be weak and the deposition will take too long. If too little oxygen is present the crystal structure of the deposited YBCO will be incorrect. Too much of either gas interferes with the deposition process and causes films of low quality to be grown.

Figure 7.8 shows a schematic diagram of an ICM sputtering system.

[6]As with PLD, the amount of oxygen in the chamber is usually not great enough to ensure the correct crystal structure and the sample has to undergo an annealing phase after deposition.

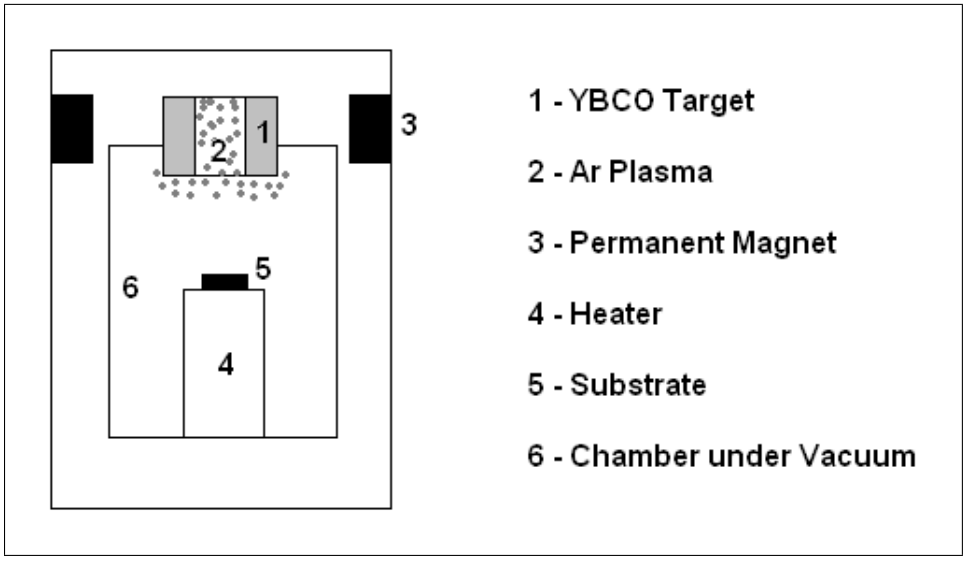

Figure 7.8: Cutaway schematic of an ICM system.

7.4.5 Photolithography

After a thin film of YBCO is deposited onto the substrate, the layout of the SQUID is etched into it. To do this, photolithography techniques are used to create a pattern on the YBCO layer that is then etched away using argon-ion milling techniques that are described in Section 7.4.6. In this section the photolithographic techniques are described.

Photolithography requires a number of steps that need to be performed with great care in order to avoid degradation of the YBCO layer. The first step is to cover the YBCO sample with a photosensitive resist layer. Then, the photoresist layer is exposed to UV light through the chrome mask. This softens the exposed areas[7]. The next step is to develop the photoresist. This removes the softened photoresist layers.

The (positive tone) photolithographic process is graphically illustrated in Figure 7.9.

[7]In this section the use of positive tone photoresist is described. When using negative tone photoresist, the UV exposed areas harden, causing the areas that were not exposed to be etched away by the developer.

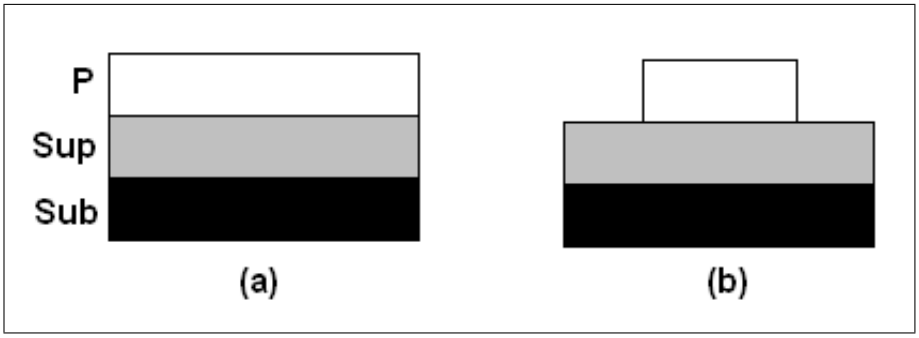

Figure 7.9: Photolithography process. (a) Sample after photoresist is applied. (b) Sample after developing. P - Photoresist layer; Sup - Superconductor layer; Sub - Substrate

The sample is coated with photoresist by spinning the sample in a photoresist spinner. Depending on the photoresist used the spin time to coat the sample in a layer of a certain thickness will vary.

After the material is coated with photoresist it is exposed to UV light through the chrome mask. The time that the coated material needs to be exposed varies for different photoresists. Care must be taken that the mask is placed chrome-side down, ensuring that only areas that are meant to be exposed to UV are. Care must also be taken during this step to line up the mask in such a way that the Josephson junction structures cross the bicrystal, bi-epitaxial or step-edge line before the material is exposed to UV light.

Each photoresist has its own developer, and again, the time that the material must remain in the developer depends on what photoresist is used. After development the developer is washed off the substrate with deionised water.

After the photoresist layer has been applied to the sample, and after the development, the material is placed on a hotplate for a short time to dry the sample.

It should also be noted that if small structures are to be made (smaller than $10\mu m$) more viscous photoresists outperform their less viscous counterparts.

The photolithography process needs to be done in a clean work area, as the smallest particle of dust can hinder the patterning process. Also, all work must be performed under safe lights, i.e. lights that contain only yellow or red wavelengths. Other wavelengths of light may destroy the photoresist layer.

7.4.6 Milling

After the photoresist layer has been developed, leaving the pattern to be etched into the YBCO layer, the sample has to undergo a milling phase.

At the University of Stellenbosch the milling of the substrate is done using a dry-etching technique called argon-ion milling. Argon plasma, ignited using an RF current, is focused onto the sample, etching away the top layer. This technique is very similar to ICM sputtering, except that in this case the target is the sample itself.

The argon ions bombarding the sample etch away both the photoresist and the exposed YBCO, but since the photoresist layer is much thicker the YBCO is etched off before the photoresist layer is completely destroyed, thus protecting the unexposed areas of the YBCO layer. After milling the sample is washed in a acetone bath to remove any excess photoresist.

Figure 7.10 shows the milling process.

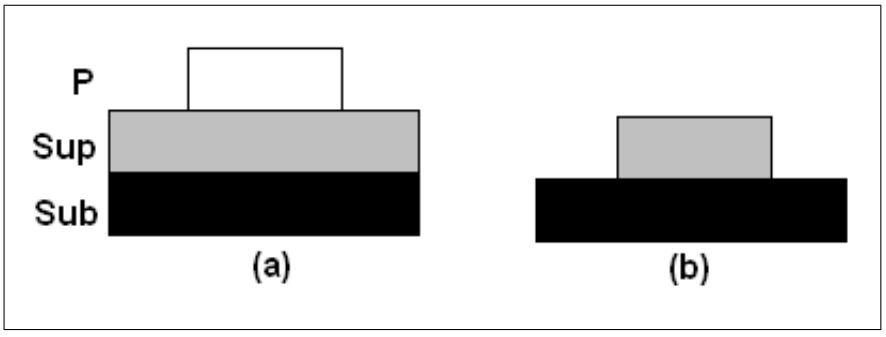

Figure 7.10: Milling process. (a) Sample after photoresist is applied and developed. (b) Sample after milling. P - Photoresist layer; Sup - Superconductor layer; Sub - Substrate

7.4.7 Contacts

In order to connect the device to the electronic equipment a conducting material needs to be deposited onto contact pads so that contact wires can be connected to the sample. The best materials to use for contact pads are the noble metals such as silver and gold. These materials can be deposited using any number of different methods. At the University of Stellenbosch thermal evaporation is usually used.

Again a mask must be manufactured through which the gold can be deposited onto the material. This mask, however, usually consists of a thin copper plate with holes drilled at the appropriate positions, and as such is much cheaper and much easier to manufacture than the chrome mask. These masks are manufactured in-house.

After the contact metal is deposited, contact wires need to be bonded to the pads under a microscope. This is done using a sonic bonder. The entire device will then be mounted in a magnetic resistant case, and can then be connected to electronics for testing.

Chapter 8

SQUID detected NMR

8.1 Introduction

Nuclear Magnetic Resonance (NMR) is a widely used tool finding applications in a plethora of areas today.

Historically, the primary driving force in nuclear magnetic resonance spectroscopy and magnetic resonance imaging has been to ever higher magnetic field strengths [97]. This movement to ever increasing magnetic field strengths is largely motivated by increasing requirements of sensitivity and spectral dispersion [98].

In NMR experiments, the precessing magnetization induces a voltage in conventional Faraday detectors that is proportional to ωM, where ω is the Larmor frequency and M is the nett magnetization of the spins. Since both the magnetization M and the Larmor frequency ω scale with applied magnetic field strength B_0, the voltage induced in the Faraday detector scales as B_0^2. The signal-to-noise ratio therefore dramatically increases as the applied magnetic field strength increases. [99]

In SQUID detected NMR the main idea is to reduce the applied magnetic field strength, working in the mT, μT or even nT range (conventional NMR work in the range of $1T$ to $10T$, with some applications requiring fields of up to 20T or more).

This chapter explains the motivation for using weak magnetic fields in NMR and ways in which to detect NMR signals using SQUIDs.

8.2 Motivation for SQUID detected NMR

The information contained in an NMR signal is limited to the spectral resolution of the signal. The spectral resolution is determined by the width of the NMR lines [100]. In order to attain the spectral resolution necessary, the magnetic fields in an NMR experiment need to be very homogeneous (usually close to a few parts per billion). This homogeneity is achieved by supplementing the large magnets with sophisticated shim coils [100].

The combination of the requirements that the magnets need to be extremely strong[1] and extremely homogeneous, makes the magnets needed to operate a conventional NMR machine exceptionally large and expensive.

High-field NMR also suffers from an endemic problem. Special variations in magnetic susceptibility in materials lead to local magnetic field gradients that cause distortion and limit the resolution [99].

An appealing alternative approach to conventional NMR is to use much weaker magnetic fields. In weak magnetic fields the problems of inhomogeneous broadening and spatial variations in susceptibility all but vanish [99, 100]. By using weak magnetic fields, then, the requirement for homogeneity greatly relaxes. This greatly reduces both the cost and the size of the required magnets.

Low field NMR techniques also offer advantages other than the reduced cost and size of systems. Low field NMR machines could easily be portable, could be designed to allow ex-situ NMR where the sample is not restricted to be inside the magnet bore, and, in certain applications could use the earth's magnetic field which is free and relatively homogeneous [97].

At low fields however, the NMR signal becomes extremely difficult to measure using conventional Faraday detectors (because the induced voltage in the detector scales as B_0^2). The Superconducting Quantum Interference Device, however, measures magnetic flux directly, rather than the change in magnetic flux like the Faraday detector. The measured signal therefore scales as B_0 rather than B_0^2 [99]. The SQUID is also orders of magnitude more sensitive than the conventional Faraday detector [64]. This results in higher S/N ratios in low fields than with conventional Faraday detectors [99], and motivates the use of SQUIDs to detect low field NMR signals.

It is important to note that chemical shifts are unresolved at low fields. The

[1] To achieve such large magnetic fields, superconducting magnets are used.

J-coupling interactions, however, are unaffected by field strength and remain visible, acting as signatures of specific covalent bonds [100].

8.3 Detecting NMR signals using SQUIDs

SQUID detected NMR has made a wide variety of measurements possible. In his comprehensive 1998 review, Greenburg [101] lists more than 100 different SQUID-based NMR experiments. These experiments demonstrate the diversity of the field with experiments focusing on different nuclei, low- and high-T_c SQUIDs and measurements of NMR in gasses, solids and liquids at various temperatures.

In most of the early research into SQUID detected NMR, the SQUID was used to detect NMR signals in continuous wave mode. However, pulsed NMR is generally the more powerful technique [102].

8.3.1 Continuous Wave Spectroscopy

In SQUID detected continuous wave (cw) NMR spectroscopy [103, 104, 105, 106, 107, 7], the change in magnetization of a sample is directly measured as the excitation magnetic field frequency is swept through the resonance frequency of the nuclear spins [102]. At resonance, the nuclear spins absorb power from the RF field, changing the magnetization.

Figure 8.1 shows a schematic diagram of a cw NMR spectrometer.

8.3.2 Pulsed Spectroscopy

Although cw NMR spectroscopy is useful in some cases, pulsed techniques are much more powerful and allow information to be obtained from samples that isn't available in cw spectroscopy [102].

Pulsed spectroscopy is conventional NMR and was introduced in Chapter 3. Using SQUIDs, however, instead of Faraday detectors means that the magnetic fields required can be much weaker.

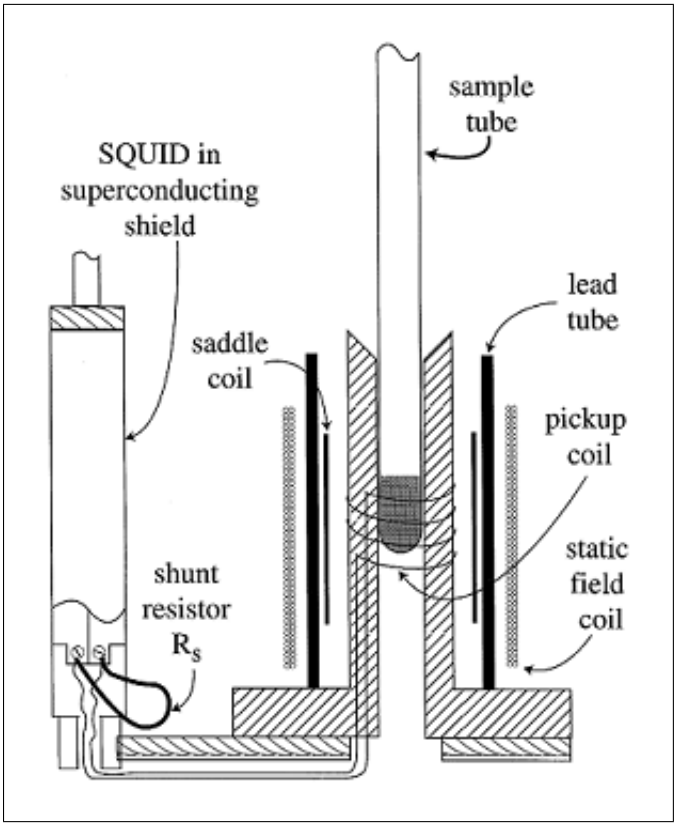

Figure 8.1: Schematic diagram of a SQUID detected cw NMR spectrometer [7].

Recently, a great deal of research has been done on detecting NMR signals from room temperature samples [101, 108], using both low-T_c [109, 110, 100, 97, 111] and high-T_c [112, 99, 113, 114, 8] SQUIDs.

Using low-T_c SQUIDs, Körber et al. [111] were recently successful in detecting NMR signals in nanotesla fields. Using high-T_c SQUIDs, Qiu et al. [113] had success measuring NMR signals from room temperature samples using the earth's magnetic field, while Liao et al. [8] succeeded in measuring J-couplings of room temperature samples using fields in the microtesla range as recently as 2009.

Figure 8.2 shows a schematic diagram of a SQUID detected NMR system. This is the system used by Liao et al. [8].

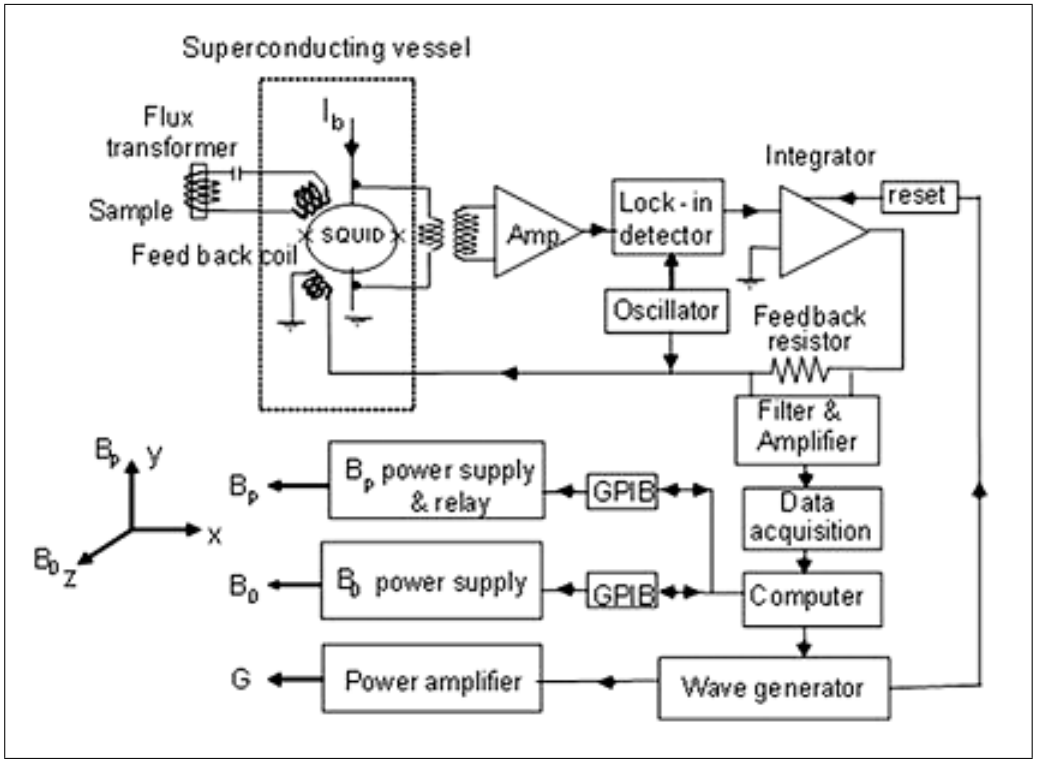

Figure 8.2: Schematic diagram of a SQUID detected pulsed NMR spectrometer [8].

In the experiment shown in Figure 8.2, three magnetic fields are applied to the sample under study: the measurement field B_0, which remains on during the entire experiment, the prepolarizing[2] field B_p, which only remains on for a few seconds before the measurement of the FID, and the sinusoidal magnetic field B_1 which is pulsed to flip the nuclear spins in the sample. The measurement field B_0 is directed in the z-direction, while the pre-polarization field B_p and the sinusoidal B_1 field is directed in the y-direction. The SQUID is positioned perpendicular to the $z-y$ plane in order to detect the FID. Figure 8.3 shows the timing diagram of the different magnets in this experiment. [8]

[2]See Section 8.4.

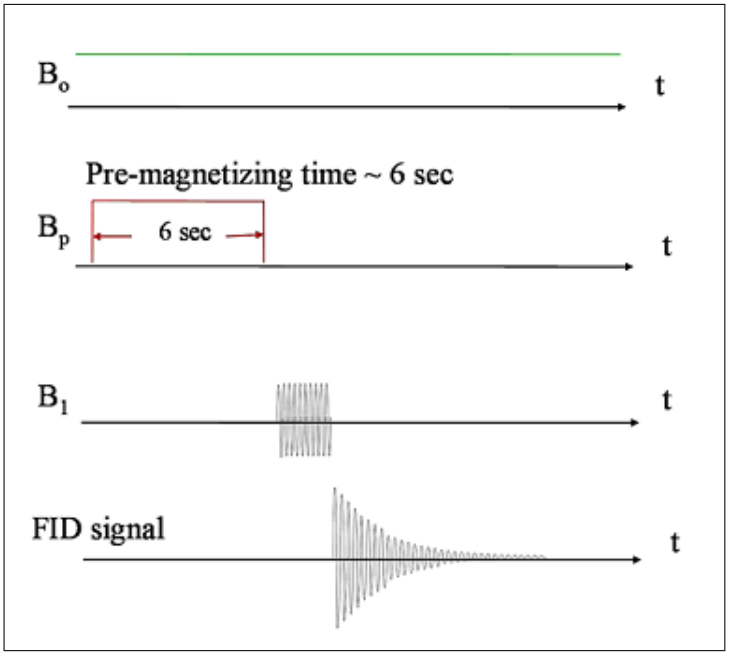

Figure 8.3: Timing diagram for magnets in SQUID detected pulsed NMR experiment [8].

8.4 Prepolarization

Although the SQUID is a very sensitive device, it is well known that the magnetization of a sample can be increased well above its equilibrium value by several means, making it even easier to detect NMR signals [108]. A method called prepolarization [115, 116] is especially attractive as it very simple to implement and can greatly improve the S/N ratio of the NMR signal.

Prepolarization involves applying a magnetic field to a sample that is much stronger than the measurement field. This prepolarizing field is then switched off non-adiabatically (in a short time compared to the NMR period) before the sinusoidal magnetic pulse that flips the spins. The prepolarizing field is applied perpendicularly to the measurement field.

Figure 8.4 shows the evolution of the magnetization of a sample in a SQUID detected NMR experiment using prepolarization, as well as the pulse sequences of the magnetic fields applied to the sample.

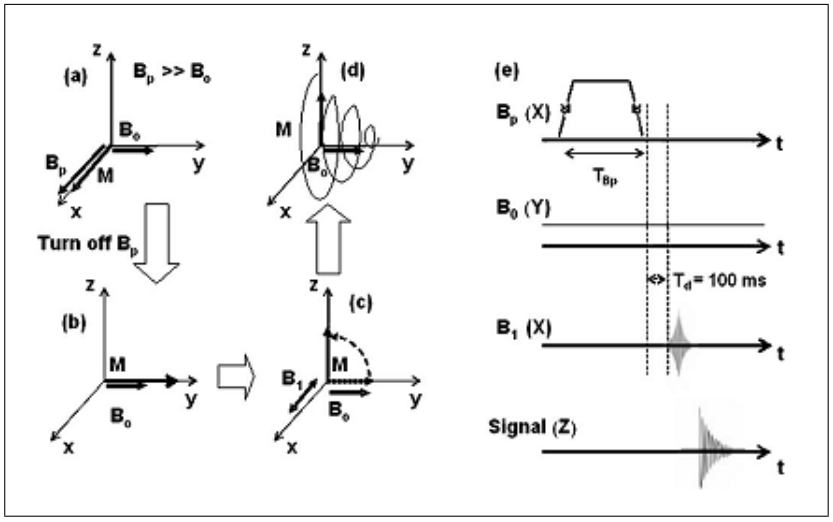

Figure 8.4: Evolution of the magnetization of a sample in a SQUID detected NMR experiment. (a) The magnetization is almost entirely along the x-axis, with the prepolarization field in the x-direction and the measurement field in the y-direction. (b) The magnetization is in the y-direction after the prepolarization field is switched off. (c) A $(\pi/2)$ pulse flips the magnetization into the z-direction. (d) The magnetization precesses in the x-z-plane, creating the NMR signal. (e) The pulse sequence of the magnetic fields applied to the sample. The direction of each magnetic field is indicated in brackets after its name. [9]

Recently prepolarization was used in experiments of SQUID detected NMR using high-T_c SQUIDs [117, 9, 8]. Liao et al. [9] studied the effect of different parameters of the prepolarizing field (strength of prepolarizing field, time sample is in prepolarizing field before measurement, delay time before sinusoidal field pulse after prepolarization field is turned off) on the NMR signal. They found that the S/N ratio of the NMR signal increased linearly with prepolarization field strength, while the resolution of the signal remained constant. They also found that, generally, longer exposure of samples to the prepolarization field[3] and shorter delays before measurement after the prepolarization field is turned off results in increased NMR signal strength. This motivates the use of prepolarization in high-T_c SQUID detected NMR applications.

[3]For a given field strength, the magnetization of the sample can only reach a certain value. This value is approached exponentially. Therefore, after a certain amount of time there will be no gain in NMR signal strength for longer prepolarization times. For a $10mT$ prepolarization field, Liao et al. found the optimum prepolarization time to be between 5 and 6 seconds.

Chapter 9

Simulations

9.1 Introduction

Since both SQUIDs and NMR experiments rely on complex mechanisms of operation, it is necessary to simulate these systems in order to fully understand their working.

This chapter explores methods that can be used to simulate both SQUIDs and NMR experiments.

For SQUIDs, computerized numerical analysis can be done using standard SPICE (Simulation Program with Integrated Circuit Emphasis) techniques. Many different versions of SPICE exist. In this thesis only Linear Technologies' *LTSpice IV* [118] is considered[1]. The ways in which *SPICE* can be used to simulate SQUIDs are described in this chapter. In order to simulate thermal noise in SQUIDs The Mathworks' *MATLAB R2007a* [86] was used.

The simulation of NMR experiments is a very large field and relies heavily on advanced quantum mechanics that falls outside the scope of this thesis, and as such, only basic simulations and calculations are explored in this chapter. For a much more thorough treatment see references [2] and [10].

This chapter starts with the simulation of Josephson junctions, and then moves on to simulate SQUIDs. The chapter concludes with a brief discussion of the basic techniques used to simulate NMR experiments.

[1]For the remainder of the chapter, *SPICE* refers to *Linear Technologies LTSpice IV*.

9.2 Josephson Junction Simulations

The behaviour of a Josephson junction[2] is governed by the current-phase and voltage-phase (4.6.12) and (4.6.5), repeated below for convenience.

$$i = I_c sin(\varphi) + \frac{v}{R_n}, \tag{9.2.1}$$

$$\frac{d\varphi}{dt} = \frac{2\pi}{\Phi_0} v. \tag{9.2.2}$$

(9.2.1) can easily be modelled in *SPICE* using a resistor in parallel with a voltage-dependant current source. To model the phase in *SPICE*, note that (9.2.2) can be rewritten as

$$v = \frac{\Phi_0}{2\pi} \frac{d\varphi}{dt}. \tag{9.2.3}$$

From (9.2.3) it can be seen that the voltage across a junction is analogous to the current flowing through a capacitor, with the phase across a junction being analogous to the voltage across a capacitor. We therefore have

$$v = \frac{\Phi_0}{2\pi} \frac{d\varphi}{dt} \;\Leftrightarrow\; i_c = C \frac{dv_c}{dt}, \tag{9.2.4}$$

where i_c is the current through a capacitor, v_c is the voltage across it and C is its capacitance.

Using (9.2.4) one can model the phase across the junction easily with a voltage-dependant current source in series with a capacitor.

The complete *SPICE* model for a Josephson junction is shown in Figure 9.1.

[2]In this section we consider only RSJs. The simulation of other junctions falls outside the scope of this thesis.

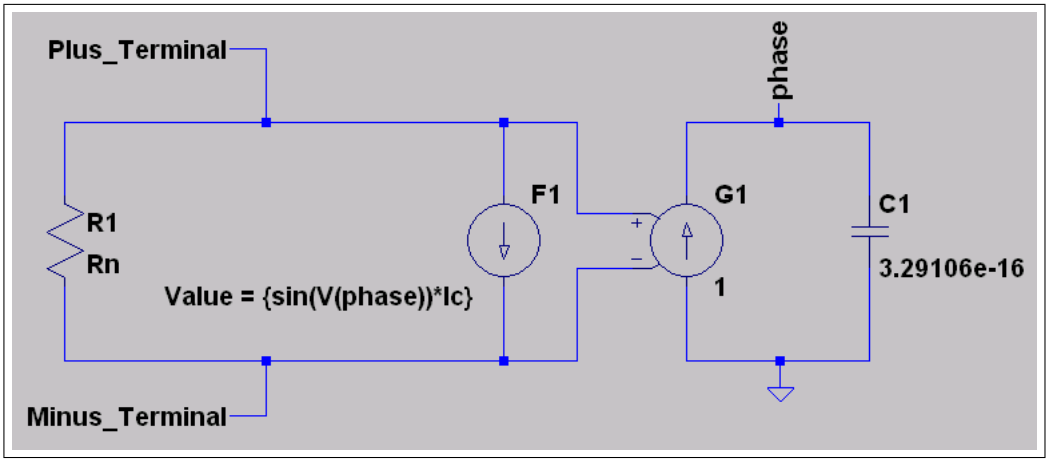

Figure 9.1: *SPICE* model of a Josephson junction. Note the value of C is equal to $\frac{\Phi_0}{2\pi}$.

Using the Josephson junction model shown in Figure 9.1 with a critical current $I_c = 10\mu A$ and a normal state resistance $R_n = 10\Omega$, various simulations were done.

Figure 9.2 shows the result of a simulation where a current of $20\mu A$ was applied to the junction. Note that a periodic voltage appears across the junction under these operating conditions.

If the applied current is made smaller than the critical current, no voltage appears across the junction, as shown in Figure 9.3, the result of a simulation with a current of $5\mu A$ applied to the junction.

Figure 9.4 shows the result of a simulation where a current of $11\mu A$ is applied to the junction.

From these simulation results it can be seen that a periodic voltage starts to appear across the Josephson junction as soon as the applied current exceeds the junction's critical current. This is in accordance with the theory of the Josephson junction developed in Section 4.6.

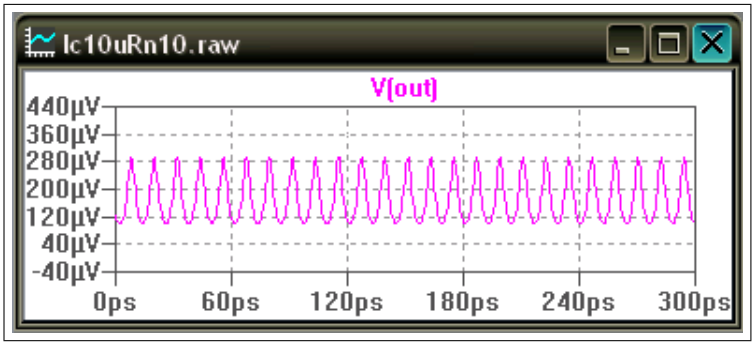

Figure 9.2: Simulation results of a Josephson junction with $I_c = 10\mu A$ and $R_n = 10\Omega$ with an applied current of $20\mu A$. Note that *V(out)* is the voltage across the junction.

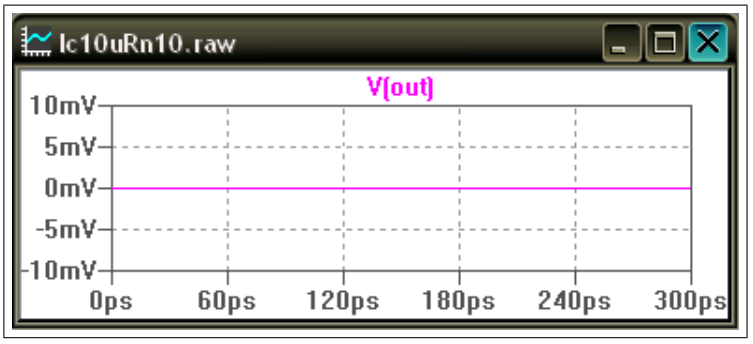

Figure 9.3: Simulation results of a Josephson junction with $I_c = 10\mu A$ and $R_n = 10\Omega$ with an applied current of $5\mu A$. Note that *V(out)* is the voltage across the junction.

To better understand the effects of noise on Josephson junctions, simulations are essential. *SPICE* is a very versatile program, but cannot simulate noise sources. To overcome this problem a PWL current source with a mean-square value of

$$i_{rms}^2 = \frac{4k_BTB}{R_n} \tag{9.2.5}$$

(where B is the bandwidth of the noise, k_B is Boltzmann's constant, T is the temperature and R_n is the normal state resistance of the Josephson junction) is placed in parallel with the normal state resistance of a Josephson junction

in Figure 9.1. This current source simulates the thermal noise present in the Josephson junction.

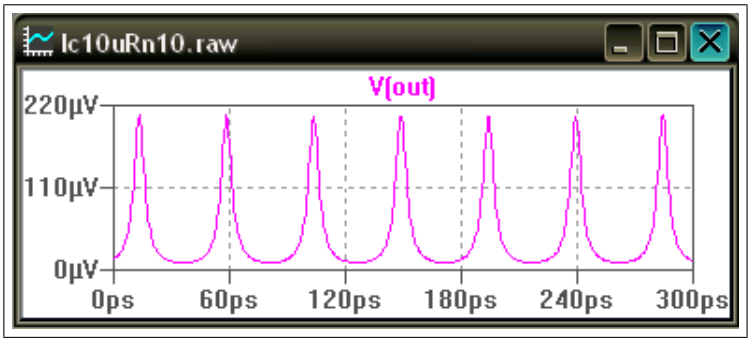

Figure 9.4: Simulation results of a Josephson junction with $I_c = 10\mu A$ and $R_n = 10\Omega$ with an applied current of $11\mu A$. Note that *V(out)* is the voltage across the junction.

The current source points are generated using *MATLAB* [5]. The "randn" function in *MATLAB* generates normally distributed random numbers. Noise is generated by using this function to generate a number of noise points which are then multiplied by the RMS value of thermal noise given by (9.2.5).

The bandwidth B in (9.2.5) must be chosen smaller than $1.6THz$ (this is the frequency at which thermal noise ceases to be white at 77 K).

Appendix D can be consulted for the *MATLAB* code used to generate the noise.

The simulation results are shown in Figure 9.5 and Figure 9.6. It can clearly be seen in Figure 9.5 that the phase across the junction makes sudden jumps of 2π radians between relatively stable values. Each jump is accompanied by a voltage spike across the junction. This phenomenon is known as Thermally Activated Phase Slippage or TAPS [119] and results in the broadening of the junction's spectral density (as seen in Figure 9.6) and rounding of the junction's current-voltage characteristic curve. (In these simulations a noise bandwidth of $500GHz$ was used. This large bandwidth was chosen to clearly show the effects of noise on the Josephson junction.)

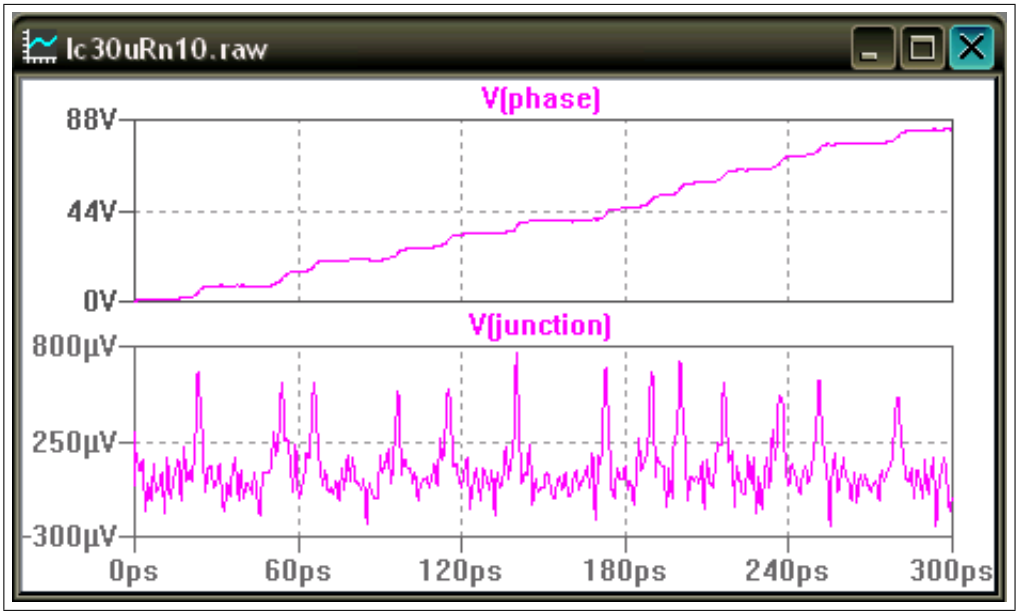

Figure 9.5: Simulation results of a Josephson with noise. Here $I_c = 30\mu A$ and $R_n = 10\Omega$ with an applied current of $31\mu A$.

Figure 9.6 shows the power spectral density broadening effects of noise on the Josephson junction. The fundamental frequency can still be seen in the output of the junction with noise, but the harmonics are masked.

9.3 SQUID simulations

In this section the DC SQUID is simulated using *SPICE*. The *SPICE* model for the Josephson junction developed in the previous section is used to model the DC SQUID.

Figure 9.7 shows the *SPICE* model of the DC SQUID used in this section. Note that the SQUID loop L_{SQ} is split up into two equal inductances.

In order to simulate a flux applied to the SQUID loop, a current source is connected to two $40pH$ inductances, as seen in Figure 9.8. These two inductances are coupled to the SQUID loop inductances with a coupling factor of $k = 1$.

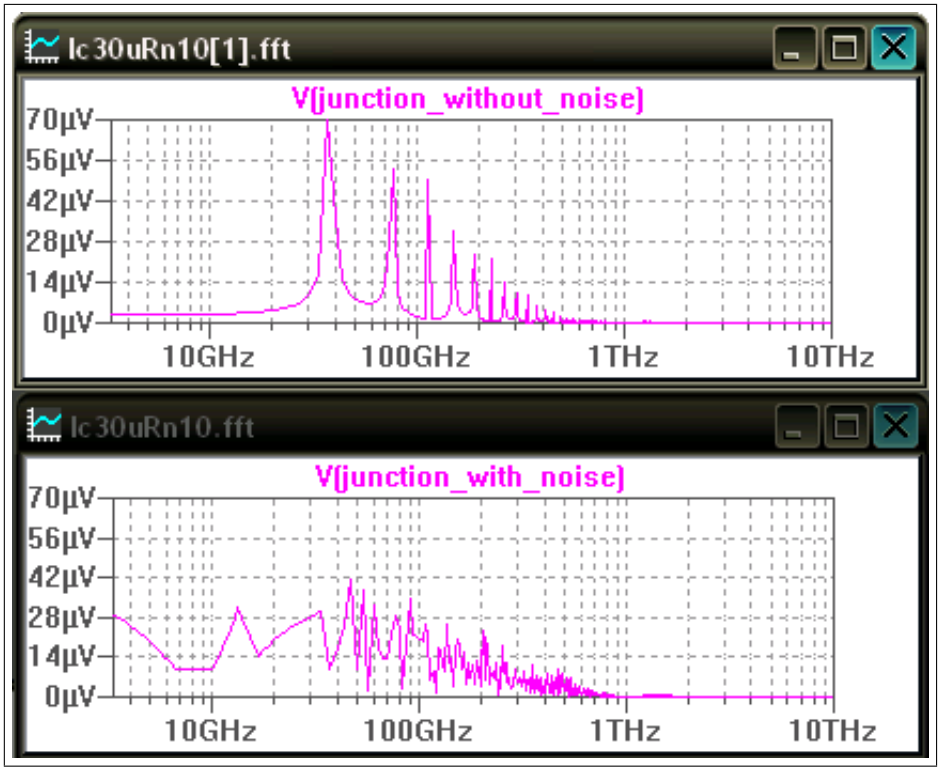

Figure 9.6: Broadening of Josephson junction power spectral density due to noise.

In order to take the average of the SQUID output voltage a $500MHz$, 2-pole Butterworth filter is modelled using an ideal voltage-controlled voltage source, as seen in Figure 9.9. An ideal voltage-controlled voltage source is used so as not to load the SQUID.

Three different SQUIDs were simulated, each with a different screening parameter β_L: SQUIDs with $\beta_L = 3$, $\beta_L = 1$ and $\beta_L = 1/2$. Josephson junction parameters of $I_c = 10\mu A$ and $R_n = 10\Omega$ were chosen for the SQUIDs.

A SQUID with a loop inductance of $L_{SQ} = 310.17pH$ yields a screening parameter of $\beta_L = 3$. The coupling factor of $k = 1$ between the SQUID loop and the input inductor yields a mutual inductance of $M = k\sqrt{L_{SQ}L_i} = 157.52 \times 10^{-12}A^{-1}$. This normalizes to $M = 76179\Phi_0/A$, or $1/M = 13.127\mu A\Phi_0$, meaning that for every $13.127\mu A$ flowing through the input inductor one fluxon is coupled into the SQUID loop.

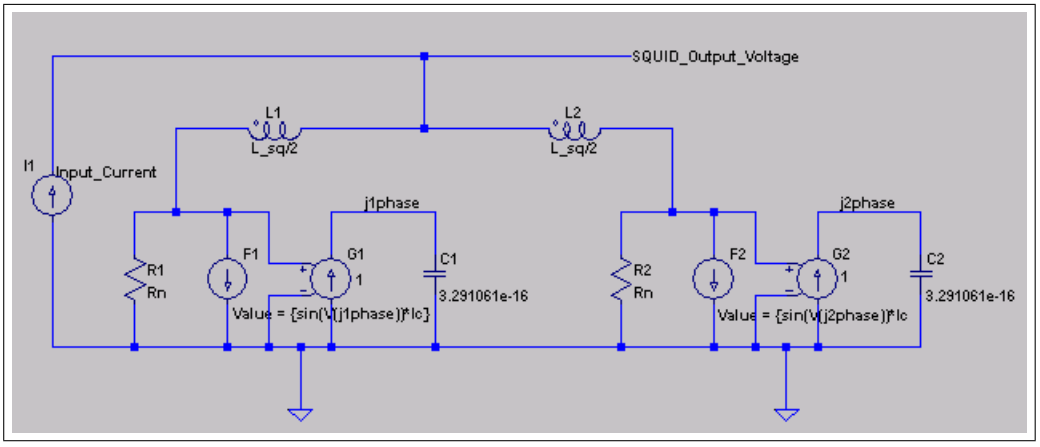

Figure 9.7: *SPICE* model of DC SQUID.

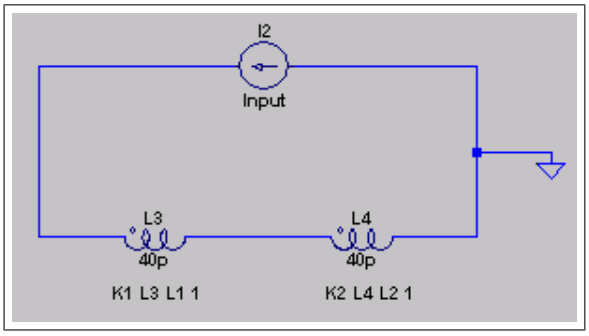

Figure 9.8: *SPICE* model of inductances used to apply flux to simulated SQUID loop.

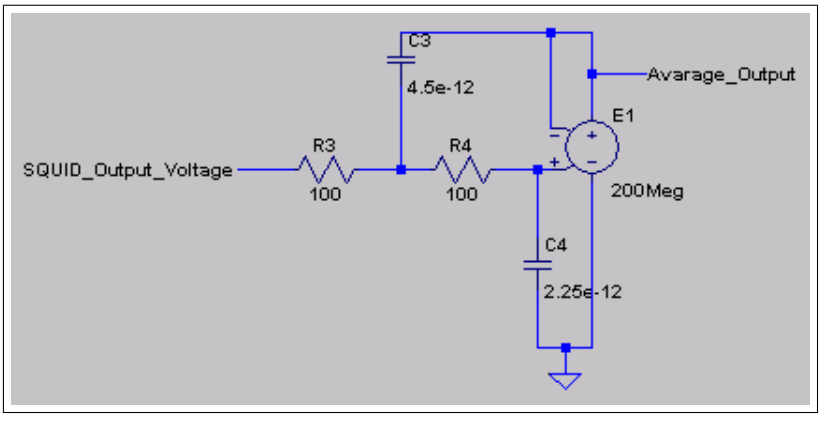

Figure 9.9: *SPICE* model for $500MHz$, 2-pole Butterworth filter.

Table 9.1: Properties of Simulated SQUIDs.

β_L	**SQUID Loop Inductance** (L_{SQ}) (pH)	**Normalized Mutual Inductance** (M) (Φ_0/A)	$1/M$ ($\mu A/\Phi_0$)
3	310.17	76179	13.127
1	103.39	43982	22.737
1/2	51.695	31100	32.154

For a SQUID with $\beta_L = 1$ a SQUID loop inductance of $L_{SQ} = 103.39pH$ is needed. This yields a normalized mutual inductance of $M = 43982\Phi_0/A$, or $1/M = 22.737\mu\Phi/A$, meaning that for every $22.737\mu A$ flowing through the input inductor, one fluxon is coupled into the SQUID loop.

For a SQUID with $\beta_L = 1/2$ a SQUID loop inductance of $L_{SQ} = 51.695pH$ is needed. This yields a normalized mutual inductance of $M = 31100\Phi_0/A$, or $1/M = 32.154\mu\Phi/A$, meaning that for every $32.154\mu A$ flowing through the input inductor, one fluxon is coupled into the SQUID loop.

Table 9.1 sums up the parameters for the three SQUIDs that were simulated.

Noise simulations were done by simulating noise sources in *MATLAB*, as in the previous section. The noise temperature used was 77 kelvin.

9.3.1 DC SQUID Current-Voltage Response

The current-voltage response of each SQUID was simulated by sweeping the input current from $-4I_c$ to $4I_c$ and measuring the voltage output. The normalized output voltage (V_{SQ}/V_c) was plotted against the normalized input current (I_{Input}/I_c).

Four simulations were done for each SQUID. A simulation with no thermal noise and applied flux of $\Phi_a = \Phi_0$ and $\Phi_a = \Phi_0/2$, and a simulation with thermal noise with a $500MHz$ bandwidth and applied flux of $\Phi_a = \Phi_0$ and $\Phi_a = \Phi_0/2$.

Figure 9.10 shows the results of simulations done on a SQUID with $\beta_L = 3$, while Figure 9.11 and Figure 9.12 show the results of simulations done on

SQUIDs with $\beta_L = 1$ and $\beta_L = 1/2$ respectively. Note that the results of the simulations with $\beta_a = \Phi_0$ and $\beta_a = \Phi_0/2$ are plotted on the same axis in each case.

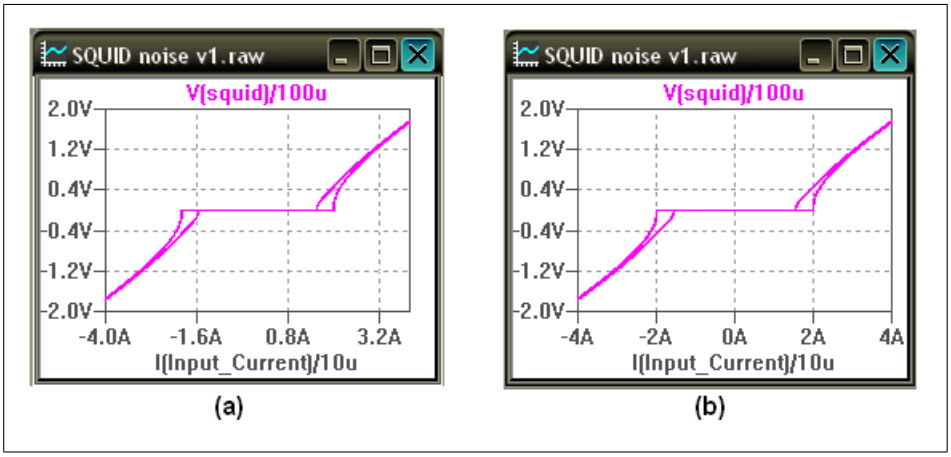

Figure 9.10: *SPICE* simulation results of DC SQUID with $\beta_L = 3$: current-voltage relationship. (a) No thermal noise present. (b) Thermal noise with $500MHz$ bandwidth present. Note that the outside I-V curve shows the response to an applied flux of Φ_0, while the inside I-V curve shows the response to an applied flux of $\Phi_0/2$.

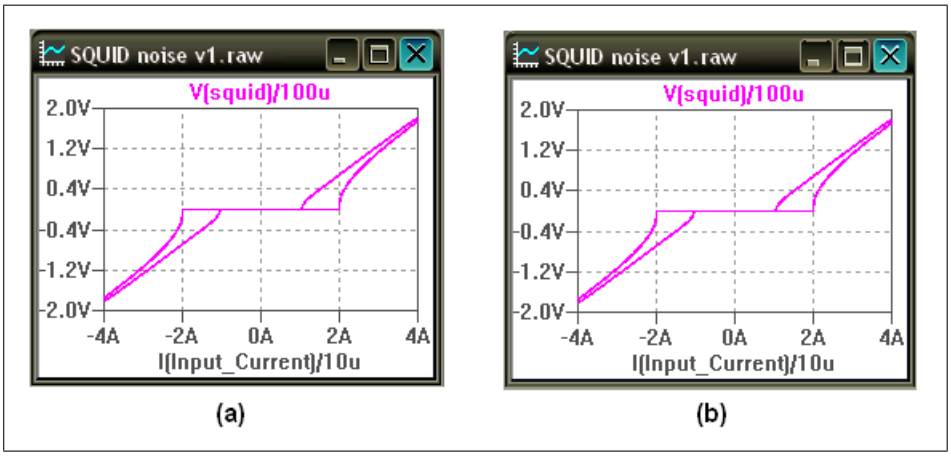

Figure 9.11: *SPICE* simulation results of DC SQUID with $\beta_L = 1$: current-voltage relationship. (a) No thermal noise present. (b) Thermal noise with $500MHz$ bandwidth present. Note that the outside I-V curve shows the response to an applied flux of Φ_0, while the inside I-V curve shows the response to an applied flux of $\Phi_0/2$.

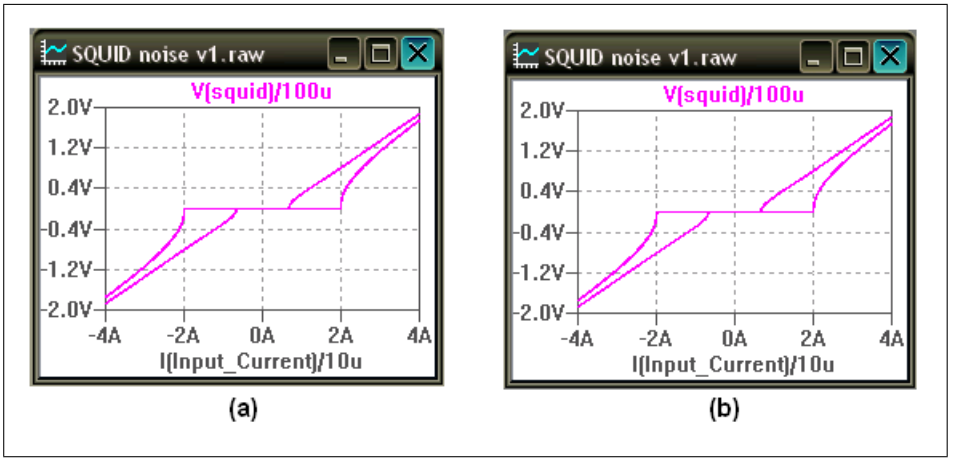

Figure 9.12: *SPICE* simulation results of DC SQUID with $\beta_L = 1/2$: current-voltage relationship. (a) No thermal noise present. (b) Thermal noise with $500MHz$ bandwidth present. Note that the outside I-V curve shows the response to an applied flux of Φ_0, while the inside I-V curve shows the response to an applied flux of $\Phi_0/2$.

The results of these simulations agree with the theory developed in Chapter 5. Notice that the effect of the thermal noise is too small to be noticeable over the large current sweep. Notice also that the modulation depth of SQUIDs decreases with increasing β_L, but that SQUID sensitivity increases. This can be seen from the fact that, for larger values of β_L, a smaller current must be applied to the input inductors in order to couple in the same amount of flux.

9.3.2 DC SQUID Response to Large Flux Input

The flux-to-voltage response of the SQUID was also simulated. In these simulations the bias current was set to[3] $I_b = 3.4I_c = 34\mu A$, while the applied flux was swept from $\Phi_a = -3\Phi_0$ to $\Phi_a = 3\Phi_0$.

For each of the three SQUIDs, a simulation with no thermal noise present, a simulation with thermal noise with $1MHz$ bandwidth present and a simulation with excessive thermal noise with a $500MHz$ bandwidth present were done. The results of the flux-to-voltage simulations are shown in Figures 9.13 (SQUID with $\beta_L = 3$), 9.14 (SQUID with $\beta_L = 1$) and 9.15 (SQUID with $\beta_L = 1/2$).

[3]Simulations show that the bias current is at its optimum value when $3.3I_c \leq I_b \leq 3.5I_c$ [5, 37].

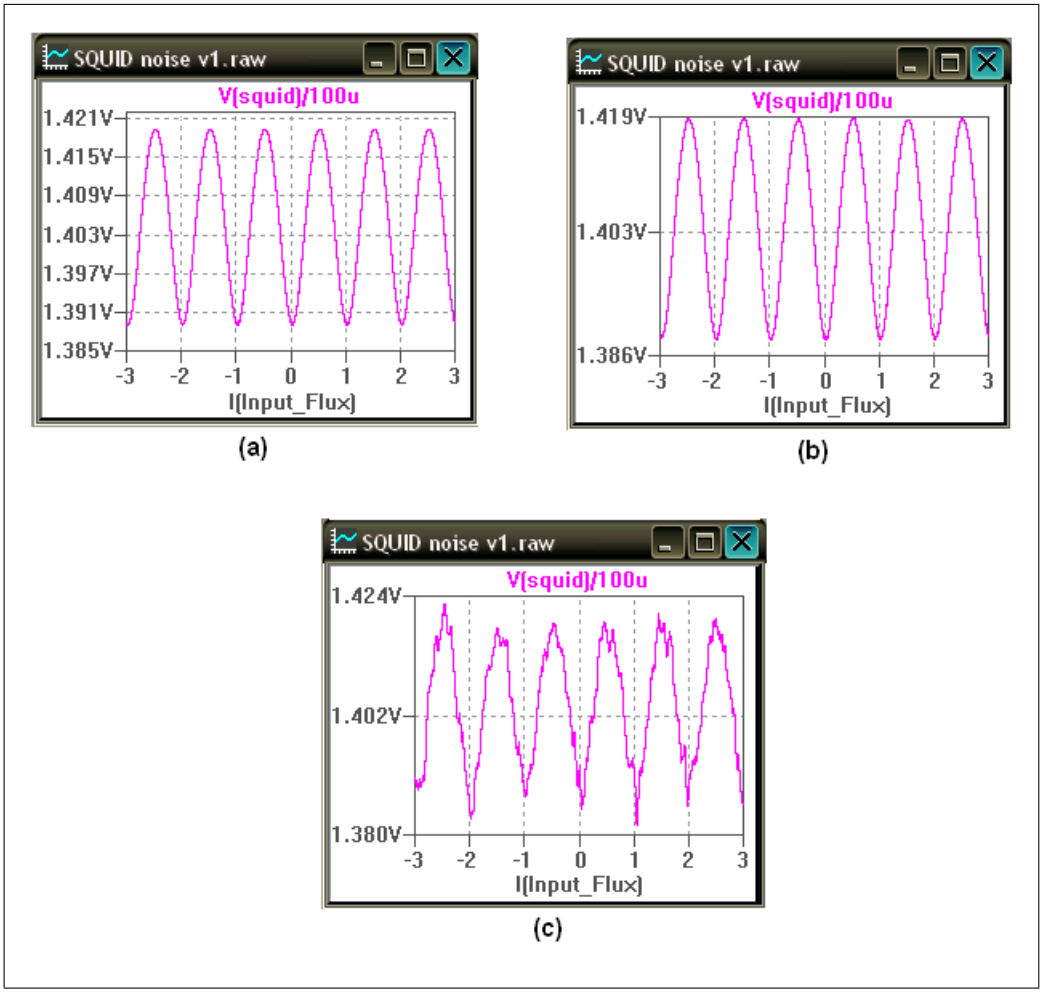

Figure 9.13: *SPICE* simulation results of DC SQUID with $\beta_L = 3$: flux-voltage relationship. (a) No thermal noise present. (b) Thermal noise with $1MHz$ bandwidth present (c) Thermal noise with $500MHz$ bandwidth present. The applied flux is swept from $-3\Phi_0$ to $3\Phi_0$.

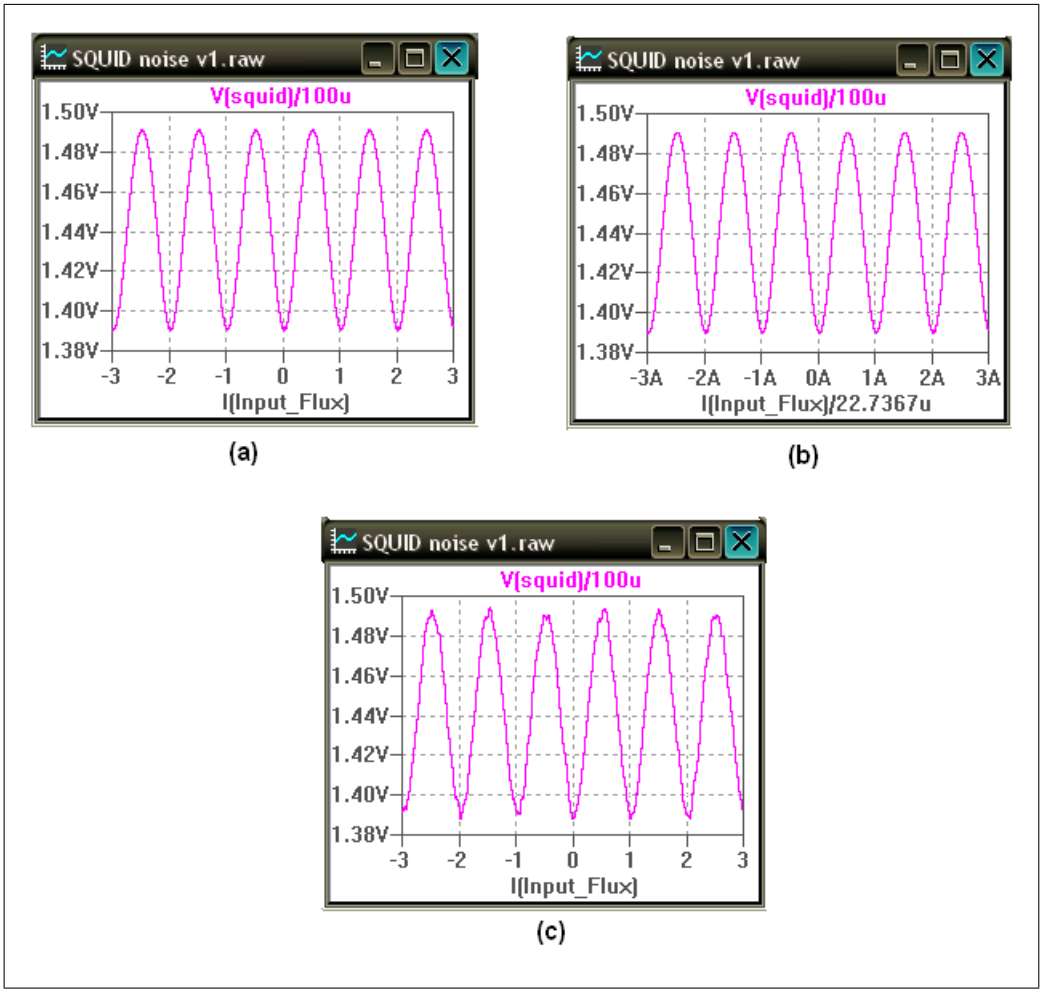

Figure 9.14: *SPICE* simulation results of DC SQUID with $\beta_L = 1$: flux-voltage relationship. (a) No thermal noise present. (b) Thermal noise with $1MHz$ bandwidth present (c) Thermal noise with $500MHz$ bandwidth present. The applied flux is swept from $-3\Phi_0$ to $3\Phi_0$.

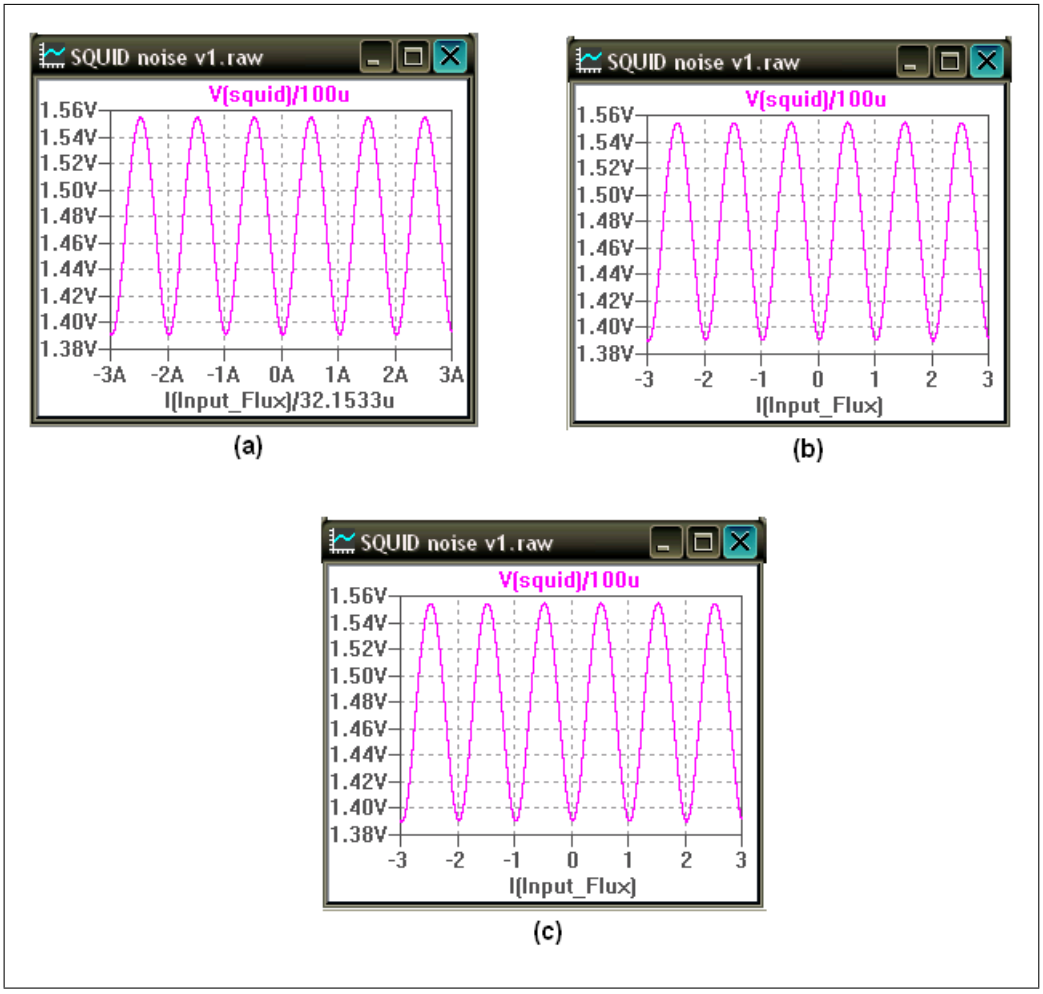

Figure 9.15: *SPICE* simulation results of DC SQUID with $\beta_L = 1/2$: flux-voltage relationship. (a) No thermal noise present. (b) Thermal noise with $1MHz$ bandwidth present (c) Thermal noise with $500MHz$ bandwidth present. The applied flux is swept from $-3\Phi_0$ to $3\Phi_0$.

From the results it can be seen that SQUIDs with a lower β_L value are less susceptible to noise, and that they have a larger modulation depth. These advantages comes at a price, however, as they are also less sensitive.

9.3.3 DC SQUID Small Signal Response

In order to simulate the small signal response of a SQUID, the SQUID is biased at its optimum operating point W by applying a biasing current of $I_b = 34\mu A$

and a biasing flux of $\Phi_b = \Phi_0/2$. A $40MHz$ signal with an amplitude of $\Phi_a = \Phi_0/4\pi$ (6.2.2) is then applied.

Again, three SQUIDs were simulated, each with a different value of β_L ($\beta_L = 3$, $\beta_L = 1$ and $\beta_L = 1/2$). These SQUIDs were also simulated under conditions with no thermal noise present, thermal noise with a bandwidth of $1MHz$ present and thermal noise with a bandwidth of $500MHz$ present.

The results of these small signal response simulations are shown in Figures 9.16 (SQUID with $\beta_L = 3$), 9.17 (SQUID with $\beta_L = 1$) and 9.18 (SQUID with $\beta_L = 1/2$).

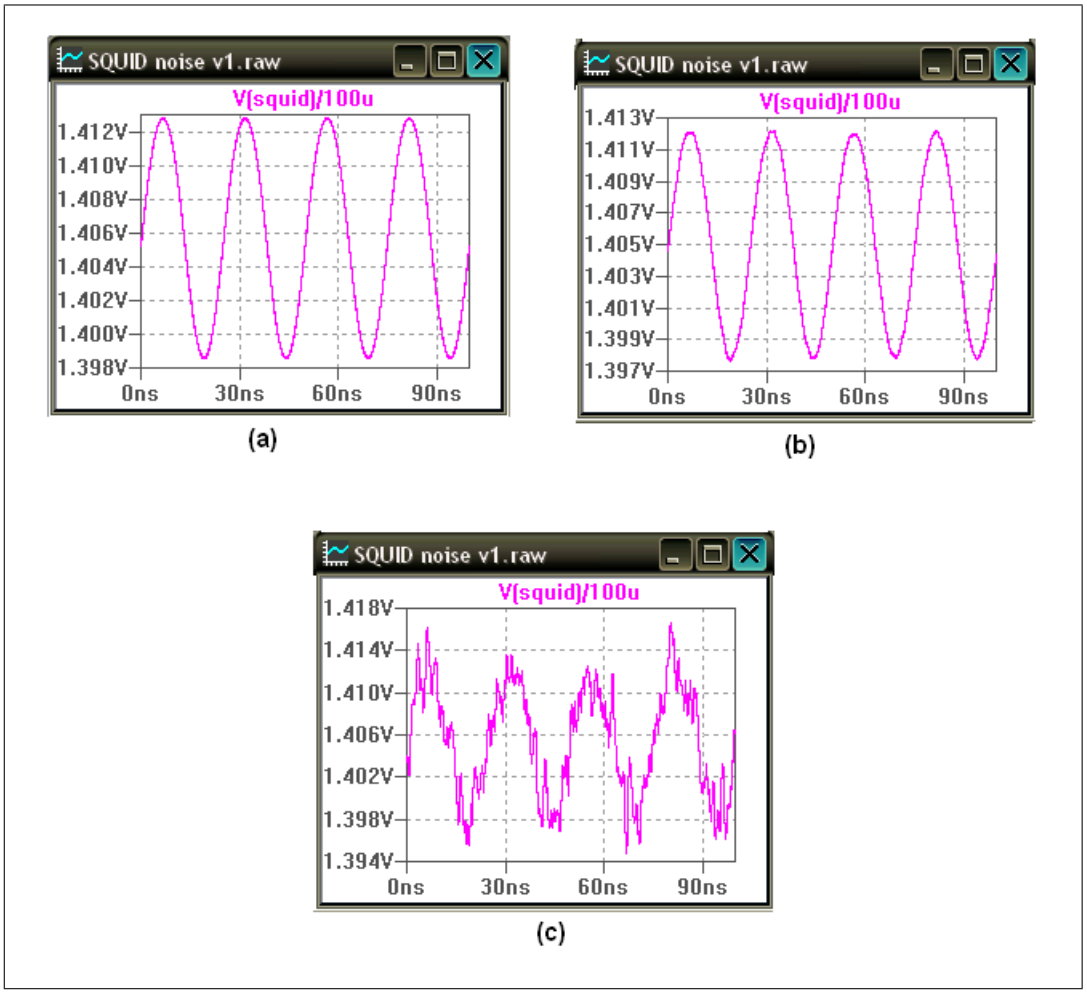

Figure 9.16: *SPICE* simulation results of DC SQUID with $\beta_L = 3$: small signal response. (a) No thermal noise present. (b) Thermal noise with $1MHz$ bandwidth present (c) Thermal noise with $500MHz$ bandwidth present.

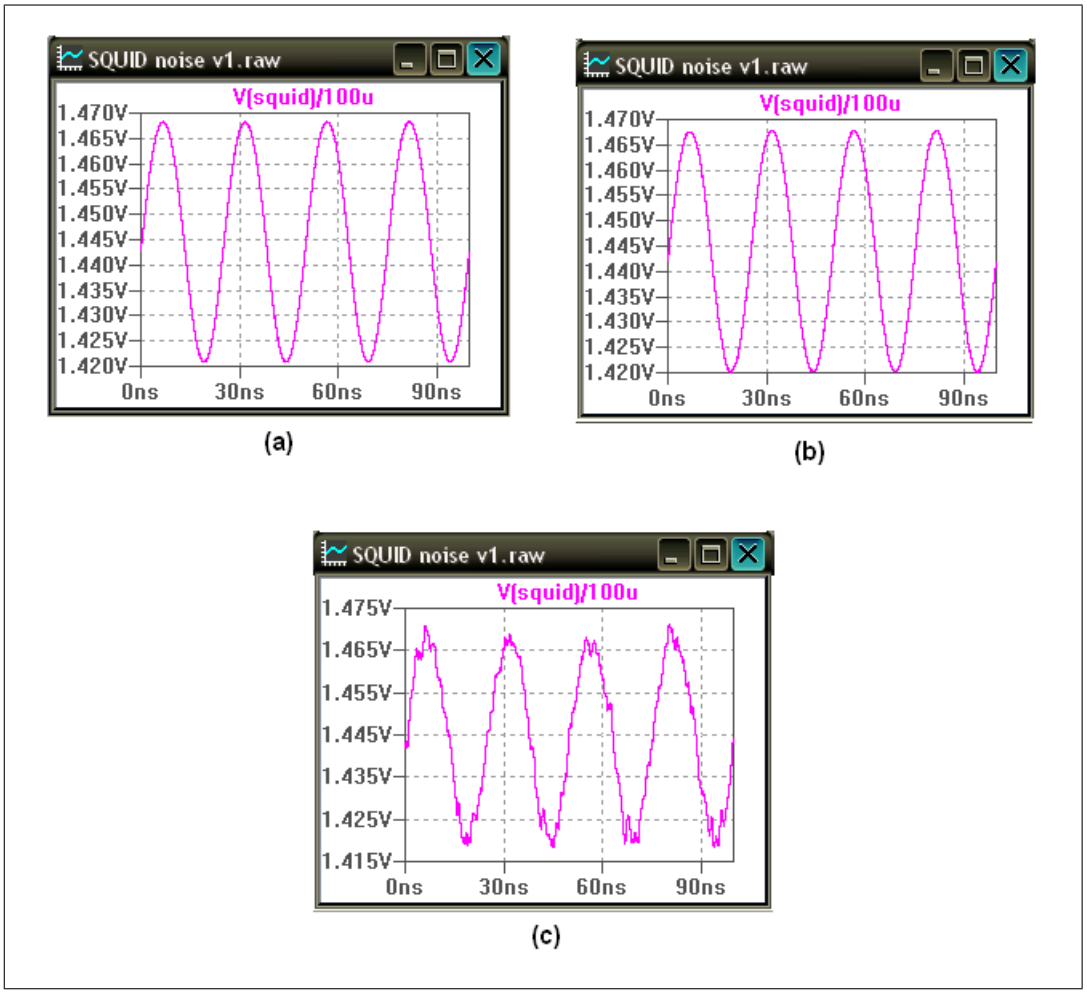

Figure 9.17: *SPICE* simulation results of DC SQUID with $\beta_L = 1$: small signal response. (a) No thermal noise present. (b) Thermal noise with $1MHz$ bandwidth present (c) Thermal noise with $500MHz$ bandwidth present.

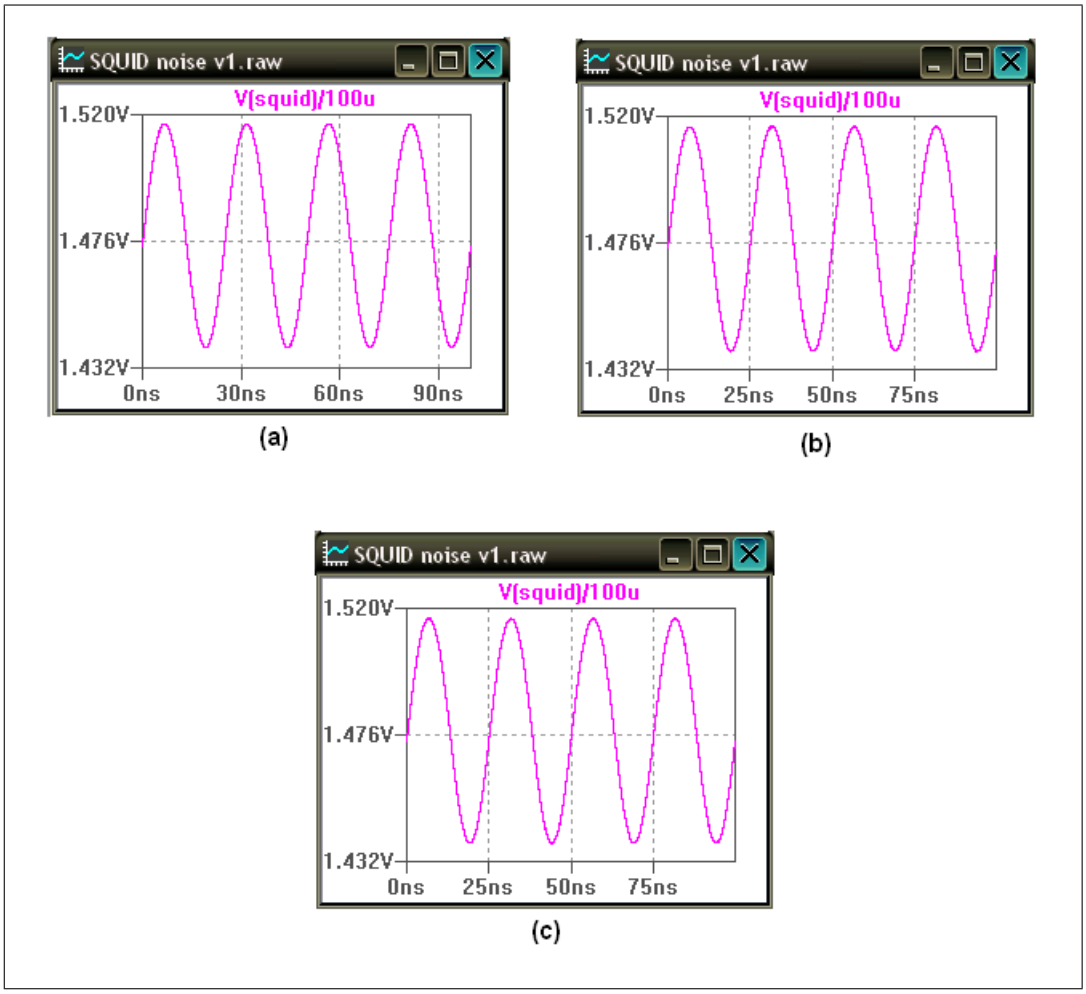

Figure 9.18: *SPICE* simulation results of DC SQUID with $\beta_L = 1/2$: small signal response. (a) No thermal noise present. (b) Thermal noise with $1MHz$ bandwidth present (c) Thermal noise with $500MHz$ bandwidth present.

From the results of the simulation it can be seen that for $\Phi_a \leq \Phi_0/4\pi$ the response of a SQUID biased at the optimal working point W is linear, as expected from the theory developed in Chapter 6. Again it is evident from the results that the sensitivity of a SQUID to noise increases and the modulation depth decreases with increasing β_L.

9.4 NMR Simulations

In order to fully understand the operation of NMR it is necessary to simulate spins in a magnetic field. In this section simulations of spins in magnetic fields done in *MATLAB* are reported[4]. First a single spin-1/2 particle in a magnetic field is simulated under various conditions. Then an ensemble of non-interacting spin-1/2 particles is investigated. Finally the J-coupling terms between spin-1/2 particles in a molecule are also included in the simulations and the simulated low field NMR spectrums of two substances are reported. All *MATLAB* programmes are listed in Appendix D.

9.4.1 ^1H Nucleus in a Magnetic Field

First, a single ^1H nucleus in a magnetic field was simulated.

A ^1H nucleus consists of a single proton with spin $s = 1/2$. For the spin 1/2 system, there are just two eigenstates, $|\frac{1}{2}\left(\frac{1}{2}\right)\rangle$ and $|\frac{1}{2}\left(-\frac{1}{2}\right)\rangle$. These eigenstates can be represented by

$$\chi_+ = \begin{bmatrix} 1 \\ 0 \end{bmatrix} \tag{9.4.1}$$

and

$$\chi_- = \begin{bmatrix} 0 \\ 1 \end{bmatrix} \tag{9.4.2}$$

respectively, and the general state of a particle can be represented by

$$\chi = \begin{bmatrix} a \\ b \end{bmatrix} = a\chi_+ + b\chi_-, \tag{9.4.3}$$

with the normalization constraint

$$|a|^2 + |b|^2 = 1. \tag{9.4.4}$$

[4]This section presumes that the reader is familiar with the basic concepts of quantum mechanics, and only the most important equations and results are listed. Please refer to Appendix A for a brief introduction to quantum mechanics.

The spin operators for a spin 1/2 particle are 2×2 matrices, with

$$\mathbf{S} = \frac{\hbar}{2}\sigma, \tag{9.4.5}$$

where

$$\sigma_x = \begin{bmatrix} 0 & 1 \\ 1 & 0 \end{bmatrix}, \quad \sigma_y = \begin{bmatrix} 0 & -\imath \\ \imath & 0 \end{bmatrix} \text{ and } \quad \sigma_z = \begin{bmatrix} 1 & 0 \\ 0 & -1 \end{bmatrix} \tag{9.4.6}$$

are the Pauli spin matrices.

A ^1H nucleus has a magnetic dipole moment μ of (3.3.2)

$$\mu = \gamma \mathbf{S}, \tag{9.4.7}$$

where γ is the gyromagnetic ratio. When this particle is placed in a uniform magnetic field $\mathbf{B}$ orientated in the z-direction[5] it experiences a torque that tries to line it up parallel with the field. This torque has an energy of

$$\mathbf{H} = -\mu \cdot \mathbf{B} \tag{9.4.8}$$

associated with it [32]. The Hamiltonian of the particle (in matrix form) in the magnetic field therefore becomes

$$\mathbf{H} = -\gamma \mathbf{B} \cdot \mathbf{S} = -\gamma B_0 \mathbf{S_z} = -\frac{\gamma B_0 \hbar}{2} \begin{bmatrix} 1 & 0 \\ 0 & -1 \end{bmatrix}, \tag{9.4.9}$$

where B_0 is the strength of the magnetic field.

The Hamiltonian $\mathbf{H}$ has the same eigenstates as $\mathbf{S_z}$,

$$\begin{aligned} \chi_+ &\text{ with energy } E_+ = -(\gamma B_0 \hbar)/2, \\ \chi_- &\text{ with energy } E_- = +(\gamma B_0 \hbar)/2, \end{aligned} \tag{9.4.10}$$

and is time independent, so the general solution of the time-dependant Schrödinger equation

$$\imath\hbar \frac{\partial \chi}{\partial t} = \mathbf{H}\chi \tag{9.4.11}$$

[5]This assumption can be made without any loss of generality.

is given as

$$\chi(t) = a\chi_+ e^{-\imath E_+ t/\hbar} + b\chi_- e^{-\imath E_- t/\hbar}, \tag{9.4.12}$$

where a and b are the initial conditions [32],

$$\chi(0) = \begin{bmatrix} a \\ b \end{bmatrix}. \tag{9.4.13}$$

A *MATLAB* program was written to evaluate the expectation values of S_x, S_y and S_z, given by

$$\begin{aligned} \langle S_x \rangle &= \chi(t)\mathbf{S_x}\chi(t)^\dagger, \\ \langle S_y \rangle &= \chi(t)\mathbf{S_y}\chi(t)^\dagger, \\ \text{and } \langle S_z \rangle &= \chi(t)\mathbf{S_z}\chi(t)^\dagger \end{aligned} \tag{9.4.14}$$

(where the † symbol denotes the Hermetian conjugate) using (9.4.12).

Starting with a ^1H nucleus in a random spin state, the evolution of $\langle S_x \rangle$, $\langle S_y \rangle$ and $\langle S_z \rangle$ in a static z-directed magnetic field with a strength of $0.2\mu T$ is calculated. The results are shown in Figure 9.19.

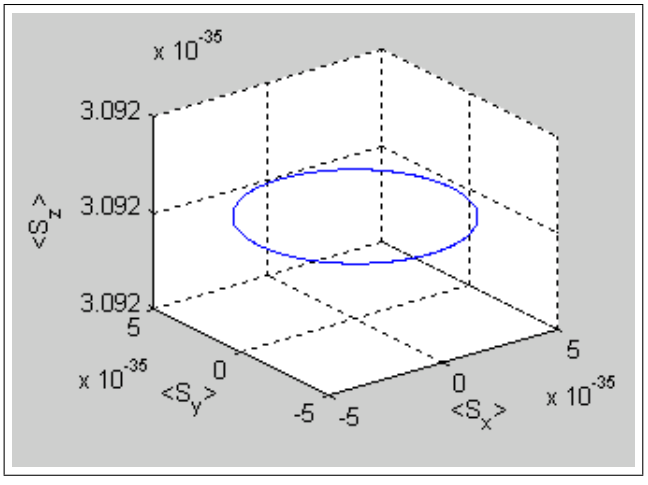

Figure 9.19: Results of a *MATLAB* simulation of a ^1H nucleus in a z-directed magnetic field: Evolution of the expectation value of spin $\langle S \rangle$

From Figure 9.19 it can be seen that the (expectation value of the) spin

precesses around the magnetic field. This is consistent with the theory introduced in Chapter 3. Although not shown here, simulations with x- and y-directed magnetic fields yield the same results.

To determine the speed of the precession $\langle S_x \rangle$ or $\langle S_y \rangle$ can be plotted against time. Figure 9.20 shows $\langle S_x \rangle$ plotted against time. From this figure it can be seen that the spin precesses around the z-axis once every 0.1175 seconds, or at $f = 8.51Hz$. This is equivalent to $\omega = 2\pi f = 53.5rad.s^{-1}$, which is the same as the theoretically predicted value of $\omega = \gamma B_0$.

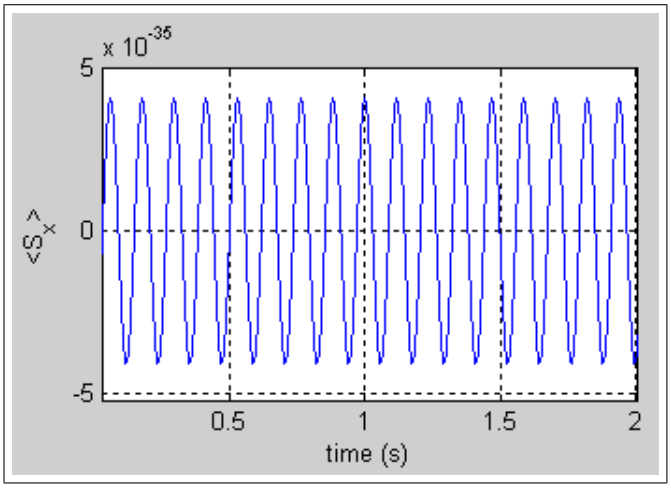

Figure 9.20: Results of a *MATLAB* simulation of a ^1H nucleus in a z-directed magnetic field: $\langle S_x \rangle$ vs. Time

9.4.2 ^1H Nucleus with Fluctuations in a Magnetic Field

As discussed in Chapter 3 the motion of the spins in a sample causes the spins to slightly change their orientations and align themselves to the magnetic field. This alignment process can be modelled by generating a random number from a normal distribution and comparing it to some bias value. If the number is greater than the bias value, the spin is adjusted toward the lower energy value, while if the number is less than the bias value, the spin is adjusted away from the lower energy state.

Figure 9.21 shows the *MATLAB* code used for this calculation.

```
if (randn(1) <= 0.05)                    %Bias toward lower energy level = 0.05
    a = a - abs(randn(1))*(1-a)*timestep; %Move closer to higher energy value
    if (b>0)                             %Correct b such that |a|^2+|b|^2=1
        b = sqrt(1-a*a);
    else
        b = -sqrt(1-a*a);
    end
else
    a = a + abs(randn(1))*(1-a)*timestep; %Move closer to lower energy value
    if (b>0)                             %Correct b such that |a|^2+|b|^2=1
        b = sqrt(1-a*a);
    else
        b = -sqrt(1-a*a);
    end
end
```

Figure 9.21: *MATLAB* code used to model fluctuation in spin during precession. a and b represent the spin state's values (9.4.3).

Using the code in Figure 9.21 a simulation was performed on a single ^1H nucleus. The results are shown in Figure 9.22. Note that the chosen bias value (0.05) and the adjustment made to the spin are much larger than practical values. These values were chosen so that the effect of these fluctuations on the spins can be easily seen in the simulation. In real-world systems, the bias toward one state is extremely small.

Note that in Figure 9.22 the spin starts precessing at $\langle S_z \rangle \approx 2 \times 10^{-35}$ and the subsequent fluctuations in its spin state causes it to start to align with the z-axis. The final (after 5 seconds) value of $\langle S_z \rangle$ is approximately 2.75×10^{-35}.

9.4.3 Flipped ^1H Nucleus in a Magnetic Field

In this section we simulate what happens to a single spin 1/2 in a z-directed magnetic field when the spin is allowed to precess in the magnetic field for a while and is then rotated by $\pi/2$ radians around the x-axis.

The operator for rotation around the x-axis for a spin-1/2 particle is given by [2]

$$R_x(\phi) = \begin{bmatrix} \cos(\phi/2) & -\imath \sin(\phi/2) \\ -\imath \sin(\phi/2) & \cos(\phi/2) \end{bmatrix}. \tag{9.4.15}$$

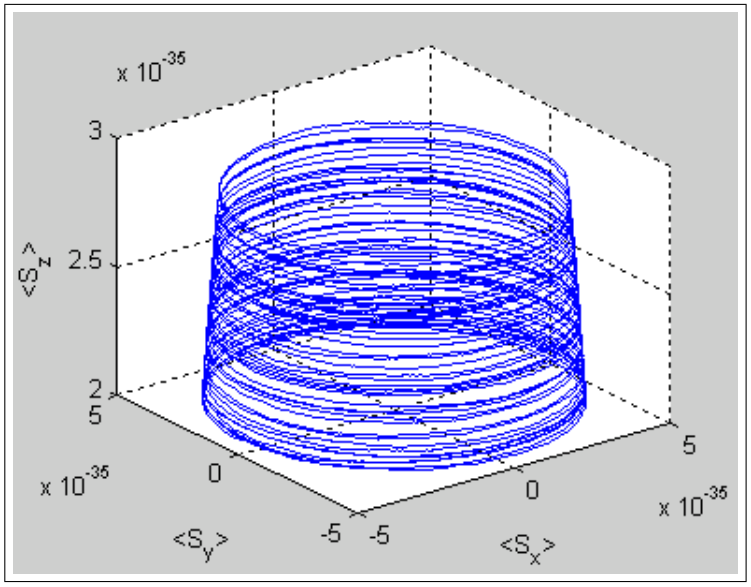

Figure 9.22: Simulation of 1^H nucleus in a z-directed magnetic field with spin fluctuations.

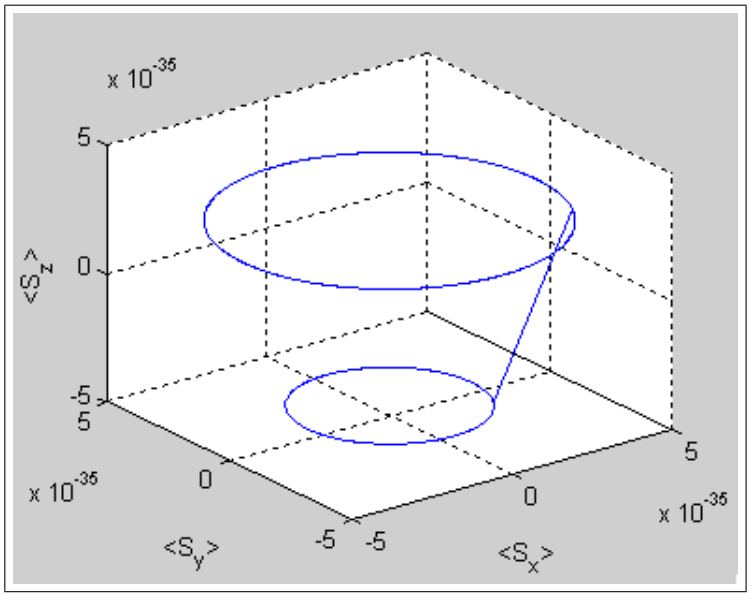

Figure 9.23: Simulation of rotation of 1^H nucleus in a z-directed magnetic field.

In order to flip the spin by an angle ϕ around the x-axis, the particle's state is sandwiched between the rotation matrix given in (9.4.15) and its adjoint.

Figure 9.23 shows the result of a simulation where a spin in a z-directed magnetic field is rotated by $\pi/2$ radians.

In the simulation results shown in Figure 9.23 the spin starts with $\langle S_z \rangle \approx -5 \times 10^{-35}$. After the spin is rotated by $\pi/2$ radians, the spin has $\langle S_z \rangle \approx 2.5 \times 10^{-35}$. From these results it can be seen that the spin precesses in the normal way after it has been rotated. This is in accordance with the theory discussed in Chapter 3.

9.4.4 Ensemble of ^1H Nuclei in a Magnetic Field

Consider now a sample containing many spin-1/2 particles.

The Hamiltonian $\mathbf{H}$ describing the system of N spins in a (low) magnetic field is given by [10]

$$\mathbf{H} = -B_0 \sum_{i=1}^{N} \gamma_i \mathbf{I_{zi}} + 2\pi \sum_{i=1}^{N} \sum_{j>i} J_{ij} \mathbf{I_i} \cdot \mathbf{I_j}, \tag{9.4.16}$$

where B_0 is the strength of the applied magnetic field[6] and J_{ij} is the J-coupling constant between spin i and spin j. $\mathbf{I_i}$ and $\mathbf{I_j}$ represent different spins in the sample[7].

It is importnt to note that in conventional high field NMR (9.4.16) is simplified by using the so-called "Secular Approximation" [2, 10]. In low field NMR, however, this simplification is not valid and the full Hamiltonian as stated in (9.4.16) must be used. The secular approximation therefore falls outside the scope of this thesis.

To simulate the ensemble of spins a mathematical tool called a density matrix is used. A density matrix is a mathematical construct that represents the statistical state of a quantum mechanical system [10]. It has a number of convenient properties which simplifies the tracking of the evolution of complex quantum systems as a function of time and is therefore well suited to simulate low-field NMR.

The density matrix is derived from the ensemble average of the states of the various particles in a system. The initial state of the density matrix is

[6] Here, again, assume the magnetic field is orrientated in the z-direction.

[7] The method of constructing these spin matrices is described in Appendix B

given as [10]

$$\rho(0) = \frac{e^{-\mathbf{H}/k_B T}}{\mathrm{Tr}\{e^{\mathbf{H}/k_B T}\}}, \tag{9.4.17}$$

where k_B is Boltzmann's constant, T is the temperature of the sample and $\mathrm{Tr}\{\ldots\}$ denotes the trace of a matrix.

By using the high-temperature approximation $|\mathbf{H}| \ll k_B T$, which holds for all temperatures above a few millikelvin, the initial state of the density matrix given in (9.4.17) can be simplified using a first order Taylor expansion to [10]

$$\begin{aligned} \rho(0) &= \frac{\mathbf{1} - \mathbf{H}/k_b T}{\mathrm{Tr}\{\mathbf{1} - \mathbf{H}/k_B T\}} \\ &= \frac{1}{2s+1}\left(\mathbf{1} - \frac{\mathbf{H}}{k_B T}\right), \end{aligned} \tag{9.4.18}$$

where $\mathbf{1}$ is the identity matrix and s is the spin quantum number of the nuclei in the system. This equation can be simplified even further if we neglect the first term (no matter how the system is perturbed the identity matrix will never give rise to an observable magnitization) and the scaling factor of the second term (we wish only to correctly represent the form of the simulated spectra and their relative peak hights) of the expansion given in (9.4.18). The density matrix therefore reduces to simply

$$\rho(0) \approx \mathbf{H}. \tag{9.4.19}$$

The initial value of the density matrix provides a starting point for the simulation of low-field NMR. This represents the thermal equilibrium value of the ensemble. In order to simulate an NMR spectrum, the density matrix has to be perturbed and evolved with time.

In a basic NMR experiment the sample is perturbed by applying an RF (or, in the case of low field NMR, ULF) magnetic pulse. As described in Chapter 3 this pulse is equivalent to rotating all the spins in the sample by a certain angle, ϕ. This is equivalent to rotating the density matrix by ϕ. This can be accomplished by sandwiching the density matrix between the rotation matrix in (9.4.15) and its adjoint[8]. If we assume that the rotation associated with the

[8]This rotates the density matrix by a angle ϕ about the x-axis. If other rotations are required, $\mathbf{R_x}$ can be substituted with $\mathbf{R_y}$ or $\mathbf{R_z}$ listed in Appendix B

RF (ULF) pulse is instantanious we find

$$\rho(0^+) = \mathbf{R_x}\rho(0)\mathbf{R_x}^\dagger. \tag{9.4.20}$$

This signals the start of the NMR experiment simulation.

In order to evolve the system for a time period δt after rotation we sandwich the density matrix between the evolution operator $\mathbf{U}(\delta t)$ and its adjoint. Therefore, to evolve the density matrix by $t = n(\delta t)$ the evolution operator is applied n times. Therefore

$$\rho(t) = \mathbf{U}(\delta t)\ldots\mathbf{U}(\delta t)\rho(0^+)\mathbf{U}^\dagger(\delta t)\ldots\mathbf{U}^\dagger(\delta t). \tag{9.4.21}$$

The evolution operator is given by [2, 10]

$$\mathbf{U}(\delta t) = e^{-\imath\mathbf{H}(\delta t)}. \tag{9.4.22}$$

The application of the rotation operator to the density matrix allows the NMR simulation to start, while successive application of the evolution operator allows the evolution of the density matrix to be tracked. The final mathematical tool needed to simulate an NMR experiment is a way to measure the magnitization. This can be accieved by exploiting one of the most powerful properties of the density matrix. By simply applying an observation operator to the density matrix and then taking the trace of the result one can perform a measurement on the system. We therefore have

$$\langle\mathbf{I_{obs}}\rangle = \mathrm{Tr}\{\mathbf{I_{obs}}\rho(t)\}, \tag{9.4.23}$$

where $\mathbf{I_{obs}}$ is the observation operator. In the simulation described here the projection of the spin onto the x-axis is required, therefore $\mathbf{I_{obs}}$ becomes

$$\mathbf{I_{obs}} = \sum_{n=1}^{N}(\mathbf{I_{xn}}), \tag{9.4.24}$$

where N is the number of spins in the ensemble[9]

[9]Actually, N represents the number of spins in the ensemble that we wish to observe. An example of a situation where a spin would not be observed is when a ^{13}C particle interacts with a ^1H particle. The ^{13}C particle will produce a J-coupling effect on the ^1H particle, but would not react to the RF (ULF) magnetic pulse or be observed in the final stage of

By using these methods, then, simulations of on an ensemble of interacting spins in a magnetic field can be done. Note that relaxation is neglected in these simulations.

To demonstrate these simulations an ensemble of non-interacting ^1H particles was simulated. In this simulation the Hamiltonian given in (9.4.16) reduces to

$$\mathbf{H} = -B_0 \sum_{i=1}^{N} \gamma_i \mathbf{I_{zi}} \tag{9.4.25}$$

because there are no J-coupling interactions between the particles.

In this simulation the evolution of the x-directed magnetization of an ensemble of six[10] spin-1/2 particles in a z-directed magnetic field with strength $50\mu T$ is investigated. Figure 9.24 shows the evolution of the x-directed magnitization after the ensemble has been rotated by $\pi/2$ radians around the x-axis, while Figure 9.25 shows the Fast Fourier Transform (FFT) of the measured signal. The x-directed magnitization oscillates sinusoidally at a frequency of $2128.9Hz$ as expected from the theory.

---

the experiment.

[10]These numerical simulations are very taxing on computer hardware, and simulations with more than 6 spins take a prohibitively long amount of time to complete.

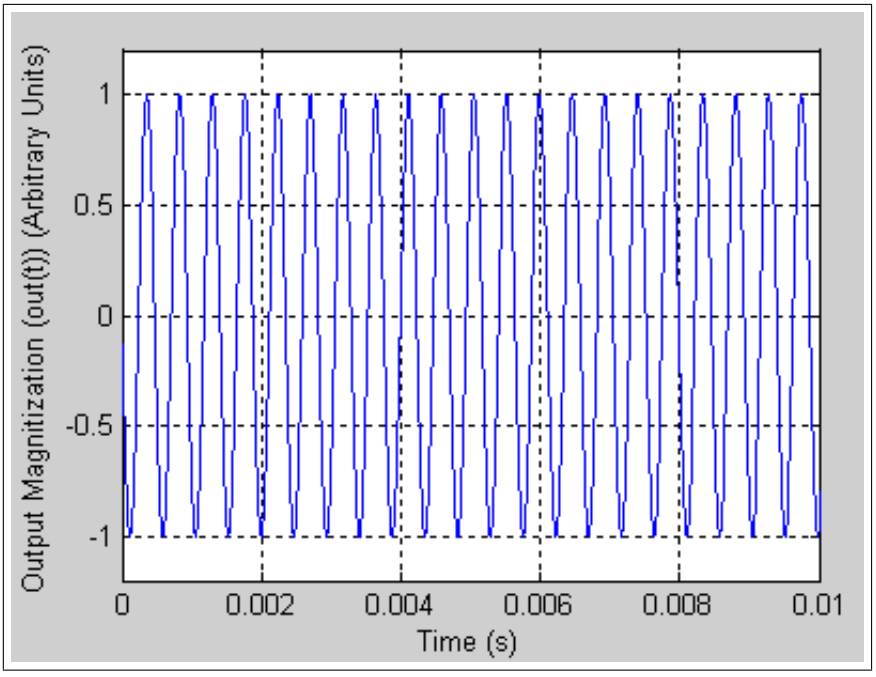

Figure 9.24: Simulation results of the traverse magnitization of an ensemble of 6 non-interacting spin-1/2 particles in a $50\mu T$ z-directed magnetic field.

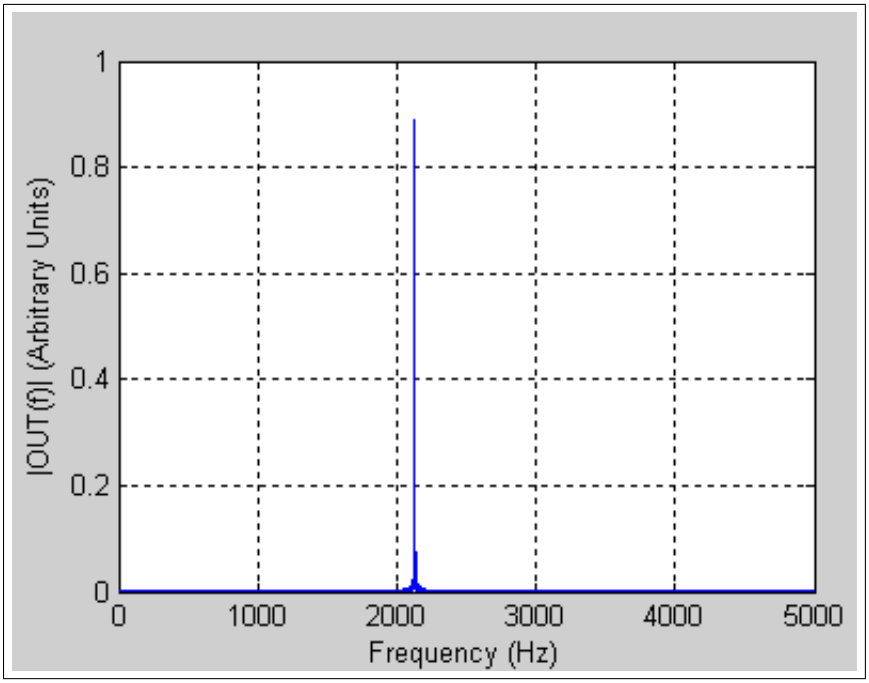

Figure 9.25: Simulation results showing the FFT of the traverse magnitization of an ensemble of 6 non-interacting spin-1/2 particles in a $50\mu T$ z-directed magnetic field.

The above simulation shows the expected result when measuring a sample where the spins do not interact with each other (i.e. there is no J-coupling)[11] for example in a sample of pure H_2O. If the spins do interact with each other, however, the J-coupling terms of (9.4.16) cannot be ignored as in (9.4.25), and the full Hamiltonian must be used. In this case the spectrum splits because of the J-coupling interaction.

We can use the process described above to simulate the results of a low-field NMR experiment on certain substances. Consider, for example, a molecule of dischloroacetaldehyde, shown in Figure 9.26.

[11] In low field NMR chemical shifts are negligible so it is ignored.

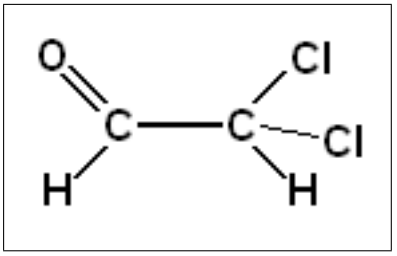

Figure 9.26: A dichloroacetaldehyde molecule.

This molecule has several isotopomers containing five types of magnetic spins: ^{1}H, ^{2}H, ^{13}C, ^{35}Cl and ^{37}Cl. ^{2}H and ^{13}C nuclei have low natural abundance, and we can therefore ignore these nuclei. Although the ^{35}Cl and ^{37}Cl nuclei are abundant, they have large electrical quadropole moments and relax rapidly. They can therefore also be ignored. We are left with only the ^{1}H nuclei [2]. These nuclei interact with each other through J-coupling. Their J-coupling constant is $J_{12} = 2.9Hz$ [2].

Figure 9.27 shows the simulated spectrum of dichloroacetaldehyde. It can clearly be seen that the peak at $2128.9Hz$ is split into two distinct peaks because of the J-coupling between the protons in the system. (This simulation is again done in a z-directed magnetic field of $50\mu T$.)

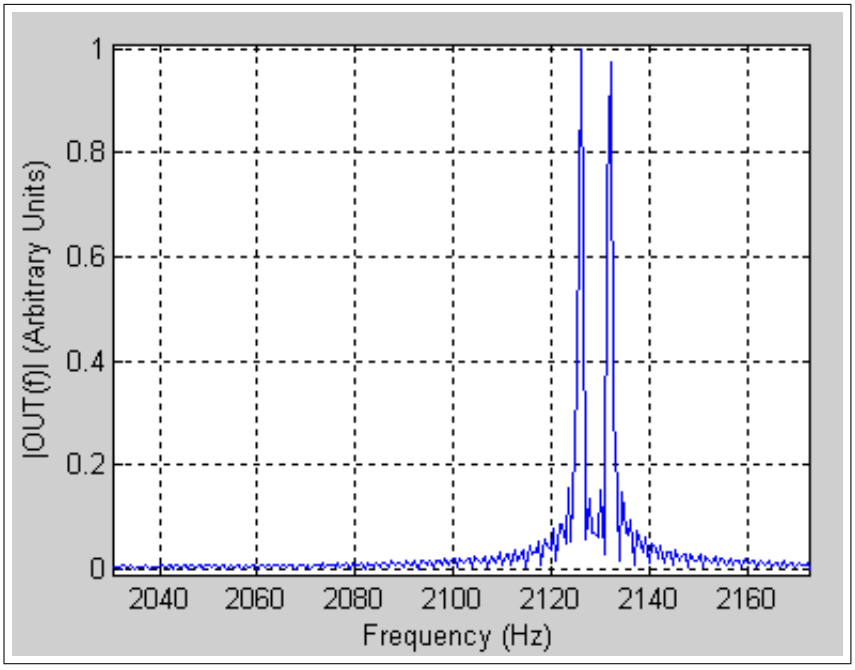

Figure 9.27: Simulation results showing the FFT of the traverse magnitization of an ensemble of 2 interacting spin-1/2 particles in a $50\mu T$ z-directed magnetic field. This is the simulated spectrum of dichloroacetaldehyde in a $50\mu T$ magnetic field.

Figure 9.29 shows the simulated spectrum of $2, 2, 2$-trifluoroethanol (shown in Figure 9.28) in a $53.9\mu T$ magnetic field, while Figure 9.30 shows a spectrum of $2, 2, 2$-trifluoroethanol that was obtained experimentally, as reported by [10]. Comparison of Figures 9.29 and 9.30 shows that the numerical simulations accurately predict the shape of the obtained spectrum.

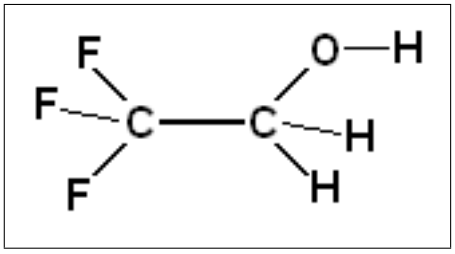

Figure 9.28: A $2, 2, 2$-trifluoroethanol molecule.

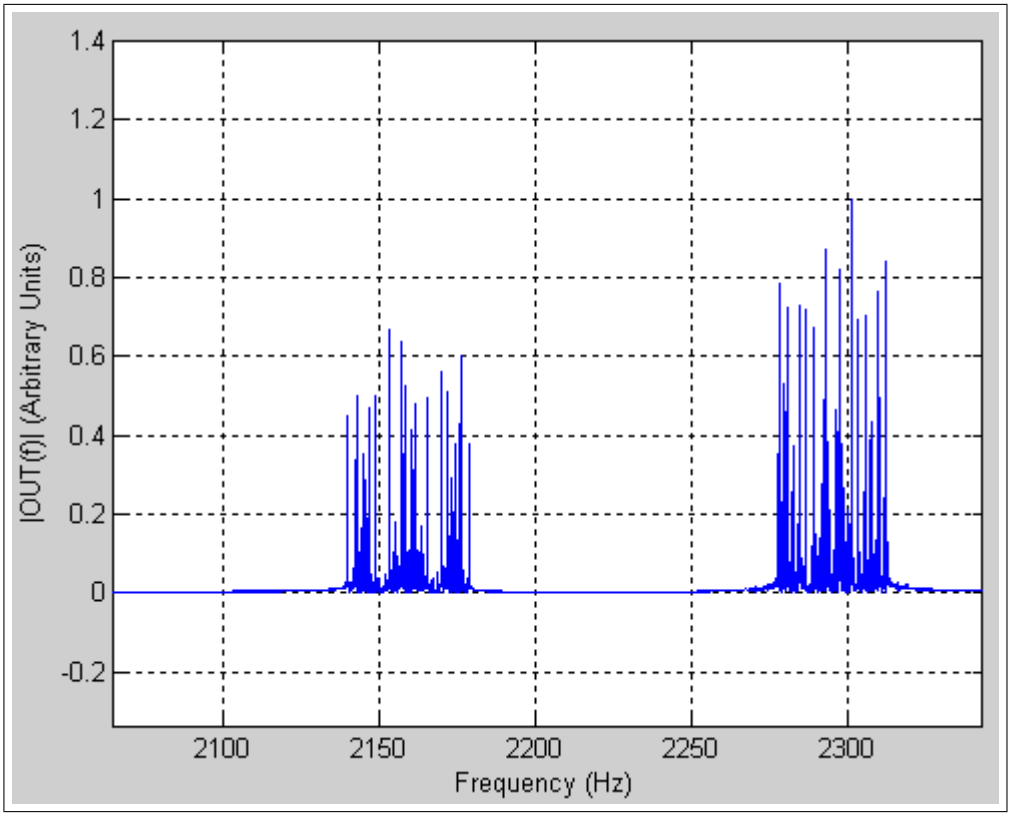

Figure 9.29: Simulation results showing the FFT of the traverse magnitization of an ensemble of 6 interacting spin-1/2 particles in a $53.9\mu T$ z-directed magnetic field. This is the simulated spectrum of $2,2,2$-trifluoroethanol in a $53.9\mu T$ magnetic field.

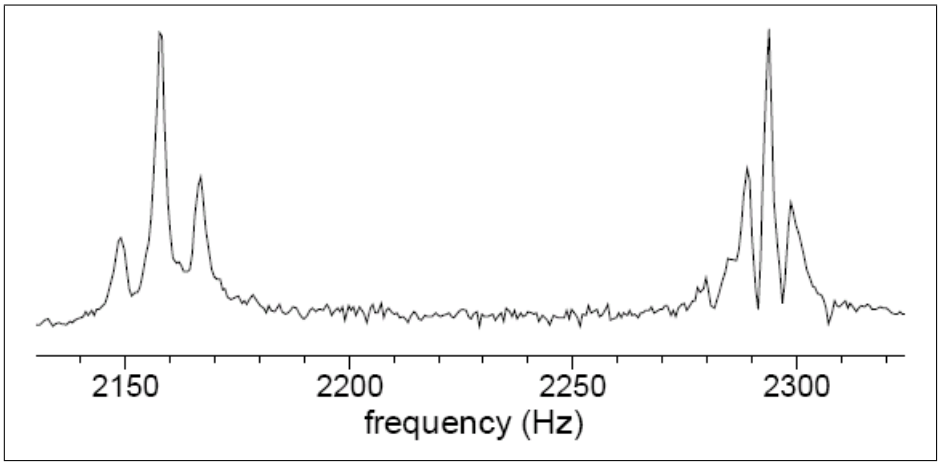

Figure 9.30: Experimentally obtained spectrum of $2,2,2$-trifluoroethanol in a $53.9\mu T$ magnetic field, as reported by [10].

Chapter 10

Design and Fabrication

10.1 Introduction

This chapter describes the design and fabrication of the SQUID detected NMR spectrometer undertaken in this study. The spectrometer consists of two main components - the SQUID and the NMR magnet setup. These components were designed using the theory, methods and techniques described in the previous chapters. This chapter also includes a section on the design and manufacture of a Flux Locked Loop.

10.2 SQUID Design and Manufacture

Using the theory and techniques described in Chapters 5 and 7 a SQUID was to be designed and manufactured to detect the NMR signals from a sample. For this process four $10 \times 10 \times 0.5mm$ $SrTiO_3$ bicrystal substrates were purchased from *MTI Crystal Inc.*. These bicrystals had a misorientation angle of $\theta = 36°$ and were polished on one side.

As these substrates are very expensive valuable practical experience with all the manufacturing techniques was built up before using the bicrystals by experimenting with much more inexpensive single crystal MgO substrates. Although Josephson junctions cannot be manufactured on these substrates[1] the goal was to gain experience in the manufacturing process without damaging

[1]Step-edge and bi-epitaxial junctions can be manufactured on these substrates, but require more than one deposition step, aren't very reproducible and are very difficult to manufacture and characterize. They were therefore not attempted here.

the more expensive substrates. Using the bicrystal substrates was attempted only after sufficient confidence in using the manufacturing machines was attained.

Around twenty attempts were made to create different structures on *MgO* substrates using ICM deposition to deposit YBCO, photolithography techniques to create a pattern on the substrate and argon-ion milling to etch the pattern into the YBCO. Contact pads were also deposited onto these test samples using thermal evaporation, and contact wires were bonded to these pads using ultrasonic bonding techniques in order to gain confidence in the procedures.

For all photolithography, the positive tone photoresist *ma-P1225* was used, along with the developer *ma-D331*, both manufactured by *Micro Resist Technology*. The ICM, argon-ion mill and thermal evaporator are all in-house built devices. The wire-bonder used is a *West-Bond Model 7400A* ultrasonic wire bonder.

As discussed in Chapter 7 the first step in the fabrication process involves depositing a layer of YBCO onto the substrate. To start the deposition a strong vacuum was created around the YBCO target and the substrate in the ICM. A vacuum of below $20\mu inHg$ is recommended. A mixture of oxygen and argon was then introduced into the chamber. The gasses were mixed with a ratio of $1:1$. After the gasses were added, the pressure inside the chamber was about $200\mu inHg$. The oxygen was introduced to ensure that the deposited YBCO grew with the desired crystal structure so as to be superconducting. After the gasses were introduced the substrate was heated to $780°C$ and left at this temperature for 1.5 hours. This was done to ensure that all contaminants in the chamber had been evaporated before deposition. After this step, the substrate was cooled to $740°C$. Once the substrate was at this temperature a large voltage was applied across the target (around $200V$). This voltage ignited the plasma. Once the plasma was ignited, the current supplied to the ICM could be varied. For the deposition done the current was set such that around $70W$ of energy was supplied to the plasma. YBCO was deposited under these conditions for 75 minutes. After the deposition, the plasma was dissipated and the substrate was cooled to $460°C$. During the cooling the vacuum was switched off and the chamber was flooded with oxygen. This was done to anneal the deposited YBCO so as to ensure the correct crystal structure of the

film. The substrate was left at $460°C$ for 30 minutes in an oxygen atmosphere. After the annealing step the substrate was left to cool down.

After the substrate had cooled, a layer of photoresist was deposited onto it. Photoresist was spun onto the sample at $4000rpm$ for $15s$, yielding a thickness of about $1.5\mu m$. After this the sample was baked on a hotplate at $115°C$ for one minute. It was then exposed to UV light through a chrome mask for $30s$ and developed, leaving the pattern on th chrome mask etched into the photoresist. The substrate was then baked again on a hotplate at $115°C$, this time for 5 minutes, to harden the photoresist.

The substrate was then milled using an argon-ion mill to remove the YBCO not covered by photoresist. The milling of the substrate is a dry-etching technique. The substrate was milled for about 45 minutes, with the machine regularly turned off and the progress checked. This was done to ensure that the substrate wasn't over-milled and that the plasma did not burn the photoresist causing it to bubble and create uneven structures.

After milling the remaining photoresist was removed using acetone.

During the preliminary tests it was determined that the heating element in the ICM could be improved. The old element required the substrate to be adhered to it using silver conductive paste to ensure even heating. This often led to substrates being broken when they were to be removed. The silver paste was also difficult to clean off the substrates.

An improved heating element was therefore designed and fabricated. This heating element was designed with a small stainless steel weight that could clamp the substrate onto the heating element in order to ensure even heating of the substrate. The clamp was designed in such a way as to keep YBCO from being deposited onto the sides of the substrate, ensuring that the bicrystal line of bicrystal substrates could be visible after deposition.

Figure 10.1 shows a photograph of the new heating element.

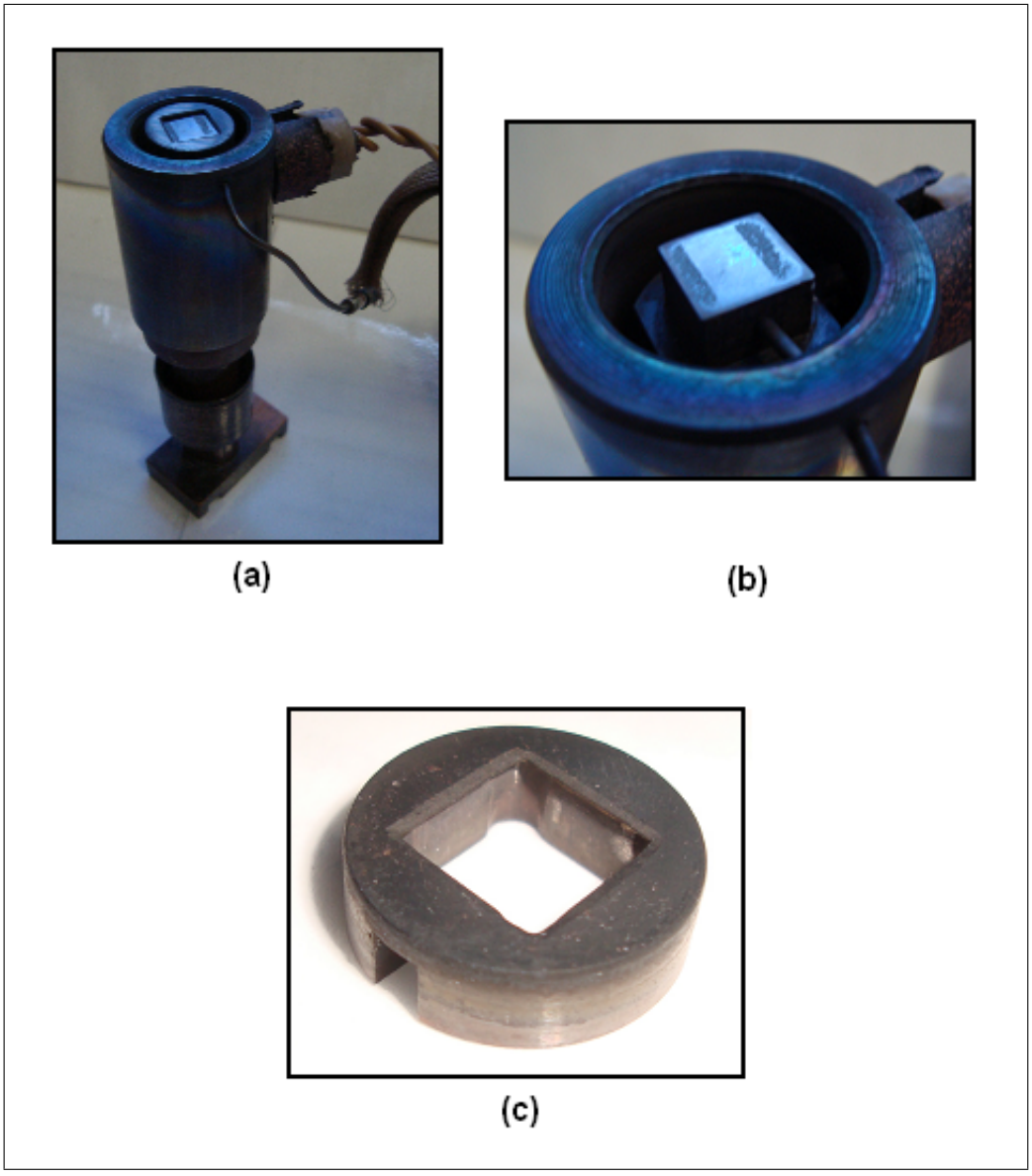

Figure 10.1: New heating element for the ICM at the Department of Electrical and Electronic Engineering at the University of Stellenbosch. (a) New heating element. (b) Close-up of sample holder on heating element. (c) Close-up of sample clamp.

The critical current of the Josephson junctions in a DC SQUID is a critical parameter and needs to be known in order for a DC SQUID to be designed properly. Unfortunately it is impossible to predict the critical current, and a physical characterization step has to be performed. As such it was decided to use two of the four bicrystal substrates to manufacture Josephson junctions.

A mask of a design with 10 Josephson junctions with line widths ranging from $2\mu m$ to $10\mu m$ was available and was used for this process.

When using bicrystals it is important to align the mask accurately before the sample is exposed to UV light so as to ensure that the Josephson junction structures are fabricated over the bicrystal line. The bicrystal line, however, is difficult to see, and cannot be seen through the deposited YBCO. To see the bicrystal line a light illuminates the substrate from the side. Care must be taken to ensure that the light irradiating the sample does not contain UV wavelengths that can react with the photoresist. The light source must illuminate the sample from the side because the bicrystal line does not reflect light incident perpendicular to the substrate (see Figure 10.2).

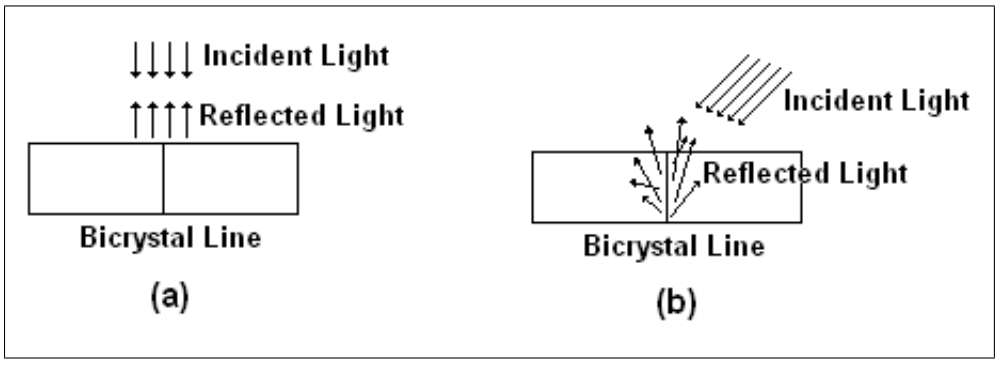

Figure 10.2: Light incident on a bicrystal line. (a) Light incident perpendicular to the bicrystal line is not reflected by the bicrystal line, and the bicrystal line is therefore invisible. (b) Light incident at a angle is scattered by the bicrystal line, making it visible.

Alignment marks on the chrome mask allows the mask to be perfectly aligned.

The fabrication process for the first junction structure on an $SrTiO_3$ bicrystal substrate was successful, resulting in the structures shown in Figure 10.3[2].

[2]Note that the contact wires had broken off during testing before this photograph was taken. They are therefore not visible in this photograph.

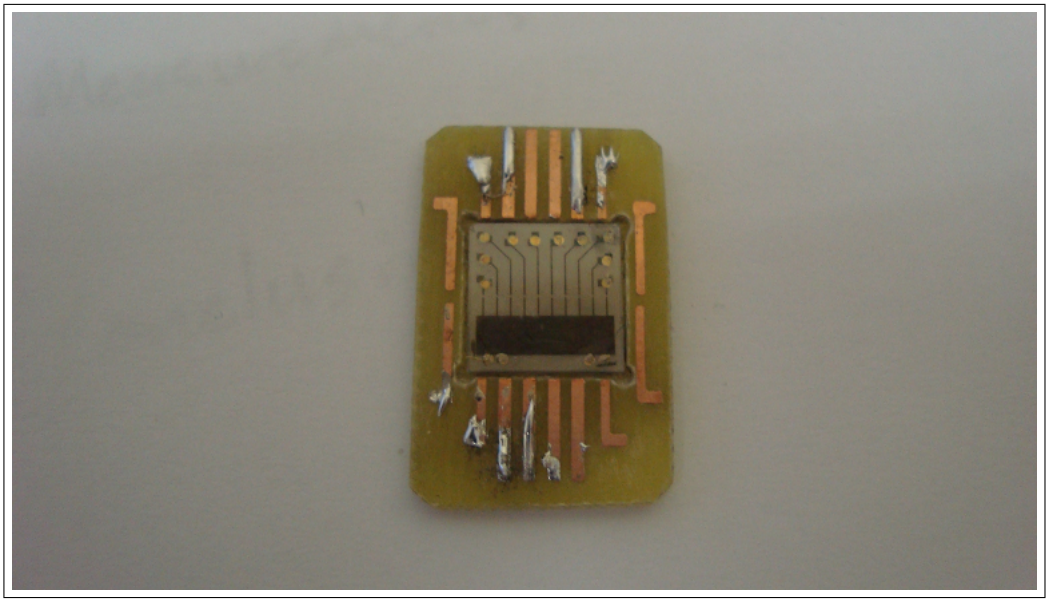

Figure 10.3: Fabricated Josephson junctions on a $SrTiO_3$ bicrystal mounted on a PCB.

These structures, however, did not show Josephson behaviour. Indeed, further testing revealed that these structures had lost their superconducting ability. The cause of this failure was determined to be ion damage to the YBCO crystal structure caused by the argon-ion milling process.

Another attempt was made to fabricate Josephson junctions on an $SrTiO_3$ bicrystal substrate, this time using a small device to periodically shield the substrate during milling, thus causing less damage to the YBCO crystal. Unfortunately an accident during the development phase of the photolithographic process saw the substrate being exposed to water, destroying the YBCO layer.

As two of the available four substrates had been used, it was decided to abandon the characterization of the Josephson junctions and the design of a new DC SQUID and rather fabricate a SQUID that had previously been designed at the University of Stellenbosch. A SQUID designed by F. W. Graser [6] was to be fabricated. From the fabricated SQUID the critical parameters could be measured and used to design the flux locked loop.

Unfortunately both attempts to create a SQUID were unsuccessful. During the first attempt an accident during the photolithography process caused the photoresist to be uneven. This was realized too late and caused the sample to mill unevenly. The second attempt was thwarted by a malfunction of the ICM

during deposition causing a non-superconducting layer to be deposited onto the substrate. Repeated annealing steps to try and reclaim superconductivity from the layer had no effect.

With all four substrates destroyed the goal of fabricating a working DC SQUID became unachievable at this point in time.

Another avenue was sought. The University of Stellenbosch was in possession of a commercially purchased DC SQUID. The *M1000* high-T_c magnetometer manufactured by *Star Cryoelectronics* has many features that make it attractive for this application[3]. It features low rms field noise (better than $100fT/Hz^{1/2}$) and is hermetically sealed protecting the sensitive YBCO layer from degradation.

A flux locked loop was designed for the *M1000* using the theory developed in Chapter 6. This design can be found in Section 10.4.

Unfortunately it was discovered that the *M1000* SQUID purchased by the University of Stellenbosch was in the so-called *M19* package and not the *Button* package, and therefore did not have a feedback loop. The designed FLL could therefore not be used with the SQUID.

10.3 NMR Spectrometer Design and Manufacture

The NMR spectrometer consists of two electromagnets that generate magnetic fields as shown in Figure 8.4. To accomplish this the magnets are arranged in Helmholtz pairs, as shown schematically in Figure 10.4, to produce homogeneous magnetic fields. The two Helmholtz pairs are arranged so that the magnetic fields are perpendicular to each other. A coil is placed in the centre of these electromagnets, with its radial axis in the same plane as the perpendicular magnetic fields. In other words, the two Helmholtz pairs produce magnetic fields in the x- and y-directions, and the coil measures the magnetization in the z-direction. The measurement coil is connected to another coil that is magnetically coupled to the SQUID sensor. This is done so that the sensitive SQUID device is removed from the strong magnetic fields developed by the electromagnets.

[3]The datasheet for the *M1000* can be found in Appendix E.

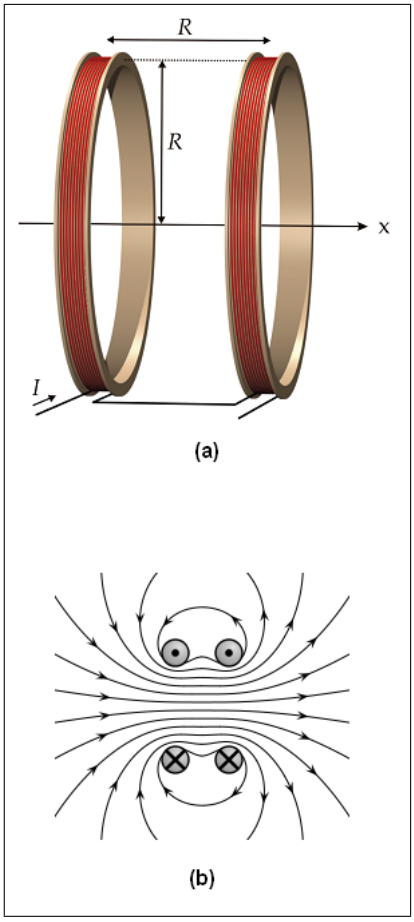

Figure 10.4: A Helmholtz pair. (a) Physical construction. [11] (b) Generated magnetic field. [12]

The Department of Electrical and Electronic Engineering at the University of Stellenbosch was in possession of two electromagnets in Helmholtz pair configuration used in previous work. These magnets, shown in Figures 10.5 and 10.6 are ideal for this application[4].

[4]These magnets are actually too large for this application, but the purpose of this study was to show the feasibility of SQUID detected NMR, and these magnets provide an excellent starting point for a prototype machine.

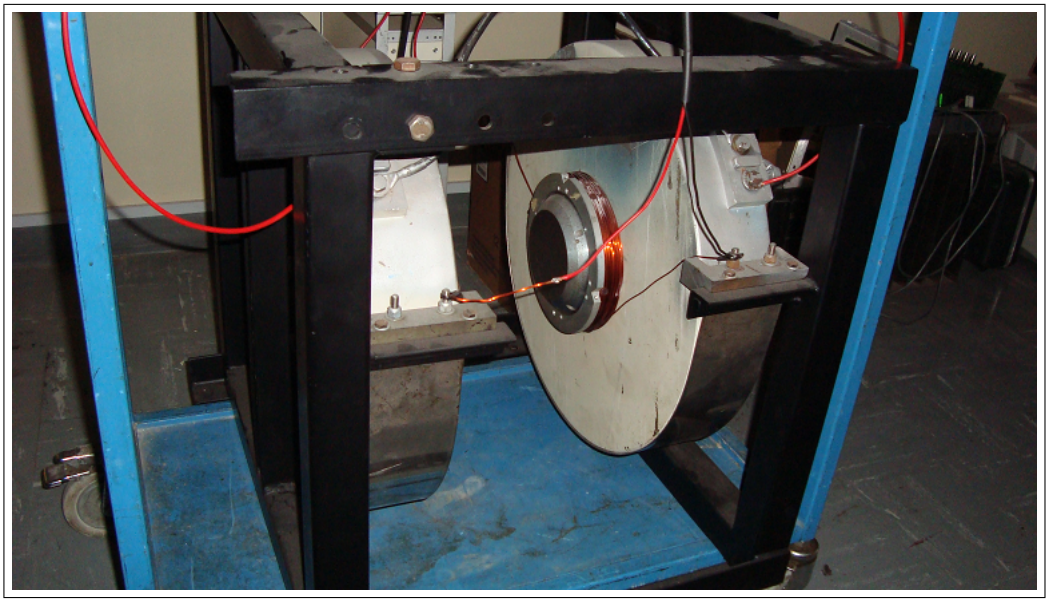

Figure 10.5: Electromagnet in Helmholtz pair configuration for x-directed magnetic field.

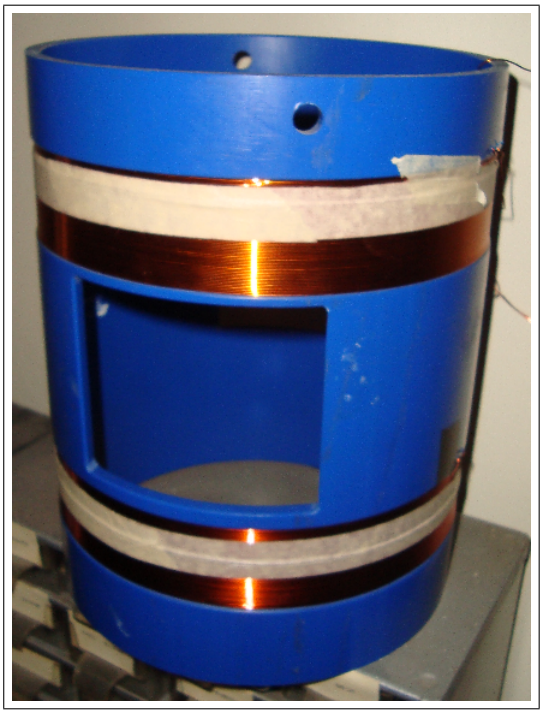

Figure 10.6: Electromagnet in Helmholtz pair configuration for y-directed magnetic field.

These magnets were wired to power supplies and measurements were done on them using a Hall probe in order to determine the strength of each magnetic field. From the measurements it was determined that the first Helmholtz pair (pictured in Figure 10.5) produced a magnetic field of strength $1mT$ for each $0.267A$ applied to it. The first Helmholtz pair was to be used as the pre-polorizing magnetic field, and as such needed to have quite a strong magnetic field. A magnetic field strength of $45mT$ was chosen for the magnet, meaning that it would require $12A$ flowing through it.

The measurements also determined that the second Helmholtz pair (pictured in Figure 10.6) needed $0.5\mu A$ flowing through it for each $1\mu T$ produced. This coil was to be the measurement field, and as such required a much weaker magnetic field than that of the pre-polorizing field. A magnetic field strength of $200\mu T$ was chosen for the measurement field.

Finally, the RF (ULF in the case of low-field NMR) field was also needed in order to rotate the spins in the sample and cause the sample's magnetization to rotate in the x-z-plane. The first Helmholtz pair is again used for this purpose. The pulse has to have a frequency of (from (3.3.3)) $f = (200 \times 10^{-6})(267.522 \times 10^{6})/(2\pi) = 8.52kHz$.

The magnets need to be switched on and off at the correct times. In order to accomplish this a control board was designed and built. Figures 10.7 and 10.8 shows the schematic of the control board, while Figure 10.9 shows the completed control board.

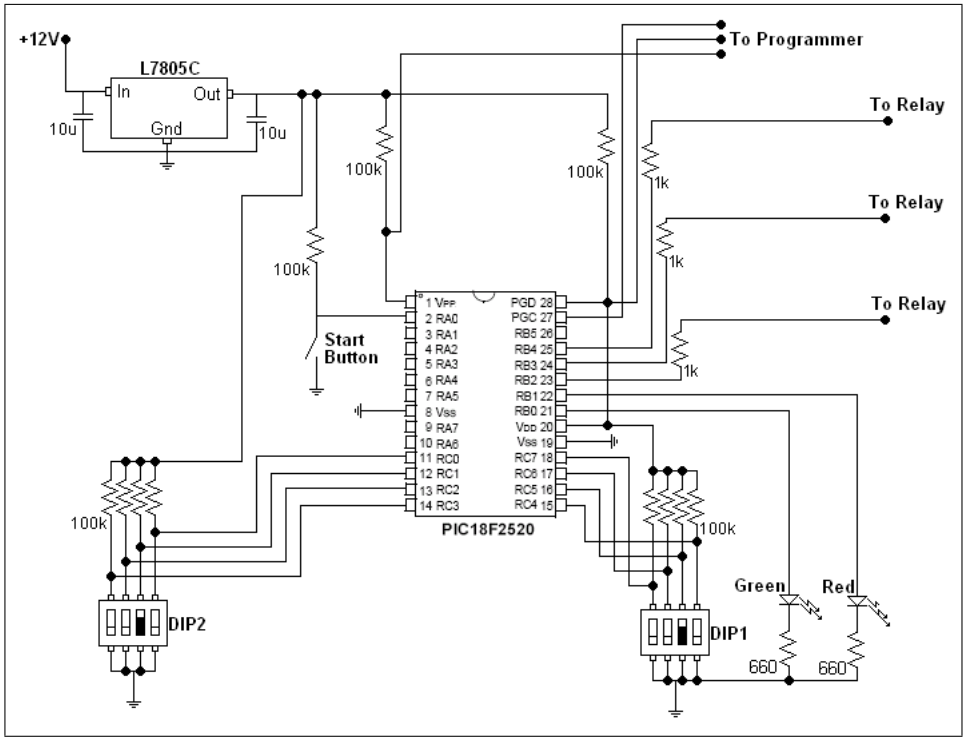

Figure 10.7: Schematic for the control board for the NMR spectrometer.

The control board uses a *PIC18F2520* processor[5] manufactured by *Microchip*. The control board works off a $12V$ power supply and switches three relay switches in the correct order. Two large relays with $15A$ ratings (labelled "A" in Figure 10.9) control the current to the first Helmholtz pair (pictured if Figure 10.5) and a smaller relay (labelled "B" in Figure 10.9) controls the connection between the pickup coil and the SQUID input coil.

[5]For the datasheet, see Appendix E.

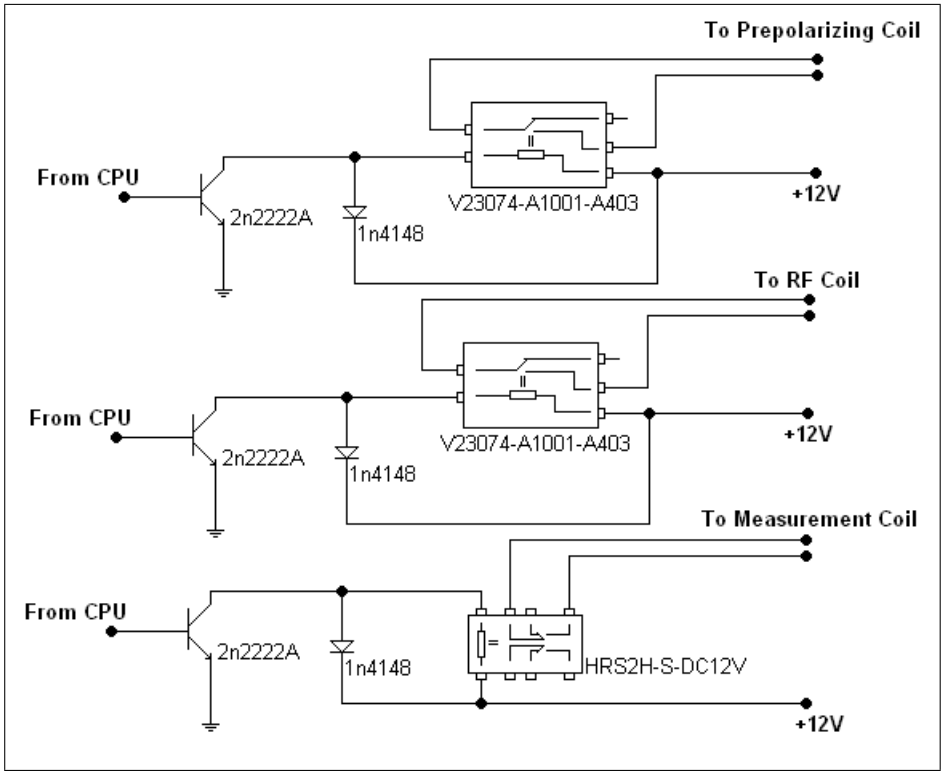

Figure 10.8: Schematic of relay connections on control board.

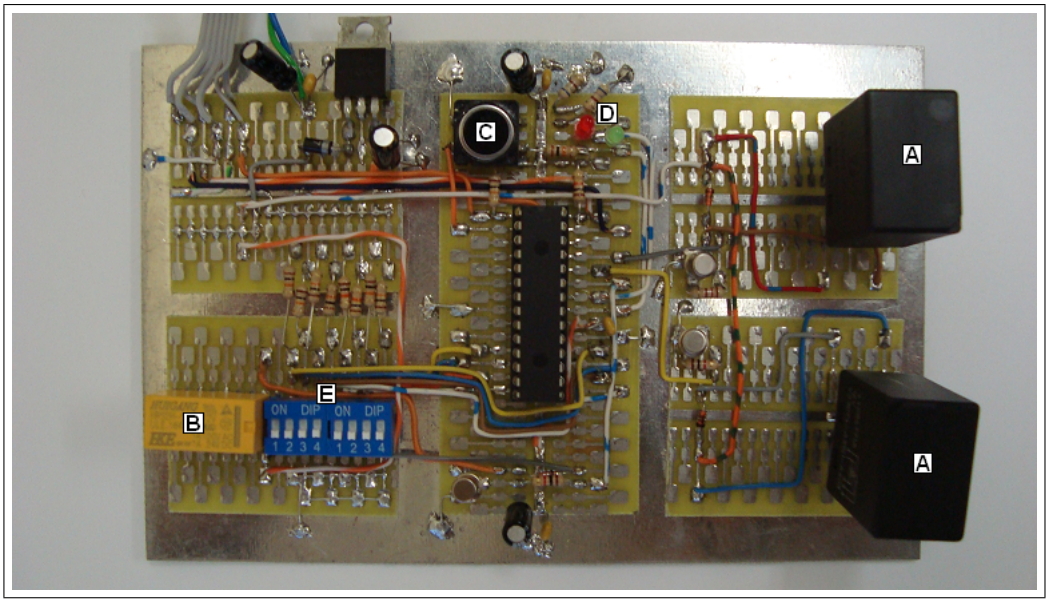

Figure 10.9: Control board for NMR spectrometer.

The control board is programmed to execute the pre-programmed experimental procedure a certain amount of times when the button (labelled "C" in Figure 10.9) is pressed. Two LEDs (labelled "D" in Figure 10.9) indicate the current status of the program. A red LED indicates that an experiment is underway and a green LED signals that the board is ready to execute an experiment.

The amount of times the experiment program runs is determined by two DIP switches (labelled "E" in Figure 10.9). The DIP switches can be seen as a byte representing a number between 0 and 255. Each switch corresponds to a bit in the byte (switch 4 on the right package represents the least significant bit while switch 1 on the left package represents the most significant bit). The number of times the experiment program executes equals the number read from the DIP switches when the button ("C") is pressed, plus one. Therefore, if the DIP switch reads 0 (as would be the case in Figure 10.9) when the button is pressed, the program executes once.

The processor was programmed to execute the experiment more than once so that signal averaging could be used if the one-shot experiment yielded excessively noisy results.

The processor was programmed in *C* using *Microchip's MPLab* [120] and the *MCC18* compiler [121], together with a *PICkit 2* programmer. The program is listed in Appendix D.

Pseudo code for the experiment algorithm is shown in Figure 10.10.

In order to read out the signal from the SQUID a A/D converter is also required. For this study a $LabJackU6$ system was to be used.

```
//Repeat forever:
//Note that the measurement field is always on and never has to be switched.

If button is pressed:
      1.    Turn off green LED.
      2.    Turn on red LED.
      3.    Read number off DIP switches. (int num)
      4.    Repeat num times:
            i.    Switch relay controlling prepolarizing magnet on.
            ii.   Wait for 10s.      //Prepolarizze the sample
            iii.  Switch relay controlling prepolarizing magnet off.
            iv.   Wait for 0.5s
            v.    Switch relay controlling RF magnet on.
            vi.   Wait for 1s.       //Irradiate the sample with sinusoidal magnetic field.
            vii.  Switch relay controlling RF magnet off.
            viii. Wait for 0.1s.
            ix.   Switch relay controlling pickup coil on.
            x.    Wait for 5s.       //measurement is done in this time
            xi.   Switch relay controlling pickup coil off.
            xii.  Wait for 10s.      //Delay to ensure sample completely relaxes
                                     //    before next measurement cycle
      5.    Trun off red LED.
      6.    Turn on green LED.
```

Figure 10.10: Pseudo code for experiment algorithm.

10.4 Design of a Flux Locked Loop

In this section the design, simulation and fabrication of a flux locked loop is described. The FLL is designed for the *M1000* high-T_c magnetometer manufactured by *Star Cryoelectronics*. The design follows the theory developed in Chapter 6. All datasheets are given in Appendix E.

10.4.1 Design

The FLL is designed to use a direct readout scheme, so no matching circuit is required. Figure 10.11 shows the basic layout of the FLL.

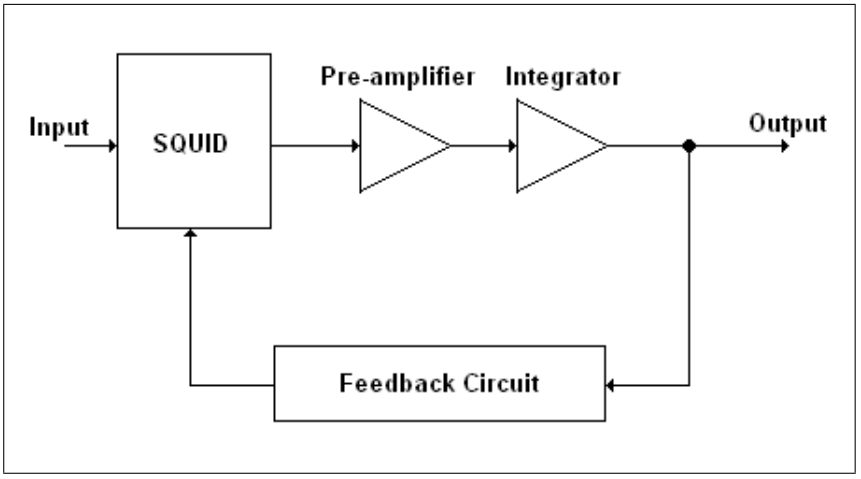

Figure 10.11: Basic layout of flux locked loop.

From (6.4.3) we have that the gain of the SQUID is given by

$$G_{SQ} = \frac{M_f}{R_f} V_\Phi, \tag{10.4.1}$$

where R_f is the resistance of the feedback circuit and M_f is the mutual inductance between the feedback inductor and the SQUID loop, given by the familiar equation

$$M_f = k\sqrt{L_f L_{SQ}}, \tag{10.4.2}$$

with L_f the feedback inductance, L_{SQ} the SQUID loop inductance and k the coupling constant between the two.

(10.4.1) simplifies (using the fact that at the optimum working point $V_\Phi = 2V_c/\Phi_0$) as follows:

$$\begin{aligned} G_{SQ} &= \frac{M_f}{R_f} V_\Phi \\ &= \frac{M_f}{R_f} \frac{2V_c}{\Phi_0} \\ &= \frac{M_f}{R_f} \frac{2I_c R_n}{\Phi_0} \\ &= \frac{M_f}{R_f} \frac{200 \times 10^{-6}}{\Phi_0}, \end{aligned} \tag{10.4.3}$$

where I_c is the critical current of the Josephson junctions in the SQUID (obtained from the datasheet as $I_c = 10\mu A$), R_n is the normal state resistance of the Josephson junctions in the SQUID (obtained from the datasheet as $R_n = 10\Omega$), $V_c = I_c R_n$, and Φ_0 is the magnetic flux quantum.

The gain of the pre-amplifier is [37]

$$\begin{aligned} A &= \frac{1}{G_{SQ}} \\ &= \frac{\Phi_0}{200 \times 10^{-6}} \frac{R_f}{M_f}. \end{aligned} \tag{10.4.4}$$

To work out the value of R_f/M_f we inspect the feedback electronics, consisting of a resistor R_f in series with a inductor L_f. L_f couples with the SQUID loop with a mutual inductance M_f. The feedback electronics are shown in Figure 10.12.

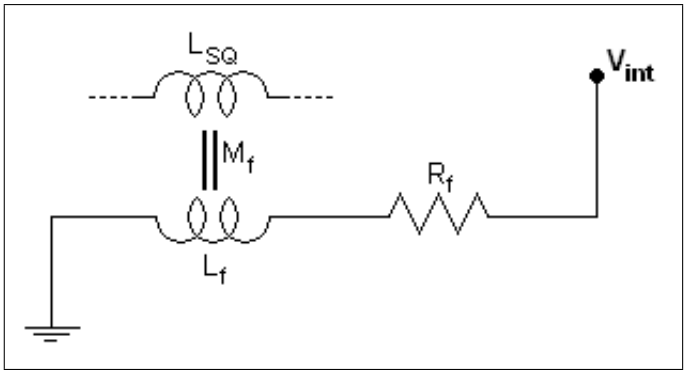

Figure 10.12: Flux locked loop feedback electronics.

From Figure 10.12 we find (assuming the impedance of L_f is negligible)

$$V_{int} - I_f R_f = 0, \tag{10.4.5}$$

where V_{int} is the voltage at the output of the integrator and I_f is the current flowing through the feedback loop. We therefore have

$$V_{int} = I_f R_f. \tag{10.4.6}$$

But, if Φ_f is the flux threading the SQUID loop due to L_f, we have

$$I_f = \frac{\Phi_f}{M_f}. \tag{10.4.7}$$

Therefore,

$$V_{int} = \frac{\Phi_f}{M_f} R_f = \Phi_f \frac{R_f}{M_f}. \tag{10.4.8}$$

This design uses a $\pm 5V$ power supply. We therefore design for the maximum value of V_{int} to be $4.5V$ We also choose the measurement range of the SQUID to be $1000\Phi_0$, so between $-500\Phi_0$ and $500\Phi_0$. (10.4.8) therefore yields

$$4.5 = 500\Phi_0 \frac{R_f}{M_f}. \tag{10.4.9}$$

Therefore

$$\frac{R_f}{M_f} = \frac{9 \times 10^{-3}}{\Phi_0}. \tag{10.4.10}$$

From the datasheet we find $1/M_f = 7\Phi_0/\mu A$. Therefore, the feedback resistor is found to have a value of $R_f = 1.2857 k\Omega$, and backward substitution yields the gain of the pre-amplifier to be $A = 45$.

For the amplifier we choose a standard non-inverting configuration, as shown in Figure 10.13.

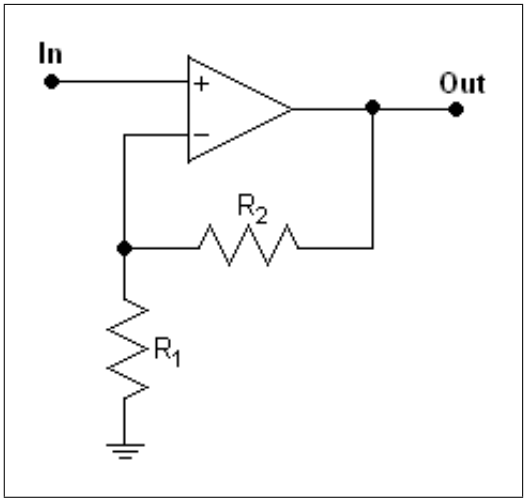

Figure 10.13: Schematic of the flux locked loop pre-amplifier design.

The non-inverting amplifier shown in Figure 10.13 has a voltage gain of

$$G = \frac{V_{out}}{V_{in}} = \frac{R_1 + R_2}{R_1}. \tag{10.4.11}$$

Choosing $R_1 = 100\Omega$, R_2 is required to be $4.4k\Omega$ for a pre-amplifier gain of 45.

The final step is to design an integrator. We choose a simple op-amp current integrator design, shown in Figure 10.14.

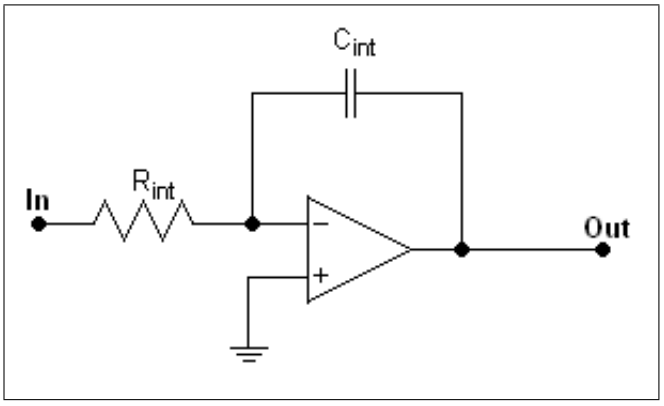

Figure 10.14: Schematic of the flux locked loop integrator design.

We design the integrator to have a unity-gain frequency f_1 of $80MHz$.

Therefore

$$f_1 = \frac{1}{2\pi R_{int} C_{int}} = 80 \times 10^6. \tag{10.4.12}$$

Choosing $R_{int} = 100\Omega$ yields $C_{int} = 20pF$.

The full design is shown in Figure 10.15

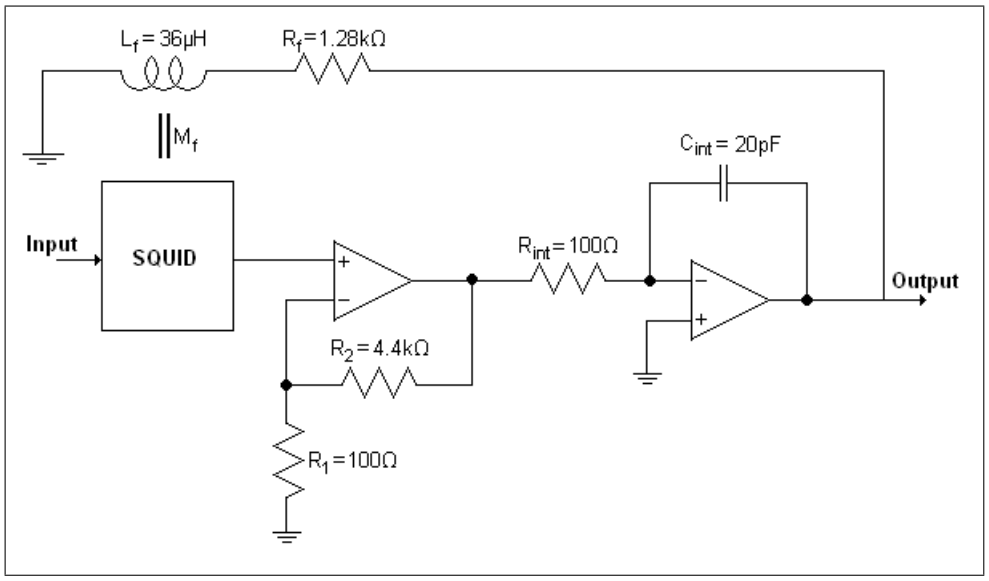

Figure 10.15: Schematic of the full flux locked loop design.

10.4.2 Simulation

In order to simulate the FLL we again use the *SPICE* model of a SQUID developed in Chapter 9. This model, however, has to be modified slightly. The simulated SQUID has a voltage sensitivity of $V_\Phi = 200mV_c/\Phi_0$, so the pre-amplifier gain has to be adjusted to $A = 450$.

The feedback inductances (again split into two equal inductances of $18\mu H$) couple to the SQUID inductances with a coupling factor of $k = 1$. The value of M_f, and therefore of R_f, has to be adjusted to compensate. For a coupling constant of $k = 1$ the mutual inductance between the feedback inductance and the SQUID inductance becomes $M_f = 29.505 \times 10^6(\Psi_0/A)$, so that the feedback resistor becomes $R_f = 294.47k\Omega$.

The op-amps are implemented with ideal voltage-controlled voltage sources in order to increase the speed of simulation.

Figure 10.16 shows the *SPICE* model used to simulate the FLL.

Figure 10.17 shows the output of the FLL when the input flux is swept from 0 to $+\Psi_0$, and then down to $-\Psi_0$. This confirms the linearizing behaviour of the FLL. Figure 10.18 shows the response of the FLL to a sinusoidal flux input with an amplitude of Φ_0 and a $10MHz$ frequency, while Figure 10.19 shows the response of the FLL to a sinusoidal flux input with an amplitude of Φ_0 and a $50MHz$ frequency. These simulations confirm that the FLL allows the SQUID to act as a linear flux-to-voltage transformer. The final simulation results, shown in Figure 10.20 show the response of the FLL to a sinusoidal flux input with an amplitude of $10\Phi_0$ and a $10MHz$ frequency. The FLL does not have the slew rate required to "keep up" at this frequency, and the output signal is distorted.

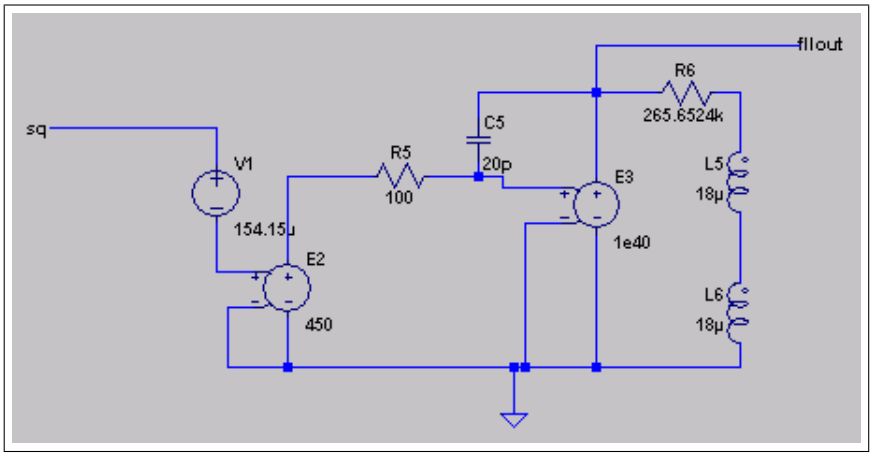

Figure 10.16: *SPICE* model used for the simulation of the FLL.

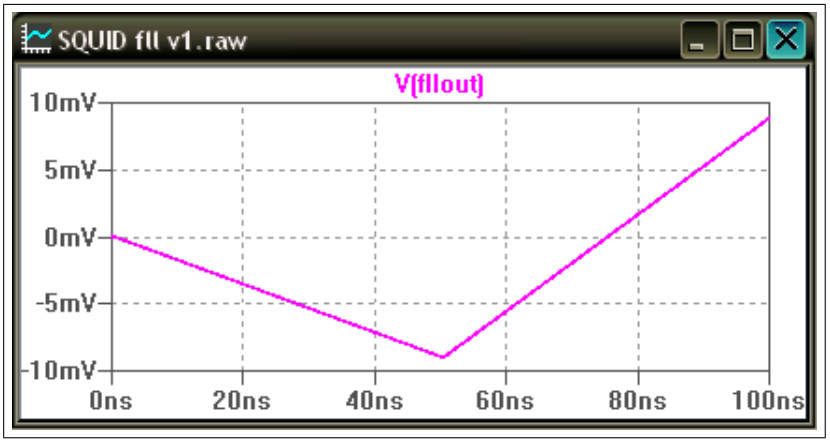

Figure 10.17: Simulation results of FLL with the input flux of the SQUID linearly varied between 0 and Φ_0, and then to $-\Psi_0$.

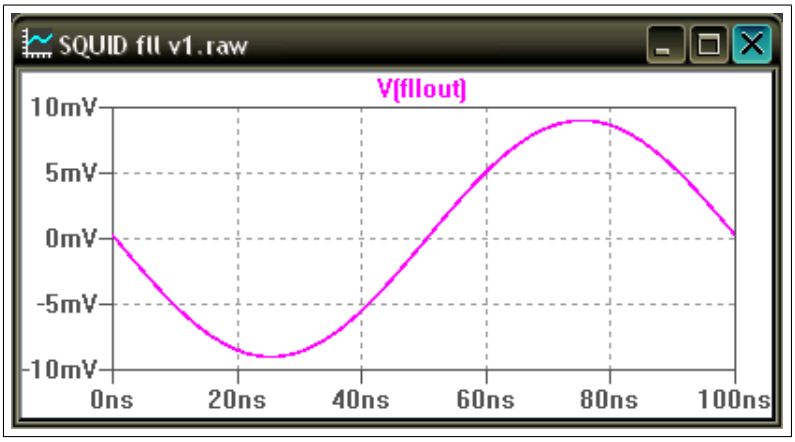

Figure 10.18: Simulation results of FLL with the input flux of the SQUID a sinusoidal signal with an amplitude of Φ_0 and a $10MHz$ frequency.

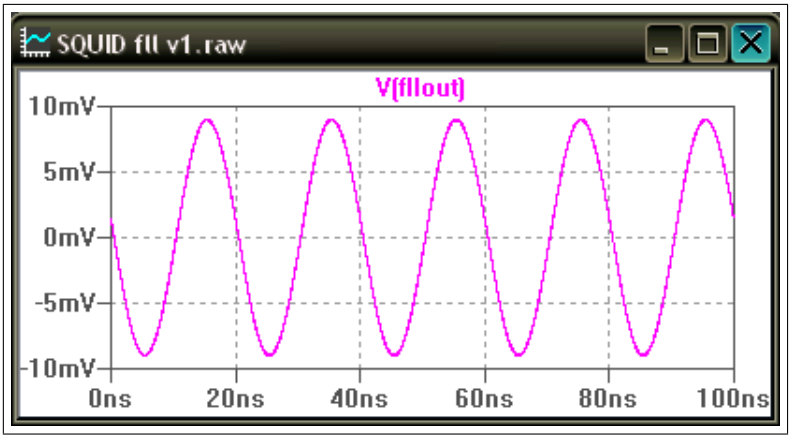

Figure 10.19: Simulation results of FLL with the input flux of the SQUID a sinusoidal signal with an amplitude of Φ_0 and a $50MHz$ frequency.

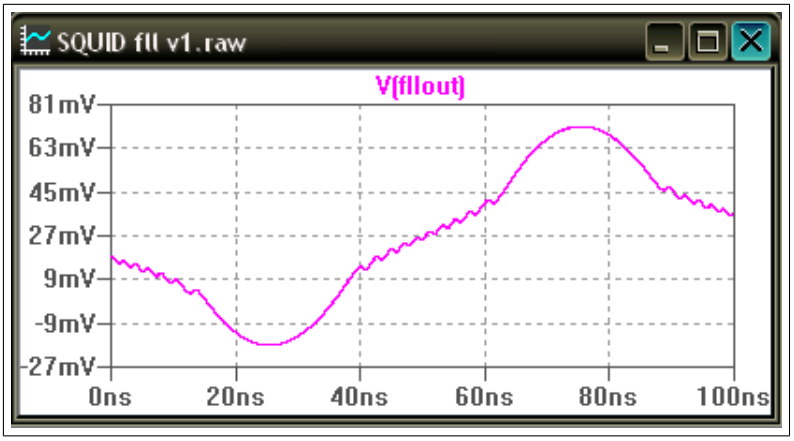

Figure 10.20: Simulation results of FLL with the input flux of the SQUID a sinusoidal signal with an amplitude of $10\Phi_0$ and a $10MHz$ frequency.

10.4.3 Fabrication

The choice of op-amp is very important in the fabrication of the FLL. Op-amps with high slew-rates, high GBW, low noise characteristics and low input bias currents so as not to load the SQUID are required. For this study, the *OPA657* op-amp was chosen[6]. This op-amp has a slew rate of 700 (for a $1V$ step), a very high GBW of $1.6GHz$ and low noise characteristics of $4.8nV/H\sqrt{Hz}$ voltage

[6]Refer to Appendix E for the datasheet.

noise and $1.3 \times 10^{-3} pA/\sqrt{Hz}$ current noise. This op-amp is also a FET-type op-amp, meaning it has a very low input bias current ($20 \times 10^{-6} \mu A$).

Figure 10.21 shows a photograph of a complete FLL. There are three potentiometers visible. These vary the pre-amplifier op-amp offset voltage, the integrator offset voltage and the pre-amplifier gain. For the FLL pictured the pre-amplifier gain can be varied between 45 and 4500. The FLL runs off a $\pm 5V$ power source.

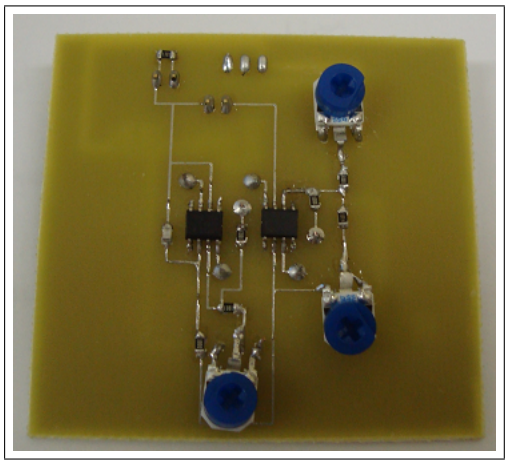

Figure 10.21: Fabricated FLL.

Chapter 11

Measurements and Results

11.1 Introduction

In this chapter the techniques used for measurements on SQUIDs and Josephson junctions are described. The results of the theory, design, simulation, fabrication, and measurements are also given.

11.2 Cryogenic Cooling and the Measurement of Superconductive Properties

For Josephson junctions and SQUIDs to operate they need to be cooled to below the material's critical temperature. For YBCO, this temperature is around 93 kelvin. This temperature is above the boiling point of liquid nitrogen. As such, devices fabricated from YBCO can be submerged into a liquid nitrogen bath for operation.

This technique is simple, but does suffer a few problems. The rapid cooling of the sample associated with immersing it in a bath of liquid nitrogen can cause the contact wires to break off, or the sample to dislodge from the circuit board. Furthermore, water reacts with YBCO, causing it to lose its superconductive properties, meaning that ice crystals forming on a sample when removing the sample from the nitrogen bath can cause irreversible damage to the YBCO layer, destroying the sample.

An alternative method is to cool the sample using a cryogenic cooler. Cryogenic coolers are mechanical refrigeration units that extract heat from the sam-

ple and cool it down to operating temperatures. These machines can cause EMI and are generally more expensive than using cryogenic liquids such as liquid nitrogen for cooling, but boast improved portability.

Cryogenic cooling machines gradually cool the sample and allow one to investigate the superconductive properties of a thin-film layer as the temperature decreases. This is important since different manufacturing procedures can produce films with widely varying characteristics.

The Department of Electrical and Electronic Engineering at the University of Stellenbosch possesses two cryogenic cooling units. For high-T_c superconductors the cryogenic cooler shown in Figure 11.1 is used for testing. The control unit for the cryogenic cooler shown in Figure 11.1 is shown in Figure 11.2.

As a new heating element was designed and fabricated, tests were performed to investigate the superconductive properties of YBCO thin-film layers grown using the new heating element. This was accomplished by placing a sample between two coils, as shown in Figure 11.3. The first coil produces a time-varying magnetic field, while the second measures the magnetic field coupled into it via Faraday induction. The temperature of the entire setup is then gradually lowered. When the YBCO on the sample becomes superconductive it expels all magnetic fields from its interior. We therefore expect its magnetic susceptibility to go to zero, and the second coil to stop measuring the changing magnetic field produced by the first coil.

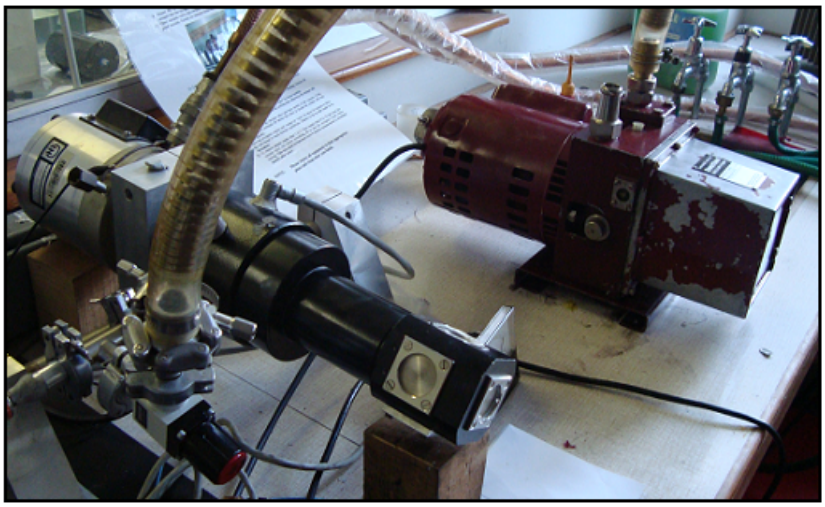

(a)

(b)

Figure 11.1: Cryogenic cooler setup. (a) The cooling chamber and the vacuum pump. (b) The cryogenic cooling unit.

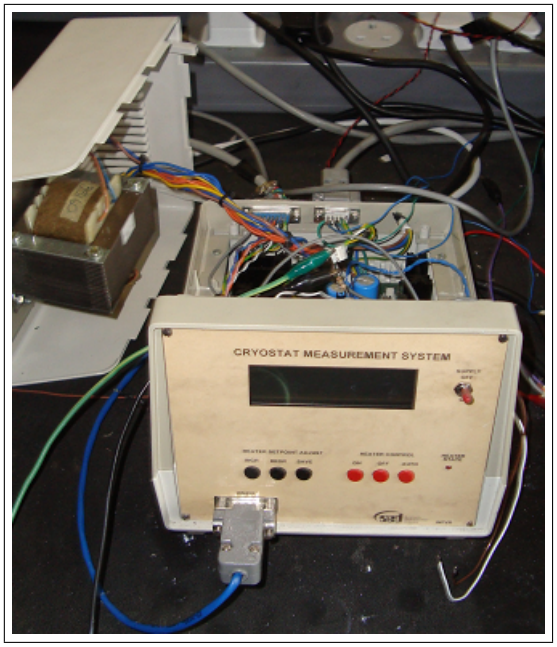

Figure 11.2: Control unit for cryogenic cooler.

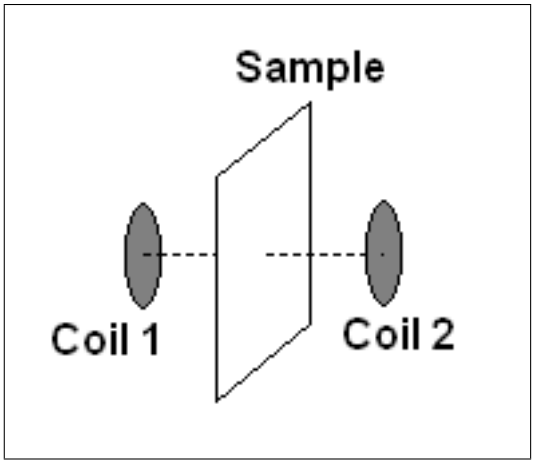

Figure 11.3: Susceptibility test setup.

Figure 11.4 show a representative result from such testing. Here it can be seen that the sample becomes superconductive below 94 kelvin.

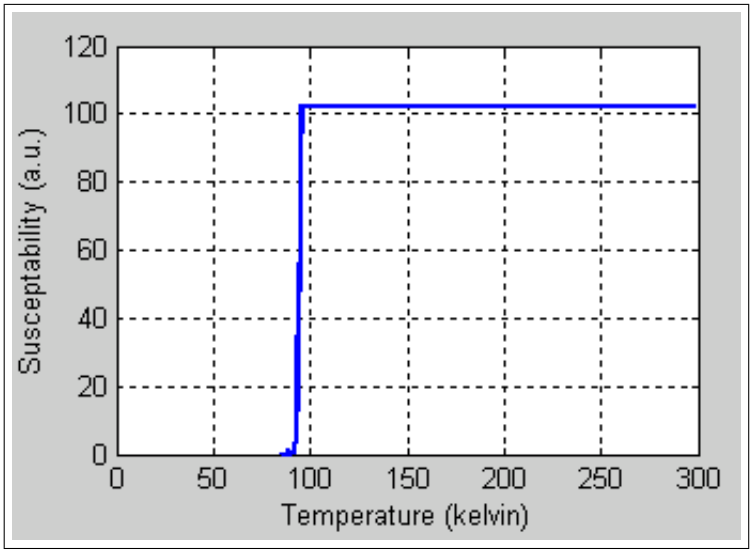

Figure 11.4: Susceptibility test results of a YBCO layer grown using the new heating element.

These tests confirm that films grown using the new heating element are of high-quality.

11.3 Four-Point Measurement Setup

The usual way of measuring the resistance of a device is to apply a current and, using the same connection wires, measure the voltage generated across the device. This is known as the *two-point* measurement technique [37]. This technique ignores the resistance of the wires used for the measurement.

For large resistances, the *two-point* measurement technique produces very accurate measurements. For example, a device with a resistance $R_d = 100k\Omega$ connected to a current source providing a current of $I = 100\mu A$ generates a voltage of $10V$ across it. If the wires connecting the device to the measuring equipment has a resistance of $R_w = 0.1\Omega$ it generates a voltage of only $10\mu V$ across it, meaning that the error in the measured voltage across the device is only $100 \times 10^{-6}\%$. [37]

For devices with small resistances, however, the *two-point* measurement technique causes large errors to occur. If in the previous example the device only has a resistance of 1Ω the error in measurement becomes 10%, which is unacceptable.

An alternative method is to connect the current source and the voltage measurement device to the device under test using two different sets of wires, as shown in Figure 11.5. This is known as the *four-point* measurement technique, and is much more accurate than the *two-point* measurement technique.

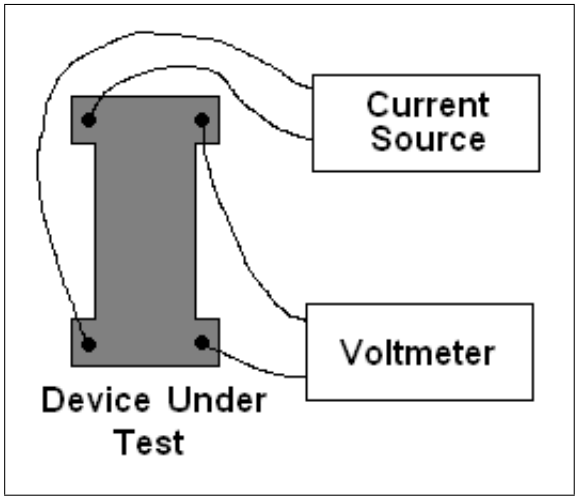

Figure 11.5: Four-Point measurement setup.

This technique requires that the voltmeter have a very high input impedance to prevent inaccurate measurements.

The *Mr. SQUID* setup constructed by *Conductus* [122] comes with a measurement device capable of performing *four-point* measurements. As such, this device, pictured Figure 11.6, can be used to measure the parameters of Josephson junctions and SQUIDs.

11.4 Results of Study

11.4.1 Results of Theoretical Study

This thesis presents the theory and principles of fruit quality, nuclear magnetic resonance, superconductivity and SQUIDs. These concepts were researched in order to create a low-field, SQUID detected NMR spectrometer capable of investigating the internal quality of fruit. Concepts that allow this goal to be reached were fully explored, and, although no working machine was fabricated,

provide a strong theoretical framework from which to design and fabricate such a machine.

Figure 11.6: *Mr. SQUID* control and measurement box.

11.4.2 Results of Simulation and Design

Extensive simulations were undertaken in order to understand the working of SQUIDs and NMR. These simulations, described in Chapter 9, confirm the theoretical working of SQUIDs and NMR as described by the theory.

Simulations of NMR J-couplings were also undertaken and used to simulate the spectra that would be obtained from certain substances.

The methods used to simulate SQUIDs and NMR in this thesis can easily be used and allow for the design and manufacture of a low-field, SQUID detected NMR spectrometer.

11.4.3 Results of Fabrication and Testing

Although many attempts were made and extensive practical experience was gained in the fabrication techniques and processes, no working SQUID was fabricated. As such, although all other parts of the low-field, SQUID detected NMR spectrometer were designed and manufactured, no tests could be performed to validate the design. This being said, the design of the machine flows from rigorous theoretical foundations, and is expected to perform as expected if a working SQUID were to be sourced.

Chapter 12

Conclusion

12.1 Review of Chapters

This thesis provides a theoretical and practical framework for the understanding, simulation, design and fabrication of a SQUID detected low-field NMR spectrometer. This thesis is designed to be relatively self-contained so as to serve as a single reference work for future research. As such, the theory is developed from first principles with appropriate mathematical rigour where deemed necessary for a complete understanding of the material presented.

As the eventual goal of this work is to create a SQUID detected NMR spectrometer that can measure the internal quality of fruit, the thesis started with a description of the concept of fruit quality in Chapter 2. Fruit quality was defined and the ways in which it is measured was introduced. The chapter also included a section on the physiology and quality of table grapes, as this is the fruit that the study set out to investigate.

After Chapter 2, the thesis moved on to describe the theory of nuclear magnetic resonance in Chapter 3. The thesis introduced the concepts in an intuitive manner, often neglecting precise mathematical descriptions in preference of more intuitive physical models. The theory described in this chapter lays the foundation for understanding all nuclear magnetic resonance phenomena, both high-field (traditional) and low-field.

The next section of the thesis set out to describe superconducting quantum interference devices. In order to achieve this, the theory and principles of superconductivity was introduced in Chapter 4, while SQUIDs and SQUID electronics were described in Chapters 5 and 6 respectively. These chapters

include detailed theoretical analysis of the working of SQUIDs, and provide the reader with a solid understanding of these devices.

In Chapter 7 this thesis deals with the fabrication of SQUIDs. The chapter described the constraints involved when designing DC SQUIDs, and introduced several methods of fabricating Josephson junctions using high-T_c superconductors. Special attention was given to the fabrication facilities available at the Department of Electrical and Electronic Engineering at the University of Stellenbosch.

In Chapter 8 this thesis combined the concepts of NMR and SQUIDs and described the working of SQUID detected NMR.

Simulations of SQUIDs and NMR and how they were done were reported in Chapter 9. Josephson junctions as well as different SQUIDs were simulated and compared. This chapter also included a description of NMR simulations. A single spin-1/2 particle in a magnetic field was simulated in order to support the models of NMR operation developed in Chapter 3. The chapter also described how simulations of ensembles of interacting spins could be simulated, and the low-field NMR spectra of certain chemical compounds were predicted.

The design and fabrication of the low-field SQUID detected NMR spectrometer undertaken in this study was described in Chapter 10, while the measurements and results of the fabricated system were described in Chapter 11. These chapters describe the design process, as well as measurement techniques that can be used.

In accordance with the goal of keeping this thesis relatively self-contained, it also contains several appendices that describe the fundamentals of quantum mechanics and quantum spin.

12.2 Review of Results

The goal of this study was to investigate the feasibility of using SQUID detected low-field NMR to investigate the internal quality of fruit. This thesis introduced the reader to the basic theory and principles needed to understand SQUIDs and NMR, and used this theory to suggest a spectrometer design that meets the requirement of evaluating internal fruit quality. This thesis also evaluated the merits of using low-field, SQUID detected NMR to measure the internal quality of fruit. The theory and arguments presented motivate

the application of SQUID detected NMR spectroscopy to internal fruit quality measurements.

Simulations of the various elements of a SQUID detected NMR spectrometer were reported, as well as extensive coverage of the principles on which these simulations are based. These simulations allow one to gain further insight into the operation of SQUIDs and NMR that cannot be attained by purely mathematical analysis. Methods of simulating the spectra of chemical substances in low-field environments were also introduced.

This thesis also gave special attention to the principles and techniques that can be used to design and manufacture Josephson junctions, SQUIDs and SQUID detected NMR spectrometers. During this study a prototype spectrometer was designed and partially fabricated. The spectrometer could not be completed as no working SQUID could be fabricated.

This thesis is designed to be used as a reference work for future work, and strives to be self-contained. The thesis introduces concepts from first principles, allowing the reader to quickly understand the most important concepts while pointing to areas throughout where further research could be directed.

12.3 Future Work

There is still much research to be completed in this field. The eventual goal of this research is to create a fully functional NMR spectrometer that can easily measure the internal quality of fruit. This spectrometer can then be used in a pre- or postharvest environment.

The first step toward this goal is to create a working prototype SQUID detected NMR spectrometer. The spectrometer described in this thesis could easily be used as the basis of such a prototype. In order to create such a prototype a working DC SQUID is required. SQUIDs can be manufactured at the University of Stellenbosch, or purchased. *MagQu* now markets SQUIDs specifically designed for NMR applications.

Alternatively, *MagQu* also markets an entire SQUID detected NMR spectrometer setup. Purchasing a setup such as this would save development time and allow research to quickly proceed to the next phase.

With a working prototype research can be focused on fruit measurements. Determining which quality aspects of fruit can be measured using NMR and

how to achieve such measurements is a subject of continual research [123, 124, 15, 125, 126, 127], and work on low-field NMR would be invaluable in creating an on-line sorting device.

Another important goal of future research is the miniaturization of the SQUID detected NMR spectrometer setup to make it feasible as an on-line sorting device. Furthermore, with enough miniaturization, the spectrometer could also be used as a hand-held device, which would be invaluable to farmers and growers in the field [128], allowing them to select the perfect time to harvest.

If the spectrometer is to be used as an on-line sorting device, research into the effect of moving fruit targets on the measured spectra needs to be completed. The motion of targets could cause undesirable effects on the spectrum, as described by S-.M Kim et al. [129].

Furthermore, the theory and principles described in this thesis could possibly be extended to allow for SQUID detected MRI imaging of fruit. This would allow for information about the physical structure of fruit to be measured.

The field of SQUID detected NMR is relatively young, but offers great advantages and holds great promise for investigating fruit. With further research this field of study has the potential to revolutionize the way fruit is grown, picked, sorted and packaged.

Appendices

Appendix A

Quantum Mechanical Formalism

A.1 Introduction

This Appendix develops the formalism of quantum mechanics. The idea is to cast the fundamental concepts of quantum theory into the elegant language of linear algebra. This allows practical calculations and helps to illuminate the fundamental theory [32].

This Appendix starts with a review of the fundamental concepts of quantum theory. It then introduces the formalism of function spaces and casts the fundamental theory into it. After the formalism has been introduced one of the most important concepts of quantum mechanics, the uncertainty principle, is examined. The Appendix concludes with an examination the angular momentum of a particle as an example of the new formalism.

A.2 Review of Quantum Theory

As in classical mechanics, the main subject of quantum mechanics is to determine the position of a particle at a specific time. From this one can determine any dynamical variable of interest (momentum, velocity, etc). Quantum mechanics, however, approaches this problem in a very different way than does classical mechanics. In quantum mechanics one searches for a particle's wavefunction, $\Psi(x,t)$, given by the Schrödinger equation [32]

$$\imath\hbar\frac{\partial\Psi}{\partial t} = -\frac{\hbar^2}{2m}\frac{\partial^2\Psi}{\partial x^2} + V\Psi, \tag{A.2.1}$$

where V is the potential energy function and $\hbar$ is Planck's (modified) constant $(h/2\pi)$.

What exactly the wave function *means* is provided by Max Born's statistical interpretation, published in 1926 [130], that states that $|\Psi(x,t)|^2$ gives the probability of finding the particle at a point x at time t. This interpretation therefore requires the following constraint, called the normalization constraint:

$$\int_{-\infty}^{+\infty} |\Psi(x,t)|^2 dx = 1. \tag{A.2.2}$$

The statistical interpretation can be used to calculate expectation values of physically measurable quantities. An expectation value is the average value obtained if a certain quantity is measured on a number of independent particles, each in the same state. The expectation value of position in one dimension, x, is given by

$$\begin{aligned} \langle x \rangle &= \int_{-\infty}^{+\infty} x|\Psi(x,t)|^2 dx \\ &= \int_{-\infty}^{+\infty} \Psi^* x \Psi dx. \end{aligned} \tag{A.2.3}$$

To determine the expectation value of momentum, note that, classically, $p = mv$, where p is the momentum of the particle, m is its mass and v is its velocity. We can therefore write [32]

$$\begin{aligned} \langle p \rangle &= m\langle v \rangle \\ &= m\frac{d\langle x \rangle}{dt}. \end{aligned} \tag{A.2.4}$$

$d\langle x \rangle/dt$ is given by [32]

$$\frac{d\langle x \rangle}{dt} = -\frac{\imath\hbar}{m}\int_{-\infty}^{+\infty} \Psi^* \frac{\partial \Psi}{\partial x} dx, \tag{A.2.5}$$

so Equation A.2.4 reduces to

$$\langle p \rangle = \int_{-\infty}^{+\infty} \Psi^* (\frac{\hbar}{\imath}\frac{\partial}{\partial x})\Psi dx. \tag{A.2.6}$$

We therefore have two operators, one that represents position (x) and one that

represents momentum $((\hbar/\imath)(\partial/\partial x))$. All other dynamical values of interest can be written in terms of these two operators, and in their expectation values can be obtained in the same way. In general, therefore, we have

$$\langle Q(x,p)\rangle = \int_{-\infty}^{+\infty} \Psi^* Q(x, \frac{\hbar}{\imath}\frac{\partial}{\partial x})\Psi dx. \tag{A.2.7}$$

If the potential function V is time independent we can solve the Schrödinger equation by the method of separation of variables. The wave function then becomes

$$\Psi(x,t) = \psi(x)f(t). \tag{A.2.8}$$

It is then easy to show that the function $f(t)$ takes the form

$$f(t) = e^{-\imath Et/\hbar}, \tag{A.2.9}$$

while the time independent wave function $\psi(x)$ can be calculated by solving the differential equation

$$-\frac{\hbar^2}{2m}\frac{d^2\psi}{dx^2} + V\psi = E\psi, \tag{A.2.10}$$

where E the energy associated with the state [32]. Equation A.2.10 is known as the time independent Schrödinger equation.

A.3 Extending the Schrödinger Equation to Three Dimensions

The (time dependant) Schrödinger equation is given by (Equation A.2.1, repeated here in a slightly different form for convenience) [131]

$$E\Psi = H\Psi, \tag{A.3.1}$$

where

$$E = \imath\hbar\frac{\partial}{\partial t}, \tag{A.3.2}$$

and

$$H = -\frac{\hbar^2}{2m}\frac{\partial^2}{\partial x^2} + V. \tag{A.3.3}$$

H is called the Hamiltonian of the system, and can be obtained from the classical energy

$$\frac{1}{2}mv^2 + V = \frac{1p}{2m} + V \tag{A.3.4}$$

by using the standard substitution

$$p \to \frac{\hbar}{\imath}\frac{\partial}{\partial x}. \tag{A.3.5}$$

Equations A.3.1, A.3.2 and A.3.5 generalize to three dimensions in a straightforward way, yielding

$$p_x \to \frac{\hbar}{\imath}\frac{\partial}{\partial x}, \quad p_y \to \frac{\hbar}{\imath}\frac{\partial}{\partial y}, \quad p_z \to \frac{\hbar}{\imath}\frac{\partial}{\partial z}, \tag{A.3.6}$$

or

$$\vec{p} \to \frac{\hbar}{\imath}\nabla. \tag{A.3.7}$$

herefore

$$\imath\hbar\frac{\partial\Psi}{\partial t} = -\frac{\hbar^2}{2m}\nabla^2\Psi + V\Psi, \tag{A.3.8}$$

where

$$\nabla^2 = \frac{\partial^2}{\partial x^2} + \frac{\partial^2}{\partial y^2} + \frac{\partial^2}{\partial z^2} \tag{A.3.9}$$

is called the Laplacian in Cartesian coordinates.

A.4 Function Spaces

This section recasts functions into the familiar language of linear algebra. Function spaces are vector spaces in which the "vectors" become functions. To see if a class of functions (for example the class of all polynomials, or the

class of all periodic functions with period 2π) constitute valid "vectors", one simply needs to verify that they adhere to the axioms of a vector space [132]. It is easy to verify that they do for many cases[1].

The inner product of two functions is defined by [32]

$$\langle f|g\rangle = \int_{-\infty}^{+\infty} f(x)^* g(x) dx. \tag{A.4.1}$$

This inner product may not converge, so to insure that the function space constitutes an inner product space certain constraints have to be placed on the functions. It turns out [32] that a sufficient requirement is that all functions in the space have to be square integrable:

$$\int_{-\infty}^{+\infty} |f(x)|^2 dx < \infty. \tag{A.4.2}$$

A complete inner product space (a function space that includes the limits of all sequences of functions that fall inside the space) is called a Hilbert space[2].

In function spaces linear operators act as linear transformations so long as they carry the functions they are working on into other functions in the space and they satisfy the linearity condition

$$\hat{T}(a|\alpha\rangle + b|\beta\rangle) = a(\hat{T}|\alpha\rangle) + b(\hat{T}|\beta\rangle). \tag{A.4.3}$$

A Hermitian operator is one that satisfies the condition

$$\langle\alpha|\hat{T}\beta\rangle = \langle\hat{T}\alpha|\beta\rangle, \tag{A.4.4}$$

where $\hat{T}$ is the operator, a and b are scalars and $|\alpha\rangle$ and $|\beta\rangle$ are functions in the space.

[1]Not all classes of functions constitute valid choices for a function space. For example, the class of all functions with minimum values equal to -3. Multiplication by a constant factor of 3, for example, would mean that a function would have a minimum value of -6, and therefore fall outside the space.

[2]Quantum mechanics is concerned with a special Hilbert space called $L_2(-\infty, \infty)$ which is the set of all square integrable functions on the interval $-\infty < x < \infty$. For the rest of this Appendix, *Hilbert Space* refers to $L_2(-\infty, \infty)$.

A.5 Formalism

With the tools developed in the previous sections it is now possible to recast quantum mechanics into the language of linear algebra. This is done by stating four postulates.

Firstly, the state of a particle is represented by its (normalized) wave function $\Psi(x,t)$, therefore

1. The state of a particle is represented by a normalized vector $|\Psi\rangle$ in a Hilbert Space.

All observables are functions of x and p and are expressed as quantum mechanical operators that can be obtained from its classical equivalent by the substitution [32]

$$p \to \frac{\hbar}{\imath}\frac{\partial}{\partial x}. \tag{A.5.1}$$

The expectation value of an observable can then be calculated by taking the inner product:

$$\langle Q \rangle = \langle \Psi | \hat{Q} \Psi \rangle. \tag{A.5.2}$$

Note that the expectation value of an observable must be real, so the following must hold:

$$\langle \Psi | \hat{Q} \Psi \rangle = \langle \Psi | \hat{Q} \Psi \rangle^* = \langle \hat{Q} \Psi | \Psi \rangle. \tag{A.5.3}$$

It therefore follows that the operators for observable quantities must be Hermitian. We therefore have

2. Observable quantities are represented by Hermitian operators and their expectation values can be calculated using inner products.

Although observables in general do not yield reproducible values under measurement (that is the reason we work with expectation values), some observables are determinate. The determinate states of an observable Q are

eigenvectors of $\hat{Q}$ [32]. We therefore have

3. A measurement of the observable Q on a particle in state $|\Psi\rangle$ is determinate if and only if the state $|\Psi\rangle$ is an eigenvector of $\hat{Q}$. The value measured under such circumstances is the associated eigenvalue.

In order to determine the probability of measuring a certain value (up to this point all that can be calculated is the average result of a measurement of an observable on a particle in a certain state) an extension of postulate 3 is introduced. This postulate is called the generalized statistical interpretation [32].

4. A measurement on a particle in the state $|\Psi\rangle$ of an observable Q is certain to return one of the eigenvalues of $\hat{Q}$. The probability that a certain eigenvalue λ will be returned is equal to the absolute square of the λ-component of $|\Psi\rangle$ when expressed in the orthonormal basis of eigenvectors.

For postulate 4 to hold the eigenfunctions of $\hat{Q}$ must span the space. This is not always the case for an operator in the infinite dimensional Hilbert space, but we will take it as an axiom of quantum mechanics that observables have operators for which this holds.

A.6 The Uncertainty Principle

This Section introduces the uncertainty principle.

Consider an observable, A. The standard deviation of measurements of the observable on a particle in a state $|\Phi\rangle$ is given by

$$\begin{aligned} \sigma_A^2 &= \langle(\hat{A} - \langle A\rangle)^2\rangle \\ &= \langle\Psi|(\hat{A} - \langle A\rangle)^2\Psi\rangle \\ &= \langle(\hat{A} - \langle A\rangle)\Psi|(\hat{A} - \langle A\rangle)\Psi\rangle \end{aligned} \tag{A.6.1}$$

(as $(\hat{A} - \langle A\rangle)$ is Hermitian).

Setting $|f\rangle = (\hat{A} - \langle A\rangle)|\Psi\rangle$ we have that

$$\sigma_A^2 = \langle f|f\rangle. \tag{A.6.2}$$

Similarly, for another observable B we have

$$\sigma_B^2 = \langle g|g\rangle \tag{A.6.3}$$

where $|g\rangle = (\hat{B} - \langle B\rangle)|\Psi\rangle$.

The Cauchy-Schwartz inequality, however, states that

$$\sigma_A^2\sigma_B^2 = \langle f|f\rangle\langle g|g\rangle \geq |\langle f|g\rangle|^2, \tag{A.6.4}$$

and, combined with the fact that, for any complex number z,

$$|z|^2 = (Re(z))^2 + (Im(z))^2 \geq (Im(z))^2 = \left[\frac{1}{2i}(z - z^*)\right]^2, \tag{A.6.5}$$

we have (by setting $z = \langle f|g\rangle$) that

$$\sigma_A^2\sigma_B^2 \geq \left(\frac{1}{2i}[\langle f|g\rangle - \langle g|f\rangle]\right)^2. \tag{A.6.6}$$

But

$$\begin{aligned}
\langle f|g\rangle &= \langle(\hat{A} - \langle A\rangle)\Psi|(\hat{B} - \langle B\rangle)\Psi\rangle \\
&= \langle\Psi|(\hat{A} - \langle A\rangle)(\hat{B} - \langle B\rangle)\Psi\rangle \\
&= \langle\Psi|(\hat{A}\hat{B} - \hat{A}\langle B\rangle - \hat{B}\langle A\rangle + \langle A\rangle\langle B\rangle)\Psi\rangle \\
&= \langle\Psi|\hat{A}\hat{B}\Psi\rangle - \langle B\rangle\langle\Psi|\hat{A}\Psi\rangle - \langle A\rangle\langle\Psi|\hat{B}\Psi\rangle + \langle A\rangle\langle B\rangle\langle\Psi|\Psi\rangle \\
&= \langle\hat{A}\hat{B}\rangle - \langle B\rangle\langle A\rangle - \langle A\rangle\langle B\rangle + \langle A\rangle\langle B\rangle \\
&= \langle\hat{A}\hat{B}\rangle - \langle A\rangle\langle B\rangle,
\end{aligned} \tag{A.6.7}$$

and, similarly,

$$\langle g|f\rangle = \langle\hat{B}\hat{A}\rangle - \langle A\rangle\langle B\rangle, \tag{A.6.8}$$

so

$$\begin{aligned} \langle f\ g\rangle - \langle g|f\rangle &= \langle \hat{A}\hat{B}\rangle - \langle \hat{B}\hat{A}\rangle \\ &= \langle [\hat{A},\hat{B}]\rangle, \end{aligned} \tag{A.6.9}$$

where

$$[\hat{A},\hat{B}] = \hat{A}\hat{B} - \hat{B}\hat{A} \tag{A.6.10}$$

is called the commutator of the two operators.

Combining Equation A.6.9 with Equation A.6.6 yields the uncertainty principle, given as

$$\sigma_A^2\sigma_B^2 \geq \left(\frac{1}{2\imath}\langle [\hat{A},\hat{B}]\rangle\right)^2. \tag{A.6.11}$$

The uncertainty principle states that any two observables whose operators are incompatible (i.e. do not commute) do not share a complete set of eigenvectors. It is therefore impossible to simultaneously measure these two observables precisely. There always exists uncertainty in the measurement, and this uncertainty is not because of faulty equipment or bad measurements but because of a fundamental property of quantum mechanics[3].

A.7 Angular Momentum

As an example of the quantum mechanical formalism developed in this Appendix the angular momentum of a particle is analyzed in this section.

To develop the quantum mechanical operator associated with angular momentum we note that, classically, angular momentum is given by

$$\vec{L} = \vec{r}\times\vec{p}, \tag{A.7.1}$$

[3]Obviously observables whose operators do commute can be precisely measured simultaneously.

or

$$\begin{aligned} L_x &= yp_z - zp_y \\ L_y &= zp_x - xp_z \\ L_z &= xp_y - yp_x. \end{aligned} \tag{A.7.2}$$

By using the standard substitution (Equation A.5.1) the quantum mechanical operators for angular momentum therefore become

$$\begin{aligned} L_x &= \frac{\hbar}{\imath}\left(y\frac{\partial}{\partial z} - z\frac{\partial}{\partial y}\right) \\ L_y &= \frac{\hbar}{\imath}\left(z\frac{\partial}{\partial x} - x\frac{\partial}{\partial z}\right) \\ L_z &= \frac{\hbar}{\imath}\left(x\frac{\partial}{\partial y} - y\frac{\partial}{\partial x}\right). \end{aligned} \tag{A.7.3}$$

We now wish to find the eigenfunctions and eigenvalues of these operators. Notice that the angular momentum operators do not commute. In fact

$$\begin{aligned} [L_x, L_y] &= \imath\hbar L_z \\ [L_y, L_z] &= \imath\hbar L_x \\ [L_z, L_x] &= \imath\hbar L_y. \end{aligned} \tag{A.7.4}$$

Therefore, according to the uncertainty principle, we cannot find simultaneous eigenfunctions for these operators. However, the square of the total angular momentum,

$$L^2 = L_x^2 + L_y^2 + L_z^2 \tag{A.7.5}$$

does commute with the angular momentum operators, L_x, L_y and L_z. It follows, of course, that simultaneous eigenfunctions for these operators and L^2 can be found. We can therefore find an f for which

$$L^2 f = \lambda f \quad \text{and} \quad L_z f = \mu f \tag{A.7.6}$$

holds, where λ is the eigenvalue of the L^2 operator corresponding to f and μ is the eigenvalue of L_z corresponding to f.

Let us now introduce the operator $L_{\pm}$, defined as

$$L_{\pm} = L_x \pm \imath L_y. \tag{A.7.7}$$

We then have

$$[L_z, L_{\pm}] = \pm\hbar L_{\pm} \quad \text{and} \quad [L^2, L_{\pm}] = 0. \tag{A.7.8}$$

If f is a eigenfunction of L^2 and L_z we then have that (using Equation A.7.6)

$$\begin{aligned} L^2(L_{\pm}f) &= L_{\pm}(L^2 f) \\ &= L_{\pm}(\lambda f) \\ &= \lambda(L_{\pm}f), \end{aligned} \tag{A.7.9}$$

and (again using Equation A.7.6, together with Equation A.7.8)

$$\begin{aligned} L_z(L_{\pm}f) &= (L_z L_{\pm} - L_{\pm}L_z)f + L_{\pm}L_z f \\ &= \pm\hbar L_{\pm}f + L_{\pm}(\mu f) \\ &= (\mu \pm \hbar)(L_{\pm}f). \end{aligned} \tag{A.7.10}$$

Therefore, if f is an eigenfunction of L^2 then $L_{\pm}f$ is also an eigenfunction of L^2 and has an eigenvalue of λ (Equation A.7.9), and if f is an eigenfunction of L_z then $L_{\pm}f$ is also an eigenfunction of L_z and has an eigenvalue of $\mu \pm \hbar$ (Equation A.7.10). $L_{\pm}$ is therefore called a "ladder" operator as it raises or lowers the eigenvalue of L_z by $\hbar$.

For a given value of λ we can therefore obtain a "ladder" of states, each state separated by one unit of $\hbar$ in the eigenvalue of L_z [32]. Each successive "rung" of the ladder can be reached by applying either the raising (L_+) or the lowering (L_-) operator. But there are only a limited number of states. To see this, suppose we "climb" the "ladder" by applying successive raising operators, L_+. Eventually we will reach a state for which the z-component exceeds the total, and this is impossible. There therefore has to exist a "top rung", f_t for which [32]

$$L_+ f_t = 0. \tag{A.7.11}$$

If we let the top rung have a eigenvalue of $l\hbar$ we then have that

$$L_z f_t = \hbar l f_t \quad \text{and} \quad L^2 f_t = \lambda f_t. \tag{A.7.12}$$

We can write the total angular momentum operator L^2 in terms of the ladder operator $L_\pm$ as follows [32]

$$L^2 f_t = L_\pm L_\mp + L_z^2 \mp \hbar L_z, \tag{A.7.13}$$

from which it follows that

$$\lambda = \hbar^2 l(l+1). \tag{A.7.14}$$

Using the same argument, there exists a "bottom rung", f_b, with eigenvalue $\hbar\bar{l}$ for which

$$L_- f_b = 0, \tag{A.7.15}$$

from which follows that

$$\lambda = \hbar^2 \bar{l}(\bar{l}-1). \tag{A.7.16}$$

Comparing Equations A.7.14 and A.7.16 we find that either $\bar{l} = l+1$, which cannot be (the "top rung" cannot be lower than the "bottom rung"), or that $\bar{l} = -l$. The eigenvalues of L_z are therefore $m\hbar$, where m is an integer and $-l \leq m \leq l$. In particular, if there are N integer steps between $-l$ and l it follows that $l = -l + N$, so that $l = N/2$, from which it follows that l must have either a integer value or a half-integer value. We therefore find that the eigenfunctions are characterized by the numbers l and m, with

$$L^2 f_l^m = \hbar^2 l(l+1) f_l^m \,\text{and}\, L_z f_l^m = m\hbar f_l^m. \tag{A.7.17}$$

where

$$l = 0, 1/2, 1, 3/2, \ldots \,\text{and}\, m = -l, -l+1, \ldots, l-1, l. \tag{A.7.18}$$

To determine the eigenfunctions f_l^m we rewrite L_x, L_y and L_z into spherical

coordinates. This yields

$$L^2 = -\hbar^2 \left[\frac{1}{\sin\theta} \frac{\partial}{\partial\theta} \left(\sin\theta \frac{\partial}{\partial\theta} \right) + \frac{1}{\sin^2\theta} \frac{\partial^2}{\partial\phi^2} \right], \tag{A.7.19}$$

which in turn yields

$$\begin{aligned} L^2 f_l^m &= -\hbar^2 \left[\frac{1}{\sin\theta} \frac{\partial}{\partial\theta} \left(\sin\theta \frac{\partial}{\partial\theta} \right) + \frac{1}{\sin^2\theta} \frac{\partial^2}{\partial\phi^2} \right] \\ &= \hbar^2 l(l+1) f_l^m, \end{aligned} \tag{A.7.20}$$

and

$$\begin{aligned} L_z f_l^m &= \frac{\hbar}{\imath} \frac{\partial}{\partial\phi} f_l^m \\ &= m\hbar f_l^m. \end{aligned} \tag{A.7.21}$$

This system of equations results in the solution of f_l^m being the spherical harmonic function $Y_l^m(\theta, \phi)$. Therefore the eigenfunctions of L^2 and L_z are the spherical harmonics [32].

By using purely algebraic reasoning we have deduced both the eigenvalues and the eigenfunctions of the angular momentum operators. This example proves the power of the algebraic quantum mechanical formalism.

Appendix B

Quantum Spin

B.1 Introduction

In this appendix quantum spin is introduced and described. The appendix introduces the basic concepts of quantum spin and then uses it to describe the concept of quantum indeterminacy. It concludes with a description of the mathematics of an ensemble of spin particles.

B.2 Quantum Spin

In classical mechanics, objects have two kinds of angular momentum – orbital angular momentum associated with orbital motion around a centre of mass (for example the earth orbiting the sun) and spin angular momentum associated with rotation of the body (for example the Earth rotating about its own axis). This distinction is really just a matter of convenience, though, as an object possessing spin angular momentum can also be thought of as a collection of particles, each possessing an orbital angular momentum (think of the Earth as a collection of rocks, each of which orbits around the centre of the Earth at the same speed as the Earth's rotation).

Quantum mechanics, however, deals with point particles. As these have no structure, they can only have orbital angular momentum. It turns out, however, that each of these point particles also has an intrinsic property that has many similarities with classical spin. This quantum mechanical phenomenon is therefore, rather unimaginatively, called spin as well.

The algebraic theory of quantum spin is analogous to the theory of angu-

lar momentum as described in Appendix A. The fundamental commutation relations are given as

$$\begin{aligned} [S_x, S_y] &= \imath\hbar S_z \\ [S_y, S_z] &= \imath\hbar S_x \\ [S_z, S_x] &= \imath\hbar S_y, \end{aligned} \tag{B.2.1}$$

while the eigenvectors of S^2 and S_z satisfy, as before,

$$S^2|s(m)\rangle = \hbar^2 s(s+1)|s(m)\rangle \quad \text{and} \quad S_z|s(m)\rangle = m\hbar|s(m)\rangle, \tag{B.2.2}$$

where s and m are given by

$$s = 0, 1/2, 1, 3/2, \ldots \quad \text{and} \quad m = -s, -s+1, \ldots, s-1, s. \tag{B.2.3}$$

Unlike angular momentum, each species of particle has a specific value of s that is fixed. The most important case is when $s = 1/2$, and only this case is considered in this thesis. For spin-1/2 particles only two eigenstates exist, $|\frac{1}{2}\left(\frac{1}{2}\right)\rangle$ and $|\frac{1}{2}\left(-\frac{1}{2}\right)\rangle$. These eigenstates can be represented by

$$\chi_+ = \begin{bmatrix} 1 \\ 0 \end{bmatrix} \tag{B.2.4}$$

and

$$\chi_- = \begin{bmatrix} 0 \\ 1 \end{bmatrix} \tag{B.2.5}$$

respectively, and the general state of a particle can be represented by

$$\chi = \begin{bmatrix} a \\ b \end{bmatrix} = a\chi_+ + b\chi_-, \tag{B.2.6}$$

with the normalization constraint

$$|a|^2 + |b|^2 = 1. \tag{B.2.7}$$

A particle is therefore not limited to be in one of the eigenstates but can

reside in a superposition of these two states.

In spin-1/2 systems operators are represented by 2×2 matrices. The spin-1/2 system is therefore relatively easy to analyse.

B.3 Measurement of Angular Momentum: Quantum Indeterminacy

Suppose a particle is in the state χ_+ and a measurement of the z-directed spin is made. As predicted by the postulates of quantum mechanics, this measurement is sure to return a value of $\hbar/2$. But suppose a measurement of S_x is made on that particle. Because of the uncertainty principle the result of such a measurement would not be well defined. Such a measurement is sure to return either $\hbar/2$ or $-\hbar/2$, but precisely which of the two will be returned is impossible to predict. This does not mean that we do not know the state of the particle (the particle is in state χ_+), or that there is something wrong with the measurement. Rather, this indeterminacy is a feature of reality itself.

B.4 Ensemble of Spin Particles

Suppose we have two spin-1/2 particles in a system. The system now has four possible eigenstates: each particle has a possible eigenstate of χ_+ or χ_-. The entire system therefore has eigenstates:

$$\chi_+\chi_+, \quad \chi_+\chi_-, \quad \chi_-\chi_+, \quad \chi_-\chi_-. \tag{B.4.1}$$

The hamiltonian describing the system therefore becomes a 4×4 matrix given by (here, as always, we suppose the system is in a z-directed magnetic field with field stength B_0)

$$\begin{aligned} \mathbf{H} &= -B_0 \sum_{i=1}^{N} \gamma_i \mathbf{I_{zi}} + 2\pi \sum_{i=1}^{2} \sum_{j>i} J_{ij} (\mathbf{I_i} \cdot \mathbf{I_j}) \\ &= -B_0\gamma_1 \mathbf{I_{z1}} - B_0\gamma_2 \mathbf{I_{z2}} + 2\pi J_{12} (\mathbf{I_1} \cdot \mathbf{I_2}) \\ &= -B_0\gamma_1 \mathbf{I_{z1}} - B_0\gamma_2 \mathbf{I_{z2}} + 2\pi J_{12} (\mathbf{I_{z1}I_{z2}} + \mathbf{I_{x1}I_{x2}} + \mathbf{I_{y1}I_{y2}}), \end{aligned} \tag{B.4.2}$$

where J_{ij} represents the J-coupling constant between spins i and j.

The spin operators $\mathbf{I_{zk}}$, $\mathbf{I_{xk}}$ and $\mathbf{I_{yk}}$ can be calculated using the Pauli spin matrices and the identity operator given by

$$\frac{1}{2}\mathbf{1} = \frac{1}{2}\begin{bmatrix} 1 & 0 \\ 0 & 1 \end{bmatrix} \tag{B.4.3}$$

by the relation [2]

$$\begin{bmatrix} \textbf{Product} \\ \textbf{Operator} \end{bmatrix} = 2 \times \begin{bmatrix} \textbf{Operator for} \\ \textbf{Spin } \mathbf{I_1} \end{bmatrix} \otimes \begin{bmatrix} \textbf{Operator for} \\ \textbf{Spin } \mathbf{I_2} \end{bmatrix}, \tag{B.4.4}$$

where $\otimes$ represents the Kronecker product. For example, $\mathbf{I_{z1}}$ can be caclulated as follows:

$$\begin{aligned}
\mathbf{I_{z1}} &= 2 \times \mathbf{I_z} \otimes \frac{1}{2}\mathbf{1} \\
&= 2\frac{1}{2}\begin{bmatrix} 1 & 0 \\ 0 & -1 \end{bmatrix} \otimes \frac{1}{2}\begin{bmatrix} 1 & 0 \\ 0 & 1 \end{bmatrix} \\
&= \frac{1}{2}\begin{bmatrix} 1 \times \begin{bmatrix} 1 & 0 \\ 0 & 1 \end{bmatrix} & 0 \times \begin{bmatrix} 1 & 0 \\ 0 & 1 \end{bmatrix} \\ 0 \times \begin{bmatrix} 1 & 0 \\ 0 & 1 \end{bmatrix} & -1 \times \begin{bmatrix} 1 & 0 \\ 0 & 1 \end{bmatrix} \end{bmatrix} \\
&= \frac{1}{2}\begin{bmatrix} 1 & 0 & 0 & 0 \\ 0 & 1 & 0 & 0 \\ 0 & 0 & -1 & 0 \\ 0 & 0 & 0 & -1 \end{bmatrix}.
\end{aligned} \tag{B.4.5}$$

These equations generalize naturally to systems with more than two spins. When the product operators of such systems need to be calculated Equation B.4.4 generalizes as would be expected. For example, in a system of N spin-1/2 particles, calculating $\mathbf{I_{zn}}$ involves taking the Kronecker product of a series of $(n-1)$ 2×2 identity operators, the z-spin Pauli matrix $\sigma_\mathbf{z}$, and another $(N-n)$ 2×2 identity matrices [10].

Appendix C

Derivation of the London Equations

This Appendix derives the London Equations using the Macroscopic Quantum Model. The first part of the derivation can be found in Section 4.4, but is repeated here for clarity and convenience.

The fundamental assumption of the MQM is that the superelectron fluid in a superconductor can be represented by a single macroscopic wave function. This macroscopic wave function is not a proper wave function, but rather an ensemble-average of the single superelectron wave functions, and is given by

$$\Psi(\mathbf{r}) = \psi(\mathbf{r})e^{\jmath\theta(\mathbf{r})}. \tag{C.0.1}$$

This wave function can be normalized in such a way that

$$\Psi(\mathbf{r}) = [n_s(\mathbf{r})]^{\frac{1}{2}}e^{\jmath\theta(\mathbf{r})}, \tag{C.0.2}$$

where we have that n_s is the density of superelectrons in a superconductor.

In classical mechanics, the momentum of a particle with charge q and mass m in a magnetic field is given by

$$\mathbf{p} = m\mathbf{v} + q\mathbf{A}, \tag{C.0.3}$$

with $\mathbf{A}$ the magnetic vector potential associated with the magnetic field and $\mathbf{v}$ the velocity of the charged particle.

For a superelectron with mass m^* and charge q^*, Equation C.0.3 therefore

becomes

$$\mathbf{p} = m^*\mathbf{v} + q^*\mathbf{A}, \tag{C.0.4}$$

Now we can then write the momentum density of the Cooper pairs in a superconductor, each having the same momentum, as

$$n_s\mathbf{p} = n_s\left(m^*\mathbf{v} + q^*\mathbf{A}\right), \tag{C.0.5}$$

where n_s is the density of Cooper Pairs in the superconductor.

But $n_s\mathbf{p}$ is the expectation value of the canonical quantum momentum operator $-\jmath\hbar\nabla$ operating on the pair-fluid waveform [48]. Therefore

$$n_s\mathbf{p} = \langle\Psi| - \jmath\hbar\nabla|\Psi\rangle\,. \tag{C.0.6}$$

Since [48]

$$-\jmath\hbar\nabla\Psi = \hbar\left(\nabla\theta\right)\Psi, \tag{C.0.7}$$

we have that [48]

$$\mathbf{p} = \hbar\nabla\theta. \tag{C.0.8}$$

Equation C.0.4 then becomes

$$\hbar\nabla\theta = m^*\mathbf{v_s} + q^*\mathbf{A}. \tag{C.0.9}$$

The cooper pair current density is given by [48]

$$\mathbf{J_s} = n_s q^*\mathbf{v_s}. \tag{C.0.10}$$

Combining Equations C.0.9 and C.0.10, we find

$$\hbar\nabla\theta = q^*\Lambda\mathbf{J_s} + q^*\mathbf{A}, \tag{C.0.11}$$

with

$$\Lambda = \frac{m^*}{n_s\left(q^*\right)^2}. \tag{C.0.12}$$

Equations C.0.11 and C.0.12 describe the quantum mechanical flow of current in a superconductor.

Noting that the curl of the gradient of a scalar is zero we find that

$$\nabla \times \mathbf{p} = \nabla \times (\hbar \nabla \theta) = 0. \tag{C.0.13}$$

Taking the curl on both sides of Equation C.0.11 and using Equation C.0.13 combined with the Maxwell equation $\mathbf{B} = \nabla \times \mathbf{A}$ yields the second London equation:

$$\Lambda(\nabla \times \mathbf{J_s}) + \mathbf{B} = 0. \tag{C.0.14}$$

To derive the first London equation we note the influence of an electric field on the motion of the superfluid. By using Newton's second law we find

$$m^* \frac{d\mathbf{v_s}}{dt} = q^* \mathbf{E}, \tag{C.0.15}$$

where $\mathbf{v_s}$ is the velocity of a superelectron.

If we assume small spatial variations in $\mathbf{v_s}$ we can rewrite it as [48]

$$m^* \frac{\partial \mathbf{v_s}}{\partial t} = q^* \mathbf{E}, \tag{C.0.16}$$

which can be rewritten, using Equation C.0.12, as

$$\Lambda \frac{\partial \mathbf{J_s}}{\partial t} = \mathbf{E}, \tag{C.0.17}$$

which is known as the first London equation.

Appendix D

Program Listing

D.1 MATLAB Programs for Creating Segmented FastHenry Structures

Two programs were written to create segmented FastHenry structures. First, *linemaker.m* creates a segmented line with specified width, length and height. *squidmaker.m* uses *linemaker.m* in order to create structures. It first creates the line structures, and then removes any overlapping edges and nodes.

D.1.1 LINEMAKER.m

```
%************************************************%
%*                                              *%
%*        linemaker.m                           *%
%*                                              *%
%*          Creates a FastHenry model for a     *%
%*          segmented line of length x and      *%
%*          width y, with p nodes lengthwise    *%
%*          and q nodes widthwise.              *%
%*                                              *%
%*        INPUT: length of line (um): x         *%
%*               width of line (um): y          *%
%*               number of nodes lengthwise: p  *%
%*               number of nodes widthwise: q   *%
%*               starting x position: xstart    *%
%*               starting y position: ystart    *%
%*               last node number: nn           *%
%*               last edge number: n            *%
%*                                              *%
%*        OUTPUT: last node number: nodenr      *%
%*                last edge number: edgenr      *%
%*                FastHenry input file:         *%
%*                                SLINE.txt     *%
%*                                              *%
%*        Author: D.S. van Zyl                  *%
%*                                              *%
%************************************************%

function [nodenr, edgenr, nommers] = linemaker(x,y,p,q,xstart,ystart,nn,en,fid,nommersin)

nrnodes=p*q;
Nx=0;
Ny=0;
widthwidth=y/q;
lengthwidth=x/p;
j=1;
J='';
uit = '';
o='';
moetskryf=true;

for i=1:1:nrnodes,
    moetskryf=true;
    b=sprintf('N%d x=%d y=%d\n',(i+nn),(Nx+xstart),(Ny+ystart));
    [D, E, F]=strread(b,'%s %s %s');
    fileInfo = dir('squid.txt');
    fileSize = fileInfo.bytes;
    fseek(fid,0,'bof');
    while (ftell(fid) < fileSize),
        a=fgetl(fid);
        [A, B, C]=strread(a,'%s %s %s');
        if (strcmp(B,E) & strcmp(F,C)),
            uit = [uit, A];
            moetskryf=false;
        end
    end
    if (moetskryf==true),
        fprintf(fid,'N%d x=%d y=%d\n',(i+nn),(Nx+xstart),(Ny+ystart));
    else
        J=sprintf('N%d',(i+nn));
        uit = [uit, J];
    end
    if (mod((Ny+lengthwidth),(p*lengthwidth)))==0,
```

```
63 -          Nx=Nx+widthwidth;
64 -          Ny=0;
65 -      else
66 -          Ny=Ny+lengthwidth;
67 -      end
68 -  end
69 -  fprintf(fid,'\n \n');
70 -  nodenr=nn+nrnodes;
71
72 -  for (i=1:1:nrnodes),
73 -      if ((mod(i,p))~=0),
74 -          fprintf(fid,'E%d N%d N%d w=%d h=0.2 \n',(j+en),(nn+i),(nn+i+1),widthwidth);
75 -          j=j+1;
76 -      end
77 -  end
78
79 -  for (i=1:1:nrnodes),
80 -      if ((nrnodes-p)>=i),
81 -          fprintf(fid,'E%d N%d N%d w=%d h=0.2 \n',(en+j),(nn+i),(nn+i+p),lengthwidth);
82 -          j=j+1;
83 -      end
84 -  end
85 -  fprintf(fid,'\n \n');
86 -  edgenr=j-1+en;
87
88
89 -  nommers=[nommersin, uit];
90
91 -  end
92
```

D.1.2 SQUIDMAKER.m

```
1   %*************************************************%
2   %*                                               *%
3   %*        squidmaker.m                           *%
4   %*                                               *%
5   %*          Creates a FastHenry model for a      *%
6   %*          SQUID. [uses LINEMAKER.m]            *%
7   %*                                               *%
8   %*        INPUT: none                            *%
9   %*        OUTPUT: FastHenry input file:          *%
10  %*                  SQUID.txt                    *%
11  %*                                               *%
12  %*        Author: D.S. van Zyl                   *%
13  %*                                               *%
14  %*************************************************%
15
16  function squidmaker()
17
18 -  nodenr=0;
19 -  edgenr=0;
20 -  nommers='';
21
22  %create FastHenry input file, sline.txt%
23 -  fid = fopen('squid.txt','r+');
24
```

```
%set format of numbers%
format short e;

%write sline.txt header%
disp('Writing file header');
fprintf(fid,'%---------------sline.txt------------------% \n');
fprintf(fid,'* Created using SQUIDMAKER.m, by D.S. van Zyl* \n');
fprintf(fid,'\n');
fprintf(fid,'.units um \n');
fprintf(fid,'.Default z=0 lambda=0.25 \n');
fprintf(fid,'\n \n');

disp('Writing line 1');
[nodenr,edgenr,nommers]=linemaker(4,12,4,12,19,0,nodenr,edgenr,fid,nommers);
disp('Writing line 2');
[nodenr,edgenr,nommers]=linemaker(16,4,16,4,19,2,nodenr,edgenr,fid,nommers);
disp('Writing line 3');
[nodenr,edgenr,nommers]=linemaker(5,6,5,6,17,12,nodenr,edgenr,fid,nommers);
disp('Writing line 4');
[nodenr,edgenr,nommers]=linemaker(20,23,20,23,0,15,nodenr,edgenr,fid,nommers);
disp('Writing line 5');
[nodenr,edgenr,nommers]=linemaker(32,20,32,20,0,33,nodenr,edgenr,fid,nommers);
disp('Writing line 6');
[nodenr,edgenr,nommers]=linemaker(20,14,20,14,18,45,nodenr,edgenr,fid,nommers);
disp('Writing line 7');
[nodenr,edgenr,nommers]=linemaker(32,20,32,20,30,33,nodenr,edgenr,fid,nommers);
disp('Writing line 8');
[nodenr,edgenr,nommers]=linemaker(20,23,20,23,27,15,nodenr,edgenr,fid,nommers);
disp('Writing line 9');
[nodenr,edgenr,nommers]=linemaker(5,6,5,6,27,12,nodenr,edgenr,fid,nommers);
disp('Writing line 10');
[nodenr,edgenr,nommers]=linemaker(16,4,16,4,27,2,nodenr,edgenr,fid,nommers);

disp('Finishing file');
%finish file%
fprintf(fid,'.end');
fclose(fid);

disp('Fixing Edges');
%correct edges%

for i=1:2:(length(nommers)-1),
    fileInfo = dir('squid.txt');
    fileSize = fileInfo.bytes;
    fid = fopen('squid.txt','r+');
    fout = fopen('output.txt','w');
    fseek(fid,0,'bof');
    fseek(fout,0,'bof');
    while ~feof(fid)
        s = fgetl(fid);
        if (isempty(s)==false),
            if (s(1)=='E'),
                [A, B, C, D , E] = strread(s,'%s %s %s %s %s');
                if (strcmp(B,nommers(i+1)) || strcmp(C,nommers(i+1))),
                    s = strrep(s, nommers(i+1), nommers(i));
                    s=char(s);
                end
            end
        end
        fprintf(fout,'%s\n',s);
    end
    fclose(fout);
```

```
87 -      fclose(fid);
88 -      delete('squid.txt');
89 -      a=dir('output.txt');
90 -      newname='squid.txt';
91 -      movefile([a.name],[newname]);
92 -  end
93
94 -  disp('Done!');
95
96 -  end
97
```

D.2 MATLAB Programs for Simulating NMR

D.2.1 Single Nucleus in a Magnetic Field

```
1   %*************************************************%
2   %*                                               *%
3   %*        nmrsim.m                               *%
4   %*                                               *%
5   %*          Simulates quantum 1/2-spins in a     *%
6   %*          magnetic field.                      *%
7   %*                                               *%
8   %*        INPUT: none                            *%
9   %*        OUTPUT: tout, exSx, exSy and exSz      *%
10  %*                                               *%
11  %*        Author: Derrick van Zyl                *%
12  %*                                               *%
13  %*************************************************%
14
15  %clear workspace
16 -clear;
17
18
19  %define quantum constants
20 -h = 6.6262e-34;                  %Planck's constant (joule-sec)
21 -hbar = h/(2*pi);                 %hbar
22 -gamma = 267.522e6;               %Gyromagnetic ratio of 1H (rad/(s.T))
23 -Sz = (hbar/2)*[1 0;0 -1];        %Pauli spin matrix, z-direction
24 -Sx = (hbar/2)*[0 1;1 0];         %Pauli spin matrix, x-direction
25 -Sy = (hbar/2)*[0 -i;i 0];        %Pauli spin matrix, y-direction
26
27
28  %define simulation constants
29 -time = 10;                       %Simulation Time (seconds)
30 -timestep = 100e-6;               %Timestep (seconds)
31 -Bz = 0.2e-6;                     %Magnetic field strength (z-direction) (Tesla)
32 -Bx = 200e-3;                     %Magnetic field strength (x-direction) (Tesla)
33 -rotAng = pi/2;                   %Angle by which spin is rotated (rad)
34 -rotMat = [cos(rotAng/2) -i*sin(rotAng/2); -i*sin(rotAng/2) cos(rotAng/2)];
35                                   %Rotation matrix (rotation around x-axis)
36
37
38  %pre-simulation computation
39 -a = cos(2*pi*rand(1));           %a is a random real number between 0 and 1
```

```
40 -  b = sin(a);                          %Ensure b is normalized. We require |a|^2 + |b|^2 = 1;
41 -  H = -gamma*Bz*Sz;                    %Hamiltonian of system (z-directed magnetic field)
42 -  [Vh, Dh] = eigs(H);                  %Determine eigenvalues (energies) and eigentvectors
43                                         %  (observable states) of hamiltonian
44 -  EigVal1 = Dh(1,1);                   %1st Eigenvalue of H
45 -  EigVal2 = Dh(2,2);                   %2nd Eigenvalue of H
46 -  Xp = Vh(:,1);                        %Eigenvector corresponding to EigVal1
47 -  Xn = Vh(:,2);                        %Eigenvector corresponding to EigVal2
48 -  Hx = -gamma*Bx*Sx;                   %Hamiltonian of system (x-directed magnetic field)
49 -  [Vhx, Dhx] = eigs(Hx);               %Determine eigenvalues (energies) and eigentvectors
50                                         %  (observable states) of hamiltonian
51 -  EigVal1x = Dhx(1,1);                 %1st Eigenvalue of H
52 -  EigVal2x = Dhx(2,2);                 %2nd Eigenvalue of H
53 -  Xpx = Vhx(:,1);                      %Eigenvector corresponding to EigVal1
54 -  Xnx = Vhx(:,2);                      %Eigenvector corresponding to EigVal2
55
56
57    %create tout (output tim vector) and output vectors (expectation values of Sx, Sy and Sz)
58 -  tout = rand(1,round(time/timestep))';
59 -  Xt = rand(1,round(time/timestep))';
60 -  exSz = rand (1,round(time/timestep))';
61 -  exSx = rand (1,round(time/timestep))';
62 -  exSy = rand (1,round(time/timestep))';
63
64
65    %perform simulation
66 -  for (t=timestep:timestep:time)
67 -      tout(round(t/timestep),1)=t;
68 -      Xt =a*Xp*exp(-i*EigVal1*t/hbar) + b*Xn*exp(-i*EigVal2*t/hbar);
69
70    %**** For Random  Fluctuations in spin, uncomment this block ****
71    %
72    %      if (randn(1) <= 0.05)                    %Bias toward lower energy level = 0.05
73    %          a = a - abs(randn(1))*(1-a)*timestep; %Move closer to higher energy value
74    %          if (b>0)                              %Correct b such that |a|^2+|b|^2=1
75    %              b = sqrt(1-a*a);
76    %          else
77    %              b = -sqrt(1-a*a);
78    %          end
79    %      else
80    %          a = a + abs(randn(1))*(1-a)*timestep; %Move closer to lower energy value
81    %          if (b>0)                              %Correct b such that |a|^2+|b|^2=1
82    %              b = sqrt(1-a*a);
83    %          else
84    %              b = -sqrt(1-a*a);
85    %          end
86    %      end
87    %*****************************************************************
88
89
90    %**** For rotation of pi/2 radians around z-axis, uncomment this block ****
91    %
92    %      if (t==5)
93    %          state = [a b]';
94    %          newstate = rotMat*state*ctranspose(rotMat);
95    %          a = newstate(1)
96    %          b = newstate(2)
97    %      end
98    %*************************************************************************
99
100 -      exSz(round(t/timestep),1) = Xt'*Sz*Xt;    %Determine expectation value of Sz
101 -      exSx(round(t/timestep),1) = Xt'*Sx*Xt;    %Determine expectation value of Sx
102 -      exSy(round(t/timestep),1) = Xt'*Sy*Xt;    %Determine expectation value of Sy
103 -  end
104
```

D.2.2 Ensemble of Spins in a Magnetic Field

```
%************************************************%
%*                                              *%
%*        nmrsimensemble.m                      *%
%*                                              *%
%*          Simulates an ensemble of            *%
%*          quantum 1/2-spins in a              *%
%*          magnetic field.                     *%
%*                                              *%
%*        INPUT: none                           *%
%*        OUTPUT: out                           *%
%*                                              *%
%*        Author: Derrick van Zyl               *%
%*                                              *%
%************************************************%

%clear workspace
clear;


%define quantum constants
gamma = 267.522e6;                %Gyromagnetic ratio of 1H (rad/(s.T))
gammaF19 = 2.517e8;               %Gyromagnetic ratio of 19F (rad/(s.T))
Sz = (0.5)*[1 0;0 -1];            %Pauli spin matrix, z-direction
Sx = (0.5)*[0 1;1 0];             %Pauli spin matrix, x-direction
Sy = (0.5)*[0 -sqrt(-1);sqrt(-1) 0];  %Pauli spin matrix, y-direction


%define simulation constants
time = 20;                        %Simulation Time (seconds)
timestep = 100e-6;                %Timestep (seconds)
Bz = 53.9e-6;                     %Magnetic field strength (z-direction) (Tesla)
rotAng = pi/2;                    %Angle by which spin is rotated (rad)
rotMat = [cos(rotAng/2) -sqrt(-1)*sin(rotAng/2); -sqrt(-1)*sin(rotAng/2) cos(rotAng/2)];
                                  %Rotation matrix (rotation around x-axis)
numSpins = 6;                     %number of spin 1/2 particles
gammavect = [gammaF19,gammaF19,gammaF19,gamma,gamma,gamma];

%define J-coupling constants
J=zeros(6);
J(2,1) = 8.5;
J(3,1) = 5;
J(4,1) = 2;
J(5,1) = 5;
J(6,1) = 8.5;
J(3,2) = 8;
J(4,2) = 2;
J(5,2) = 0;
J(6,2) = 2;
J(4,3) = 8;
J(5,3) = 2;
J(6,3) = 0;
J(5,4) = 8;
J(6,4) = 2;
J(6,5) = 8;

%Create spin operators
for i=1:numSpins                  %Create Izi and store in opSz{i}
    ans=1;
    for j=1:(i-1)
        ans = kron(ans,(0.5)*eye(2));
    end
    ans = kron(ans,Sz);
```

```
63 -        for j=(i+1):numSpins
64 -            ans=kron(ans,(0.5)*eye(2));
65 -        end
66 -        opSz{i} = 2^(numSpins-1)*ans;
67 -    end
68
69 -    for i=1:numSpins                    %Create Ixi and store in opSx{i}
70 -        ans=1;
71 -        for j=1:(i-1)
72 -            ans = kron(ans,(0.5)*eye(2));
73 -        end
74 -        ans = kron(ans,Sx);
75 -        for j=(i+1):numSpins
76 -            ans=kron(ans,(0.5)*eye(2));
77 -        end
78 -        opSx{i} = 2^(numSpins-1)*ans;
79 -    end
80
81 -    for i=1:numSpins                    %Create Iyi and store in opSy{i}
82 -        ans=1;
83 -        for j=1:(i-1)
84 -            ans = kron(ans,(0.5)*eye(2));
85 -        end
86 -        ans = kron(ans,Sy);
87 -        for j=(i+1):numSpins
88 -            ans=kron(ans,(0.5)*eye(2));
89 -        end
90 -        opSy{i} = 2^(numSpins-1)*ans;
91 -    end
92
93
94      %Create Hamiltonian
95 -    H=0;
96 -    for (i=1:numSpins)
97 -        H=H+(-Bz*gammavect(i)*opSz{i});
98 -    end
99
100     %---Uncomment this section for J-coupling simulations---
101 -    for (i=1:(numSpins-1))
102 -        for (j=(i+1):numSpins)
103 -            H=H + J(j,i)*2*pi*(opSx{i}*opSx{j}+opSy{i}*opSy{j}-opSz{i}*opSz{j});
104 -        end
105 -    end
106     %-------------------------------------------------------
107
108     %Create Density Matrix
109 -    densityMat = H;
110
111
112     %Create Observation matrix
113 -    Iobs=0;
114 -    for (i=1:numSpins)
115 -        Iobs=Iobs+opSx{i}+sqrt(-1)*opSy{i};
116 -    end
117
118
119     %Create Rotation matrix
120 -    R=eye(2);
121 -    for (i=2:numSpins)
122 -        R=kron(R,rotMat);
123 -    end
124
```

```
125
126     %create output vector
127 -   out = rand(1,round(time/timestep))';
128
129
130     %perform simulation
131 -   U = eye(2^numSpins);   %Create Evolution operator matrix
132 -   for (i=1:100)
133 -       for (m=1:i)
134 -           if (m==1)
135 -               Hprime = sqrt(-1)*timestep*H;
136 -           else
137 -               Hprime = Hprime*sqrt(-1)*timestep*H;
138 -           end
139 -       end
140 -       U = U + Hprime/factorial(i);
141 -   end
142
143 -   pt = R*densityMat*ctranspose(R);  %Rotate density matrix to start simulation
144
145 -   for (t=timestep:timestep:time)
146 -       pt =U*pt*ctranspose(U);           %Apply n evolution operators to density matrix
147 -       out(round(t/timestep)) = trace(Iobs*pt);    %Determine expectation value of Sx
148 -   end
149
150
```

D.3 C Program for Magnet Control Board

```
1       /*******************************************/
2       /*   Magnet Control Board Program          */
3       /*                                         */
4       /*         Control Board Software          */
5       /*                                         */
6       /*         AUTHOR: D.S. van Zyl            */
7       /*                                         */
8       /*******************************************/
9
10      //-------INCLUDE------//
11      #include <p18f2520.h>
12      #include <timers.h>
13      #include <delays.h>
14
15
16
17      //------Global Variables------//
18      int counter;
19      int time;
20
21      //------Function Prototypes------//
22      void timer_interrupt(void);
23      void PICinit(void);
24      void interruptInit(void);
25      void startupDefult(void);
26
27
28
27
28
29      //------IC Settings------//
30      #pragma config OSC = INTIO67 //Set oscillator to internal oscillator, use RA6 and RA7 as ports
31      #pragma config WDT = OFF //Disable watchdog timer
32      #pragma config PBADEN = OFF //set Port B as Digital ports on reset
33      #pragma config MCLRE = OFF//disable MCLR reset
```

```
#pragma config LVP = OFF //Single-Supply ICSP disabled

#pragma code low_priority_vector=0x0018 //"...the low priority interrupt vector is at 0018h..."
void low_priority_interrupt (void)
{
 _asm GOTO timer_interrupt _endasm
}
#pragma code
#pragma interruptlow timer_interrupt
void timer_interrupt (void)
{
    INTCONbits.TMR0IF=0; //clear TMR0 overflow flag bit
    counter=counter+4;
    if (counter >= 3125) {  //every 0.1 second (8MHz/4/256 = 7812.5; counter increments by 4 every interrupt)
        counter = 0;
        time++;
    }
}



//===========================MAIN PROGRAM==============================//
void main()
{
   unsigned char numberOfRuns;
   int i;

   PICinit();
   interruptInit();
   OpenTimer0 (TIMER_INT_ON & T0_SOURCE_INT & T0_8BIT & T1_PS_1_1);
                                                    // Initialize timer0
                                                    //        (generate interrupt when counter overflows,
                                                    //        set counter size to 8 bits,
                                                    //        set clock prescaper to 1:1)
   startupDefult();

   while(1) {
        if (PORTAbits.RA0==0) {     //If button is pressed
            Delay10KTCYx(10);       //avoid button bounce
            while (PORTAbits.RA0==0);       //wait until button is released
            Delay10KTCYx(10);       //avoid button bounce
            PORTBbits.RB0 = 0; //switch off "ready" LED
            PORTBbits.RB1 = 1; //switch on "working" LED
            numberOfRuns=(~PORTC)+1;  //Read number of runs off DIP switches.
            time=0;  //Set time to 0;
            for (i=0; i< numberOfRuns; i++) {
                PORTBbits.RB4 = 1; //switch on pre-polarizing magnetic field
                while (time <= 100);   //wait for 10 seconds
                time = 0;
                PORTBbits.RB4 = 0; //switch ff pre-polarizing magnetic field
                while (time <= 5)   //wait for 0.5 seconds
                time = 0;
                PORTBbits.RB3 = 1; //switch on RF (ULF) magnetic field
                while (time < 10);  //wait for 1 second
                time = 0;
                PORTBbits.RB3 = 0; //switch off RF (ULF) magnetic field
                while (time < 1);   //wait for 0.1 second
                time = 0;
                PORTBbits.RB2 = 1; //connect measurement coil
                while (time < 5);   //wait for 5 seconds
                time = 0;
                PORTBbits.RB2 = 0; //disconnect measurement coil
                while (time < 100); //wait for 10 second
                time = 0;
            }
            PORTBbits.RB1 = 0; //switch off "working" LED
            PORTBbits.RB0 = 1; //switch on "ready" LED
        }

   }
}
//=====================================================================//
```

```
108  //----------------------Function Definitions--------------------------//
109
110  /*********************************************/
111  /*   void PICinit (void)                     */
112  /*                                           */
113  /*         Initializes PIC oscillator and    */
114  /*         port registers.                   */
115  /*                                           */
116  /*         INPUT: NONE                       */
117  /*         OUTPUT: NONE                      */
118  /*                                           */
119  /*********************************************/
120  void PICinit(void)
121  {
122      //Set internal oscillator
123        //Set IRCF<2:0> to 111 to select 8MHz opperation
124        OSCCONbits.IRCF2 = 1;
125        OSCCONbits.IRCF1 = 1;
126        OSCCONbits.IRCF0 = 1;
127
128
129      //Set all ports to DIGTAL
130        ADCON1bits.PCFG0 = 1;
131        ADCON1bits.PCFG1 = 1;
132        ADCON1bits.PCFG2 = 1;
133        ADCON1bits.PCFG3 = 1;
134
135      //Initialize Ports
136        //PORTA
137        TRISAbits.TRISA0 = 1; //Make RA0 an input
138
139        //PORTB
140        TRISBbits.TRISB0 = 0; //Make RB0 an output
141        TRISBbits.TRISB1 = 0; //Make RB1 an output
142        TRISBbits.TRISB2 = 0; //Make RB2 an output
143        TRISBbits.TRISB3 = 0; //Make RB3 an output
144        TRISBbits.TRISB4 = 0; //Make RB4 an output
145
146        //PORTC
147        TRISCbits.TRISC0 = 1; //Make RC0 an input
148        TRISCbits.TRISC1 = 1; //Make RC1 an input
149        TRISCbits.TRISC2 = 1; //Make RC2 an input
150        TRISCbits.TRISC3 = 1; //Make RC3 an input
151        TRISCbits.TRISC4 = 1; //Make RC4 an input
152        TRISCbits.TRISC5 = 1; //Make RC5 an input
153        TRISCbits.TRISC6 = 1; //Make RC6 an input
154        TRISCbits.TRISC7 = 1; //Make RC7 an input
155
156  }
157
158
159
160  /*********************************************/
161  /*   void interruptInit (void)               */
162  /*         Initializes PIC interrupt         */
163  /*         registers.                        */
164  /*                                           */
165  /*         INPUT: NONE                       */
166  /*         OUTPUT: NONE                      */
167  /*                                           */
168  /*********************************************/
169  void interruptInit(void)
170  {
171      RCONbits.IPEN=1; //enable priority levels on interrupts
172      INTCONbits.GIE=1; //enables all high priority interrupts
173      INTCONbits.PEIE=1; //enables all low priority interrupts
174      INTCON2bits.TMR0IP=0; //set TMR0 overflow interrupt priority to LOW
175      INTCONbits.TMR0IE=1; //enable TMR0 overflow interrupt
176      INTCONbits.TMR0IF=0; //clear TMR0 overflow flag bit
177  }
178
179
180
```

```
181  /*********************************************/
182  /*   void startupDefault (void)              */
183  /*         Initializes PIC ports to default  */
184  /*         initial values.                   */
185  /*                                           */
186  /*         INPUT: NONE                       */
187  /*         OUTPUT: NONE                      */
188  /*                                           */
189  /*********************************************/
190  void startupDefult(void)
191  {
192      PORTBbits.RB0 = 0; //switch off "ready" LED
193      PORTBbits.RB1 = 1; //switch on "working" LED
194      PORTBbits.RB2 = 0; //disconnect measurement coil
195      PORTBbits.RB3 = 0; //switch off RF magnetic field
196      PORTBbits.RB4 = 0; //switch off pre-polarizing magnetic field
197      Delay10KTCYx(50); //wait a few mili seconds for everything to stabalize
198      PORTBbits.RB1 = 0; //switch off "working" LED
199      PORTBbits.RB0 = 1; //switch on "ready" LED
200  }
```

Appendix E

Datasheets

E.1 Introduction

In this appendix the datasheets of the most important components used duing this study is listed. Note that only the relevant parts of each datasheet are listed.

E.2 PIC18F2520

PIC18F2420/2520/4420/4520
Data Sheet

28/40/44-Pin Enhanced Flash Microcontrollers with 10-Bit A/D and nanoWatt Technology

Note the following details of the code protection feature on Microchip devices:

- Microchip products meet the specification contained in their particular Microchip Data Sheet.
- Microchip believes that its family of products is one of the most secure families of its kind on the market today, when used in the intended manner and under normal conditions.
- There are dishonest and possibly illegal methods used to breach the code protection feature. All of these methods, to our knowledge, require using the Microchip products in a manner outside the operating specifications contained in Microchip's Data Sheets. Most likely, the person doing so is engaged in theft of intellectual property.
- Microchip is willing to work with the customer who is concerned about the integrity of their code.
- Neither Microchip nor any other semiconductor manufacturer can guarantee the security of their code. Code protection does not mean that we are guaranteeing the product as "unbreakable."

Code protection is constantly evolving. We at Microchip are committed to continuously improving the code protection features of our products. Attempts to break Microchip's code protection feature may be a violation of the Digital Millennium Copyright Act. If such acts allow unauthorized access to your software or other copyrighted work, you may have a right to sue for relief under that Act.

Trademarks

QUALITY MANAGEMENT SYSTEM
CERTIFIED BY DNV
ISO/TS 16949:2002

Microchip received ISO/TS-16949:2002 certification for its worldwide headquarters, design and wafer fabrication facilities in Chandler and Tempe, Arizona; Gresham, Oregon and design centers in California and India. The Company's quality system processes and procedures are for its PIC® MCUs and dsPIC® DSCs, KEELOQ® code hopping devices, Serial EEPROMs, microperipherals, nonvolatile memory and analog products. In addition, Microchip's quality system for the design and manufacture of development systems is ISO 9001:2000 certified.

PIC18F2420/2520/4420/4520

28/40/44-Pin Enhanced Flash Microcontrollers with 10-Bit A/D and nanoWatt Technology

Power Management Features:

- Run: CPU on, Peripherals on
- Idle: CPU off, Peripherals on
- Sleep: CPU off, Peripherals off
- Ultra Low 50nA Input Leakage
- Run mode Currents Down to 11 μA Typical
- Idle mode Currents Down to 2.5 μA Typical
- Sleep mode Current Down to 100 nA Typical
- Timer1 Oscillator: 900 nA, 32 kHz, 2V
- Watchdog Timer: 1.4 μA, 2V Typical
- Two-Speed Oscillator Start-up

Flexible Oscillator Structure:

- Four Crystal modes, up to 40 MHz
- 4x Phase Lock Loop (PLL) – Available for Crystal and Internal Oscillators
- Two External RC modes, up to 4 MHz
- Two External Clock modes, up to 40 MHz
- Internal Oscillator Block:
  - Fast wake from Sleep and Idle, 1 μs typical
  - 8 use-selectable frequencies, from 31 kHz to 8 MHz
  - Provides a complete range of clock speeds from 31 kHz to 32 MHz when used with PLL
  - User-tunable to compensate for frequency drift
- Secondary Oscillator using Timer1 @ 32 kHz
- Fail-Safe Clock Monitor:
  - Allows for safe shutdown if peripheral clock stops

Peripheral Highlights:

- High-Current Sink/Source 25 mA/25 mA
- Three Programmable External Interrupts
- Four Input Change Interrupts
- Up to 2 Capture/Compare/PWM (CCP) modules, one with Auto-Shutdown (28-pin devices)
- Enhanced Capture/Compare/PWM (ECCP) module (40/44-pin devices only):
  - One, two or four PWM outputs
  - Selectable polarity
  - Programmable dead time
  - Auto-shutdown and auto-restart

Peripheral Highlights (Continued):

- Master Synchronous Serial Port (MSSP) module Supporting 3-Wire SPI (all 4 modes) and I^2C™ Master and Slave modes
- Enhanced Addressable USART module:
  - Supports RS-485, RS-232 and LIN/J2602
  - RS-232 operation using internal oscillator block (no external crystal required)
  - Auto-wake-up on Start bit
  - Auto-Baud Detect
- 10-Bit, up to 13-Channel Analog-to-Digital (A/D) Converter module:
  - Auto-acquisition capability
  - Conversion available during Sleep
- Dual Analog Comparators with Input Multiplexing
- Programmable 16-Level High/Low-Voltage Detection (HLVD) module:
  - Supports interrupt on High/Low-Voltage Detection

Special Microcontroller Features:

- C Compiler Optimized Architecture:
  - Optional extended instruction set designed to optimize re-entrant code
- 100,000 Erase/Write Cycle Enhanced Flash Program Memory Typical
- 1,000,000 Erase/Write Cycle Data EEPROM Memory Typical
- Flash/Data EEPROM Retention: 100 Years Typical
- Self-Programmable under Software Control
- Priority Levels for Interrupts
- 8 x 8 Single-Cycle Hardware Multiplier
- Extended Watchdog Timer (WDT):
  - Programmable period from 4 ms to 131s
- Single-Supply 5V In-Circuit Serial Programming™ (ICSP™) via Two Pins
- In-Circuit Debug (ICD) via Two Pins
- Wide Operating Voltage Range: 2.0V to 5.5V
- Programmable Brown-out Reset (BOR) with Software Enable Option

Device	Program Memory		Data Memory		I/O	10-Bit A/D (ch)	CCP/ ECCP (PWM)	MSSP		EUSART	Comp.	Timers 8/16-Bit
	Flash (bytes)	# Single-Word Instructions	SRAM (bytes)	EEPROM (bytes)				SPI	Master I^2C™			
PIC18F2420	16K	8192	768	256	25	10	2/0	Y	Y	1	2	1/3
PIC18F2520	32K	16384	1536	256	25	10	2/0	Y	Y	1	2	1/3
PIC18F4420	16K	8192	768	256	36	13	1/1	Y	Y	1	2	1/3
PIC18F4520	32K	16384	1536	256	36	13	1/1	Y	Y	1	2	1/3

Pin Diagrams

28-Pin SPDIP, SOIC

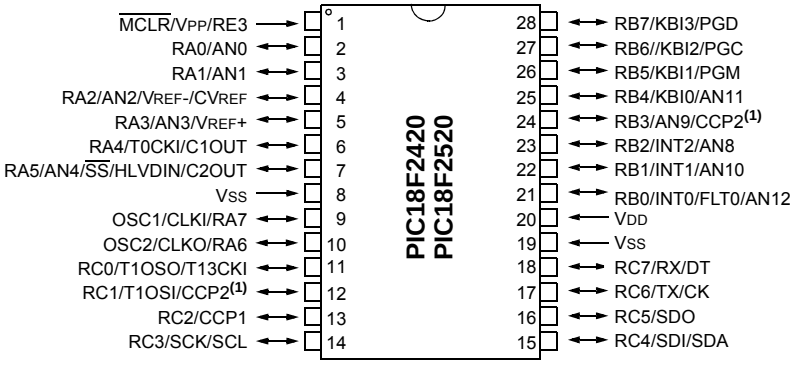

28-Pin QFN

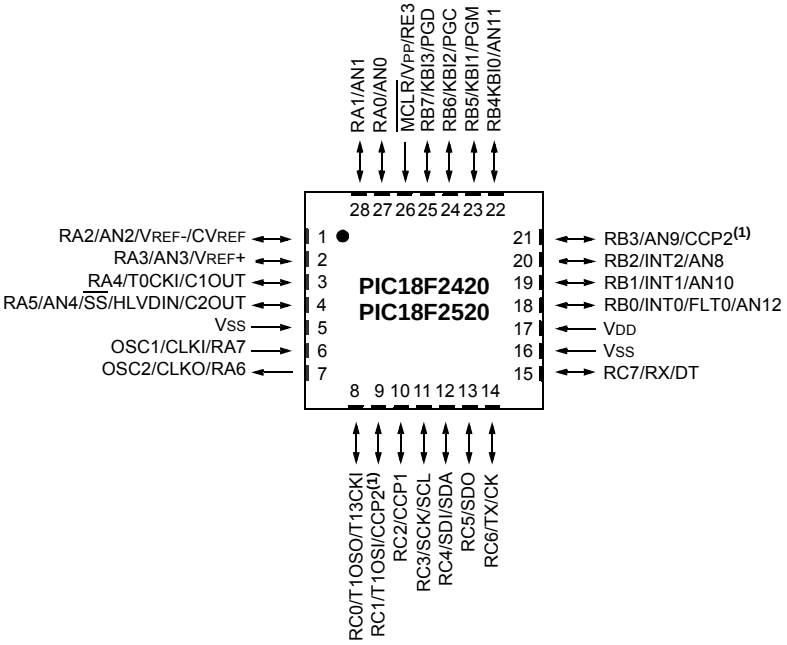

40-Pin PDIP

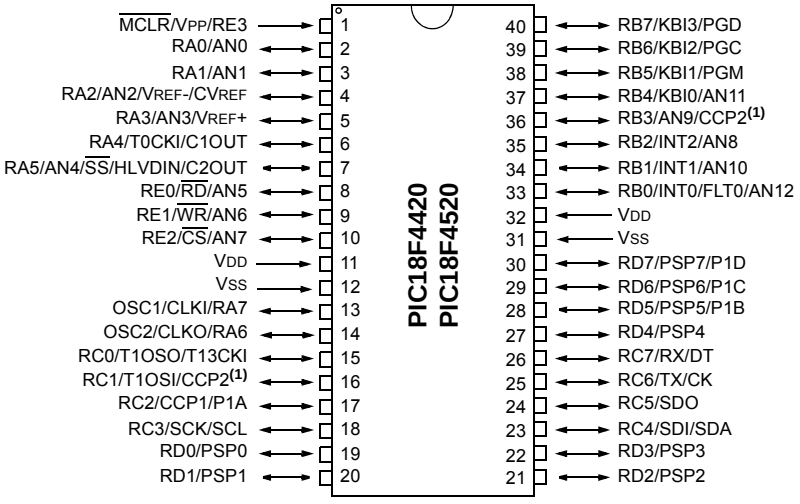

Note 1: RB3 is the alternate pin for CCP2 multiplexing.

TABLE 1-1: DEVICE FEATURES

Features	PIC18F2420	PIC18F2520	PIC18F4420	PIC18F4520
Operating Frequency	DC – 40 MHz	DC – 40 MHz	DC – 40 MHz	DC – 40 MHz
Program Memory (Bytes)	16384	32768	16384	32768
Program Memory (Instructions)	8192	16384	8192	16384
Data Memory (Bytes)	768	1536	768	1536
Data EEPROM Memory (Bytes)	256	256	256	256
Interrupt Sources	19	19	20	20
I/O Ports	Ports A, B, C, (E)	Ports A, B, C, (E)	Ports A, B, C, D, E	Ports A, B, C, D, E
Timers	4	4	4	4
Capture/Compare/PWM Modules	2	2	1	1
Enhanced Capture/Compare/PWM Modules	0	0	1	1
Serial Communications	MSSP, Enhanced USART	MSSP, Enhanced USART	MSSP, Enhanced USART	MSSP, Enhanced USART
Parallel Communications (PSP)	No	No	Yes	Yes
10-Bit Analog-to-Digital Module	10 Input Channels	10 Input Channels	13 Input Channels	13 Input Channels
Resets (and Delays)	POR, BOR, RESET Instruction, Stack Full, Stack Underflow (PWRT, OST), MCLR (optional), WDT	POR, BOR, RESET Instruction, Stack Full, Stack Underflow (PWRT, OST), MCLR (optional), WDT	POR, BOR, RESET Instruction, Stack Full, Stack Underflow (PWRT, OST), MCLR (optional), WDT	POR, BOR, RESET Instruction, Stack Full, Stack Underflow (PWRT, OST), MCLR (optional), WDT
Programmable High/Low-Voltage Detect	Yes	Yes	Yes	Yes
Programmable Brown-out Reset	Yes	Yes	Yes	Yes
Instruction Set	75 Instructions; 83 with Extended Instruction Set Enabled	75 Instructions; 83 with Extended Instruction Set Enabled	75 Instructions; 83 with Extended Instruction Set Enabled	75 Instructions; 83 with Extended Instruction Set Enabled
Packages	28-Pin SPDIP 28-Pin SOIC 28-Pin QFN	28-Pin SPDIP 28-Pin SOIC 28-Pin QFN	40-Pin PDIP 44-Pin QFN 44-Pin TQFP	40-Pin PDIP 44-Pin QFN 44-Pin TQFP

TABLE 1-2: PIC18F2420/2520 PINOUT I/O DESCRIPTIONS

Pin Name	Pin Number		Pin Type	Buffer Type	Description
	SPDIP, SOIC	QFN			
MCLR/VPP/RE3	1	26			Master Clear (input) or programming voltage (input).
MCLR			I	ST	Master Clear (Reset) input. This pin is an active-low Reset to the device.
VPP			P		Programming voltage input.
RE3			I	ST	Digital input.
OSC1/CLKI/RA7	9	6			Oscillator crystal or external clock input.
OSC1			I	ST	Oscillator crystal input or external clock source input. ST buffer when configured in RC mode; CMOS otherwise.
CLKI			I	CMOS	External clock source input. Always associated with pin function, OSC1. (See related OSC1/CLKI, OSC2/CLKO pins.)
RA7			I/O	TTL	General purpose I/O pin.
OSC2/CLKO/RA6	10	7			Oscillator crystal or clock output.
OSC2			O	—	Oscillator crystal output. Connects to crystal or resonator in Crystal Oscillator mode.
CLKO			O	—	In RC mode, OSC2 pin outputs CLKO which has 1/4 the frequency of OSC1 and denotes the instruction cycle rate.
RA6			I/O	TTL	General purpose I/O pin.

Legend: TTL = TTL compatible input
CMOS = CMOS compatible input or output
ST = Schmitt Trigger input with CMOS levels
I = Input
O = Output
P = Power

Note 1: Default assignment for CCP2 when Configuration bit, CCP2MX, is set.
2: Alternate assignment for CCP2 when Configuration bit, CCP2MX, is cleared.

TABLE 1-2: PIC18F2420/2520 PINOUT I/O DESCRIPTIONS (CONTINUED)

Pin Name	Pin Number		Pin Type	Buffer Type	Description
	SPDIP, SOIC	QFN			
					PORTA is a bidirectional I/O port.
RA0/AN0	2	27			
RA0			I/O	TTL	Digital I/O.
AN0			I	Analog	Analog input 0.
RA1/AN1	3	28			
RA1			I/O	TTL	Digital I/O.
AN1			I	Analog	Analog input 1.
RA2/AN2/VREF-/CVREF	4	1			
RA2			I/O	TTL	Digital I/O.
AN2			I	Analog	Analog input 2.
VREF-			I	Analog	A/D reference voltage (low) input.
CVREF			O	Analog	Comparator reference voltage output.
RA3/AN3/VREF+	5	2			
RA3			I/O	TTL	Digital I/O.
AN3			I	Analog	Analog input 3.
VREF+			I	Analog	A/D reference voltage (high) input.
RA4/T0CKI/C1OUT	6	3			
RA4			I/O	ST	Digital I/O.
T0CKI			I	ST	Timer0 external clock input.
C1OUT			O	—	Comparator 1 output.
RA5/AN4/$\overline{SS}$/HLVDIN/ C2OUT	7	4			
RA5			I/O	TTL	Digital I/O.
AN4			I	Analog	Analog input 4.
$\overline{SS}$			I	TTL	SPI slave select input.
HLVDIN			I	Analog	High/Low-Voltage Detect input.
C2OUT			O	—	Comparator 2 output.
RA6					See the OSC2/CLKO/RA6 pin.
RA7					See the OSC1/CLKI/RA7 pin.

Legend: TTL = TTL compatible input; CMOS = CMOS compatible input or output; ST = Schmitt Trigger input with CMOS levels; I = Input; O = Output; P = Power

Note 1: Default assignment for CCP2 when Configuration bit, CCP2MX, is set.
2: Alternate assignment for CCP2 when Configuration bit, CCP2MX, is cleared.

TABLE 1-2: PIC18F2420/2520 PINOUT I/O DESCRIPTIONS (CONTINUED)

Pin Name	Pin Number		Pin Type	Buffer Type	Description
	SPDIP, SOIC	QFN			
					PORTB is a bidirectional I/O port. PORTB can be software programmed for internal weak pull-ups on all inputs.
RB0/INT0/FLT0/AN12	21	18			
RB0			I/O	TTL	Digital I/O.
INT0			I	ST	External interrupt 0.
FLT0			I	ST	PWM Fault input for CCP1.
AN12			I	Analog	Analog input 12.
RB1/INT1/AN10	22	19			
RB1			I/O	TTL	Digital I/O.
INT1			I	ST	External interrupt 1.
AN10			I	Analog	Analog input 10.
RB2/INT2/AN8	23	20			
RB2			I/O	TTL	Digital I/O.
INT2			I	ST	External interrupt 2.
AN8			I	Analog	Analog input 8.
RB3/AN9/CCP2	24	21			
RB3			I/O	TTL	Digital I/O.
AN9			I	Analog	Analog input 9.
CCP2(1)			I/O	ST	Capture 2 input/Compare 2 output/PWM2 output.
RB4/KBI0/AN11	25	22			
RB4			I/O	TTL	Digital I/O.
KBI0			I	TTL	Interrupt-on-change pin.
AN11			I	Analog	Analog input 11.
RB5/KBI1/PGM	26	23			
RB5			I/O	TTL	Digital I/O.
KBI1			I	TTL	Interrupt-on-change pin.
PGM			I/O	ST	Low-Voltage ICSP™ Programming enable pin.
RB6/KBI2/PGC	27	24			
RB6			I/O	TTL	Digital I/O.
KBI2			I	TTL	Interrupt-on-change pin.
PGC			I/O	ST	In-Circuit Debugger and ICSP programming clock pin.
RB7/KBI3/PGD	28	25			
RB7			I/O	TTL	Digital I/O.
KBI3			I	TTL	Interrupt-on-change pin.
PGD			I/O	ST	In-Circuit Debugger and ICSP programming data pin.

Legend: TTL = TTL compatible input; CMOS = CMOS compatible input or output; ST = Schmitt Trigger input with CMOS levels; I = Input; O = Output; P = Power

Note 1: Default assignment for CCP2 when Configuration bit, CCP2MX, is set.
2: Alternate assignment for CCP2 when Configuration bit, CCP2MX, is cleared.

TABLE 1-2: PIC18F2420/2520 PINOUT I/O DESCRIPTIONS (CONTINUED)

Pin Name	Pin Number		Pin Type	Buffer Type	Description
	SPDIP, SOIC	QFN			
					PORTC is a bidirectional I/O port.
RC0/T1OSO/T13CKI	11	8			
RC0			I/O	ST	Digital I/O.
T1OSO			O	—	Timer1 oscillator output.
T13CKI			I	ST	Timer1/Timer3 external clock input.
RC1/T1OSI/CCP2	12	9			
RC1			I/O	ST	Digital I/O.
T1OSI			I	Analog	Timer1 oscillator input.
CCP2(2)			I/O	ST	Capture 2 input/Compare 2 output/PWM2 output.
RC2/CCP1	13	10			
RC2			I/O	ST	Digital I/O.
CCP1			I/O	ST	Capture 1 input/Compare 1 output/PWM1 output.
RC3/SCK/SCL	14	11			
RC3			I/O	ST	Digital I/O.
SCK			I/O	ST	Synchronous serial clock input/output for SPI mode.
SCL			I/O	ST	Synchronous serial clock input/output for I^2C™ mode.
RC4/SDI/SDA	15	12			
RC4			I/O	ST	Digital I/O.
SDI			I	ST	SPI data in.
SDA			I/O	ST	I^2C data I/O.
RC5/SDO	16	13			
RC5			I/O	ST	Digital I/O.
SDO			O	—	SPI data out.
RC6/TX/CK	17	14			
RC6			I/O	ST	Digital I/O.
TX			O	—	EUSART asynchronous transmit.
CK			I/O	ST	EUSART synchronous clock (see related RX/DT).
RC7/RX/DT	18	15			
RC7			I/O	ST	Digital I/O.
RX			I	ST	EUSART asynchronous receive.
DT			I/O	ST	EUSART synchronous data (see related TX/CK).
RE3	—	—	—	—	See $\overline{MCLR}$/VPP/RE3 pin.
VSS	8, 19	5, 16	P	—	Ground reference for logic and I/O pins.
VDD	20	17	P	—	Positive supply for logic and I/O pins.

Legend: TTL = TTL compatible input
CMOS = CMOS compatible input or output
ST = Schmitt Trigger input with CMOS levels
I = Input
O = Output
P = Power

Note 1: Default assignment for CCP2 when Configuration bit, CCP2MX, is set.
2: Alternate assignment for CCP2 when Configuration bit, CCP2MX, is cleared.

TABLE 1-3: PIC18F4420/4520 PINOUT I/O DESCRIPTIONS

Pin Name	Pin Number			Pin Type	Buffer Type	Description
	PDIP	QFN	TQFP			
MCLR/VPP/RE3	1	18	18			Master Clear (input) or programming voltage (input).
MCLR				I	ST	Master Clear (Reset) input. This pin is an active-low Reset to the device.
VPP				P		Programming voltage input.
RE3				I	ST	Digital input.
OSC1/CLKI/RA7	13	32	30			Oscillator crystal or external clock input.
OSC1				I	ST	Oscillator crystal input or external clock source input. ST buffer when configured in RC mode; analog otherwise.
CLKI				I	CMOS	External clock source input. Always associated with pin function, OSC1. (See related OSC1/CLKI, OSC2/CLKO pins.)
RA7				I/O	TTL	General purpose I/O pin.
OSC2/CLKO/RA6	14	33	31			Oscillator crystal or clock output.
OSC2				O	—	Oscillator crystal output. Connects to crystal or resonator in Crystal Oscillator mode.
CLKO				O	—	In RC mode, OSC2 pin outputs CLKO which has 1/4 the frequency of OSC1 and denotes the instruction cycle rate.
RA6				I/O	TTL	General purpose I/O pin.

Legend: TTL = TTL compatible input; CMOS = CMOS compatible input or output; ST = Schmitt Trigger input with CMOS levels; I = Input; O = Output; P = Power

Note 1: Default assignment for CCP2 when Configuration bit, CCP2MX, is set.
2: Alternate assignment for CCP2 when Configuration bit, CCP2MX, is cleared.

2.0 OSCILLATOR CONFIGURATIONS

2.1 Oscillator Types

PIC18F2420/2520/4420/4520 devices can be operated in ten different oscillator modes. The user can program the Configuration bits, FOSC<3:0>, in Configuration Register 1H to select one of these ten modes:

1. LP Low-Power Crystal
2. XT Crystal/Resonator
3. HS High-Speed Crystal/Resonator
4. HSPLL High-Speed Crystal/Resonator with PLL Enabled
5. RC External Resistor/Capacitor with FOSC/4 Output on RA6
6. RCIO External Resistor/Capacitor with I/O on RA6
7. INTIO1 Internal Oscillator with FOSC/4 Output on RA6 and I/O on RA7
8. INTIO2 Internal Oscillator with I/O on RA6 and RA7
9. EC External Clock with FOSC/4 Output
10. ECIO External Clock with I/O on RA6

2.2 Crystal Oscillator/Ceramic Resonators

In XT, LP, HS or HSPLL Oscillator modes, a crystal or ceramic resonator is connected to the OSC1 and OSC2 pins to establish oscillation. Figure 2-1 shows the pin connections.

The oscillator design requires the use of a parallel cut crystal.

Note:	Use of a series cut crystal may give a frequency out of the crystal manufacturer's specifications.

FIGURE 2-1: CRYSTAL/CERAMIC RESONATOR OPERATION (XT, LP, HS OR HSPLL CONFIGURATION)

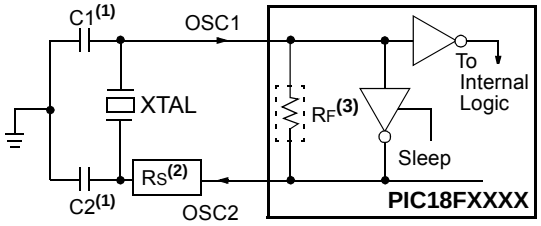

Note 1: See Table 2-1 and Table 2-2 for initial values of C1 and C2.

2: A series resistor (RS) may be required for AT strip cut crystals.

3: RF varies with the oscillator mode chosen.

TABLE 2-1: CAPACITOR SELECTION FOR CERAMIC RESONATORS

Typical Capacitor Values Used:			
Mode	**Freq**	**OSC1**	**OSC2**
XT	3.58 MHz	15 pF	15 pF
	4.19 MHz	15 pF	15 pF
	4 MHz	30 pF	30 pF
	4 MHz	50 pF	50 pF

Capacitor values are for design guidance only.

Different capacitor values may be required to produce acceptable oscillator operation. The user should test the performance of the oscillator over the expected VDD and temperature range for the application.

See the notes following Table 2-2 for additional information.

Note:	When using resonators with frequencies above 3.5 MHz, the use of HS mode, rather than XT mode, is recommended. HS mode may be used at any VDD for which the controller is rated. If HS is selected, it is possible that the gain of the oscillator will overdrive the resonator. Therefore, a series resistor should be placed between the OSC2 pin and the resonator. As a good starting point, the recommended value of RS is 330Ω.

TABLE 2-2: CAPACITOR SELECTION FOR CRYSTAL OSCILLATOR

Osc Type	Crystal Freq	Typical Capacitor Values Tested:	
		C1	C2
LP	32 kHz	30 pF	30 pF
XT	1 MHz	15 pF	15 pF
	4 MHz	15 pF	15 pF
HS	4 MHz	15 pF	15 pF
	10 MHz	15 pF	15 pF
	20 MHz	15 pF	15 pF
	25 MHz	0 pF	5 pF
	25 MHz	15 pF	15 pF

Capacitor values are for design guidance only.

These capacitors were tested with the crystals listed below for basic start-up and operation. **These values are not optimized.**

Different capacitor values may be required to produce acceptable oscillator operation. The user should test the performance of the oscillator over the expected VDD and temperature range for the application.

See the notes following this table for additional information.

Crystals Used:	
32 kHz	4 MHz
25 MHz	10 MHz
1 MHz	20 MHz

Note 1: Higher capacitance increases the stability of the oscillator but also increases the start-up time.

2: When operating below 3V VDD, or when using certain ceramic resonators at any voltage, it may be necessary to use the HS mode or switch to a crystal oscillator.

3: Since each resonator/crystal has its own characteristics, the user should consult the resonator/crystal manufacturer for appropriate values of external components.

4: Rs may be required to avoid overdriving crystals with low drive level specification.

5: Always verify oscillator performance over the VDD and temperature range that is expected for the application.

An external clock source may also be connected to the OSC1 pin in the HS mode, as shown in Figure 2-2.

FIGURE 2-2: EXTERNAL CLOCK INPUT OPERATION (HS OSC CONFIGURATION)

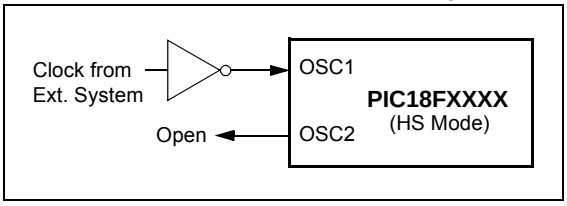

2.3 External Clock Input

The EC and ECIO Oscillator modes require an external clock source to be connected to the OSC1 pin. There is no oscillator start-up time required after a Power-on Reset or after an exit from Sleep mode.

In the EC Oscillator mode, the oscillator frequency divided by 4 is available on the OSC2 pin. This signal may be used for test purposes or to synchronize other logic. Figure 2-3 shows the pin connections for the EC Oscillator mode.

FIGURE 2-3: EXTERNAL CLOCK INPUT OPERATION (EC CONFIGURATION)

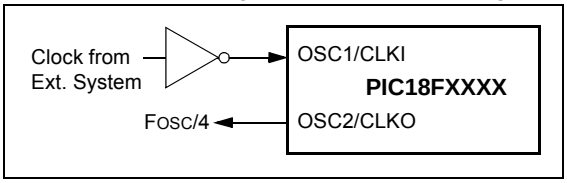

The ECIO Oscillator mode functions like the EC mode, except that the OSC2 pin becomes an additional general purpose I/O pin. The I/O pin becomes bit 6 of PORTA (RA6). Figure 2-4 shows the pin connections for the ECIO Oscillator mode.

FIGURE 2-4: EXTERNAL CLOCK INPUT OPERATION (ECIO CONFIGURATION)

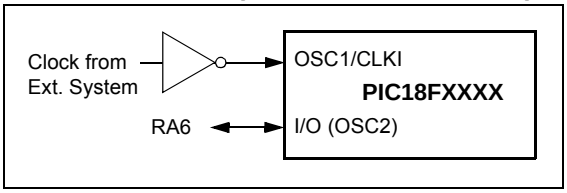

2.4 RC Oscillator

For timing insensitive applications, the "RC" and "RCIO" device options offer additional cost savings. The actual oscillator frequency is a function of several factors:

- supply voltage
- values of the external resistor (REXT) and capacitor (CEXT)
- operating temperature

Given the same device, operating voltage and temperature and component values, there will also be unit-to-unit frequency variations. These are due to factors such as:

- normal manufacturing variation
- difference in lead frame capacitance between package types (especially for low CEXT values)
- variations within the tolerance of limits of REXT and CEXT

In the RC Oscillator mode, the oscillator frequency divided by 4 is available on the OSC2 pin. This signal may be used for test purposes or to synchronize other logic. Figure 2-5 shows how the R/C combination is connected.

FIGURE 2-5: RC OSCILLATOR MODE

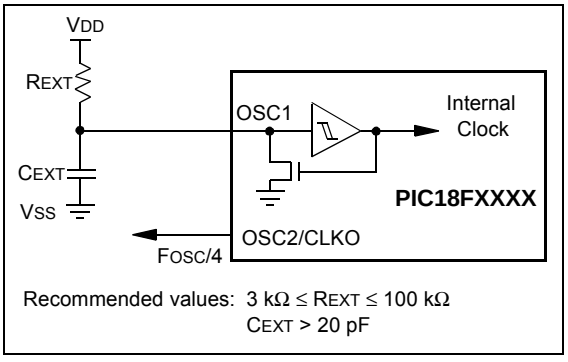

The RCIO Oscillator mode (Figure 2-6) functions like the RC mode, except that the OSC2 pin becomes an additional general purpose I/O pin. The I/O pin becomes bit 6 of PORTA (RA6).

FIGURE 2-6: RCIO OSCILLATOR MODE

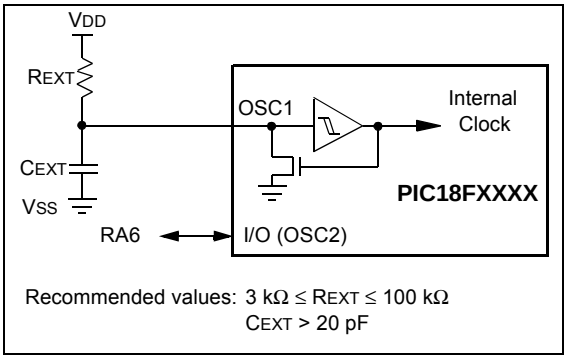

2.5 PLL Frequency Multiplier

A Phase Locked Loop (PLL) circuit is provided as an option for users who wish to use a lower frequency oscillator circuit or to clock the device up to its highest rated frequency from a crystal oscillator. This may be useful for customers who are concerned with EMI due to high-frequency crystals or users who require higher clock speeds from an internal oscillator.

2.5.1 HSPLL OSCILLATOR MODE

The HSPLL mode makes use of the HS Oscillator mode for frequencies up to 10 MHz. A PLL then multiplies the oscillator output frequency by 4 to produce an internal clock frequency up to 40 MHz. The PLLEN bit is not available in this oscillator mode.

The PLL is only available to the crystal oscillator when the FOSC<3:0> Configuration bits are programmed for HSPLL mode (= 0110).

FIGURE 2-7: PLL BLOCK DIAGRAM (HS MODE)

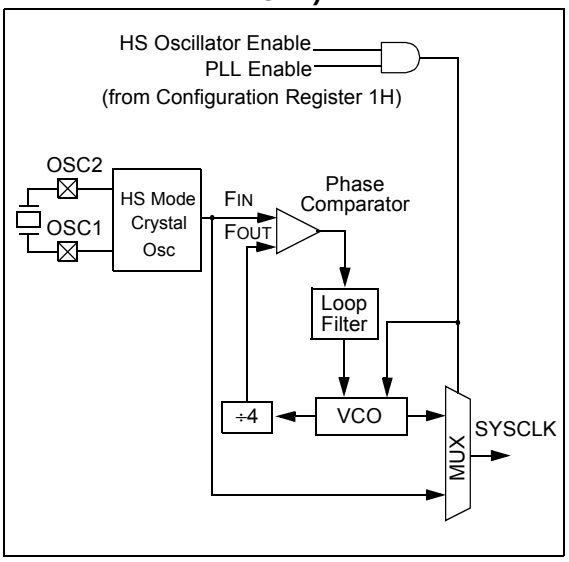

2.5.2 PLL AND INTOSC

The PLL is also available to the internal oscillator block in selected oscillator modes. In this configuration, the PLL is enabled in software and generates a clock output of up to 32 MHz. The operation of INTOSC with the PLL is described in **Section 2.6.4 "PLL in INTOSC Modes"**.

2.6 Internal Oscillator Block

The PIC18F2420/2520/4420/4520 devices include an internal oscillator block which generates two different clock signals; either can be used as the microcontroller's clock source. This may eliminate the need for external oscillator circuits on the OSC1 and/or OSC2 pins.

The main output (INTOSC) is an 8 MHz clock source which can be used to directly drive the device clock. It also drives a postscaler which can provide a range of clock frequencies from 31 kHz to 4 MHz. The INTOSC output is enabled when a clock frequency from 125 kHz to 8 MHz is selected.

The other clock source is the internal RC oscillator (INTRC), which provides a nominal 31 kHz output. INTRC is enabled if it is selected as the device clock source; it is also enabled automatically when any of the following are enabled:

- Power-up Timer
- Fail-Safe Clock Monitor
- Watchdog Timer
- Two-Speed Start-up

These features are discussed in greater detail in **Section 23.0 "Special Features of the CPU"**.

The clock source frequency (INTOSC direct, INTRC direct or INTOSC postscaler) is selected by configuring the IRCF bits of the OSCCON register (page 30).

2.6.1 INTIO MODES

Using the internal oscillator as the clock source eliminates the need for up to two external oscillator pins, which can then be used for digital I/O. Two distinct configurations are available:

- In INTIO1 mode, the OSC2 pin outputs FOSC/4, while OSC1 functions as RA7 for digital input and output.
- In INTIO2 mode, OSC1 functions as RA7 and OSC2 functions as RA6, both for digital input and output.

2.6.2 INTOSC OUTPUT FREQUENCY

The internal oscillator block is calibrated at the factory to produce an INTOSC output frequency of 8.0 MHz.

The INTRC oscillator operates independently of the INTOSC source. Any changes in INTOSC across voltage and temperature are not necessarily reflected by changes in INTRC and vice versa.

2.6.3 OSCTUNE REGISTER

The internal oscillator's output has been calibrated at the factory but can be adjusted in the user's application. This is done by writing to the OSCTUNE register (Register 2-1).

When the OSCTUNE register is modified, the INTOSC frequency will begin shifting to the new frequency. The INTRC clock will reach the new frequency within 8 clock cycles (approximately 8 * 32 μs = 256 μs). The INTOSC clock will stabilize within 1 ms. Code execution continues during this shift. There is no indication that the shift has occurred.

The OSCTUNE register also implements the INTSRC and PLLEN bits, which control certain features of the internal oscillator block. The INTSRC bit allows users to select which internal oscillator provides the clock source when the 31 kHz frequency option is selected. This is covered in greater detail in **Section 2.7.1 "Oscillator Control Register"**.

The PLLEN bit controls the operation of the frequency multiplier, PLL, in internal oscillator modes.

2.6.4 PLL IN INTOSC MODES

The 4x frequency multiplier can be used with the internal oscillator block to produce faster device clock speeds than are normally possible with an internal oscillator. When enabled, the PLL produces a clock speed of up to 32 MHz.

Unlike HSPLL mode, the PLL is controlled through software. The control bit, PLLEN (OSCTUNE<6>), is used to enable or disable its operation.

The PLL is available when the device is configured to use the internal oscillator block as its primary clock source (FOSC<3:0> = 1001 or 1000). Additionally, the PLL will only function when the selected output frequency is either 4 MHz or 8 MHz (OSCCON<6:4> = 111 or 110). If both of these conditions are not met, the PLL is disabled.

The PLLEN control bit is only functional in those internal oscillator modes where the PLL is available. In all other modes, it is forced to '0' and is effectively unavailable.

2.6.5 INTOSC FREQUENCY DRIFT

The factory calibrates the internal oscillator block output (INTOSC) for 8 MHz. However, this frequency may drift as VDD or temperature changes, which can affect the controller operation in a variety of ways. It is possible to adjust the INTOSC frequency by modifying the value in the OSCTUNE register. This has no effect on the INTRC clock source frequency.

Tuning the INTOSC source requires knowing when to make the adjustment, in which direction it should be made, and in some cases, how large a change is needed. Three compensation techniques are discussed in **Section 2.6.5.1 "Compensating with the EUSART"**, **Section 2.6.5.2 "Compensating with the Timers"** and **Section 2.6.5.3 "Compensating with the CCP Module in Capture Mode"**, but other techniques may be used.

REGISTER 2-1: OSCTUNE: OSCILLATOR TUNING REGISTER

R/W-0	R/W-0(1)	U-0	R/W-0	R/W-0	R/W-0	R/W-0	R/W-0
INTSRC	PLLEN(1)	—	TUN4	TUN3	TUN2	TUN1	TUN0
bit 7							bit 0

Legend:			
R = Readable bit	W = Writable bit	U = Unimplemented bit, read as '0'	
-n = Value at POR	'1' = Bit is set	'0' = Bit is cleared	x = Bit is unknown

bit 7 **INTSRC:** Internal Oscillator Low-Frequency Source Select bit
1 = 31.25 kHz device clock derived from 8 MHz INTOSC source (divide-by-256 enabled)
0 = 31 kHz device clock derived directly from INTRC internal oscillator

bit 6 **PLLEN:** Frequency Multiplier PLL for INTOSC Enable bit(1)
1 = PLL enabled for INTOSC (4 MHz and 8 MHz only)
0 = PLL disabled

bit 5 **Unimplemented:** Read as '0'

bit 4-0 **TUN<4:0>:** Frequency Tuning bits
011111 = Maximum frequency
• •
• •
000001
000000 = Center frequency. Oscillator module is running at the calibrated frequency.
111111
• •
• •
100000 = Minimum frequency

Note 1: Available only in certain oscillator configurations; otherwise, this bit is unavailable and reads as '0'. See **Section 2.6.4 "PLL in INTOSC Modes"** for details.

2.6.5.1 Compensating with the EUSART

An adjustment may be required when the EUSART begins to generate framing errors or receives data with errors while in Asynchronous mode. Framing errors indicate that the device clock frequency is too high. To adjust for this, decrement the value in OSCTUNE to reduce the clock frequency. On the other hand, errors in data may suggest that the clock speed is too low. To compensate, increment OSCTUNE to increase the clock frequency.

2.6.5.2 Compensating with the Timers

This technique compares device clock speed to some reference clock. Two timers may be used; one timer is clocked by the peripheral clock, while the other is clocked by a fixed reference source, such as the Timer1 oscillator.

Both timers are cleared, but the timer clocked by the reference generates interrupts. When an interrupt occurs, the internally clocked timer is read and both timers are cleared. If the internally clocked timer value is greater than expected, then the internal oscillator block is running too fast. To adjust for this, decrement the OSCTUNE register.

2.6.5.3 Compensating with the CCP Module in Capture Mode

A CCP module can use free-running Timer1 (or Timer3), clocked by the internal oscillator block and an external event with a known period (i.e., AC power frequency). The time of the first event is captured in the CCPRxH:CCPRxL registers and is recorded for use later. When the second event causes a capture, the time of the first event is subtracted from the time of the second event. Since the period of the external event is known, the time difference between events can be calculated.

If the measured time is much greater than the calculated time, the internal oscillator block is running too fast; to compensate, decrement the OSCTUNE register. If the measured time is much less than the calculated time, the internal oscillator block is running too slow; to compensate, increment the OSCTUNE register.

2.7 Clock Sources and Oscillator Switching

Like previous PIC18 devices, the PIC18F2420/2520/4420/4520 family includes a feature that allows the device clock source to be switched from the main oscillator to an alternate low-frequency clock source. PIC18F2420/2520/4420/4520 devices offer two alternate clock sources. When an alternate clock source is enabled, the various power-managed operating modes are available.

Essentially, there are three clock sources for these devices:

- Primary oscillators
- Secondary oscillators
- Internal oscillator block

The **primary oscillators** include the External Crystal and Resonator modes, the External RC modes, the External Clock modes and the internal oscillator block. The particular mode is defined by the FOSC<3:0> Configuration bits. The details of these modes are covered earlier in this chapter.

The **secondary oscillators** are those external sources not connected to the OSC1 or OSC2 pins. These sources may continue to operate even after the controller is placed in a power-managed mode.

PIC18F2420/2520/4420/4520 devices offer the Timer1 oscillator as a secondary oscillator. This oscillator, in all power-managed modes, is often the time base for functions such as a Real-Time Clock (RTC).

Most often, a 32.768 kHz watch crystal is connected between the RC0/T1OSO/T13CKI and RC1/T1OSI pins. Like the LP Oscillator mode circuit, loading capacitors are also connected from each pin to ground.

The Timer1 oscillator is discussed in greater detail in **Section 12.3 "Timer1 Oscillator"**.

In addition to being a primary clock source, the **internal oscillator block** is available as a power-managed mode clock source. The INTRC source is also used as the clock source for several special features, such as the WDT and Fail-Safe Clock Monitor.

The clock sources for the PIC18F2420/2520/4420/4520 devices are shown in Figure 2-8. See **Section 23.0 "Special Features of the CPU"** for Configuration register details.

FIGURE 2-8: PIC18F2420/2520/4420/4520 CLOCK DIAGRAM

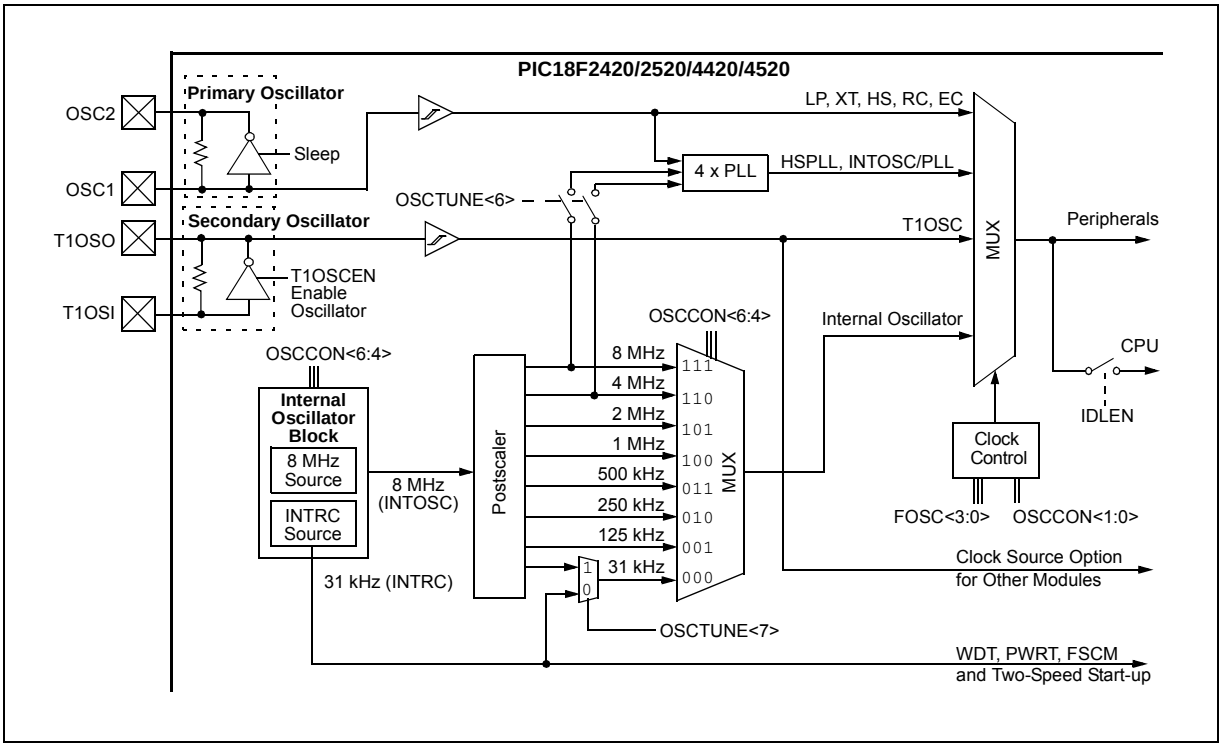

2.7.1 OSCILLATOR CONTROL REGISTER

The OSCCON register (Register 2-2) controls several aspects of the device clock's operation, both in full-power operation and in power-managed modes.

The System Clock Select bits, SCS<1:0>, select the clock source. The available clock sources are the primary clock (defined by the FOSC<3:0> Configuration bits), the secondary clock (Timer1 oscillator) and the internal oscillator block. The clock source changes immediately after one or more of the bits is written to, following a brief clock transition interval. The SCS bits are cleared on all forms of Reset.

The Internal Oscillator Frequency Select bits (IRCF<2:0>) select the frequency output of the internal oscillator block to drive the device clock. The choices are the INTRC source, the INTOSC source (8 MHz) or one of the frequencies derived from the INTOSC postscaler (31.25 kHz to 4 MHz). If the internal oscillator block is supplying the device clock, changing the states of these bits will have an immediate change on the internal oscillator's output. On device Resets, the default output frequency of the internal oscillator block is set at 1 MHz.

When a nominal output frequency of 31 kHz is selected (IRCF<2:0> = 000), users may choose which internal oscillator acts as the source. This is done with the INTSRC bit in the OSCTUNE register (OSCTUNE<7>). Setting this bit selects INTOSC as a 31.25 kHz clock source by enabling the divide-by-256 output of the INTOSC postscaler. Clearing INTSRC selects INTRC (nominally 31 kHz) as the clock source.

This option allows users to select the tunable and more precise INTOSC as a clock source, while maintaining power savings with a very low clock speed. Regardless of the setting of INTSRC, INTRC always remains the clock source for features such as the Watchdog Timer and the Fail-Safe Clock Monitor.

The OSTS, IOFS and T1RUN bits indicate which clock source is currently providing the device clock. The OSTS bit indicates that the Oscillator Start-up Timer (OST) has timed out and the primary clock is providing the device clock in primary clock modes. The IOFS bit indicates when the internal oscillator block has stabilized and is providing the device clock in RC Clock modes. The T1RUN bit (T1CON<6>) indicates when the Timer1 oscillator is providing the device clock in secondary clock modes. In power-managed modes, only one of these three bits will be set at any time. If none of these bits are set, the INTRC is providing the clock or the internal oscillator block has just started and is not yet stable.

The IDLEN bit determines if the device goes into Sleep mode or one of the Idle modes when the SLEEP instruction is executed.

The use of the flag and control bits in the OSCCON register is discussed in more detail in **Section 3.0 "Power-Managed Modes"**.

Note 1:	The Timer1 oscillator must be enabled to select the secondary clock source. The Timer1 oscillator is enabled by setting the T1OSCEN bit in the Timer1 Control register (T1CON<3>). If the Timer1 oscillator is not enabled, then any attempt to select a secondary clock source will be ignored.
2:	It is recommended that the Timer1 oscillator be operating and stable before selecting the secondary clock source or a very long delay may occur while the Timer1 oscillator starts.

2.7.2 OSCILLATOR TRANSITIONS

PIC18F2420/2520/4420/4520 devices contain circuitry to prevent clock "glitches" when switching between clock sources. A short pause in the device clock occurs during the clock switch. The length of this pause is the sum of two cycles of the old clock source and three to four cycles of the new clock source. This formula assumes that the new clock source is stable.

Clock transitions are discussed in greater detail in **Section 3.1.2 "Entering Power-Managed Modes"**.

REGISTER 2-2: OSCCON: OSCILLATOR CONTROL REGISTER

R/W-0	R/W-1	R/W-0	R/W-0	R(1)	R-0	R/W-0	R/W-0
IDLEN	IRCF2	IRCF1	IRCF0	OSTS	IOFS	SCS1	SCS0
bit 7							bit 0

Legend:			
R = Readable bit	W = Writable bit	U = Unimplemented bit, read as '0'	
-n = Value at POR	'1' = Bit is set	'0' = Bit is cleared	x = Bit is unknown

bit 7 **IDLEN:** Idle Enable bit
- 1 = Device enters an Idle mode on SLEEP instruction
- 0 = Device enters Sleep mode on SLEEP instruction

bit 6-4 **IRCF<2:0>:** Internal Oscillator Frequency Select bits
- 111 = 8 MHz (INTOSC drives clock directly)
- 110 = 4 MHz
- 101 = 2 MHz
- 100 = 1 MHz(3)
- 011 = 500 kHz
- 010 = 250 kHz
- 001 = 125 kHz
- 000 = 31 kHz (from either INTOSC/256 or INTRC directly)(2)

bit 3 **OSTS:** Oscillator Start-up Timer Time-out Status bit(1)
- 1 = Oscillator Start-up Timer (OST) time-out has expired; primary oscillator is running
- 0 = Oscillator Start-up Timer (OST) time-out is running; primary oscillator is not ready

bit 2 **IOFS:** INTOSC Frequency Stable bit
- 1 = INTOSC frequency is stable
- 0 = INTOSC frequency is not stable

bit 1-0 **SCS<1:0>:** System Clock Select bits
- 1x = Internal oscillator block
- 01 = Secondary (Timer1) oscillator
- 00 = Primary oscillator

Note 1: Reset state depends on state of the IESO Configuration bit.
2: Source selected by the INTSRC bit (OSCTUNE<7>), see text.
3: Default output frequency of INTOSC on Reset.

2.8 Effects of Power-Managed Modes on the Various Clock Sources

When PRI_IDLE mode is selected, the designated primary oscillator continues to run without interruption. For all other power-managed modes, the oscillator using the OSC1 pin is disabled. The OSC1 pin (and OSC2 pin, if used by the oscillator) will stop oscillating.

In secondary clock modes (SEC_RUN and SEC_IDLE), the Timer1 oscillator is operating and providing the device clock. The Timer1 oscillator may also run in all power-managed modes if required to clock Timer1 or Timer3.

In internal oscillator modes (RC_RUN and RC_IDLE), the internal oscillator block provides the device clock source. The 31 kHz INTRC output can be used directly to provide the clock and may be enabled to support various special features, regardless of the power-managed mode (see **Section 23.2 "Watchdog Timer (WDT)"**, **Section 23.3 "Two-Speed Start-up"** and **Section 23.4 "Fail-Safe Clock Monitor"** for more information on WDT, Fail-Safe Clock Monitor and Two-Speed Start-up). The INTOSC output at 8 MHz may be used directly to clock the device or may be divided down by the postscaler. The INTOSC output is disabled if the clock is provided directly from the INTRC output.

If Sleep mode is selected, all clock sources are stopped. Since all the transistor switching currents have been stopped, Sleep mode achieves the lowest current consumption of the device (only leakage currents).

Enabling any on-chip feature that will operate during Sleep will increase the current consumed during Sleep. The INTRC is required to support WDT operation. The Timer1 oscillator may be operating to support a Real-Time Clock. Other features may be operating that do not require a device clock source (i.e., MSSP slave, PSP, INTx pins and others). Peripherals that may add significant current consumption are listed in **Section 26.2 "DC Characteristics".**

2.9 Power-up Delays

Power-up delays are controlled by two timers so that no external Reset circuitry is required for most applications. The delays ensure that the device is kept in Reset until the device power supply is stable under normal circumstances and the primary clock is operating and stable. For additional information on power-up delays, see **Section 4.5 "Device Reset Timers"**.

The first timer is the Power-up Timer (PWRT), which provides a fixed delay on power-up (parameter 33, Table 26-10). It is enabled by clearing (= 0) the $\overline{\text{PWRTEN}}$ Configuration bit.

The second timer is the Oscillator Start-up Timer (OST), intended to keep the chip in Reset until the crystal oscillator is stable (LP, XT and HS modes). The OST does this by counting 1024 oscillator cycles before allowing the oscillator to clock the device.

When the HSPLL Oscillator mode is selected, the device is kept in Reset for an additional 2 ms, following the HS mode OST delay, so the PLL can lock to the incoming clock frequency.

There is a delay of interval, TCSD (parameter 38, Table 26-10), following POR, while the controller becomes ready to execute instructions. This delay runs concurrently with any other delays. This may be the only delay that occurs when any of the EC, RC or INTIO modes are used as the primary clock source.

TABLE 2-3: OSC1 AND OSC2 PIN STATES IN SLEEP MODE

OSC Mode	OSC1 Pin	OSC2 Pin
RC, INTIO1	Floating, external resistor should pull high	At logic low (clock/4 output)
RCIO	Floating, external resistor should pull high	Configured as PORTA, bit 6
INTIO2	Configured as PORTA, bit 7	Configured as PORTA, bit 6
ECIO	Floating, pulled by external clock	Configured as PORTA, bit 6
EC	Floating, pulled by external clock	At logic low (clock/4 output)
LP, XT and HS	Feedback inverter disabled at quiescent voltage level	Feedback inverter disabled at quiescent voltage level

Note: See Table 4-2 in **Section 4.0 "Reset"** for time-outs due to Sleep and $\overline{\text{MCLR}}$ Reset.

4.0 RESET

The PIC18F2420/2520/4420/4520 devices differentiate between various kinds of Reset:

a) Power-on Reset (POR)
b) $\overline{\text{MCLR}}$ Reset during normal operation
c) $\overline{\text{MCLR}}$ Reset during power-managed modes
d) Watchdog Timer (WDT) Reset (during execution)
e) Programmable Brown-out Reset (BOR)
f) RESET Instruction
g) Stack Full Reset
h) Stack Underflow Reset

This section discusses Resets generated by $\overline{\text{MCLR}}$, POR and BOR and covers the operation of the various start-up timers. Stack Reset events are covered in **Section 5.1.2.4 "Stack Full and Underflow Resets"**. WDT Resets are covered in **Section 23.2 "Watchdog Timer (WDT)"**.

A simplified block diagram of the On-Chip Reset Circuit is shown in Figure 4-1.

4.1 RCON Register

Device Reset events are tracked through the RCON register (Register 4-1). The lower five bits of the register indicate that a specific Reset event has occurred. In most cases, these bits can only be cleared by the event and must be set by the application after the event. The state of these flag bits, taken together, can be read to indicate the type of Reset that just occurred. This is described in more detail in **Section 4.6 "Reset State of Registers"**.

The RCON register also has control bits for setting interrupt priority (IPEN) and software control of the BOR (SBOREN). Interrupt priority is discussed in **Section 9.0 "Interrupts"**. BOR is covered in **Section 4.4 "Brown-out Reset (BOR)"**.

FIGURE 4-1: SIMPLIFIED BLOCK DIAGRAM OF ON-CHIP RESET CIRCUIT

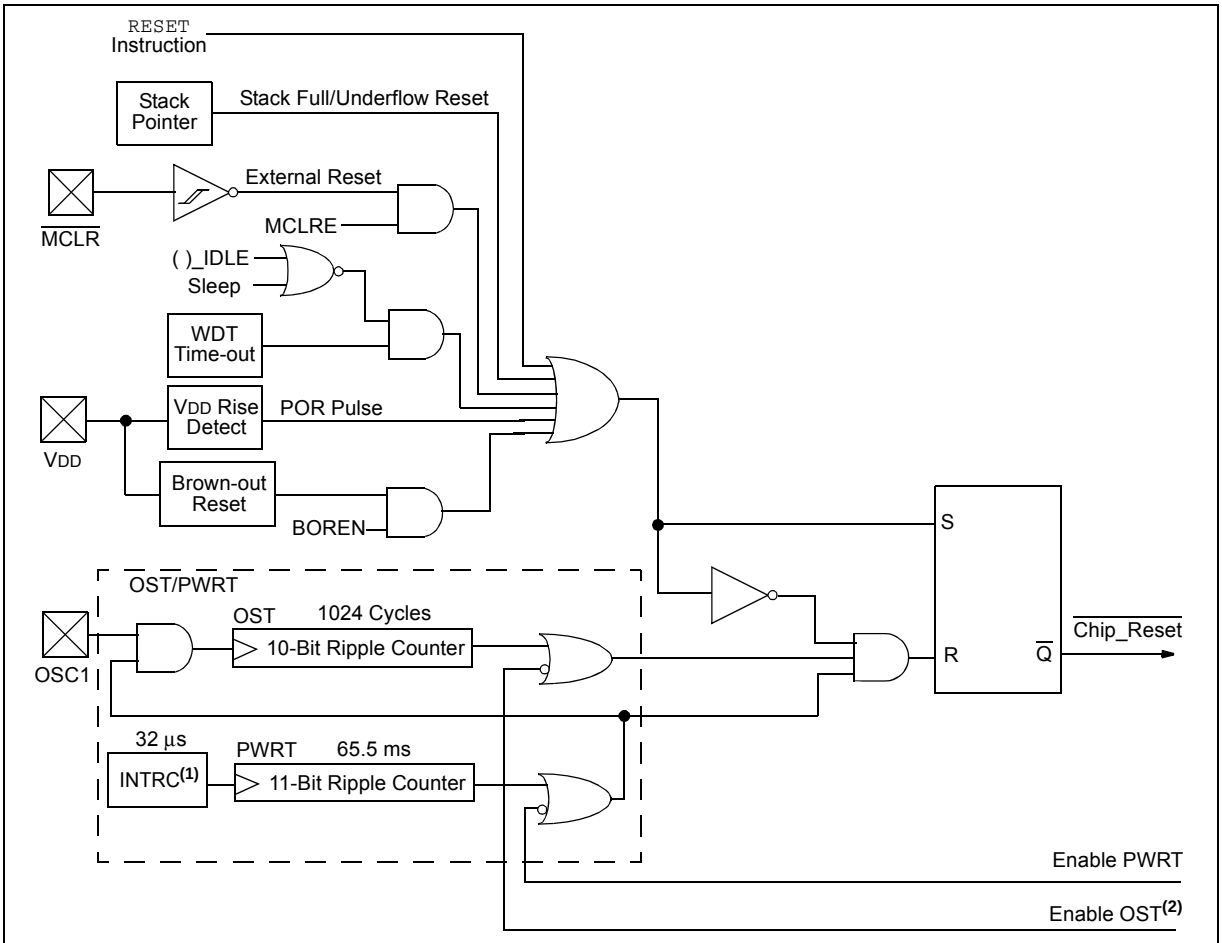

Note 1: This is the INTRC source from the internal oscillator block and is separate from the RC oscillator of the CLKI pin.
2: See Table 4-2 for time-out situations.

REGISTER 4-1: RCON: RESET CONTROL REGISTER

R/W-0	R/W-1(1)	U-0	R/W-1	R-1	R-1	R/W-0(2)	R/W-0
IPEN	SBOREN	—	$\overline{RI}$	$\overline{TO}$	$\overline{PD}$	$\overline{POR}$	$\overline{BOR}$
bit 7							bit 0

Legend:			
R = Readable bit	W = Writable bit	U = Unimplemented bit, read as '0'	
-n = Value at POR	'1' = Bit is set	'0' = Bit is cleared	x = Bit is unknown

bit 7 **IPEN:** Interrupt Priority Enable bit
1 = Enable priority levels on interrupts
0 = Disable priority levels on interrupts (PIC16CXXX Compatibility mode)

bit 6 **SBOREN:** BOR Software Enable bit(1)
If BOREN1:BOREN0 = 01:
1 = BOR is enabled
0 = BOR is disabled
If BOREN1:BOREN0 = 00, 10 or 11:
Bit is disabled and read as '0'.

bit 5 **Unimplemented:** Read as '0'

bit 4 **$\overline{RI}$:** RESET Instruction Flag bit
1 = The RESET instruction was not executed (set by firmware only)
0 = The RESET instruction was executed causing a device Reset (must be set in software after a Brown-out Reset occurs)

bit 3 **$\overline{TO}$:** Watchdog Time-out Flag bit
1 = Set by power-up, CLRWDT instruction or SLEEP instruction
0 = A WDT time-out occurred

bit 2 **$\overline{PD}$:** Power-Down Detection Flag bit
1 = Set by power-up or by the CLRWDT instruction
0 = Set by execution of the SLEEP instruction

bit 1 **$\overline{POR}$:** Power-on Reset Status bit
1 = A Power-on Reset has not occurred (set by firmware only)
0 = A Power-on Reset occurred (must be set in software after a Power-on Reset occurs)

bit 0 **$\overline{BOR}$:** Brown-out Reset Status bit
1 = A Brown-out Reset has not occurred (set by firmware only)
0 = A Brown-out Reset occurred (must be set in software after a Brown-out Reset occurs)

Note 1: If SBOREN is enabled, its Reset state is '1'; otherwise, it is '0'.
2: The actual Reset value of $\overline{POR}$ is determined by the type of device Reset. See the notes following this register and **Section 4.6 "Reset State of Registers"** for additional information.

Note 1: It is recommended that the $\overline{POR}$ bit be set after a Power-on Reset has been detected so that subsequent Power-on Resets may be detected.
2: Brown-out Reset is said to have occurred when $\overline{BOR}$ is '0' and $\overline{POR}$ is '1' (assuming that $\overline{POR}$ was set to '1' by software immediately after a Power-on Reset).

4.2 Master Clear (MCLR)

The MCLR pin provides a method for triggering an external Reset of the device. A Reset is generated by holding the pin low. These devices have a noise filter in the MCLR Reset path which detects and ignores small pulses.

The MCLR pin is not driven low by any internal Resets, including the WDT.

In PIC18F2420/2520/4420/4520 devices, the MCLR input can be disabled with the MCLRE Configuration bit. When MCLR is disabled, the pin becomes a digital input. See **Section 10.5 "PORTE, TRISE and LATE Registers"** for more information.

4.3 Power-on Reset (POR)

A Power-on Reset pulse is generated on-chip whenever VDD rises above a certain threshold. This allows the device to start in the initialized state when VDD is adequate for operation.

To take advantage of the POR circuitry, tie the MCLR pin through a resistor (1 kΩ to 10 kΩ) to VDD. This will eliminate external RC components usually needed to create a Power-on Reset delay. A minimum rise rate for VDD is specified (parameter D004). For a slow rise time, see Figure 4-2.

When the device starts normal operation (i.e., exits the Reset condition), device operating parameters (voltage, frequency, temperature, etc.) must be met to ensure operation. If these conditions are not met, the device must be held in Reset until the operating conditions are met.

POR events are captured by the POR bit (RCON<1>). The state of the bit is set to '0' whenever a POR occurs; it does not change for any other Reset event. POR is not reset to '1' by any hardware event. To capture multiple events, the user manually resets the bit to '1' in software following any POR.

FIGURE 4-2: EXTERNAL POWER-ON RESET CIRCUIT (FOR SLOW VDD POWER-UP)

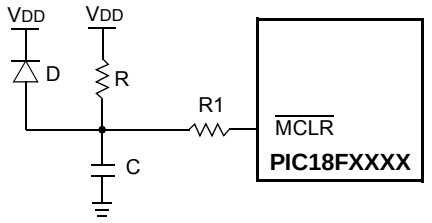

Note 1: External Power-on Reset circuit is required only if the VDD power-up slope is too slow. The diode D helps discharge the capacitor quickly when VDD powers down.

2: R < 40 kΩ is recommended to make sure that the voltage drop across R does not violate the device's electrical specification.

3: R1 ≥ 1 kΩ will limit any current flowing into MCLR from external capacitor C, in the event of MCLR/VPP pin breakdown, due to Electrostatic Discharge (ESD) or Electrical Overstress (EOS).

9.0 INTERRUPTS

The PIC18F2420/2520/4420/4520 devices have multiple interrupt sources and an interrupt priority feature that allows most interrupt sources to be assigned a high-priority level or a low-priority level. The high-priority interrupt vector is at 0008h and the low-priority interrupt vector is at 0018h. High-priority interrupt events will interrupt any low-priority interrupts that may be in progress.

There are ten registers which are used to control interrupt operation. These registers are:

- RCON
- INTCON
- INTCON2
- INTCON3
- PIR1, PIR2
- PIE1, PIE2
- IPR1, IPR2

It is recommended that the Microchip header files supplied with MPLAB® IDE be used for the symbolic bit names in these registers. This allows the assembler/compiler to automatically take care of the placement of these bits within the specified register.

In general, interrupt sources have three bits to control their operation. They are:

- **Flag bit** to indicate that an interrupt event occurred
- **Enable bit** that allows program execution to branch to the interrupt vector address when the flag bit is set
- **Priority bit** to select high priority or low priority

The interrupt priority feature is enabled by setting the IPEN bit (RCON<7>). When interrupt priority is enabled, there are two bits which enable interrupts globally. Setting the GIEH bit (INTCON<7>) enables all interrupts that have the priority bit set (high priority). Setting the GIEL bit (INTCON<6>) enables all interrupts that have the priority bit cleared (low priority). When the interrupt flag, enable bit and appropriate global interrupt enable bit are set, the interrupt will vector immediately to address 0008h or 0018h, depending on the priority bit setting. Individual interrupts can be disabled through their corresponding enable bits.

When the IPEN bit is cleared (default state), the interrupt priority feature is disabled and interrupts are compatible with PIC® mid-range devices. In Compatibility mode, the interrupt priority bits for each source have no effect. INTCON<6> is the PEIE bit, which enables/disables all peripheral interrupt sources. INTCON<7> is the GIE bit, which enables/disables all interrupt sources. All interrupts branch to address 0008h in Compatibility mode.

When an interrupt is responded to, the global interrupt enable bit is cleared to disable further interrupts. If the IPEN bit is cleared, this is the GIE bit. If interrupt priority levels are used, this will be either the GIEH or GIEL bit. High-priority interrupt sources can interrupt a low-priority interrupt. Low-priority interrupts are not processed while high-priority interrupts are in progress.

The return address is pushed onto the stack and the PC is loaded with the interrupt vector address (0008h or 0018h). Once in the Interrupt Service Routine, the source(s) of the interrupt can be determined by polling the interrupt flag bits. The interrupt flag bits must be cleared in software before re-enabling interrupts to avoid recursive interrupts.

The “return from interrupt” instruction, `RETFIE`, exits the interrupt routine and sets the GIE bit (GIEH or GIEL if priority levels are used), which re-enables interrupts.

For external interrupt events, such as the INTx pins or the PORTB input change interrupt, the interrupt latency will be three to four instruction cycles. The exact latency is the same for one or two-cycle instructions. Individual interrupt flag bits are set, regardless of the status of their corresponding enable bit or the GIE bit.

Note:	Do not use the `MOVFF` instruction to modify any of the interrupt control registers while **any** interrupt is enabled. Doing so may cause erratic microcontroller behavior.

FIGURE 9-1: PIC18 INTERRUPT LOGIC

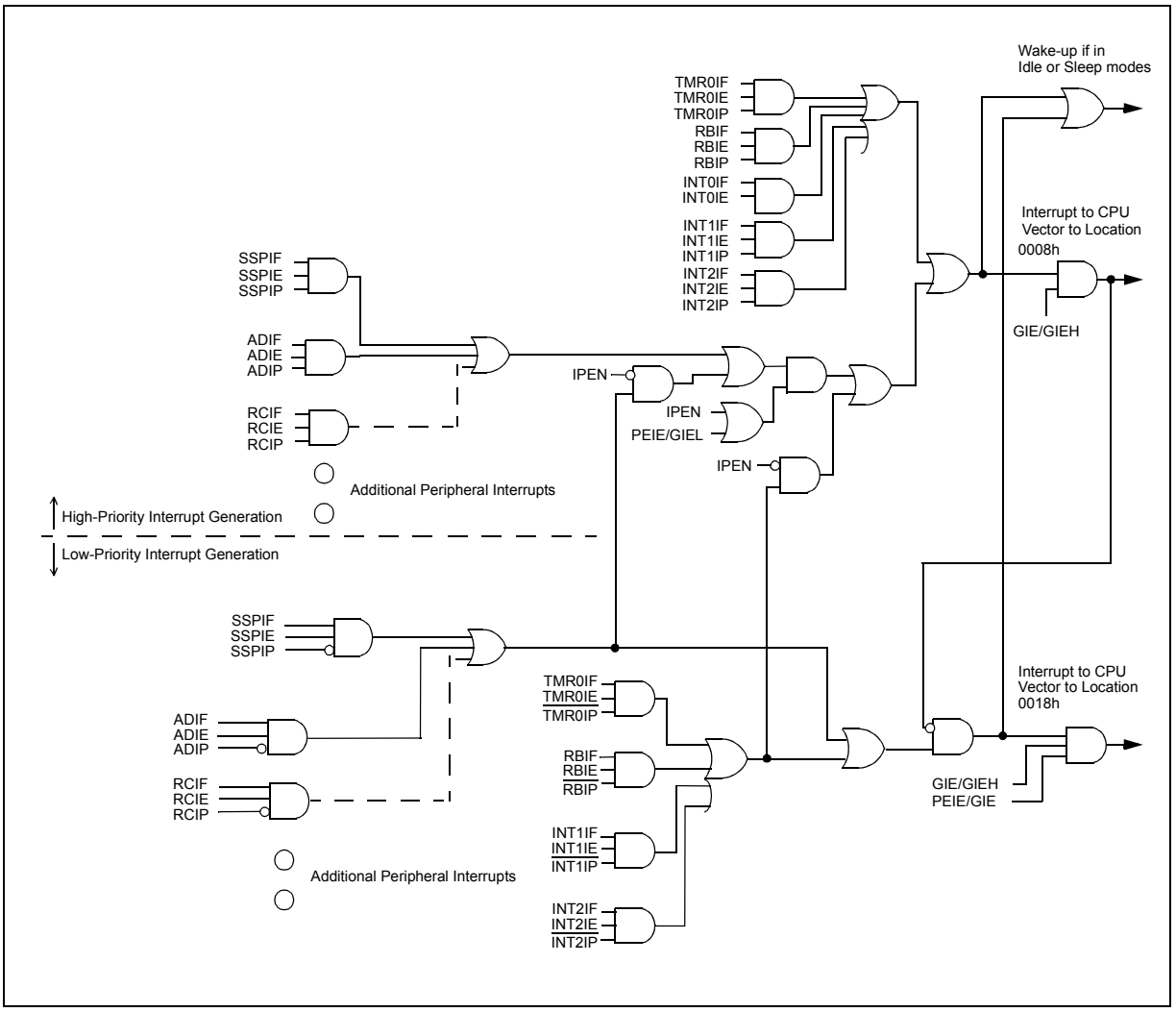

9.1 INTCON Registers

The INTCON registers are readable and writable registers, which contain various enable, priority and flag bits.

Note: Interrupt flag bits are set when an interrupt condition occurs, regardless of the state of its corresponding enable bit or the global enable bit. User software should ensure the appropriate interrupt flag bits are clear prior to enabling an interrupt. This feature allows for software polling.

REGISTER 9-1: INTCON: INTERRUPT CONTROL REGISTER

R/W-0	R/W-0	R/W-0	R/W-0	R/W-0	R/W-0	R/W-0	R/W-x
GIE/GIEH	PEIE/GIEL	TMR0IE	INT0IE	RBIE	TMR0IF	INT0IF	RBIF(1)
bit 7							bit 0

Legend:			
R = Readable bit	W = Writable bit	U = Unimplemented bit, read as '0'	
-n = Value at POR	'1' = Bit is set	'0' = Bit is cleared	x = Bit is unknown

bit 7 **GIE/GIEH:** Global Interrupt Enable bit
When IPEN = 0:
1 = Enables all unmasked interrupts
0 = Disables all interrupts
When IPEN = 1:
1 = Enables all high-priority interrupts
0 = Disables all interrupts

bit 6 **PEIE/GIEL:** Peripheral Interrupt Enable bit
When IPEN = 0:
1 = Enables all unmasked peripheral interrupts
0 = Disables all peripheral interrupts
When IPEN = 1:
1 = Enables all low-priority peripheral interrupts
0 = Disables all low-priority peripheral interrupts

bit 5 **TMR0IE:** TMR0 Overflow Interrupt Enable bit
1 = Enables the TMR0 overflow interrupt
0 = Disables the TMR0 overflow interrupt

bit 4 **INT0IE:** INT0 External Interrupt Enable bit
1 = Enables the INT0 external interrupt
0 = Disables the INT0 external interrupt

bit 3 **RBIE:** RB Port Change Interrupt Enable bit
1 = Enables the RB port change interrupt
0 = Disables the RB port change interrupt

bit 2 **TMR0IF:** TMR0 Overflow Interrupt Flag bit
1 = TMR0 register has overflowed (must be cleared in software)
0 = TMR0 register did not overflow

bit 1 **INT0IF:** INT0 External Interrupt Flag bit
1 = The INT0 external interrupt occurred (must be cleared in software)
0 = The INT0 external interrupt did not occur

bit 0 **RBIF:** RB Port Change Interrupt Flag bit(1)
1 = At least one of the RB<7:4> pins changed state (must be cleared in software)
0 = None of the RB<7:4> pins have changed state

Note 1: A mismatch condition will continue to set this bit. Reading PORTB will end the mismatch condition and allow the bit to be cleared.

REGISTER 9-2: INTCON2: INTERRUPT CONTROL REGISTER 2

R/W-1	R/W-1	R/W-1	R/W-1	U-0	R/W-1	U-0	R/W-1
$\overline{\text{RBPU}}$	INTEDG0	INTEDG1	INTEDG2	—	TMR0IP	—	RBIP
bit 7							bit 0

Legend:			
R = Readable bit	W = Writable bit	U = Unimplemented bit, read as '0'	
-n = Value at POR	'1' = Bit is set	'0' = Bit is cleared	x = Bit is unknown

bit 7 **$\overline{\text{RBPU}}$:** PORTB Pull-up Enable bit
1 = All PORTB pull-ups are disabled
0 = PORTB pull-ups are enabled by individual port latch values

bit 6 **INTEDG0:** External Interrupt 0 Edge Select bit
1 = Interrupt on rising edge
0 = Interrupt on falling edge

bit 5 **INTEDG1:** External Interrupt 1 Edge Select bit
1 = Interrupt on rising edge
0 = Interrupt on falling edge

bit 4 **INTEDG2:** External Interrupt 2 Edge Select bit
1 = Interrupt on rising edge
0 = Interrupt on falling edge

bit 3 **Unimplemented:** Read as '0'

bit 2 **TMR0IP:** TMR0 Overflow Interrupt Priority bit
1 = High priority
0 = Low priority

bit 1 **Unimplemented:** Read as '0'

bit 0 **RBIP:** RB Port Change Interrupt Priority bit
1 = High priority
0 = Low priority

Note: Interrupt flag bits are set when an interrupt condition occurs, regardless of the state of its corresponding enable bit or the global enable bit. User software should ensure the appropriate interrupt flag bits are clear prior to enabling an interrupt. This feature allows for software polling.

REGISTER 9-3: INTCON3: INTERRUPT CONTROL REGISTER 3

R/W-1	R/W-1	U-0	R/W-0	R/W-0	U-0	R/W-0	R/W-0
INT2IP	INT1IP	—	INT2IE	INT1IE	—	INT2IF	INT1IF
bit 7							bit 0

Legend:			
R = Readable bit	W = Writable bit	U = Unimplemented bit, read as '0'	
-n = Value at POR	'1' = Bit is set	'0' = Bit is cleared	x = Bit is unknown

bit 7 **INT2IP:** INT2 External Interrupt Priority bit
1 = High priority
0 = Low priority

bit 6 **INT1IP:** INT1 External Interrupt Priority bit
1 = High priority
0 = Low priority

bit 5 **Unimplemented:** Read as '0'

bit 4 **INT2IE:** INT2 External Interrupt Enable bit
1 = Enables the INT2 external interrupt
0 = Disables the INT2 external interrupt

bit 3 **INT1IE:** INT1 External Interrupt Enable bit
1 = Enables the INT1 external interrupt
0 = Disables the INT1 external interrupt

bit 2 **Unimplemented:** Read as '0'

bit 1 **INT2IF:** INT2 External Interrupt Flag bit
1 = The INT2 external interrupt occurred (must be cleared in software)
0 = The INT2 external interrupt did not occur

bit 0 **INT1IF:** INT1 External Interrupt Flag bit
1 = The INT1 external interrupt occurred (must be cleared in software)
0 = The INT1 external interrupt did not occur

Note: Interrupt flag bits are set when an interrupt condition occurs, regardless of the state of its corresponding enable bit or the global enable bit. User software should ensure the appropriate interrupt flag bits are clear prior to enabling an interrupt. This feature allows for software polling.

9.2 PIR Registers

The PIR registers contain the individual flag bits for the peripheral interrupts. Due to the number of peripheral interrupt sources, there are two Peripheral Interrupt Request Flag registers (PIR1 and PIR2).

Note 1: Interrupt flag bits are set when an interrupt condition occurs, regardless of the state of its corresponding enable bit or the Global Interrupt Enable bit, GIE (INTCON<7>).

2: User software should ensure the appropriate interrupt flag bits are cleared prior to enabling an interrupt and after servicing that interrupt.

REGISTER 9-4: PIR1: PERIPHERAL INTERRUPT REQUEST (FLAG) REGISTER 1

R/W-0	R/W-0	R-0	R-0	R/W-0	R/W-0	R/W-0	R/W-0
PSPIF(1)	ADIF	RCIF	TXIF	SSPIF	CCP1IF	TMR2IF	TMR1IF
bit 7							bit 0

Legend:			
R = Readable bit	W = Writable bit	U = Unimplemented bit, read as '0'	
-n = Value at POR	'1' = Bit is set	'0' = Bit is cleared	x = Bit is unknown

bit 7 **PSPIF:** Parallel Slave Port Read/Write Interrupt Flag bit(1)
1 = A read or a write operation has taken place (must be cleared in software)
0 = No read or write has occurred

bit 6 **ADIF:** A/D Converter Interrupt Flag bit
1 = An A/D conversion completed (must be cleared in software)
0 = The A/D conversion is not complete

bit 5 **RCIF:** EUSART Receive Interrupt Flag bit
1 = The EUSART receive buffer, RCREG, is full (cleared when RCREG is read)
0 = The EUSART receive buffer is empty

bit 4 **TXIF:** EUSART Transmit Interrupt Flag bit
1 = The EUSART transmit buffer, TXREG, is empty (cleared when TXREG is written)
0 = The EUSART transmit buffer is full

bit 3 **SSPIF:** Master Synchronous Serial Port Interrupt Flag bit
1 = The transmission/reception is complete (must be cleared in software)
0 = Waiting to transmit/receive

bit 2 **CCP1IF:** CCP1 Interrupt Flag bit
Capture mode:
1 = A TMR1 register capture occurred (must be cleared in software)
0 = No TMR1 register capture occurred
Compare mode:
1 = A TMR1 register compare match occurred (must be cleared in software)
0 = No TMR1 register compare match occurred
PWM mode:
Unused in this mode.

bit 1 **TMR2IF:** TMR2 to PR2 Match Interrupt Flag bit
1 = TMR2 to PR2 match occurred (must be cleared in software)
0 = No TMR2 to PR2 match occurred

bit 0 **TMR1IF:** TMR1 Overflow Interrupt Flag bit
1 = TMR1 register overflowed (must be cleared in software)
0 = TMR1 register did not overflow

Note 1: This bit is unimplemented on 28-pin devices and will read as '0'.

REGISTER 9-5: PIR2: PERIPHERAL INTERRUPT REQUEST (FLAG) REGISTER 2

R/W-0	R/W-0	U-0	R/W-0	R/W-0	R/W-0	R/W-0	R/W-0
OSCFIF	CMIF	—	EEIF	BCLIF	HLVDIF	TMR3IF	CCP2IF
bit 7							bit 0

Legend:			
R = Readable bit	W = Writable bit	U = Unimplemented bit, read as '0'	
-n = Value at POR	'1' = Bit is set	'0' = Bit is cleared	x = Bit is unknown

bit 7 **OSCFIF:** Oscillator Fail Interrupt Flag bit
1 = Device oscillator failed, clock input has changed to INTOSC (must be cleared in software)
0 = Device clock operating

bit 6 **CMIF:** Comparator Interrupt Flag bit
1 = Comparator input has changed (must be cleared in software)
0 = Comparator input has not changed

bit 5 **Unimplemented:** Read as '0'

bit 4 **EEIF:** Data EEPROM/Flash Write Operation Interrupt Flag bit
1 = The write operation is complete (must be cleared in software)
0 = The write operation is not complete or has not been started

bit 3 **BCLIF:** Bus Collision Interrupt Flag bit
1 = A bus collision occurred (must be cleared in software)
0 = No bus collision occurred

bit 2 **HLVDIF:** High/Low-Voltage Detect Interrupt Flag bit
1 = A high/low-voltage condition occurred (direction determined by VDIRMAG bit, HLVDCON<7>)
0 = A high/low-voltage condition has not occurred

bit 1 **TMR3IF:** TMR3 Overflow Interrupt Flag bit
1 = TMR3 register overflowed (must be cleared in software)
0 = TMR3 register did not overflow

bit 0 **CCP2IF:** CCP2 Interrupt Flag bit
Capture mode:
1 = A TMR1 register capture occurred (must be cleared in software)
0 = No TMR1 register capture occurred
Compare mode:
1 = A TMR1 register compare match occurred (must be cleared in software)
0 = No TMR1 register compare match occurred
PWM mode:
Unused in this mode.

9.3 PIE Registers

The PIE registers contain the individual enable bits for the peripheral interrupts. Due to the number of peripheral interrupt sources, there are two Peripheral Interrupt Enable registers (PIE1 and PIE2). When IPEN = 0, the PEIE bit must be set to enable any of these peripheral interrupts.

REGISTER 9-6: PIE1: PERIPHERAL INTERRUPT ENABLE REGISTER 1

R/W-0	R/W-0	R/W-0	R/W-0	R/W-0	R/W-0	R/W-0	R/W-0
PSPIE(1)	ADIE	RCIE	TXIE	SSPIE	CCP1IE	TMR2IE	TMR1IE
bit 7							bit 0

Legend:			
R = Readable bit	W = Writable bit	U = Unimplemented bit, read as '0'	
-n = Value at POR	'1' = Bit is set	'0' = Bit is cleared	x = Bit is unknown

bit 7 **PSPIE:** Parallel Slave Port Read/Write Interrupt Enable bit(1)
1 = Enables the PSP read/write interrupt
0 = Disables the PSP read/write interrupt

bit 6 **ADIE:** A/D Converter Interrupt Enable bit
1 = Enables the A/D interrupt
0 = Disables the A/D interrupt

bit 5 **RCIE:** EUSART Receive Interrupt Enable bit
1 = Enables the EUSART receive interrupt
0 = Disables the EUSART receive interrupt

bit 4 **TXIE:** EUSART Transmit Interrupt Enable bit
1 = Enables the EUSART transmit interrupt
0 = Disables the EUSART transmit interrupt

bit 3 **SSPIE:** Master Synchronous Serial Port Interrupt Enable bit
1 = Enables the MSSP interrupt
0 = Disables the MSSP interrupt

bit 2 **CCP1IE:** CCP1 Interrupt Enable bit
1 = Enables the CCP1 interrupt
0 = Disables the CCP1 interrupt

bit 1 **TMR2IE:** TMR2 to PR2 Match Interrupt Enable bit
1 = Enables the TMR2 to PR2 match interrupt
0 = Disables the TMR2 to PR2 match interrupt

bit 0 **TMR1IE:** TMR1 Overflow Interrupt Enable bit
1 = Enables the TMR1 overflow interrupt
0 = Disables the TMR1 overflow interrupt

Note 1: This bit is unimplemented on 28-pin devices and will read as '0'.

REGISTER 9-7: PIE2: PERIPHERAL INTERRUPT ENABLE REGISTER 2

R/W-0	R/W-0	U-0	R/W-0	R/W-0	R/W-0	R/W-0	R/W-0
OSCFIE	CMIE	—	EEIE	BCLIE	HLVDIE	TMR3IE	CCP2IE
bit 7							bit 0

Legend:			
R = Readable bit	W = Writable bit	U = Unimplemented bit, read as '0'	
-n = Value at POR	'1' = Bit is set	'0' = Bit is cleared	x = Bit is unknown

bit 7 **OSCFIE:** Oscillator Fail Interrupt Enable bit
1 = Enabled
0 = Disabled

bit 6 **CMIE:** Comparator Interrupt Enable bit
1 = Enabled
0 = Disabled

bit 5 **Unimplemented:** Read as '0'

bit 4 **EEIE:** Data EEPROM/Flash Write Operation Interrupt Enable bit
1 = Enabled
0 = Disabled

bit 3 **BCLIE:** Bus Collision Interrupt Enable bit
1 = Enabled
0 = Disabled

bit 2 **HLVDIE:** High/Low-Voltage Detect Interrupt Enable bit
1 = Enabled
0 = Disabled

bit 1 **TMR3IE:** TMR3 Overflow Interrupt Enable bit
1 = Enabled
0 = Disabled

bit 0 **CCP2IE:** CCP2 Interrupt Enable bit
1 = Enabled
0 = Disabled

9.4 IPR Registers

The IPR registers contain the individual priority bits for the peripheral interrupts. Due to the number of peripheral interrupt sources, there are two Peripheral Interrupt Priority registers (IPR1 and IPR2). Using the priority bits requires that the Interrupt Priority Enable (IPEN) bit be set.

REGISTER 9-8: IPR1: PERIPHERAL INTERRUPT PRIORITY REGISTER 1

R/W-1	R/W-1	R/W-1	R/W-1	R/W-1	R/W-1	R/W-1	R/W-1
PSPIP(1)	ADIP	RCIP	TXIP	SSPIP	CCP1IP	TMR2IP	TMR1IP
bit 7							bit 0

Legend:			
R = Readable bit	W = Writable bit	U = Unimplemented bit, read as '0'	
-n = Value at POR	'1' = Bit is set	'0' = Bit is cleared	x = Bit is unknown

bit 7 **PSPIP:** Parallel Slave Port Read/Write Interrupt Priority bit(1)
1 = High priority
0 = Low priority

bit 6 **ADIP:** A/D Converter Interrupt Priority bit
1 = High priority
0 = Low priority

bit 5 **RCIP:** EUSART Receive Interrupt Priority bit
1 = High priority
0 = Low priority

bit 4 **TXIP:** EUSART Transmit Interrupt Priority bit
1 = High priority
0 = Low priority

bit 3 **SSPIP:** Master Synchronous Serial Port Interrupt Priority bit
1 = High priority
0 = Low priority

bit 2 **CCP1IP:** CCP1 Interrupt Priority bit
1 = High priority
0 = Low priority

bit 1 **TMR2IP:** TMR2 to PR2 Match Interrupt Priority bit
1 = High priority
0 = Low priority

bit 0 **TMR1IP:** TMR1 Overflow Interrupt Priority bit
1 = High priority
0 = Low priority

Note 1: This bit is unimplemented on 28-pin devices and will read as '0'.

REGISTER 9-9: IPR2: PERIPHERAL INTERRUPT PRIORITY REGISTER 2

R/W-1	R/W-1	U-0	R/W-1	R/W-1	R/W-1	R/W-1	R/W-1
OSCFIP	CMIP	—	EEIP	BCLIP	HLVDIP	TMR3IP	CCP2IP
bit 7							bit 0

Legend:			
R = Readable bit	W = Writable bit	U = Unimplemented bit, read as '0'	
-n = Value at POR	'1' = Bit is set	'0' = Bit is cleared	x = Bit is unknown

bit 7 **OSCFIP:** Oscillator Fail Interrupt Priority bit
1 = High priority
0 = Low priority

bit 6 **CMIP:** Comparator Interrupt Priority bit
1 = High priority
0 = Low priority

bit 5 **Unimplemented:** Read as '0'

bit 4 **EEIP:** Data EEPROM/Flash Write Operation Interrupt Priority bit
1 = High priority
0 = Low priority

bit 3 **BCLIP:** Bus Collision Interrupt Priority bit
1 = High priority
0 = Low priority

bit 2 **HLVDIP:** High/Low-Voltage Detect Interrupt Priority bit
1 = High priority
0 = Low priority

bit 1 **TMR3IP:** TMR3 Overflow Interrupt Priority bit
1 = High priority
0 = Low priority

bit 0 **CCP2IP:** CCP2 Interrupt Priority bit
1 = High priority
0 = Low priority

9.5 RCON Register

The RCON register contains flag bits which are used to determine the cause of the last Reset or wake-up from Idle or Sleep modes. RCON also contains the IPEN bit which enables interrupt priorities.

The operation of the SBOREN bit and the Reset flag bits is discussed in more detail in **Section 4.1 "RCON Register"**.

REGISTER 9-10: RCON: RESET CONTROL REGISTER

R/W-0	R/W-1(1)	U-0	R/W-1	R-1	R-1	R/W-0(1)	R/W-0
IPEN	SBOREN	—	$\overline{RI}$	$\overline{TO}$	$\overline{PD}$	$\overline{POR}$	$\overline{BOR}$
bit 7							bit 0

Legend:			
R = Readable bit	W = Writable bit	U = Unimplemented bit, read as '0'	
-n = Value at POR	'1' = Bit is set	'0' = Bit is cleared	x = Bit is unknown

bit 7 **IPEN:** Interrupt Priority Enable bit
1 = Enable priority levels on interrupts
0 = Disable priority levels on interrupts (PIC16CXXX Compatibility mode)

bit 6 **SBOREN:** Software BOR Enable bit(1)
For details of bit operation, see Register 4-1.

bit 5 **Unimplemented:** Read as '0'

bit 4 **$\overline{RI}$:** RESET Instruction Flag bit
For details of bit operation, see Register 4-1.

bit 3 **$\overline{TO}$:** Watchdog Timer Time-out Flag bit
For details of bit operation, see Register 4-1.

bit 2 **$\overline{PD}$:** Power-Down Detection Flag bit
For details of bit operation, see Register 4-1.

bit 1 **$\overline{POR}$:** Power-on Reset Status bit(1)
For details of bit operation, see Register 4-1.

bit 0 **$\overline{BOR}$:** Brown-out Reset Status bit
For details of bit operation, see Register 4-1.

Note 1: Actual Reset values are determined by device configuration and the nature of the device Reset. See Register 4-1 for additional information.

9.6 INTx Pin Interrupts

External interrupts on the RB0/INT0, RB1/INT1 and RB2/INT2 pins are edge-triggered. If the corresponding INTEDGx bit in the INTCON2 register is set (= 1), the interrupt is triggered by a rising edge; if the bit is clear, the trigger is on the falling edge. When a valid edge appears on the RBx/INTx pin, the corresponding flag bit, INTxIF, is set. This interrupt can be disabled by clearing the corresponding enable bit, INTxIE. Flag bit, INTxIF, must be cleared in software in the Interrupt Service Routine before re-enabling the interrupt.

All external interrupts (INT0, INT1 and INT2) can wake-up the processor from Idle or Sleep modes if bit INTxIE was set prior to going into those modes. If the Global Interrupt Enable bit, GIE, is set, the processor will branch to the interrupt vector following wake-up.

Interrupt priority for INT1 and INT2 is determined by the value contained in the Interrupt Priority bits, INT1IP (INTCON3<6>) and INT2IP (INTCON3<7>). There is no priority bit associated with INT0. It is always a high-priority interrupt source.

9.7 TMR0 Interrupt

In 8-bit mode (which is the default), an overflow in the TMR0 register (FFh → 00h) will set flag bit, TMR0IF. In 16-bit mode, an overflow in the TMR0H:TMR0L register pair (FFFFh → 0000h) will set TMR0IF. The interrupt can be enabled/disabled by setting/clearing enable bit, TMR0IE (INTCON<5>). Interrupt priority for Timer0 is determined by the value contained in the interrupt priority bit, TMR0IP (INTCON2<2>). See **Section 11.0 "Timer0 Module"** for further details on the Timer0 module.

9.8 PORTB Interrupt-on-Change

An input change on PORTB<7:4> sets flag bit, RBIF (INTCON<0>). The interrupt can be enabled/disabled by setting/clearing enable bit, RBIE (INTCON<3>). Interrupt priority for PORTB interrupt-on-change is determined by the value contained in the interrupt priority bit, RBIP (INTCON2<0>).

9.9 Context Saving During Interrupts

During interrupts, the return PC address is saved on the stack. Additionally, the WREG, STATUS and BSR registers are saved on the Fast Return Stack. If a fast return from interrupt is not used (see **Section 5.3 "Data Memory Organization"**), the user may need to save the WREG, STATUS and BSR registers on entry to the Interrupt Service Routine. Depending on the user's application, other registers may also need to be saved. Example 9-1 saves and restores the WREG, STATUS and BSR registers during an Interrupt Service Routine.

EXAMPLE 9-1: SAVING STATUS, WREG AND BSR REGISTERS IN RAM

```
MOVWF   W_TEMP                  ; W_TEMP is in virtual bank
MOVFF   STATUS, STATUS_TEMP     ; STATUS_TEMP located anywhere
MOVFF   BSR, BSR_TEMP           ; BSR_TMEP located anywhere
;
; USER ISR CODE
;
MOVFF   BSR_TEMP, BSR           ; Restore BSR
MOVF    W_TEMP, W               ; Restore WREG
MOVFF   STATUS_TEMP, STATUS     ; Restore STATUS
```

10.0 I/O PORTS

Depending on the device selected and features enabled, there are up to five ports available. Some pins of the I/O ports are multiplexed with an alternate function from the peripheral features on the device. In general, when a peripheral is enabled, that pin may not be used as a general purpose I/O pin.

Each port has three registers for its operation. These registers are:

- TRIS register (Data Direction register)
- PORT register (reads the levels on the pins of the device)
- LAT register (Data Latch register)

The Data Latch (LAT register) is useful for read-modify-write operations on the value that the I/O pins are driving.

A simplified model of a generic I/O port, without the interfaces to other peripherals, is shown in Figure 10-1.

FIGURE 10-1: GENERIC I/O PORT OPERATION

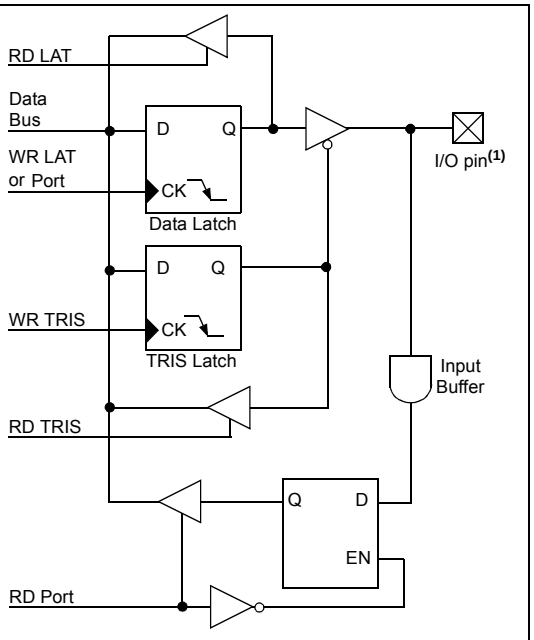

Note 1: I/O pins have diode protection to VDD and VSS.

10.1 PORTA, TRISA and LATA Registers

PORTA is an 8-bit wide, bidirectional port. The corresponding Data Direction register is TRISA. Setting a TRISA bit (= 1) will make the corresponding PORTA pin an input (i.e., put the corresponding output driver in a high-impedance mode). Clearing a TRISA bit (= 0) will make the corresponding PORTA pin an output (i.e., put the contents of the output latch on the selected pin).

Reading the PORTA register reads the status of the pins, whereas writing to it, will write to the port latch.

The Data Latch (LATA) register is also memory mapped. Read-modify-write operations on the LATA register read and write the latched output value for PORTA.

The RA4 pin is multiplexed with the Timer0 module clock input and one of the comparator outputs to become the RA4/T0CKI/C1OUT pin. Pins RA6 and RA7 are multiplexed with the main oscillator pins; they are enabled as oscillator or I/O pins by the selection of the main oscillator in the Configuration register (see **Section 23.1 "Configuration Bits"** for details). When they are not used as port pins, RA6 and RA7 and their associated TRIS and LAT bits are read as '0'.

The other PORTA pins are multiplexed with analog inputs, the analog VREF+ and VREF- inputs and the comparator voltage reference output. The operation of pins RA<3:0> and RA5 as A/D Converter inputs is selected by clearing or setting the control bits in the ADCON1 register (A/D Control Register 1).

Pins RA0 through RA5 may also be used as comparator inputs or outputs by setting the appropriate bits in the CMCON register. To use RA<3:0> as digital inputs, it is also necessary to turn off the comparators.

Note:	On a Power-on Reset, RA5 and RA<3:0> are configured as analog inputs and read as '0'. RA4 is configured as a digital input.

The RA4/T0CKI/C1OUT pin is a Schmitt Trigger input. All other PORTA pins have TTL input levels and full CMOS output drivers.

The TRISA register controls the direction of the PORTA pins, even when they are being used as analog inputs. The user must ensure the bits in the TRISA register are maintained set when using them as analog inputs.

EXAMPLE 10-1: INITIALIZING PORTA

```
CLRF    PORTA   ; Initialize PORTA by
                ; clearing output
                ; data latches
CLRF    LATA    ; Alternate method
                ; to clear output
                ; data latches
MOVLW   07h     ; Configure A/D
MOVWF   ADCON1  ; for digital inputs
MOVWF   07h     ; Configure comparators
MOVWF   CMCON   ; for digital input
MOVLW   0CFh    ; Value used to
                ; initialize data
                ; direction
MOVWF   TRISA   ; Set RA<3:0> as inputs
                ; RA<5:4> as outputs
```

TABLE 10-1: PORTA I/O SUMMARY

Pin	Function	TRIS Setting	I/O	I/O Type	Description
RA0/AN0	RA0	0	O	DIG	LATA<0> data output; not affected by analog input.
		1	I	TTL	PORTA<0> data input; disabled when analog input enabled.
	AN0	1	I	ANA	A/D input channel 0 and comparator C1- input. Default input configuration on POR; does not affect digital output.
RA1/AN1	RA1	0	O	DIG	LATA<1> data output; not affected by analog input.
		1	I	TTL	PORTA<1> data input; disabled when analog input enabled.
	AN1	1	I	ANA	A/D input channel 1 and comparator C2- input. Default input configuration on POR; does not affect digital output.
RA2/AN2/ VREF-/CVREF	RA2	0	O	DIG	LATA<2> data output; not affected by analog input. Disabled when CVREF output enabled.
		1	I	TTL	PORTA<2> data input. Disabled when analog functions enabled; disabled when CVREF output enabled.
	AN2	1	I	ANA	A/D input channel 2 and comparator C2+ input. Default input configuration on POR; not affected by analog output.
	VREF-	1	I	ANA	A/D and comparator voltage reference low input.
	CVREF	x	O	ANA	Comparator voltage reference output. Enabling this feature disables digital I/O.
RA3/AN3/VREF+	RA3	0	O	DIG	LATA<3> data output; not affected by analog input.
		1	I	TTL	PORTA<3> data input; disabled when analog input enabled.
	AN3	1	I	ANA	A/D input channel 3 and comparator C1+ input. Default input configuration on POR.
	VREF+	1	I	ANA	A/D and comparator voltage reference high input.
RA4/T0CKI/C1OUT	RA4	0	O	DIG	LATA<4> data output.
		1	I	ST	PORTA<4> data input; default configuration on POR.
	T0CKI	1	I	ST	Timer0 clock input.
	C1OUT	0	O	DIG	Comparator 1 output; takes priority over port data.
RA5/AN4/$\overline{SS}$/ HLVDIN/C2OUT	RA5	0	O	DIG	LATA<5> data output; not affected by analog input.
		1	I	TTL	PORTA<5> data input; disabled when analog input enabled.
	AN4	1	I	ANA	A/D input channel 4. Default configuration on POR.
	$\overline{SS}$	1	I	TTL	Slave select input for MSSP module.
	HLVDIN	1	I	ANA	High/Low-Voltage Detect external trip point input.
	C2OUT	0	O	DIG	Comparator 2 output; takes priority over port data.
OSC2/CLKO/RA6	RA6	0	O	DIG	LATA<6> data output. Enabled in RCIO, INTIO2 and ECIO modes only.
		1	I	TTL	PORTA<6> data input. Enabled in RCIO, INTIO2 and ECIO modes only.
	OSC2	x	O	ANA	Main oscillator feedback output connection (XT, HS and LP modes).
	CLKO	x	O	DIG	System cycle clock output (FOSC/4) in RC, INTIO1 and EC Oscillator modes.
OSC1/CLKI/RA7	RA7	0	O	DIG	LATA<7> data output. Disabled in external oscillator modes.
		1	I	TTL	PORTA<7> data input. Disabled in external oscillator modes.
	OSC1	x	I	ANA	Main oscillator input connection.
	CLKI	x	I	ANA	Main clock input connection.

Legend: DIG = Digital level output; TTL = TTL input buffer; ST = Schmitt Trigger input buffer; ANA = Analog level input/output; x = Don't care (TRIS bit does not affect port direction or is overridden for this option).

TABLE 10-2: SUMMARY OF REGISTERS ASSOCIATED WITH PORTA

Name	Bit 7	Bit 6	Bit 5	Bit 4	Bit 3	Bit 2	Bit 1	Bit 0	Reset Values on page
PORTA	RA7(1)	RA6(1)	RA5	RA4	RA3	RA2	RA1	RA0	52
LATA	LATA7(1)	LATA6(1)	PORTA Data Latch Register (Read and Write to Data Latch)						52
TRISA	TRISA7(1)	TRISA6(1)	PORTA Data Direction Register						52
ADCON1	—	—	VCFG1	VCFG0	PCFG3	PCFG2	PCFG1	PCFG0	51
CMCON	C2OUT	C1OUT	C2INV	C1INV	CIS	CM2	CM1	CM0	51
CVRCON	CVREN	CVROE	CVRR	CVRSS	CVR3	CVR2	CVR1	CVR0	51

Legend: — = unimplemented, read as '0'. Shaded cells are not used by PORTA.

Note 1: RA<7:6> and their associated latch and data direction bits are enabled as I/O pins based on oscillator configuration; otherwise, they are read as '0'.

10.2 PORTB, TRISB and LATB Registers

PORTB is an 8-bit wide, bidirectional port. The corresponding Data Direction register is TRISB. Setting a TRISB bit (= 1) will make the corresponding PORTB pin an input (i.e., put the corresponding output driver in a high-impedance mode). Clearing a TRISB bit (= 0) will make the corresponding PORTB pin an output (i.e., put the contents of the output latch on the selected pin).

The Data Latch register (LATB) is also memory mapped. Read-modify-write operations on the LATB register read and write the latched output value for PORTB.

EXAMPLE 10-2: INITIALIZING PORTB

```
CLRF    PORTB   ; Initialize PORTB by
                ; clearing output
                ; data latches
CLRF    LATB    ; Alternate method
                ; to clear output
                ; data latches
MOVLW   0Fh     ; Set RB<4:0> as
MOVWF   ADCON1  ; digital I/O pins
                ; (required if config bit
                ; PBADEN is set)
MOVLW   0CFh    ; Value used to
                ; initialize data
                ; direction
MOVWF   TRISB   ; Set RB<3:0> as inputs
                ; RB<5:4> as outputs
                ; RB<7:6> as inputs
```

Each of the PORTB pins has a weak internal pull-up. A single control bit can turn on all the pull-ups. This is performed by clearing bit, RBPU (INTCON2<7>). The weak pull-up is automatically turned off when the port pin is configured as an output. The pull-ups are disabled on a Power-on Reset.

Note: On a Power-on Reset, RB<4:0> are configured as analog inputs by default and read as '0'; RB<7:5> are configured as digital inputs.

By programming the Configuration bit, PBADEN, RB<4:0> will alternatively be configured as digital inputs on POR.

Four of the PORTB pins (RB<7:4>) have an interrupt-on-change feature. Only pins configured as inputs can cause this interrupt to occur (i.e., any RB<7:4> pin configured as an output is excluded from the interrupt-on-change comparison). The input pins (of RB<7:4>) are compared with the old value latched on the last read of PORTB. The "mismatch" outputs of RB<7:4> are ORed together to generate the RB Port Change Interrupt with Flag bit, RBIF (INTCON<0>).

This interrupt can wake the device from the Sleep mode, or any of the Idle modes. The user, in the Interrupt Service Routine, can clear the interrupt in the following manner:

a) Any read or write of PORTB (except with the MOVFF (ANY), PORTB instruction).
b) Clear flag bit, RBIF.

A mismatch condition will continue to set flag bit, RBIF. Reading PORTB will end the mismatch condition and allow flag bit, RBIF, to be cleared.

The interrupt-on-change feature is recommended for wake-up on key depression operation and operations where PORTB is only used for the interrupt-on-change feature. Polling of PORTB is not recommended while using the interrupt-on-change feature.

RB3 can be configured by the Configuration bit, CCP2MX, as the alternate peripheral pin for the CCP2 module (CCP2MX = 0).

TABLE 10-3: PORTB I/O SUMMARY

Pin	Function	TRIS Setting	I/O	I/O Type	Description
RB0/INT0/FLT0/ AN12	RB0	0	O	DIG	LATB<0> data output; not affected by analog input.
		1	I	TTL	PORTB<0> data input; weak pull-up when $\overline{\text{RBPU}}$ bit is cleared. Disabled when analog input enabled.(1)
	INT0	1	I	ST	External interrupt 0 input.
	FLT0	1	I	ST	Enhanced PWM Fault input (ECCP1 module); enabled in software.
	AN12	1	I	ANA	A/D input channel 12.(1)
RB1/INT1/AN10	RB1	0	O	DIG	LATB<1> data output; not affected by analog input.
		1	I	TTL	PORTB<1> data input; weak pull-up when $\overline{\text{RBPU}}$ bit is cleared. Disabled when analog input enabled.(1)
	INT1	1	I	ST	External Interrupt 1 input.
	AN10	1	I	ANA	A/D input channel 10.(1)
RB2/INT2/AN8	RB2	0	O	DIG	LATB<2> data output; not affected by analog input.
		1	I	TTL	PORTB<2> data input; weak pull-up when $\overline{\text{RBPU}}$ bit is cleared. Disabled when analog input enabled.(1)
	INT2	1	I	ST	External interrupt 2 input.
	AN8	1	I	ANA	A/D input channel 8.(1)
RB3/AN9/CCP2	RB3	0	O	DIG	LATB<3> data output; not affected by analog input.
		1	I	TTL	PORTB<3> data input; weak pull-up when $\overline{\text{RBPU}}$ bit is cleared. Disabled when analog input enabled.(1)
	AN9	1	I	ANA	A/D input channel 9.(1)
	CCP2(2)	0	O	DIG	CCP2 compare and PWM output.
		1	I	ST	CCP2 capture input
RB4/KBI0/AN11	RB4	0	O	DIG	LATB<4> data output; not affected by analog input.
		1	I	TTL	PORTB<4> data input; weak pull-up when $\overline{\text{RBPU}}$ bit is cleared. Disabled when analog input enabled.(1)
	KBI0	1	I	TTL	Interrupt-on-pin change.
	AN11	1	I	ANA	A/D input channel 11.(1)
RB5/KBI1/PGM	RB5	0	O	DIG	LATB<5> data output.
		1	I	TTL	PORTB<5> data input; weak pull-up when $\overline{\text{RBPU}}$ bit is cleared.
	KBI1	1	I	TTL	Interrupt-on-pin change.
	PGM	x	I	ST	Single-Supply In-Circuit Serial Programming™ mode entry (ICSP™). Enabled by LVP Configuration bit; all other pin functions disabled.
RB6/KBI2/PGC	RB6	0	O	DIG	LATB<6> data output.
		1	I	TTL	PORTB<6> data input; weak pull-up when $\overline{\text{RBPU}}$ bit is cleared.
	KBI2	1	I	TTL	Interrupt-on-pin change.
	PGC	x	I	ST	Serial execution (ICSP) clock input for ICSP and ICD operation.(3)
RB7/KBI3/PGD	RB7	0	O	DIG	LATB<7> data output.
		1	I	TTL	PORTB<7> data input; weak pull-up when $\overline{\text{RBPU}}$ bit is cleared.
	KBI3	1	I	TTL	Interrupt-on-pin change.
	PGD	x	O	DIG	Serial execution data output for ICSP and ICD operation.(3)
		x	I	ST	Serial execution data input for ICSP and ICD operation.(3)

Legend: DIG = Digital level output; TTL = TTL input buffer; ST = Schmitt Trigger input buffer; ANA = Analog level input/output; x = Don't care (TRIS bit does not affect port direction or is overridden for this option).

Note 1: Configuration on POR is determined by the PBADEN Configuration bit. Pins are configured as analog inputs by default when PBADEN is set and digital inputs when PBADEN is cleared.

2: Alternate assignment for CCP2 when the CCP2MX Configuration bit is '0'. Default assignment is RC1.

3: All other pin functions are disabled when ICSP or ICD are enabled.

TABLE 10-4: SUMMARY OF REGISTERS ASSOCIATED WITH PORTB

Name	Bit 7	Bit 6	Bit 5	Bit 4	Bit 3	Bit 2	Bit 1	Bit 0	Reset Values on page
PORTB	RB7	RB6	RB5	RB4	RB3	RB2	RB1	RB0	52
LATB	PORTB Data Latch Register (Read and Write to Data Latch)								52
TRISB	PORTB Data Direction Register								52
INTCON	GIE/GIEH	PEIE/GIEL	TMR0IE	INT0IE	RBIE	TMR0IF	INT0IF	RBIF	49
INTCON2	$\overline{\text{RBPU}}$	INTEDG0	INTEDG1	INTEDG2	—	TMR0IP	—	RBIP	49
INTCON3	INT2IP	INT1IP	—	INT2IE	INT1IE	—	INT2IF	INT1IF	49
ADCON1	—	—	VCFG1	VCFG0	PCFG3	PCFG2	PCFG1	PCFG0	51

Legend: — = unimplemented, read as '0'. Shaded cells are not used by PORTB.

10.3 PORTC, TRISC and LATC Registers

PORTC is an 8-bit wide, bidirectional port. The corresponding Data Direction register is TRISC. Setting a TRISC bit (= 1) will make the corresponding PORTC pin an input (i.e., put the corresponding output driver in a high-impedance mode). Clearing a TRISC bit (= 0) will make the corresponding PORTC pin an output (i.e., put the contents of the output latch on the selected pin).

The Data Latch register (LATC) is also memory mapped. Read-modify-write operations on the LATC register read and write the latched output value for PORTC.

PORTC is multiplexed with several peripheral functions (Table 10-5). The pins have Schmitt Trigger input buffers. RC1 is normally configured by Configuration bit, CCP2MX, as the default peripheral pin of the CCP2 module (default/erased state, CCP2MX = 1).

When enabling peripheral functions, care should be taken in defining TRIS bits for each PORTC pin. Some peripherals override the TRIS bit to make a pin an output, while other peripherals override the TRIS bit to make a pin an input. The user should refer to the corresponding peripheral section for additional information.

Note:	On a Power-on Reset, these pins are configured as digital inputs.

The contents of the TRISC register are affected by peripheral overrides. Reading TRISC always returns the current contents, even though a peripheral device may be overriding one or more of the pins.

EXAMPLE 10-3: INITIALIZING PORTC

```
CLRF    PORTC   ; Initialize PORTC by
                ; clearing output
                ; data latches
CLRF    LATC    ; Alternate method
                ; to clear output
                ; data latches
MOVLW   0CFh    ; Value used to
                ; initialize data
                ; direction
MOVWF   TRISC   ; Set RC<3:0> as inputs
                ; RC<5:4> as outputs
                ; RC<7:6> as inputs
```

TABLE 10-5: PORTC I/O SUMMARY

Pin	Function	TRIS Setting	I/O	I/O Type	Description
RC0/T1OSO/ T13CKI	RC0	0	O	DIG	LATC<0> data output.
		1	I	ST	PORTC<0> data input.
	T1OSO	x	O	ANA	Timer1 oscillator output; enabled when Timer1 oscillator enabled. Disables digital I/O.
	T13CKI	1	I	ST	Timer1/Timer3 counter input.
RC1/T1OSI/CCP2	RC1	0	O	DIG	LATC<1> data output.
		1	I	ST	PORTC<1> data input.
	T1OSI	x	I	ANA	Timer1 oscillator input; enabled when Timer1 oscillator enabled. Disables digital I/O.
	CCP2(1)	0	O	DIG	CCP2 compare and PWM output; takes priority over port data.
		1	I	ST	CCP2 capture input.
RC2/CCP1/P1A	RC2	0	O	DIG	LATC<2> data output.
		1	I	ST	PORTC<2> data input.
	CCP1	0	O	DIG	ECCP1 compare or PWM output; takes priority over port data.
		1	I	ST	ECCP1 capture input.
	P1A(2)	0	O	DIG	ECCP1 Enhanced PWM output, channel A. May be configured for tri-state during Enhanced PWM shutdown events. Takes priority over port data.
RC3/SCK/SCL	RC3	0	O	DIG	LATC<3> data output.
		1	I	ST	PORTC<3> data input.
	SCK	0	O	DIG	SPI clock output (MSSP module); takes priority over port data.
		1	I	ST	SPI clock input (MSSP module).
	SCL	0	O	DIG	I^2C™ clock output (MSSP module); takes priority over port data.
		1	I	I^2C/SMB	I^2C clock input (MSSP module); input type depends on module setting.
RC4/SDI/SDA	RC4	0	O	DIG	LATC<4> data output.
		1	I	ST	PORTC<4> data input.
	SDI	1	I	ST	SPI data input (MSSP module).
	SDA	1	O	DIG	I^2C data output (MSSP module); takes priority over port data.
		1	I	I^2C/SMB	I^2C data input (MSSP module); input type depends on module setting.
RC5/SDO	RC5	0	O	DIG	LATC<5> data output.
		1	I	ST	PORTC<5> data input.
	SDO	0	O	DIG	SPI data output (MSSP module); takes priority over port data.
RC6/TX/CK	RC6	0	O	DIG	LATC<6> data output.
		1	I	ST	PORTC<6> data input.
	TX	1	O	DIG	Asynchronous serial transmit data output (EUSART module); takes priority over port data. User must configure as output.
	CK	1	O	DIG	Synchronous serial clock output (EUSART module); takes priority over port data.
		1	I	ST	Synchronous serial clock input (EUSART module).
RC7/RX/DT	RC7	0	O	DIG	LATC<7> data output.
		1	I	ST	PORTC<7> data input.
	RX	1	I	ST	Asynchronous serial receive data input (EUSART module).
	DT	1	O	DIG	Synchronous serial data output (EUSART module); takes priority over port data.
		1	I	ST	Synchronous serial data input (EUSART module). User must configure as an input.

Legend: DIG = Digital level output; TTL = TTL input buffer; ST = Schmitt Trigger input buffer; ANA = Analog level input/output; I^2C/SMB = I^2C/SMBus input buffer; x = Don't care (TRIS bit does not affect port direction or is overridden for this option).

Note 1: Default assignment for CCP2 when the CCP2MX Configuration bit is set. Alternate assignment is RB3.

2: Enhanced PWM output is available only on PIC18F4520 devices.

TABLE 10-6: SUMMARY OF REGISTERS ASSOCIATED WITH PORTC

Name	Bit 7	Bit 6	Bit 5	Bit 4	Bit 3	Bit 2	Bit 1	Bit 0	Reset Values on page
PORTC	RC7	RC6	RC5	RC4	RC3	RC2	RC1	RC0	52
LATC	PORTC Data Latch Register (Read and Write to Data Latch)								52
TRISC	PORTC Data Direction Register								52

11.0 TIMER0 MODULE

The Timer0 module incorporates the following features:

- Software selectable operation as a timer or counter in both 8-bit or 16-bit modes
- Readable and writable registers
- Dedicated 8-bit, software programmable prescaler
- Selectable clock source (internal or external)
- Edge select for external clock
- Interrupt-on-overflow

The T0CON register (Register 11-1) controls all aspects of the module's operation, including the prescale selection. It is both readable and writable.

A simplified block diagram of the Timer0 module in 8-bit mode is shown in Figure 11-1. Figure 11-2 shows a simplified block diagram of the Timer0 module in 16-bit mode.

REGISTER 11-1: T0CON: TIMER0 CONTROL REGISTER

R/W-1	R/W-1	R/W-1	R/W-1	R/W-1	R/W-1	R/W-1	R/W-1
TMR0ON	T08BIT	T0CS	T0SE	PSA	T0PS2	T0PS1	T0PS0
bit 7							bit 0

Legend:			
R = Readable bit	W = Writable bit	U = Unimplemented bit, read as '0'	
-n = Value at POR	'1' = Bit is set	'0' = Bit is cleared	x = Bit is unknown

bit 7 **TMR0ON:** Timer0 On/Off Control bit
1 = Enables Timer0
0 = Stops Timer0

bit 6 **T08BIT**: Timer0 8-Bit/16-Bit Control bit
1 = Timer0 is configured as an 8-bit timer/counter
0 = Timer0 is configured as a 16-bit timer/counter

bit 5 **T0CS**: Timer0 Clock Source Select bit
1 = Transition on T0CKI pin
0 = Internal instruction cycle clock (CLKO)

bit 4 **T0SE**: Timer0 Source Edge Select bit
1 = Increment on high-to-low transition on T0CKI pin
0 = Increment on low-to-high transition on T0CKI pin

bit 3 **PSA**: Timer0 Prescaler Assignment bit
1 = TImer0 prescaler is not assigned. Timer0 clock input bypasses prescaler.
0 = Timer0 prescaler is assigned. Timer0 clock input comes from prescaler output.

bit 2-0 **T0PS<2:0>**: Timer0 Prescaler Select bits
111 = 1:256 Prescale value
110 = 1:128 Prescale value
101 = 1:64 Prescale value
100 = 1:32 Prescale value
011 = 1:16 Prescale value
010 = 1:8 Prescale value
001 = 1:4 Prescale value
000 = 1:2 Prescale value

11.1 Timer0 Operation

Timer0 can operate as either a timer or a counter; the mode is selected with the T0CS bit (T0CON<5>). In Timer mode (T0CS = 0), the module increments on every clock by default unless a different prescaler value is selected (see **Section 11.3 "Prescaler"**). If the TMR0 register is written to, the increment is inhibited for the following two instruction cycles. The user can work around this by writing an adjusted value to the TMR0 register.

The Counter mode is selected by setting the T0CS bit (= 1). In this mode, Timer0 increments either on every rising or falling edge of pin RA4/T0CKI. The incrementing edge is determined by the Timer0 Source Edge Select bit, T0SE (T0CON<4>); clearing this bit selects the rising edge. Restrictions on the external clock input are discussed below.

An external clock source can be used to drive Timer0; however, it must meet certain requirements to ensure that the external clock can be synchronized with the internal phase clock (TOSC). There is a delay between synchronization and the onset of incrementing the timer/counter.

11.2 Timer0 Reads and Writes in 16-Bit Mode

TMR0H is not the actual high byte of Timer0 in 16-bit mode; it is actually a buffered version of the real high byte of Timer0 which is not directly readable nor writable (refer to Figure 11-2). TMR0H is updated with the contents of the high byte of Timer0 during a read of TMR0L. This provides the ability to read all 16 bits of Timer0 without having to verify that the read of the high and low byte were valid, due to a rollover between successive reads of the high and low byte.

Similarly, a write to the high byte of Timer0 must also take place through the TMR0H Buffer register. The high byte is updated with the contents of TMR0H when a write occurs to TMR0L. This allows all 16 bits of Timer0 to be updated at once.

FIGURE 11-1: TIMER0 BLOCK DIAGRAM (8-BIT MODE)

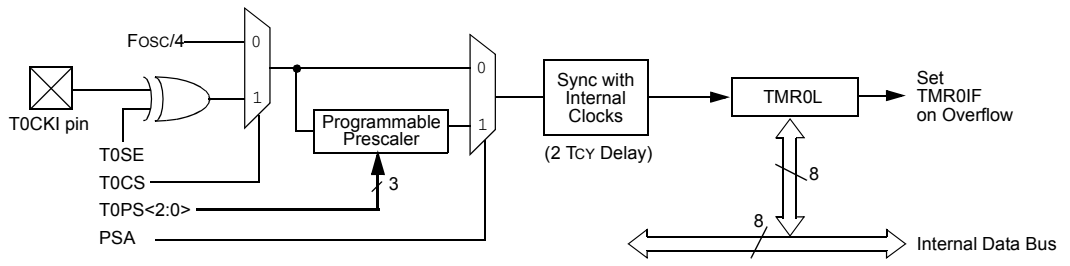

Note: Upon Reset, Timer0 is enabled in 8-bit mode with clock input from T0CKI max. prescale.

FIGURE 11-2: TIMER0 BLOCK DIAGRAM (16-BIT MODE)

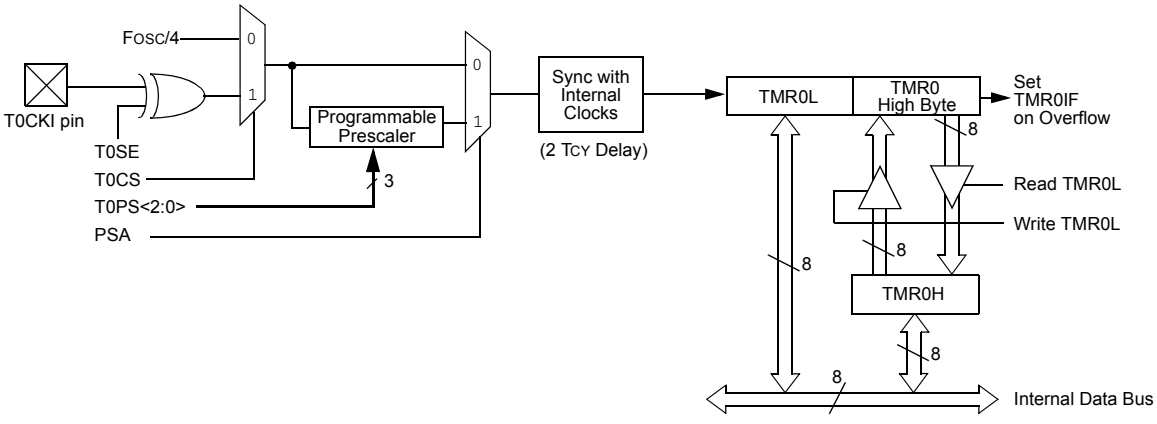

Note: Upon Reset, Timer0 is enabled in 8-bit mode with clock input from T0CKI max. prescale.

11.3 Prescaler

An 8-bit counter is available as a prescaler for the Timer0 module. The prescaler is not directly readable or writable; its value is set by the PSA and T0PS<2:0> bits (T0CON<3:0>) which determine the prescaler assignment and prescale ratio.

Clearing the PSA bit assigns the prescaler to the Timer0 module. When it is assigned, prescale values from 1:2 through 1:256 in power-of-2 increments are selectable.

When assigned to the Timer0 module, all instructions writing to the TMR0 register (e.g., `CLRF TMR0`, `MOVWF TMR0`, `BSF TMR0`, etc.) clear the prescaler count.

Note:	Writing to TMR0 when the prescaler is assigned to Timer0 will clear the prescaler count but will not change the prescaler assignment.

11.3.1 SWITCHING PRESCALER ASSIGNMENT

The prescaler assignment is fully under software control and can be changed "on-the-fly" during program execution.

11.4 Timer0 Interrupt

The TMR0 interrupt is generated when the TMR0 register overflows from FFh to 00h in 8-bit mode, or from FFFFh to 0000h in 16-bit mode. This overflow sets the TMR0IF flag bit. The interrupt can be masked by clearing the TMR0IE bit (INTCON<5>). Before re-enabling the interrupt, the TMR0IF bit must be cleared in software by the Interrupt Service Routine.

Since Timer0 is shut down in Sleep mode, the TMR0 interrupt cannot awaken the processor from Sleep.

TABLE 11-1: REGISTERS ASSOCIATED WITH TIMER0

Name	Bit 7	Bit 6	Bit 5	Bit 4	Bit 3	Bit 2	Bit 1	Bit 0	Reset Values on page
TMR0L	Timer0 Register Low Byte								50
TMR0H	Timer0 Register High Byte								50
INTCON	GIE/GIEH	PEIE/GIEL	TMR0IE	INT0IE	RBIE	TMR0IF	INT0IF	RBIF	49
T0CON	TMR0ON	T08BIT	T0CS	T0SE	PSA	T0PS2	T0PS1	T0PS0	50
TRISA	RA7(1)	RA6(1)	RA5	RA4	RA3	RA2	RA1	RA0	52

Legend: Shaded cells are not used by Timer0.

Note 1: PORTA<7:6> and their direction bits are individually configured as port pins based on various primary oscillator modes. When disabled, these bits read as '0'.

26.0 ELECTRICAL CHARACTERISTICS

Absolute Maximum Ratings(†)

Ambient temperature under bias ..... -40°C to +125°C
Storage temperature ..... -65°C to +150°C
Voltage on any pin with respect to V_{SS} (except V_{DD} and $\overline{MCLR}$) ..... -0.3V to (V_{DD} + 0.3V)
Voltage on V_{DD} with respect to V_{SS} ..... -0.3V to +7.5V
Voltage on $\overline{MCLR}$ with respect to V_{SS} **(Note 2)** ..... 0V to +13.25V
Total power dissipation **(Note 1)** 1.0W
Maximum current out of V_{SS} pin ..... 300 mA
Maximum current into V_{DD} pin ..... 250 mA
Input clamp current, I_{IK} (V_I < 0 or V_I > V_{DD}) ..... ±20 mA
Output clamp current, I_{OK} (V_O < 0 or V_O > V_{DD}) ..... ±20 mA
Maximum output current sunk by any I/O pin ..... 25 mA
Maximum output current sourced by any I/O pin ..... 25 mA
Maximum current sunk by all ports ..... 200 mA
Maximum current sourced by all ports ..... 200 mA

Note 1: Power dissipation is calculated as follows:
$P_{dis} = V_{DD} \times \{I_{DD} - \sum I_{OH}\} + \sum \{(V_{DD} - V_{OH}) \times I_{OH}\} + \sum(V_{OL} \times I_{OL})$

2: Voltage spikes below V_{SS} at the $\overline{MCLR}$/V_{PP}/RE3 pin, inducing currents greater than 80 mA, may cause latch-up. Thus, a series resistor of 50-100Ω should be used when applying a "low" level to the $\overline{MCLR}$/V_{PP}/RE3 pin, rather than pulling this pin directly to V_{SS}.

† **NOTICE:** Stresses above those listed under "Absolute Maximum Ratings" may cause permanent damage to the device. This is a stress rating only and functional operation of the device at those or any other conditions above those indicated in the operation listings of this specification is not implied. Exposure to maximum rating conditions for extended periods may affect device reliability.

E.3 OPA657U

www.ti.com

SBOS197E – DECEMBER 2001 – REVISED DECEMBER 2008

1.6GHz, Low-Noise, FET-Input OPERATIONAL AMPLIFIER

FEATURES

- HIGH GAIN BANDWIDTH PRODUCT: 1.6GHz
- HIGH BANDWIDTH 275MHz (G = +10)
- LOW INPUT OFFSET VOLTAGE: ±0.25mV
- LOW INPUT BIAS CURRENT: 2pA
- LOW INPUT VOLTAGE NOISE: 4.8nV/$\sqrt{Hz}$
- HIGH OUTPUT CURRENT: 70mA
- FAST OVERDRIVE RECOVERY

APPLICATIONS

- WIDEBAND PHOTODIODE AMPLIFIER
- WAFER SCANNING EQUIPMENT
- ADC INPUT AMPLIFIER
- TEST AND MEASUREMENT FRONT END
- HIGH GAIN PRECISION AMPLIFIER

DESCRIPTION

The OPA657 combines a high gain bandwidth, low distortion, voltage-feedback op amp with a low voltage noise JFET-input stage to offer a very high dynamic range amplifier for high precision ADC (Analog-to-Digital Converter) driving or wideband transimpedance applications. Photodiode applications will see improved noise and bandwidth using this decompensated, high gain bandwidth amplifier.

Very low level signals can be significantly amplified in a single OPA657 gain stage with exceptional bandwidth and accuracy. Having a high 1.6GHz gain bandwidth product will give > 10MHz signal bandwidths up to gains of 160V/V (44dB). The very low input bias current and capacitance will support this performance even for relatively high source impedances.

Broadband photodetector applications will benefit from the low voltage noise JFET inputs for the OPA657. The JFET input contributes virtually no current noise while for broadband applications, a low voltage noise is also required. The low 4.8nV/$\sqrt{Hz}$ input voltage noise will provide exceptional input sensitivity for higher bandwidth applications. The example shown below will give a total equivalent input noise current of 1.8pA/$\sqrt{Hz}$ over a 10MHz bandwidth.

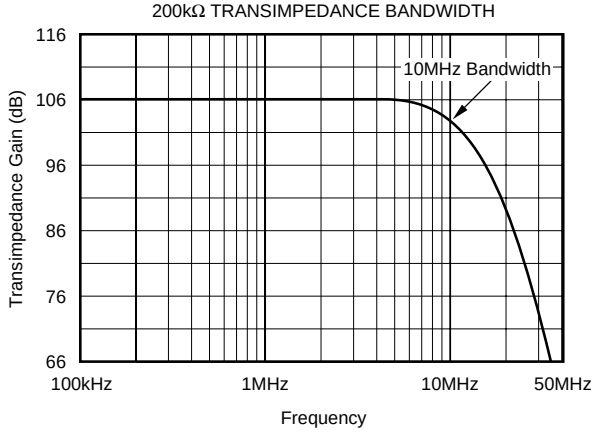

RELATED OPERATIONAL AMPLIFIER PRODUCTS

DEVICE	V_S (V)	BW (MHz)	SLEW RATE (V/µS)	VOLTAGE NOISE (nV/√HZ)	AMPLIFIER DESCRIPTION
OPA355	+5	200	300	5.80	Unity-Gain Stable CMOS
OPA655	±5	400	290	6	Unity-Gain Stable FET-Input
OPA656	±5	500	170	7	Unity-Gain Stable FET-Input
OPA627	±15	16	55	4.5	Unity-Gain Stable FET-Input
THS4601	±15	180	100	5.4	Unity-Gain Stable FET-Input

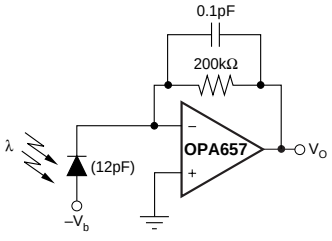

Wideband Photodiode Transimpedance Amplifier

ABSOLUTE MAXIMUM RATINGS[1]

Supply Voltage	±6.5V
Internal Power Dissipation	See Thermal Characteristics
Differential Input Voltage	$\pm V_S$
Input Voltage Range	$\pm V_S$
Storage Temperature Range	–65°C to +125°C
Lead Temperature	+260°C
Junction Temperature (T_J)	+175°C
ESD Rating (Human Body Model)	2000V
(Machine Model)	200V

NOTE: (1) Stresses above these ratings may cause permanent damage. Exposure to absolute maximum conditions for extended periods may degrade device reliability. These are stress ratings only, and functional operation of the device at these or any other conditions beyond those specified is not implied.

ELECTROSTATIC DISCHARGE SENSITIVITY

This integrated circuit can be damaged by ESD. Texas Instruments recommends that all integrated circuits be handled with appropriate precautions. Failure to observe proper handling and installation procedures can cause damage.

ESD damage can range from subtle performance degradation to complete device failure. Precision integrated circuits may be more susceptible to damage because very small parametric changes could cause the device not to meet its published specifications.

PACKAGE/ORDERING INFORMATION[1]

PRODUCT	PACKAGE-LEAD	PACKAGE DESIGNATOR	SPECIFIED TEMPERATURE RANGE	PACKAGE MARKING	ORDERING NUMBER[2]	TRANSPORT MEDIA, QUANTITY
OPA657U	SO-8 Surface Mount	D	–40°C to +85°C	OPA657U	OPA657U	Rails, 100
"	"	"	"	"	OPA657U/2K5	Tape and Reel, 2500
OPA657UB	SO-8 Surface Mount	D	–40°C to +85°C	OPA657UB	OPA657UB	Rails, 100
"	"	"	"	"	OPA657UB/2K5	Tape and Reel, 2500
OPA657N	SOT23-5	DBV	–40°C to +85°C	A57	OPA657N/250	Tape and Reel, 250
"	"	"	"	"	OPA657N/3K	Tape and Reel, 3000
OPA657NB	SOT23-5	DBV	–40°C to +85°C	A57	OPA657NB/250	Tape and Reel, 250
"	"	"	"	"	OPA657NB/3K	Tape and Reel, 3000

NOTE: (1) For the most current package and ordering information, see the Package Option Addendum located at the end of this document, or see the TI website at www.ti.com.

PIN CONFIGURATIONS

Top View **SO-8**

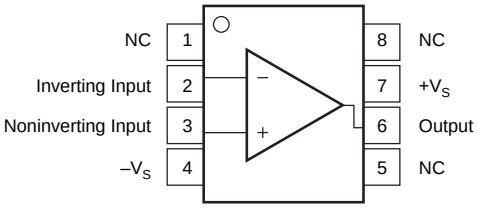

Top View **SOT23-5**

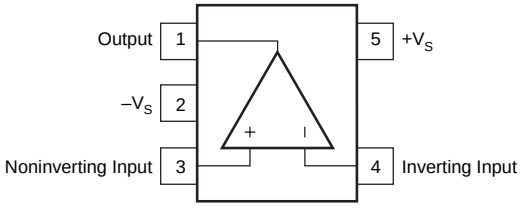

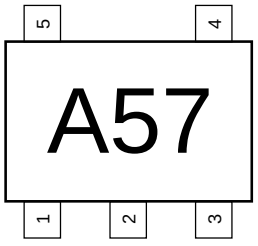

Pin Orientation/Package Marking

ELECTRICAL CHARACTERISTICS: $V_S = \pm 5V$

$R_F = 453\Omega$, $R_L = 100\Omega$, and G = +10, unless otherwise noted. Figure 1 for AC performance.

PARAMETER	CONDITIONS	OPA657U, N (Standard-Grade) TYP +25°C	MIN/MAX OVER TEMPERATURE +25°C(1)	0°C to 70°C(2)	–40°C to +85°C(2)	UNITS	MIN/MAX	TEST LEVEL(3)
AC PERFORMANCE (Figure 1)								
Small-Signal Bandwidth	G = +7, V_O = 200mV$_{PP}$	350				MHz	Typ	C
	G = +10, V_O = 200mV$_{PP}$	275				MHz	Typ	C
	G = +20, V_O = 200mV$_{PP}$	90				MHz	Typ	C
Gain-Bandwidth Product	G > +40	1600				MHz	Typ	C
Bandwidth for 0.1dB flatness	G = +10, 2V$_{PP}$	30				MHz	Typ	C
Peaking at a Gain of +7		7				dB	Typ	C
Large-Signal Bandwidth	G = +10, 2V$_{PP}$	180				MHz	Typ	C
Slew Rate	G = +10, 1V Step	700				V/µs	Typ	C
Rise-and-Fall Time	0.2V Step	1				ns	Typ	C
Settling Time to 0.02%	G = +10, V_O = 2V Step	20				ns	Typ	C
Harmonic Distortion	G = +10, f = 5MHz, V_O = 2V$_{PP}$							C
2nd-Harmonic	R_L = 200Ω	–70				dBc	Typ	C
	R_L > 500Ω	–74				dBc	Typ	C
3rd-Harmonic	R_L = 200Ω	–99				dBc	Typ	C
	R_L > 500Ω	–106				dBc	Typ	C
Input Voltage Noise	f > 100kHz	4.8				nV/√Hz	Typ	C
Input Current Noise	f > 100kHz	1.3				fA/√Hz	Typ	**C**
DC PERFORMANCE(4)								
Open-Loop Voltage Gain (A_{OL})	V_{CM} = 0V, R_L = 100Ω	70	**65**	64	63	dB	Min	A
Input Offset Voltage	V_{CM} = 0V	±0.25	**±1.8**	±2.2	±2.6	mV	Max	A
Average Offset Voltage Drift	V_{CM} = 0V	±2	**±12**	±12	±12	µV/°C	Max	A
Input Bias Current	V_{CM} = 0V	±2	**±20**	±1800	±5000	pA	Max	A
Input Offset Current	V_{CM} = 0V	±1	**±10**	±900	±2500	pA	Max	A
INPUT								
Most Positive Input Voltage(5)		+2.5	**+2.0**	+1.9	+1.8	V	Min	A
Most Negative Input Voltage(5)		–4.0	**–3.5**	–3.4	–3.3	V	Min	A
Common-Mode Rejection Ratio (CMRR)	V_{CM} = ±0.5V	89	**83**	81	79	dB	Min	A
Input Impedance								
Differential		10^{12} || 0.7				Ω || pF	Typ	C
Common-Mode		10^{12} || 4.5				Ω || pF	Typ	C
OUTPUT								
Voltage Output Swing	No Load	±3.9	±3.7			V	Typ	B
	R_L = 100Ω	±3.5	**±3.3**	±3.2	±3.1	V	Min	A
Current Output, Sourcing		+70	**50**	48	46	mA	Min	A
Current Output, Sinking		–70	**–50**	–48	–46	mA	Min	A
Closed-Loop Output Impedance	G = +10, f = 0.1MHz	0.02				Ω	Typ	C
POWER SUPPLY								
Specified Operating Voltage		±5				V	Typ	A
Maximum Operating Voltage Range			**±6**	±6	±6	V	Max	A
Maximum Quiescent Current		14	**16**	16.2	16.3	mA	Max	A
Minimum Quiescent Current		14	**11.7**	11.4	11.1	mA	Min	A
Power-Supply Rejection Ratio (+PSRR)	+V_S = 4.50V to 5.50V	80	**76**	74	72	dB	Min	A
(–PSRR)	–V_S = 4.50V to –5.50V	68	**62**	60	58	dB	Min	A
TEMPERATURE RANGE								
Specified Operating Range: U,N Package		–40 to 85				°C	Typ	
Thermal Resistance, θ_{JA}	Junction-to-Ambient							
U: SO-8		125				°C/W	Typ	
N: SOT23-5		150				°C/W	Typ	

NOTES: (1) Junction temperature = ambient for 25°C specifications.

(2) Junction temperature = ambient at low temperature limit: junction temperature = ambient +20°C at high temperature limit for over temperature specifications.

(3) Test Levels: (A) 100% tested at 25°C. Over temperature limits by characterization and simulation. (B) Limits set by characterization and simulation. (C) Typical value only for information.

(4) Current is considered positive out-of-node. V_{CM} is the input common-mode voltage.

(5) Tested < 3dB below minimum specified CMRR at ±CMIR limits.

ELECTRICAL CHARACTERISTICS: V_S = ±5V: High Grade DC Specifications[1]

R_F = 453Ω, R_L = 100Ω, and G = +10, unless otherwise noted.

PARAMETER	CONDITIONS	OPA657UB, NB (High-Grade)						
		TYP	MIN/MAX OVER TEMPERATURE					
		+25°C	+25°C[2]	0°C to 70°C[3]	–40°C to +85°C[3]	UNITS	MIN/ MAX	TEST LEVEL[4]
Input Offset Voltage	V_{CM} = 0V	±0.1	**±0.6**	±0.85	±0.9	mV	Max	A
Input Offset Voltage Drift	V_{CM} = 0V	±2	**±6**	±6	±6	µV/°C	Max	A
Input Bias Current	V_{CM} = 0V	±1	**±5**	±450	±1250	pA	Max	A
Input Offset Current	V_{CM} = 0V	±0.5	**±5**	±450	±1250	pA	Max	A
Common-Mode Rejection Ratio (CMRR)	V_{CM} = ±0.5V	98	**91**	89	87	dB	Min	A
Power-Supply Rejection Ratio (+PSRR)	$+V_S$ = 4.5V to 5.5V	82	**78**	76	74	dB	Min	A
(–PSRR)	$–V_S$ = –4.5V to –5.5V	74	**68**	66	64	dB	Min	A

NOTES: (1) All other specifications are the same as the standard-grade.

(2) Junction temperature = ambient for 25°C specifications.

(3) Junction temperature = ambient at low temperature limit: junction temperature = ambient +20°C at high temperature limit for over temperature specifications.

(4) Test Levels: (A) 100% tested at 25°C. Over temperature limits by characterization and simulation.

E.4 M1000

1 DESCRIPTION

The Model M1000 High-T_c dc SQUID magnetometer is fabricated from a single layer of $YBa_2Cu_3O_{7-x}$ (YBCO) using a bicrystal grain-boundary Josephson junction technology. The magnetometer design consists of a large-area pickup loop connected in parallel with the SQUID inductance. An external magnetic field sensed by the pickup loop is coupled to the SQUID by direct injection. Excellent low-noise performance is achieved with this single-layer design, even at low frequencies (<1 Hz) using AC current bias.

The magnetometer die are mounted on a standard FR-4 button-shaped printed circuit board using cryogenic epoxy. Current and voltage connections to the chip are made using gold ribbon ultrasonic wire-bonds. Two 200 Ω resistors connected in parallel (110 Ω at 77 K) mounted on the button-shaped pc board allow the magnetometer to be heated above T_c to deflux the SQUID if necessary. Embedded in the pc board button of the Model M1000 magnetometer is a wire-wound copper feedback coil for closed-loop operation using standard feedback electronics. The magnetometer button is encapsulated and hermetically sealed using a glass-epoxy (G-10) cover and attached to a G-10 sensor package that houses an impedance matching circuit for conventional room temperature readout electronics. The package also includes a mounting flange that is fitted with a 10-pin LEMO connector to simplify electrical connections to the magnetometer. Optional mating cryogenic cables are available from STAR Cryoelectronics. For applications requiring a small form factor, two different magnetometer button-only configurations are available. The standard button described above is available with three tapped screw holes for rear mounting or an optional button design is available with clearance holes through the button to simplify installation from the front (M19 package assembly).

The M1000 dc SQUID magnetometer is simple to operate using pcSQUID™, STAR Cryoelectronics' advanced PC-based closed-loop feedback and readout electronics. For button-only installations, the single-transformer option in the feedback loop electronics may be used, eliminating the need for any cooled matching circuitry.

FEATURES

- Low rms field noise of better than 100 fT/Hz^{½}.
- Large-area pickup loop for applications requiring high magnetic field resolution.
- Compact, hermetically-sealed magnetometer package design.
- Standard sensor assembly includes cooled matching circuitry and LEMO connector interface; optional right-angle mounting is available for transverse field measurements.
- Optional magnetometer button-only package may be installed without any cooled matching circuit for applications requiring small foot print.

2 SPECIFICATIONS

Table 2.1 Specifications, M1000v12 dual SQUID magnetometer for operation in ambient fields.

Parameter	Value			
Pickup loop size	9.2 mm × 7.6 mm OD, 3.8 mm ×2.6 mm ID			
Feedback coil inductance L_f	N/A			
Operating temperature	75 to 79 K (77 K typical)			
	Min.	Typ.	Max.	Unit
SQUID critical current $2I_C$	10	20	100	μA
SQUID resistance $R/2$	1	5	10	Ω
Feedback mutual inductance $1/M_f$	-	-	-	$\mu A/\Phi_0$
Voltage swing ΔV	20	30	-	μV
Field calibration	7	8.5	10	nT/Φ_0
Field noise $S_B^{1/2}(f)$, f > 10 Hz	-	-	100	$fT/Hz^{1/2}$
Temp. coefficient at 77K	-	1	-	nT/K
Heater power (~110 Ohm at 77 K)	-	-	2	W
Heat time to normalize	-	-	10	Sec
Storage temperature (dry)	0	20	40	°C

Table 2.2 Specifications, M1000v14 magnetometer.

Parameter	Value			
Pickup loop size	9.3 mm × 8.5 mm OD, 3.8 mm ×3.0 mm ID			
Feedback coil inductance L_f	36 μH (wire-wound copper coil)			
Operating temperature	75 to 79 K (77 K typical)			
	Min.	Typ.	Max.	Unit
SQUID critical current $2I_C$	10	20	100	μA
SQUID resistance $R/2$	1	5	10	Ω
Feedback mutual inductance $1/M_f$	4	7	10	$\mu A/\Phi_0$
Voltage swing ΔV	20	30	-	μV
Field calibration	7	10	13	nT/Φ_0
Field noise $S_B^{1/2}(f)$, f > 10 Hz	-	-	100	$fT/Hz^{1/2}$
Temp. coefficient at 77K	-	1	-	nT/K
Heater power (Ohm at 77 K)	-	-	2	W
Heat time to normalize	-	-	5	Sec
Storage temperature (dry)	0	20	40	°C

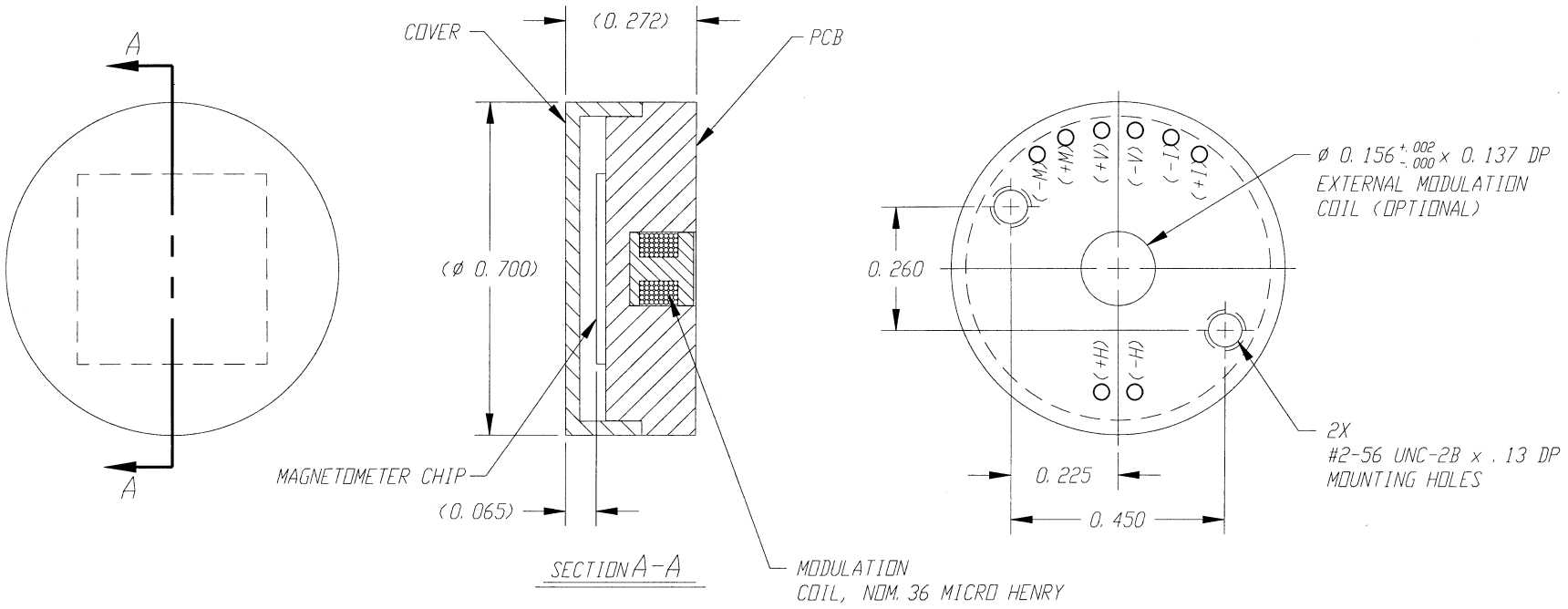

NOTES: UNLESS OTHERWISE SPECIFIED.

1 MATL: COVER G-10
PCB FR-4

2 ALL CONTACT VIAS ARE WITHIN ø 0.639

Figure 3.2 Mechanical specifications, M1000 magnetometer button package.

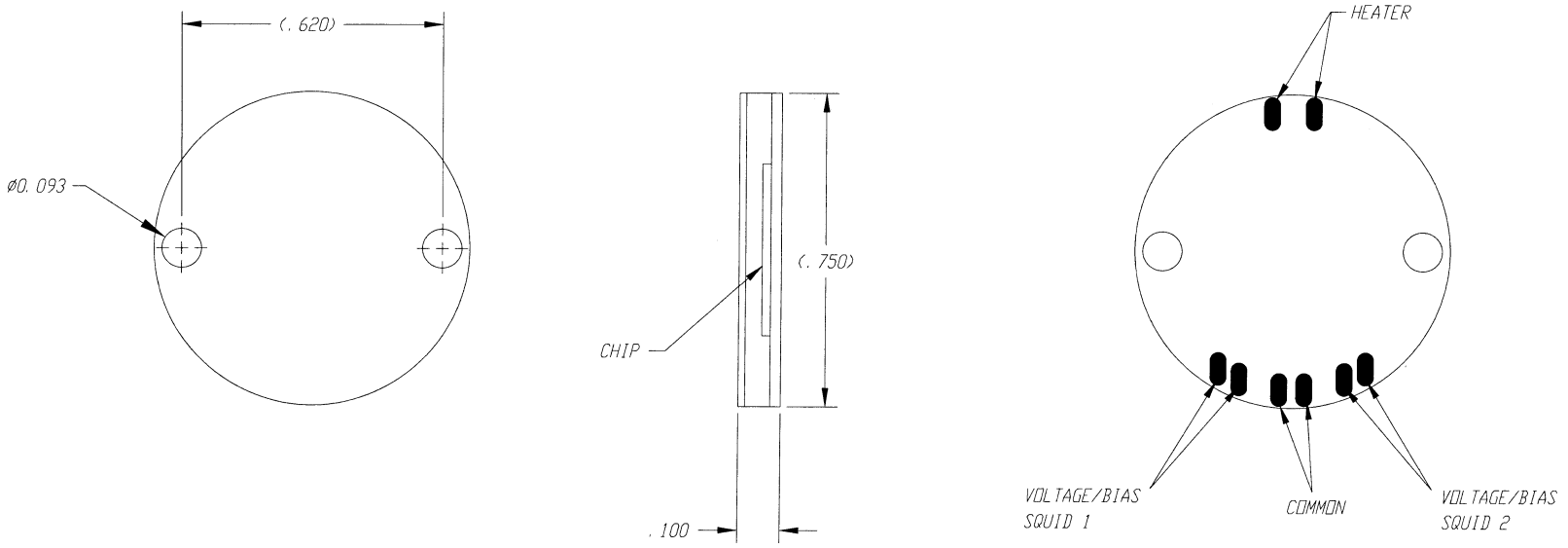

Figure 3.3 Mechanical specifications, M19 package.

Bibliography

[1] Sloof, M., Tijskens, L. and Wilkinson, E.: Concepts for modelling the quality of perishable products. *Trends in Food Science and Technology.*, vol. 7, pp. 165–171, 1996.

[2] Levitt, M.H.: *Spin Dynamics, 2nd Edition.* John Wiley & Sons, 2008.

[3] . Photograph by Mai-Linh Doan.

[4] Orlando, T.P. and Delin, K.A.: *Foundations of Applied Superconductivity.* Addison-Wesley Publishing Company, 1991.

[5] Conradie, E.H.: *The Design and Manufacture of DC SQUID Magnetometers.* Master's thesis, University of Stellenbosch, 1998.

[6] Graser, F.W.: *A Reproducible Design and Manufacturing Process for SQUID Magnetometers.* Master's thesis, University of Stellenbosch, 2005.

[7] Connor, C.: Low frequency magnetic resonance with a dc squid. *Adv. Magn. Opt. Reson.*, vol. 15, pp. 201–263, 1990.

[8] Liao, S.-H., Yang, H.-C., Horng, H.-E., Yang, S.Y., Chen, H.H., Hwang, D.W. and Hwang, L.-P.: Sensitive j-coupling spectroscopy using high-t_c superconducting quantum interference devices in magnetic fields as low as microteslas. *Supercond. Sci. Technol.*, vol. 22, p. 045008, 2009.

[9] Liao, S.-H., Horng, H.-E., Yang, H.-C. and Yang, S.-Y.: Longitudal relaxation time detection using high-t_c superconductive quantum interference device magnetometer. *Journal of Applied Physics*, vol. 102, p. 033914, 2007.

[10] Halse, M.E.: *Multi-acquisition and multi-dimensional earth's field nuclear magnetic resonance spectroscopy.* Ph.D. thesis, Victoria University of Wellington, 2009.

[11] . Picture by Ansgar Hellwig.

[12] . Picture by Geek3.

[13] Salunkhe, D. and Kadam, S. (eds.): *Handbook of Fruit Science and Technology: Production, Composition, Storage and Processing.* Marcel Dekker, Inc., 1995.

[14] van Zyl, A.: *The Application of Fourier Transform Near Infrared (FT-NIR) Spectroscopy in the Wine, Fruit and Dried Fruit Industries of South Africa.* Master's thesis, University of Stellenbosch, 2000.

[15] Hills, B.P. and Clark, C.J.: Quality assessment of horticultural products by nmr. *Annual Reports on NMR Spectroscopy*, vol. 50, pp. 75–120, 2003.

[16] Tijskens, L.M.: *Fruit and Vegitable Quality: An Integrate View, Chapter 7.* Technomic Publishing Co., Inc., 2000.

[17] Meulenberg, M. and Broens, D.: Trends in de prodictie van voedingsmiddelen. inzicht in ketens helpt bij ketenvorming. *Voedingsmiddelen technologie*, vol. 29, no. 12, pp. 19–25, 1996.

[18] Wierenga, B.: Multidimentional models for the analysis of consumers' perception and preferences with respect to agricultural and food products. *Journal of Agricultural Economics*, vol. 31, no. 1, pp. 83–97, 1980.

[19] Frewer, L., Raats, M. and Shepard, R.: Modelling the media: the transmission of risk information in the british quality press. *IMA Journal of Mathematics Applied in Business and Industry*, vol. 5, pp. 235–247, 1993/1994.

[20] Steenkamp, J.-B.E.M.: *Product quality: an investigation into the concept and how it is perceived by consumers.* Ph.D. thesis, Agricultural University Wageningen, The Netherlands, 1989.

[21] Knee, M. (ed.): *Fruit Quality and its Biological Basis.* Sheffield Academic Press, 2002.

[22] Durst, R.A.: "ph", in accessscience@mcgraw-hill, http://www.accessscience.com, doi 10.1036/1097-8542.504000.

[23] Filler, A.: The history, development, and impact of computed imaging in neurological diagnosis and neurosurgery: Ct, mri, dti. 2009.
Available at: `http://dx.doi.org/10.1038/npre.2009.3267.3`

[24] Mehra, J; Rechenberg, H.: *The Historical Development of Quantum Theory.* Springer, 2000.

[25] Rabi, I.I., Zacharias, J.R., Millman, S. and Kusch, P.: A new method of measuring nuclear magnetic moment. *Phys. Rev.*, vol. 53, p. 318, 1938.

[26] Purcell, E.M., Torrey, H.C. and Pound, R.V.: Resonance absorption by nuclear magnetic moments in a solid. *Phys. Rev.*, vol. 69, pp. 37–38, 1945.

[27] Bloch, F.: Nuclear induction. *Phys. Rev.*, vol. 70, pp. 460–474, 1946.

[28] Bloch, F. and Hansen, W.: Methods and means for chemical analysis by nuclear inductions. 1951.

[29] Carr, H.: Effects of diffusion on free precession in nuclear magnetic resonance experiments. *Phys. Rev.*, vol. 94, pp. 630–638, 1954.

[30] Meiboom, S. and Gill, D.: Modified spin-echo method for measuring nuclear relaxation times. *Rev. Sci. Instr.*, vol. 29, pp. 688–691, 1958.

[31] Hahn, E.L.: Spin echoes. *Phys. Rev.*, vol. 80, pp. 580–594, 1950.

[32] Griffiths, D.J.: *Introduction to Quantum Mechanics*. Prentice Hall, 1995.

[33] Hahn, E.P. and Das, T.P.: *Nuclear Quadrupole Resonance Spectroscopy*. Academic Press, 1958.

[34] Berger, S. and Braun, S.: *200 and more NMR Experiments: A Practical Course*. Wiley-VCH, 2004.

[35] Onnes, H.K.: The resistance of pure mercury at helium temperatures. *Comm. Leiden*, vol. 120b, 1911.

[36] Onnes, H.K.: The disappearance of resistivity of mercury. *Comm. Leiden*, vol. 122b, 1911.

[37] Burger, W.A.: *The Design and Analysis of a DC SQUID for a SQUID Microscope*. Master's thesis, University of Stellenbosch, 2008.

[38] Meissner, W. and Ochsenfeld, R.: Ein neuer effekt bei eintritt der supraleitfähigkeit. *Naturwissenschaften*, vol. 21, no. 44, pp. 787–788, 1933.

[39] Gorter, C.J. and Casimir, H.B.G.: *Physik. Z.*, vol. 35, p. 963, 1934.

[40] London, F. and London, H.: The electromagnetic equations of the supraconductor. *Proceedings of the Royal Society of London. Series A, Mathematical and Physical Sciences*, vol. 149, no. 866, pp. 71–88, 1935.

[41] Ginzburg, V.L. and Landau, L.D.: *Zh. Eksp. Teor. Fiz.*, vol. 20, p. 1064, 1950.

[42] Cooper, L.N.: Bound electron pairs in a degenerate fermi gas. *Phys. Rev*, vol. 104, pp. 1189 – 1190, 1956.

[43] Bardeen, J., Cooper, L.N. and Schrieffer, J.R.: Microscopic theory of superconductivity. *Phys. Rev.*, vol. 106, pp. 162 – 164, 1957.

[44] Bardeen, J., Cooper, L.N. and Schrieffer, J.R.: Theory of superconductivity. *Phys. Rev.*, vol. 108, p. 1175, 1957.

[45] Bednorz, J.G. and Müller, K.A.: Possible high t_c superconductivity in the ba-la-cu-o system. *Zeit. Phys. B.*, vol. 64, p. 189, 1986.

[46] Wu, M.K., Ashburn, J.R., Thorng, C.J., Hor, P.H., Meng, R.L., Gao, L., Huang, Z.J., Wang, Y.Q. and Chu, C.W.: Superconductivity at 93k in a new mixed-phase y-ba-cu-o compound system at ambient pressure. *Phys. Rev. Letters*, vol. 58, no. 9, pp. 908–910, 1987.

[47] Chu, C.W., Gao, L., Chen, F., Huang, Z.J., Meng, R.L. and Xue, Y.Y.: Superconductivity above 150 k in $hgba_2ca_2cu_3o_{8+\delta}$ at high pressures. *Nature*, vol. 365, pp. 323–325, 1993.

[48] Duzer, T.V. and Turner, C.W.: *Principles of Superconductive Devices and Circuits, Second Edition.* Prentice Hall PTR, 1999.

[49] Mourachkine, A.: *Room-Temperature Superconductivity.* Cambridge International Science Publishing, 2004.

[50] Doss, J.D.: *Engineer's guide to high-temperature superconductivity.* John Wiley & Sons, 1989.

[51] Rottier, P.A.: *Establishing a process for the fabrication of high-quality HT_c SQUIDs.* Master's thesis, University of Stellenbosch, 2002.

[52] Knox-Davies, E.C.: *The Design and Fabrication of a High-T_c DC SQUID Gradiometer.* Master's thesis, University of Stellenbosch, 1999.

[53] Khare, N.: *Handbook of High Temperature Superconductor Electronics.* Marcel Deker, Inc., 2003.

[54] Josephson, B.: Possible new effects in superconductive tunnelling. *Physics Letters*, vol. 1, no. 7, pp. 251–253, 1962.

[55] Anderson, P. and Rowell, J.: Probable observation of the josephson superconducting tunneling effect. *Phys. Rev. Letters*, vol. 10, pp. 230–232, 1963.

[56] Likharev, K.: Superconducting weak links. *Rev. Mod. Phys.*, vol. 51, no. 1, p. 101, 1979.

[57] Stewart, W.C.: Current-voltage characteristics of josephson junctions. *App. Phys. Letters*, vol. 12, p. 277, 1968.

[58] McCumber, D.E.: Effect of the ac impedance on the dc voltage-current characteristics of superconductor weak link structures. *Journal of Applied Physics*, vol. 391, p. 3113, 1968.

[59] Weinstock, H. and Ralsten, R.W. (eds.): *The New Superconducting Electrionics, NATO ASI Series*. Kluwer Academic Press, 1993.

[60] Barone, A. and Paterno, G.: *Physics and Applications of the Josephson Effect*. John Wiley and Sons, 1982.

[61] Barone, A. (ed.): *Principles and Applications of Superconducting Quantum Inteference Devices*. World Scientific Publishing, 1992.

[62] Enpuku, K., Maruo, T. and Minotani, T.: Effect of large dielectric constant of $srtio_3$ substrate on the characteristics of high t_c dc superconducting quantum inteference device. *Journal of Applied Physics*, vol. 80, no. 2, p. 1207, 1996.

[63] Gallop, J.: *SQUIDs, The Josephson Effects and Superconducting Electronics*. IOP Publishing Ltd, Adam Hilger Series, 1991.

[64] Clarke, J. and Braginski, A.I. (eds.): *The SQUID Handbook, Vol. I Fundamentals and Technology of SQUIDs and SQUID Systems*. Wiley-VCH verlag GmbH and Co. KGaA, 2004.

[65] Kadin, A.M.: *Introduction to Superconducting Circuits*. John Wiley & Sons, Inc., 1999.

[66] Eidelloth, W., Gallagher, W., Robertazzi, R., Koch, R., Oh, B. and Sandstrom, R.: Wet etch process for patterning insulators suitable for epitaxial high t_c superconducting thin film multilevel electronic circuits. *App. Phys. Letters*, vol. 59, no. 10, pp. 1257–1259, 1991.

[67] Ludwig, F., D.Koelle, Dantsker, D., Nemeth, D., Miklich, A., Clarke, J. and Thomson, R.: Low noise $yba_2cu_3o_{7-\delta} - srtio_3 - yba_2cu_3o_{7-\delta}$ multilayers for

improved superconducting magnetometers. *App. Phys. Letters*, vol. 66, no. 3, pp. 373–375, 1995.

[68] Drung, D., Dantsker, E., Ludwig, F., Koch, H., Kleiner, R., Clarke, J., Krey, S., Reimer, D., David, B. and Doessel, O.: Low noise $yba_2cu_3o7-\delta$ squid magnetometers operated with additional positive feedback. *App. Phys. Letters*, vol. 68, no. 2, pp. 1856–1857, 1996.

[69] Lin, J., Haung, T., Wang, J., Lu, H., Tu, S., Yang, S. and Hsu, S.: $yba_2cu_3o_{7-\delta}$ dc squid on mgo bicrystal substrate with flux transformer. *IEEE Transactions on Applied Superconductivity*, vol. 3, no. 1, pp. 2438–2441, 1993.

[70] Koelle, D., Miklich, A., Ludwig, F., Dantsker, E., Nemeth, D. and Clarke, J.: High performance dc squid magnetometers with single layer $yba_2cu_3o_{7-\delta}$ flux transformers. *Appl. Phys. Letters*, vol. 63, no. 26, pp. 3630–3632, 1993.

[71] Grundler, D., David, B. and Doessel, O.: Experimental investigation of the kinetic inductance in $yba_2cu_3o_7$ square washer superconducting quantum interference devices. *J. Appl. Phys.*, vol. 77, no. 10, pp. 5273–5277, 1995.

[72] Koelle, D., Miklich, A., Ludwig, F., Dantsker, E., Nemeth, D. and Clarke, J.: Dc squid magnetometers from single layers of $yba_2cu_3o_{7-\delta}$. *Appl. Phys. Letters*, vol. 63, no. 16, pp. 2271–2273, 1993.

[73] Ziemer, R. and Tranter, W.: *Principles of Communication, Fifth Edition.* John Wiley and Sons, Inc., 2002.

[74] Enpuku, K., Shimomure, Y. and Kisu, T.: Effect of thermal noise on the characteristics of a high t_c superconducting quantum interference devices. *J. Appl. Phys.*, vol. 73, no. 11, pp. 7929–7934, 1993.

[75] Koch, R., Eidelloth, W., Oh, B., Robertazzi, R., Andrek, S. and Gallagher, W.: Identifying the source of 1/f noise in squids made from high-temperature superconductors. *Appl. Phys. Letters*, vol. 60, no. 4, pp. 507–509, 1992.

[76] Dantsker, E., Tanaka, S. and Clarke, J.: High t_c superconducting quantum interference devices with slots or holes: Low 1/f noise in ambient magnetic fields. *App. Phys. Letters*, vol. 70, no. 15, pp. 2037–2039, 1997.

[77] Oyama, H., Kuriki, S. and Matsuda, M.: Effects of flux dam on low-frequency noise in high t_c squid magnetometers. *IEEE Transactions on Applied Superconductivity*, vol. 11, no. 1, pp. 1331–1334, 2001.

[78] ter Brake, H., Aaenink, W., van den Bosch, P., Hilgenkamp, J., Flokstra, J. and Rogalla, H.: Temperature dependance of the effective sensing area of high t_c dc squids. *Supercond. Sci. Technol.*, vol. 10, pp. 512–515, 1997.

[79] Ogata, K.: *Modern Control Engineering, Fourth Edition.* Prentice Hall, Inc., 2002.

[80] Drung, D., Cantor, R., Peters, M., Scheer, H. and Koch, H.: Low-noise high speed dc superconducting quantum interference device magnetometer with simplified feedback electronics. *App. Phys. Letters*, vol. 57, no. 4, p. 406, 1990.

[81] Enpuku, K., Tokita, G., Maruo, T. and Minotani, T.: Parameter dependencies of characteristics of a high t_c dc superconducting quantum interference device. *J. Appl. Phys.*, vol. 78, no. 11, pp. 3498–3503, 1995.

[82] Whitely, S.R.: *FastHenry Version 3.0wr*, p. Availiabile from the Whiteley Research Homepage: http://www.srware.com, 2001.

[83] Kamon, M., Tsuk, M.J. and Whitely, J.K.: Fasthenry: A multipole-accelerated 3-d inductance extraction program. *IEEE Transactions on Microwave Theory and Techniques*, vol. 42, no. 9, pp. 1750–1758, 1994.

[84] Kamon, M., Silveira, L.M., Smithhisler, C. and White, J.: *FastHenry's User Guide*, vol. Massachusetts Institute of Technology, 1996.

[85] Fourie, C.J.: *A Tool Kit for the Design of Superconducting Programmable Gate Arrays.* Ph.D. thesis, University of Stellenbosch, 2003.

[86] *MATLAB R2007a*, . The Mathworks, Inc.: Homepage: http://www.mathworks.com.

[87] Dimos, D., Chaudhari, P. and Mannhart, J.: Superconducting transport properties of grain boundries in $yba_2cu_3o_7$ bicrystals. *Physical Review B*, vol. 41, no. 7, pp. 4038–4049, 1990.

[88] Schmidl, F., Gross, R., Husemann, K.D., Schneidewind, H. and Seidel, P.: Superconducting transport propperties of step-edge josephson junctions. *IEEE Transactions on Applied Superconductivity*, vol. 3, no. 1, p. 2349, 1993.

[89] Luine, J., Bulman, J., Burch, J., Daly, K., Lee, A., Pettiette-Hall, C., Schwarzbek, S. and Miller, D.: Characteristics of high performance yba_2cu_3o7 step-edge junctions. *Applied Physics Letters*, vol. 61, no. 9, p. 1128, 1992.

[90] Char, K., Colclough, M., Garrison, S.M., Newman, N. and Zaharchuk, G.: Bi-epitaxial grain boundry junctions in $yba_2cu_3o_7$. *Applied Physics Letters*, vol. 59, no. 6, p. 733, 1991.

[91] Char, K., Colclough, M.S., Lee, L.P. and Zaharchuk, G.: Extension of the bi-epitaxial josephson junction process to various substrates. *Applied Physics Letters*, vol. 59, no. 17, p. 2177, 1991.

[92] Beck, A., Stenzel, A., Froehlich, O.M., Gerber, R., Gerdemann, R., Alff, L., Mayer, B., Gross, R., Marx, A., Villegier, J.C. and Moriceau, H.: Fabrication and superconducting transport properties of bicrystal grain boundry josephson junctions on different substrates. *IEEE Transactions on Applied Superconductivity*, vol. 5, no. 2, p. 2192, 1995.

[93] Robertazzi, R.P., Koch, R.H., Laibowitz, R.B. and Gallagher, W.J.: $y_1ba_2cu_3o_7/mgo/y_1ba_2cu_3o_7$ edge josephson junctions. *IEEE Transactions on Applied Superconductivity*, vol. 3, no. 1, p. 2030, 1993.

[94] Pauza, A.J., Booij, W.E., Herrmann, K., Moore, D.F., Blamire, M.G., Rudman, D.A. and Vale, L.R.: Electron-beam damaged high-temperature superconductor josephson junctions. *Journal of Applied Physics*, vol. 82, no. 11, p. 5612, 1997.

[95] Büttner, U.: Personal Communication.

[96] Phillips, J.M.: Substrate selection for high-temperature superconducting thin films. *Journal of Applied Physics*, vol. 79, pp. 1829–1848, 1995.

[97] Matlachov, A.N., Volegov, P.L., Espy, M.A., George, J.S. and Kraus, R.H.: Squid detected nmr in microtesla fields. *Journal of Magnetic Resonance*, vol. 170, pp. 1–7, 2004.

[98] Appelt, S., Kühn, H., Häsing, F.W. and Blümich, B.: Chemical analysis by ultrahigh-resolution nuclear magnetic resonance in the earth's magnetic field. *Nature Physics*, vol. 2, pp. 105–108, 2006.

[99] Schlenga, K., McDermott, R., Clarke, J., de Souza, R.E., Wong-Foy, A. and Pines, A.: Low-field magnetic resonance imaging with a high-t_c dc superconducting quantum interference device. *Applied Physics Letters*, vol. 75, no. 23, pp. 3695–3697, 1999.

[100] McDermott, R., Trabesinger, A.H., Mück, M., Hahn, E.L., Pines, A. and Clarke, J.: Liquid-state nmr and scalar couplings in microtesla magnetic fields. *Science*, vol. 295, pp. 2247–2249, 2002.

[101] Greenburg, Y.S.: Application of superconducting quantum interference devices to nuclear magnetic resonance. *Reviews of Modern Physics*, vol. 70, no. 1, pp. 175–222, 1998.

[102] Augustine, M.P., TonThat, D.M. and Clarke, J.: Squid detected nmr and nqr. *Solid State Nuclear Magnetic Resonance*, vol. 11, pp. 139–156, 1998.

[103] Day, E.P.: Detection of nmr using a josephson-junction magnetometer. *Physical Review Letters*, vol. 29, no. 9, pp. 540–542, 1972.

[104] Silver, A.H. and Zimmerman, J.E.: Multiple quantum resonance spectroscopy through weakly connected superconductors. *Applied Physics Letters*, vol. 10, p. 142, 1968.

[105] Meredith, D.J., Pickett, G.R. and Symko, O.: Application of a squid magnetometer to nmr at low temperatures. *Journal of Low Temperature Physics*, vol. 13, p. 607, 1973.

[106] Hirschkoff, E.C., Symko, O., Vant-Hull, L.L. and Wheatley, J.C.: Observation of the static nuclear magnetism of pure metallic copper in low magnetic fields. *Journal of Low Temperature Physics*, vol. 2, p. 653, 1970.

[107] Suzuki, H., Higashino, Y. and Ohtsuka, T.: Squid nmr studies of tmpo4. *Journal of Low Temperature Physics*, vol. 41, p. 449, 1980.

[108] Clarke, J. and Braginski, A.I. (eds.): *The SQUID Handbook, Vol. 2 Applications of SQUIDs and SQUID Systems.* Wiley-VCH, 2006.

[109] Seton, H.C., Bussell, D.M., Hutchison, J.M., Nicholson, I. and Lurie, D.J.: Dc squid based nmr detection from room temperature samples. *Phys. Med. Biol.*, vol. 37, no. 11, pp. 2133–2138, 1992.

[110] Kumar, S., Thorson, B.D. and Avrin, W.F.: Broadband squid nmr with room-temperature samples. *Journal of Magnetic Resonance, Series B*, vol. 107, pp. 252–259, 1995.

[111] Körber, R., Casey, A., Shibahara, A., Piscitelli, M., Cowan, B.P., Lusher, C.P., Saunders, J., Drung, D. and Schurig, T.: Nuclear magnetic resonance on room

temperature samples in nanotesla fields using a two-stage dc superconducting quantum interference device sensor. *Applied Physics Letters*, vol. 91, p. 142501, 2007.

[112] Kumar, S., Matthews, R., Haupt, S.G., Lathrop, D.K., Takigawa, M., Rozen, J.R., Brown, S.L. and Koch, R.H.: Nuclear magnetic resonance using a high temperature superconducting quantum interference device. *Applied Physics Letters*, vol. 70, no. 8, pp. 1037–1039, 1997.

[113] Qui, L., Zhang, Y., Krause, H.-J., Braginski, A.I., Burghoff, M. and Trahms, L.: Nuclear magnetic resonance in the earth's magnetic field using a nitrogen-cooled superconducting quantum interference device. *Applied Physics Letters*, vol. 91, p. 072505, 2007.

[114] Zhang, Y., Qiu, L., Krause, H.-J., Hartwig, S., Burghoff, M. and Trahms, L.: Liquid state nuclear magnetic resonance at low fields using a nitrogen cooled superconducting quantum interference device. *Applied Physics Letters*, vol. 90, p. 182503, 2007.

[115] Packard, M. and Varian, R.: Free nuclear induction in the earth's magnetic field. *Phys. Rev.*, vol. 93, pp. 941–941, 1954.

[116] Planinsic, G., Stepisink, J. and Kos, M.: Relaxation-time measurement and imaging in the earth's magnetic field. *Journal of Magnetic Resonance, Series A*, vol. 110, p. 170, 1994.

[117] Yang, H.-C., Liao, S.-H., Horng, H.-E., Kuo, S.-L., Chen, H.-H. and Yang, S.Y.: Enhancement of nuclear magnetic resonance in microtesla magnetic field with prepolarization field detected with high-t_c superconducting quantum interference device. *Applied Physics Letters*, vol. 88, p. 252505, 2006.

[118] *LTSpice IV*, . Linear Technologies: Homepage: www.linear.com.

[119] Gross, R., Chaudhari, P., Dimos, D., Gupta, A. and Koren, G.: Thermally activated phase slippage in high t_c grain-boundry josephson junctions. *Physical Review Letters*, vol. 64, no. 2, p. 228, 1990.

[120] Microchip: *MPLab IDE Version 8.5*, .

[121] Microchip: *MPLAB C Compiler for PIC18 MCUs v3.35*, .

[122] *Mr. SQUID user's guide*. Conductus Inc. / STAR Cryoelectronics, 25-A Brisbane Court, Santa Fe, NM 87508.

[123] Cho, S.I., Stroshine, R.L., Baianu, I.C. and Krutz, G.W.: Nondestructive sugar content measurements of intact fruit using spin-spin relaxation time (t_2) measurements by pulsed ^1h magnetic resonance. *Transactions of the ASAE (USA)*, vol. 36, no. 4, pp. 1217–1221, 1993.

[124] Abbott, J.A.: Quality measurement of fruits and vegitables. *Postharvest Biology and Technology*, vol. 15, pp. 207–225, 1998.

[125] Hills, B.P.: Applications of low-field nmr to food science. *Annual Reports on NMR Spectroscopy*, vol. 58, pp. 177–230, 2006.

[126] Qiu, L., Zhang, Y., Krause, H.-J., Braginski, A.I. and Offenhäusser, A.: Low-field nmr measurement procedure when squid detectection is used. *Journal of Magnetic Resonance*, vol. 196, pp. 101–104, 2008.

[127] Jayasena, V. and Cameron, I.: ^{0}brix/acid ratio as a predictor of consumer acceptability of crimson seedless table grapes. *Journal of Food Quality*, vol. 31, pp. 736–750, 2008.

[128] van Zyl, B.: Personal Communication.

[129] Kim, S.-M., Chen, P., McCarthy, M. and Zion, B.: Fruit internal quality evaluation using on-line nuclear magnetic resonance sensors. *J. agric. Engng Res.*, vol. 74, pp. 293–301, 1999.

[130] Born, M.: Zur quantenmechanik der stoβvorgänge. *Zeit. Phys. A.*, vol. 37, pp. 863–867, 1926.

[131] van Zyl, A.J.: *Basic Concepts of Random Matrix Theory.* Master's thesis, University of Stellenbosch, 2005.

[132] Anton, H. and Rorres, C.: *Elementary Linear Algebra (Applications Version), 8th Edition.* Wiley, 2000.